

DIFFUSE TOMOGRAPHY OF ABSORBING AND FLUORESCENT OPTICAL
EXOGENOUS CONTRAST GUIDED BY SIMULTANEOUSLY ACQUIRED
MAGNETIC RESONANCE IMAGES

A Thesis
Submitted to the Faculty
in partial fulfillment of the requirements for the
degree of

Doctor of Philosophy

by

SCOTT CHRISTIAN DAVIS

Thayer School of Engineering
Dartmouth College
Hanover, New Hampshire

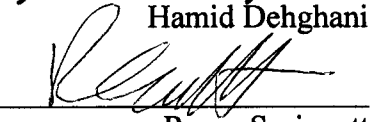
May 2008

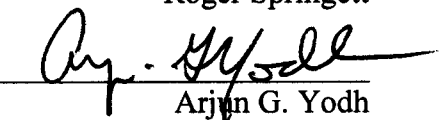
Examining Committee:

Chairman 
Brian W. Pogue

Member 
Keith D. Paulsen

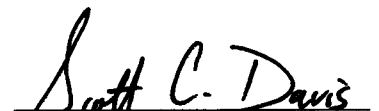
Member 
Hamid Dehghani

Member 
Roger Springett

Member 
Arjun G. Yodh

Charles K. Barlow
Dean of Graduate Studies

© 2008 Trustees of Dartmouth College


Signature of Author

Abstract

Fluorescent molecules targeted to reveal information on tissue function have been used as research tools in *ex vivo* and subsurface characterization of diseased tissue for years. Exploiting this specificity for *in vivo* imaging through centimeters of tissue is a challenging problem due to high signal attenuation from light absorption and elastic scattering. Therefore, diagnostic imaging of exogenous contrast agents through tissue requires model-based techniques which even under the best of circumstances suffer from relatively poor spatial-resolution and non-uniform sensitivity throughout the imaging field.

These challenges are addressed by incorporating tissue structural information derived from a highly resolved clinical imaging modality into diffuse fluorescence and spectrally-constrained absorption tomographic image reconstruction routines. A multi-channel spectroscopic molecular imaging system capable of collecting spectrally-resolved near-infrared transmission and luminescent data from within an MRI bore was developed for imaging exogenous fluorescence contrast in small animals and human breast. Anatomical information from simultaneously acquired magnetic resonance images incorporated into the optical image reconstruction algorithms was shown to dramatically improve the spatial and contrast resolutions of heterogeneously distributed fluorescence activity in breast-sized tissue phantoms. Pilot studies of brain tumors (gliomas) in a small number of mice demonstrated spatially-guided fluorescence imaging of epidermal growth factor receptor (EGFR) using a targeted optical fluorophore. Tomographic images of fluorescence activity were confirmed by histopathology.

Finally, multi-wavelength imaging techniques which incorporate the molar extinction spectra of the constituent chromophores, including those of exogenously administered drugs, can be used to quantify concentrations of hemoglobin, water, oxygen saturation and the contrast agent. Simulated and experiemntal phantom data show that it is feasible to use spectrally-constrained absorption tomography to recover concentrations of exogenous contrast directly, especially for high drug concentrations. However, in cases where drug concentrations are lower, absorption-based measurements are much less sensitive than those derived from fluorescence emission.

Acknowledgements

I extend my sincere gratitude to Brian Pogue. To me, Brian has found the perfect balance between facilitating his students' independence as researchers and providing advice and guidance. I believe this to be one of the most important qualities of an effective advisor. My independence, research aptitude, professional development and graduate studies in general have been enriched by Professor Pogue's mentoring. I also value his and his family's friendship. I am eager to continue working with Brian in the future.

I thank my other advisor, Keith Paulsen. The resources Keith has helped make available to his students must be unique in the world and I feel privileged to have worked here. Our discussions and brainstorming sessions have been stimulating and productive and he has always been extremely supportive of all of my work. Working with Keith directly on grant proposals taught me invaluable lessons about research funding and has made me a more productive, and perhaps even tenacious, researcher.

I came away from my first meeting with Hamid Dehghani thinking that he asks insightful questions, and many of them. Hamid's inquisitiveness became a cornerstone of our collaborative work. Working with Hamid on a daily was always been productive and enjoyable and he seems to have a gift for inspiring his students to produce high quality, interesting work. I also value his and his family's friendship, as well as the unrelenting supply of Toblerone chocolate bars.

My professional relationship with colleague and friend Summer Gibbs-Strauss represents what I believe to be an ideal scientific collaboration. Our complimentary expertise, mutual dedication to high quality work, and absolutely selfless approach to collaborative

work facilitated research and learning that I believe was greater than the sum of its parts. I certainly owe most of my working knowledge of biology to Summer.

I am grateful for having the opportunity to work with Roger Springett. His expertise in optics, biology, and spectroscopy had a great impact on this work. I also thank Roger for dedicating a large portion of his time to manufacturing optical systems for this project, and for serving on my thesis committee.

I thank Arjun Yodh for traveling to Hanover to serve on my thesis committee. His comments and insights have shaped the future directions of the projects in this thesis.

I would also like to thank Shudong Jiang for her assistance in the lab and, of course, for the frequent and “spirited” discussions. In truth, these discussions always had a positive impact on the resulting work. Shudong keeps the lab running and is often willing to drop what she is doing to assist students with laboratory systems.

I thank my other colleagues and friends at Dartmouth, Colin Carpenter, Jia Wang, Phani Yalavarthy, Philip Perrinez, Subha Srinivasan, Pablo Fernandez, Julia O’hara, Kim Samkoe, Ben Bolinger, Fred Leblond, Zhiqiu Li, Ashley Laughney, and Venkat Krishnaswamy.

Returning to school after several years was an interesting transition. I thank Simon Shepherd for helping remind me how much I enjoy learning. He is an inspiring teacher and effective ski coach. I am confident that this year’s private ski lesson will make the difference between a 2nd and 3rd to last finish in next year’s Wonalancet 10K, with no additional training.

I was fortunate to work with two very dedicated and innovative undergraduates, Stephen Tuttle and Max Friedman, who routinely stayed well beyond normal working hours to complete experiments. I wish both of them the best of luck in future endeavors.

I also would like to thank Thayer school for fostering an excellent environment in which to learn. The commitment to student's success is evident and the professional and courteous staff made the experience enjoyable and productive.

I thank my parents, Ginger and Steve who have always cultivated and encouraged my curiosity, creativity, and inquisitive nature. Mom, you are the strongest, most selfless and loving person I know. Dad, I try every day to model your patience and character as a father (and physicist, of course). I have so much respect for both of you.

The time in which this thesis materialized witnessed a marriage to my sweetheart, Anne, and the birth of another sweetheart, Heidi. These years have been all the more rewarding with Anne's patience, support, laughter, and love. I appreciate you, Anne, and appreciate all that you have shouldered, especially in these past few years. Heidi, you are an absolute delight and have done so much to lift the spirits of our family in difficult times.

This work was funded by Philips Research Hamburg, National Institutes of Health grants RO1 CA109558, RO1 CA69544, U54 CA105480, and the Department of Defense Breast Cancer pre-doctoral fellowship BC051058.

Dedication

Dedicated to my mom, Virginia Davis

Table of Contents

Approval Page.....	i
Abstract.....	ii
Acknowledgements.....	iv
Dedication.....	vii
Table of Contents.....	viii
List of Tables.....	xii
List of Figures and Illustrations.....	xiii
CHAPTER ONE: INTRODUCTION AND BACKGROUND.....	1
CHAPTER TWO: INSTRUMENTATION.....	9
2.1 System Design.....	10
2.1.1 Optical Detection System.....	11
2.1.2 Light collection and delivery.....	13
2.1.3 Light sources.....	17
2.1.4 Patient/animal interface.....	18
2.1.5 Automated Acquisition.....	22
2.2 Frequency Domain Measurements.....	24
2.3 Summary.....	25
CHAPTER THREE: MODELING AND IMAGE RECONSTRUCTION TECHNIQUES.....	27
3.1 Fluorescence imaging.....	27
3.1.1 Modeling fluorescence fields.....	27
3.1.2 Fluorescence image reconstruction.....	32
3.2 Chromophore concentration recovery using spectral priors.....	37
3.3 Incorporating Spatial Priors.....	39
3.3.1 Soft spatial priors.....	40
3.3.2 “Hard” spatial priors.....	42
3.3.3 A brief note on modeling and reconstruction software developed for this work.....	43
CHAPTER FOUR: CONTRAST AGENTS AND TISSUE PHANTOMS.....	45
4.1 Exogenous Contrast Agents.....	45
4.1.1 Lutetium Texaphyrin and Gadolinium Texaphyrin.....	45
4.1.2 Indocyanine Green.....	46
4.1.3 IRDye 800CW EGF.....	48
4.1.4 Protoporphyrin IX.....	48
4.2 Photophysical features of the probes.....	50
4.3 Tissue Simulating Phantoms.....	52
CHAPTER FIVE: SYSTEM VALIDATION AND PERFORMANCE.....	56
5.1 System validation.....	56
5.1.1 Exposure time linearity.....	56
5.1.2 Wavelength accuracy.....	57

5.1.3 Filter OD calculation	60
5.1.4 Excitation source rejection	64
5.1.5 Nature of the “bleed-through” signal	64
5.2 Optical Data Processing.....	72
5.2.1 Baseline/dark current correction.....	72
5.2.2 Detector calibration	73
5.2.3 Source calibration.....	74
5.2.4 Fluorescence emission spectral fitting and data-model calibration.....	75
5.2.5 Alternative data processing approach.....	81
5.3 Homogeneous Fitting.....	82
5.4 System Performance	84
5.4.1 Repeatability.....	84
5.4.2 Sensitivity.....	85
5.5 Discussion and Summary.....	89
CHAPTER SIX: SPATIAL PRIOR IMPLEMENTATIONS FOR FLUORESCENCE TOMOGRAPHY	92
6.1 LuTex imaging using soft priors.....	93
6.1.1 Simulation studies	93
6.1.2 LuTex phantom studies: Perfect uptake	96
6.1.3 Simulation results	99
6.1.4 LuTex phantom results: Perfect uptake.....	103
6.1.5 Discussion.....	105
6.2 ICG phantom imaging: Imperfect drug uptake.....	106
6.2.1 Seventy millimeter pilot phantom	106
6.2.2 Ninety millimeter, single-inclusion phantoms	108
6.2.2.1 Methods	108
6.2.2.2 Results and Discussion	109
6.2.3 Three layer phantom.....	116
6.2.3.1 Methods	116
6.2.3.2 Results and Discussion	117
6.3 Summary.....	118
CHAPTER SEVEN: PILOT MRI-FMT STUDIES FOR IMAGING MURINE GLIOMAS	121
7.1 Initial Attempts at Sparse Data Sampling and Loose Fiber Coupling in MRI- FMT	121
7.1.1 Imaging endogenous PPIX fluorescence.....	123
7.1.1.1 Two region segmentation.....	123
7.1.1.2 Three region segmentation: False positive	124
7.1.2 Imaging ALA-induced PPIX fluorescence.....	126
7.1.3 Summary.....	127
7.2 EGFR imaging feasibility pilot study	128
7.2.1 Methods	128
7.2.2 Results	130
7.2.3 Ex vivo validation.....	131
7.2.4 Summary.....	133

CHAPTER EIGHT: EGF-TARGETED FLUORESCENCE TO MONITOR ERBITUX TREATMENT OF GLIOMAS IN MURINE MODELS	135
8.1 Methods	136
8.1.1 Mouse preparation and study parameters	136
8.1.2 Fiber positioning and MR image segmentation.....	137
8.2 Results and Discussion	141
8.2.1.1 Absence of visible tumors in the MR images.....	141
8.2.2 Homogeneous fitting	144
8.2.3 Image reconstruction	149
8.3 Summary.....	151
 CHAPTER NINE: IMAGING OF MR-DETECTABLE U-251 TUMORS USING FLUORESCENT EGF PROBE.....	153
9.1 Methods	154
9.1.1 Mouse preparation	154
9.1.2 Fiber positioning and MR Image segmentation	154
9.1.3 Confirmation of tumor-detection in MR images	158
9.2 Results.....	161
9.2.1 Homogenous fitting results and discussion	161
9.2.2 Image recovery results and discussion	167
9.2.2.1 A brief note on regularization.....	172
9.2.3 Ex-vivo validation of tumor-bearing subjects	174
9.3 Summary	182
 CHAPTER TEN: COMPARING SENSITIVITY OF FLUORESCENCE AND ABSORPTION-BASED MEASUREMENTS FOR DIFFUSE OPTICAL TOMOGRAPHY	184
10.1 Methods	186
10.1.1 Simulations.....	186
10.1.2 Phantom studies.....	188
10.2 Results.....	189
10.2.1 Simulation studies	189
10.2.1.1 Perturbations as a function of Quantum Yield.....	189
10.2.1.2 Quantum Yield Threshold	193
10.2.2 Phantom results	197
10.3 Discussion and summary	198
 CHAPTER ELEVEN: DIRECT RECOVERY OF CONTRAST AGENT CONCENTRATION USING SPECTRALLY CONSTRAINED IMAGE RECONSTRUCTION: A FEASIBILITY STUDY	202
11.1 Chromophore recovery using spectrally constrained reconstruction.....	205
11.1.1 Methods	205
11.1.1.1 Simulations: LuTex and ICG imaging.....	205
11.1.1.2 Phantom data.....	206
11.1.2 Results	207
11.1.2.1 Simulation results	207
11.1.2.2 Phantom results.....	209

11.1.3 Discussion.....	210
11.2 . Future directions: Combining recovered chromophore concentrations and fluorescence data to reconstruct fluorescence yield.....	211
CHAPTER TWELVE: THE BEAM SOFTENING EFFECT: SPECTRAL DISTORTION OF LUMINESCENCE IN TISSUE.....	215
12.1 Introduction.....	216
12.2 Experimental Details.....	218
12.2.1 Phantom design	218
12.2.2 Modeling Light Propagation.....	219
12.3 Results and Discussion	221
12.3.1 Phantom results	221
12.3.2 Diffusion modeling.....	226
12.3.3 Implications for fluorescence tomography in deep tissue	229
12.4 Summary.....	233
CHAPTER THIRTEEN: ASSESSING IMAGING PERFORMANCE: CONTRAST- DETAIL ANALYSIS FOR FLUORESCENCE TOMOGRAPHY	235
13.1 Methods	239
13.2 Results and Discussion	242
13.3 Summary.....	248
CHAPTER FOURTEEN: CONCLUDING REMARKS.....	250
CHAPTER FIFTEEN: ONGOING STUDIES AND IDEAS.....	254
15.1 Short-term objectives.....	254
15.1.1 Animal Imaging.....	254
15.1.2 Phantom validation.....	255
15.1.3 Combining multi-wavelength FD and CW spectral tomography systems	255
15.2 Long term objectives	257
15.2.1 Imaging multiple fluorophores simultaneously in vivo.....	257
15.2.2 Exogenous optical absorption and fluorescence in the human breast	257
15.2.3 3-D imaging.....	257
15.3 New ideas.....	258
15.3.1 Spectrally-resolved fluorescence emission tomography	258
15.3.2 Quantum Yield Imaging.....	259
APPENDIX A: SPECTRAL TOMOGRAPHY INSTRUCTION MANUAL	265
APPENDIX B: NIRFAST V2 DEV DOCUMENTATION.....	295
APPENDIX C: CALIBRATION ROUTINES FOR SPECTROSCOPIC TOMOGRAPHY DATA	334
BIBLIOGRAPHY.....	386

List of Tables

Table 5.1. Neon lamp emission peak wavelengths in the NIR as measured with each spectrometer.....	60
Table 6.1. Chromophore concentrations and scattering parameter values assigned to the mesh regions in the simulation studies	95
Table 6.2. Target and recovered fluorescence yield regional contrasts for the images in Figure 6.3 and Figure 6.44. Reported ratios were calculated using the mean values in each region.....	102
Table 8.1. Student's t-tests between population arms. *Statistical significance is reported for $p < 0.05$	148
Table 9.1. Homogeneous fit values of fluorescence yield	167

List of Figures and Illustrations

Figure 2.1. Diagram of the MRI-coupled 16 channel spectroscopy system for fluorescence tomography. Long, bifurcated spectroscopy fibers couple contact mode source-detection directly into the MRI bore.	11
Figure 2.2. Top left: The spectroscopy system is built into carts which can be wheeled into the MRI control room [(a) and (b)]. Sixteen 13 meter long fiber bundles extend through ports in the wall and into the MRI bore [(c) and (d)].	12
Figure 2.3. Diagram of the bifurcated spectroscopy fibers.....	14
Figure 2.4. Diagram (left) and photograph (right) of the custom designed entrance optics. Lenses collimate the incoming light for filtering with selectable interference or ND filters and focus the light onto the spectrograph slit.....	15
Figure 2.5. A ray diagram created using Zemax software illustrates the theoretical light path through the spectrograph coupling optics.....	16
Figure 2.6. Image of the fiber array focused on the spectrometer CCD. An entrance optical system is considered aligned when this image is in focus, as above.	16
Figure 2.7. (a) Relative transversal magnetic field of the solenoid coil. The isocenter is set to 0 dB and the arrow shows the B_0 direction. (b) Sensitivity profiles along the coil axis (perpendicular to the main field, B_0) for different distances from the isocenter.	19
Figure 2.8. (a) CAD rendering of the Philips rodent coil. (b) Photograph of the coil layout showing connected strip conductors and holes to provide access for optical fibers.....	20
Figure 2.9. 3D CAD rendering, (a), and photographs of the latest generation fiber positioning system are shown. Two concentric cylinders, (b), fit snugly in the RF coil and accommodate eight optical fibers [(c) and (d)]. The outer cylinder also houses eight MR sensitive fiducials in the plane of the fiber array positioned exactly between each fiber pair as shown in (b).	21
Figure 2.10. The patient interface is a circular array of fibers that couples into a standard MRI breast coil (a), though parallel plate geometries are also under consideration (b).	22
Figure 2.11. Front panel of the spectroscopy system's image acquisition program, designed in Labview. The input controls are at left in the tab menu, and the output data can be observed at right as it is written to file. The window at the bottom left is updated continuously with acquisition status messages. Calibration filenames are provided at bottom right for real-time data calibration. ...	24

Figure 2.12. The three plane, 48 fiber frequency domain system which uses six laser diode sources and PMT detection is shown in (a). A photograph of the patient array holding a gelatin tissue phantom is shown in (b).	25
Figure 3.1. Circular, (a), and irregular, (b), 2-d FEM meshes composed of approximately 2000 nodes. The circular domain is 86 mm in diameter and the maximum diameter of the irregular domain is 108 mm. Red circles and blue x's mark the locations of 16 source-detectors.....	30
Figure 3.2. An illustration of the data produced by the fluorescence forward model used in this work is shown. The logarithm of the internal intensity field (left column) is plotted for a single source while the entire set of boundary data extracted for each source-detector pair is shown at left. Fluorophore contrast was assumed to be distributed homogeneously throughout the domain except for an elevated region marked by the white circle.....	31
Figure 3.3. A full reconstruction from measured data is a complicated process involving four separate data sets, two from each tomography system. This flow diagram outlines the fluorescence recovery procedure, including calibration steps and homogeneous fitting algorithms.....	34
Figure 3.4. A simulated test domain for fluorescence image reconstruction is shown along with associated reconstructed images. The final image of fluorescence yield is the image of interest in most studies discussed throughout this thesis. All color-bars are in units of mm^{-1}	36
Figure 3.5. A simulated test domain for multi-wavelength spectrally-constrained image reconstruction is shown in (a). Associated reconstructed images, recovered simultaneously, are shown in (b). HbO, deoxyHb, and LuTex concentrations are in mM, water is in percent and scattering parameters are dimensionless.....	39
Figure 4.1. Chemical structure and normalized absorbance and fluorescence emission spectra of Lutetium Texaphyrin are shown.....	46
Figure 4.2. Chemical structure, (a), reproduced from Prah ⁷³ , and normalized absorbance and emission spectra of ICG (b). The fluorescence spectrum was measured in turbid medium (1% IL), and the secondary peak around 720-740 nm is contamination due to excitation cross-talk and auto-fluorescence.....	47
Figure 4.3. Normalized absorbance and emission spectra of IRDye 800CW EGF Optical Probe, reproduced from the Li-Cor website ⁷⁷	48
Figure 4.4. The chemical structure of PPIX, an intermediary in the Heme biosynthesis pathway, reproduced from Prah ⁸⁷ . In (b), the normalized absorbance and fluorescence emission spectra are shown, along with a schematic of the excitation laser light wavelength and the filtering needed for effective emission detection.....	50

Figure 4.5. Extinction spectra measured for LuTex, GdTex, and ICG are shown. Values for endogenous chromophores are also shown, as compiled by Prahl ⁸⁷ , to illustrate the potential impact drugs such as ICG can have on the overall absorption profile of tissue.....	52
Figure 4.6. Examples of liquid (a), gelatin (b), and solid (c) tissue simulating phantoms.	53
Figure 4.7. Multi-layer gelatin phantoms can be produced using a series of irregularly shaped molds (a). A three layer phantom is shown in (b).....	55
Figure 5.1. The linearity of measured intensity with exposure time was verified for all spectrometer systems. Only data for detectors 1-8 are shown here.....	57
Figure 5.2. The emission spectrum of a neon lamp as measured by spectrometer #14 is shown. The red arrows indicate which emission peaks were used to calibrate the wavelength response of the cameras.....	59
Figure 5.3. Diagram of the Teflon phantom configuration for measuring optical densities of ND filters used in the system (left) and corresponding photograph (right). A fiber transmitting light from a tungsten lamp is centered on the top of the cylinder which is encircled by detection fibers.....	62
Figure 5.4. Wavelength dependent OD values calculated for 1 OD and 2 OD filters used in the spectral tomography system, each curve representing one spectrometer. Calculations were repeated for both gratings at a variety of center wavelength settings.....	63
Figure 5.5. The measured spectra through a homogenous gelatin phantom show a residual signal above the 720 nm cutoff. This phantom was illuminated with a 690 nm laser diode.....	65
Figure 5.6. A simplified diagram of the source-to-detector light path shows the location of band-pass and long-pass filters in the optical system. One of 16 spectrometers is shown and detector positions are labeled with numbers.....	66
Figure 5.7. Contamination signal measured around a 60 mm diameter cylindrical phantom containing 1% intralipid in water. Data are shown for detectors positioned 1.1 mm (a), 3.3 mm (b), 4.9 mm (c), and 5.9 mm (d) from the source...	67
Figure 5.8. Ratios between the filtered and unfiltered spectra presented in Figure 5.7, calculated pixel-by-pixel. Spectra were measured at detectors located around a cylindrical phantom containing intralipid, as depicted in Figure 5.6.....	68
Figure 5.9. Light from a broadband Tungsten source filtered with the 690 nm band-pass filter.....	69

Figure 5.10. Spectra measured at detector 4 with the long-pass filter on the source side and detector side of the optical path.	70
Figure 5.11. Spectrum measured through air between source and detector fibers.	71
Figure 5.12. Inter-detector calibration factors as a function of pixel number. Light from a tungsten lamp propagated through a homogenous Teflon phantom and was measured by all 16 spectrometers (using the 300 l/mm grating centered at 820 nm) simultaneously. For each detector, the intensity at each pixel was normalized to the maximum intensity recorded by any detector at that pixel.	74
Figure 5.13. A first order source calibration was completed by measuring the intensity at a centrally located detector (orange) while illuminating the encircling fibers sequentially.	75
Figure 5.14. Each column represents an example of a single source-detector measurement and illustrates the spectral fitting routine used to decouple fluorescence spectra from the measured signal. The algorithm determines the relative contribution of the basis spectra [bottom row, (c) and (d)] which best fits the measured spectrum. The top row [(a) and (b)] shows the measured data (solid blue line) and the spectrum composed of the sum of the basis spectra (green dotted line). These examples are from a mouse injected with Li-Cor IRdye-800 EGF.	77
Figure 5.15. A more accurate minimization is produced when the spectral fitting wavelength range is restricted and does not include the filtered region. In this case, the same data presented in Figure 5.14 data is fit for the wavelength range only above 740 nm.	78
Figure 5.16. Calibrated intensity measured at seven detector positions (single source) around a murine head. Data was processed using two different spectral fitting routines.	80
Figure 5.17. Calibrated data compared to homogeneous fit data for a homogeneous liquid phantom contain intralipid, ink and 10 nM of the fluorophore Indocyanin Green.	83
Figure 5.18. A spectral fitting routine is used to decouple fluorescence spectra from the measured signal. The spectral fitting algorithm determines the relative contribution of the basis spectra [right column, (b) and (d)] which best fits the measured spectrum. Two examples are presented above, both for a 70 mm diameter homogeneous phantom containing intralipid, ink and ICG [500 nM for graphs (a) and (b) and 100pM for graphs (c) and (d)].	87
Figure 5.19. Recovered values of fluorescence yield as a function of ICG concentration in a 70 mm liquid phantom using two methods to process the recorded data. One method implements the spectral-fitting technique to decouple background contamination across the fluorescence emission spectrum	

while the other simply integrates the measured spectrum, as would be the case if the experimental system relied on long pass filtering alone. Values were determined using a homogeneous fitting algorithm for the background optical properties as well as the fluorescence yield.....	89
Figure 6.1 A coronal T1-weighted MRI slice of a human breast is shown in (a), from which the test domain for simulation studies was derived. Darker regions indicate fibro-glandular tissue imbedded in adipose tissue indicated by lighter values. The image was acquired during a clinical exam with an MR-coupled NIR tomography system and shows the indentations caused by the fiber optic probes. The test domain (b) was a discretization of the MR image coarsely thresholded into regions. The dark red region represents adipose tissue, the orange fibro-glandular tissue and the yellow circular anomaly region was added to simulate a tumor.....	94
Figure 6.2. An example of a pair of basis spectra for the excitation and fluorescence light (in counts/s as a function of CCD pixel number) is shown in (b). These spectra were recorded for each detector prior to imaging. In practice, the basis spectra were used to perform a least squares fit to the spectrum measured for each source-detector pair to determine the relative contribution of the fluorescence and excitation light to the measured response.	98
Figure 6.3. Target and recovered values of μ_{ax} , μ_{sx}' , μ_{am} , μ_{sm}' , and fluorescence yield, $\eta\mu_{af}$, for reconstruction implementations using no prior information and with spatial prior information. In this case, the simulated cancer region was near the edge, which is known to be easier to recover without spatial priors. The image scales are at right in units of mm^{-1}	100
Figure 6.4. Target and recovered values of μ_{ax} , μ_{sx}' , μ_{am} , μ_{sm}' , and fluorescence yield, $\eta\mu_{af}$, for reconstruction implementations using no priors and spatial priors. In this case, the simulated tumor region was near the center of the imaging domain, which is known to be more difficult to recover accurately. Image scales are at right.	101
Figure 6.5. Cross sectional plots of fluorescence yield are shown for the simulated imaging domains in (a) the case with an object near the edge and (b) the case with an object near the center. In both cases, the cross section is in the y-direction just off center from $x = 0$. The solid line represents the target value, the small dotted line the recovered value using a no-priors based algorithm, and the dashed line the recovered value using spatially guided reconstruction.	102
Figure 6.6. Recovered images of fluorescence yield are shown for varying concentrations of LuTex. The 14 mm diameter fluorescent inclusion was embedded in a 55 mm diameter solid epoxy tissue simulating phantom. Images were generated from the same data using algorithms based on no-priors and spatial soft prior implementations.....	104

Figure 6.7. A narrower colorbar-scale version of the 0.3125 μM LuTex phantom images shown in Fig. 8 further illustrates the improvement in image accuracy, and removal of edge artifacts for the spatially guided algorithm. Images are of fluorescence yield in units of mm^{-1}	105
Figure 6.8. Containers shown in (a) were used to produce a 70 mm diameter liquid phantom containing an ICG heterogeneity. The ICG target-to-background concentration was 3.3:1. Images reconstructed using spatial soft priors, depicted in (c), are more accurate qualitatively and in terms of recovered contrast than images recovered without the spatial priors implementation (b).....	108
Figure 6.9. A photograph of the 92 mm diameter intralipid, ink, ICG phantom in the phantom fiber array is included in (a). The spatial prior information for an object near the edge is shown in (b).....	109
Figure 6.10. Reconstructed images of fluorescence yield for liquid phantoms containing intralipid, ink and ICG, using no spatial priors (a), soft priors (b), and hard priors (c). In this case, the simulated tumor region was just off center. Columns correspond to different tumor-to-background ICG contrasts, 1.5:1, 3.3:1, and 6.6:1 from left to right.....	112
Figure 6.11. Reconstructed images of fluorescence yield for liquid phantoms containing intralipid, ink and ICG, using no spatial priors (a), soft priors (b) and hard priors (c). In this case, the simulated tumor region was close to the edge. Columns correspond to different tumor-to-background ICG contrasts, 1.5:1, 3.3:1, and 6.6:1 from left to right.....	113
Figure 6.12. Mean values of recovered fluorescence yield in the anomaly (“Anom”) and background of the imaging domains for no priors (a), soft priors (b) and hard priors (c) reconstructions. Both phantom configurations are plotted on each graph, denoted in the legend by “(center)” and “(edge)”	114
Figure 6.13. Calculated contrast determined using mean values of recovered fluorescence yield in the anomaly and background of the imaging domains for no priors (a), soft priors (b) and hard priors (c) reconstructions. Both phantom configurations are plotted on each graph, denoted in the legend by “(center)” and “(edge)”. True ICG concentration contrast is plotted in red.....	115
Figure 6.14. A photograph of the phantom in the optical fiber array is shown in (a). The second layer contained gadolinium, which provided MR image contrast, (b), for easy image segmentation using Mimics software (c).....	117
Figure 6.15. Fluorescence yield images of the three layer phantom reconstructed using no spatial guidance (a), soft-priors (b), and hard-priors (c). All images are plotted using the same color scale.	118
Figure 7.1. The small animal coil was used with four spectroscopy fibers for simultaneous MRI and fluorescence acquisition (a). A coronal slice of a Gd-	

enhanced MR image of a mouse head is shown in (b), from which an FEM mesh is generated (c). Fibers were located using the indents on the animal tissue surface (red circles show 1 scattering depth in from the locations identified).	123
Figure 7.2. The MR image (a) and reconstructed fluorescence activity of PPIX fluorescence without ALA administration using soft priors (b) and hard priors (c).	124
Figure 7.3. The same data was used to reconstruct images using spatial guidance based on a three-region segmentation. The regions are shown in (a), while the resulting images reconstructed using the soft and hard priors techniques are presented in (b) and (c) respectively.	125
Figure 7.4. The MR image (a) and reconstructed fluorescence activity of PPIX fluorescence two hours after ALA administration using soft priors (b) and hard priors (c).	127
Figure 7.5. (a) Photograph of the coil layout showing access holes for the optical fibers. (b) The custom designed mouse bed accommodates the spectroscopy fiber bundles and fits into the rodent coil for simultaneous MRI and optical acquisition.	129
Figure 7.6. The coronal slice from gadolinium enhanced T1-weighted images of a tumor bearing mouse brain (left) is segmented into three regions using MIMICS software, identified by the blue, grey and purple colors in the image at right. The segmented image is used to generate an FEM mesh for spatially-guided fluorescence reconstruction.	130
Figure 7.7. Images of fluorescence yield for a tumor-bearing mouse reconstructed using only the outer animal boundary as prior information, (a), and hard priors for the animal exterior, brain and tumor regions (b). An image overlay of (b) on the segmented MR image is shown in (c).	131
Figure 7.8. Ex-vivo fluorescence scans of fresh tissue sections from the mouse imaged in Figure 7.7 are shown in the top row. Histology slides correspond loosely with the fluorescence images and indicate tumor growth at the base of the brain [(d)-(f)].	133
Figure 8.1. The mouse head holder shown in (a) was imaged using a micro-CT scanner, which provides strong contrast between epoxy resin and air (b). Green arrows mark the MRI fiducial channels while the other eight channels accommodate the optical fibers. Clearly, the point of conversion of the fiber array does not match the intersection of the fiducial channels.	138
Figure 8.2. Fiber contact points were positioned with reference to MRI fiducial material (a). From the intersection of lines connecting the fiducial signals, linear translations localized the converging point of the optical fibers (b). Referencing	

this center point and fiducials, the Mimics angle tool was used to mark fiber contact points (c).....	140
Figure 8.3. Representative coronal MR images of a mouse brain implanted with GFP-transfected U251 tumor cells. Images acquired using the following pulse sequences are shown: T1-weighted turbo spin echo (a), T2 FLAIR (b), T1 inversion recovery (c), and gadolinium enhanced T1 turbo spin echo (c). Some swelling in the ventricles is noted, but no discernable tumor mass.....	141
Figure 8.4. Gadolinium enhanced MRI, histology and <i>ex vivo</i> GFP fluorescence of two tumor lines. In (a), GFP-transfected tumors used in this study present no MRI enhancement and show up in the histology slides as diffuse, infiltrative sites throughout the brain. For comparison, images for the GFP-transfected 9-L tumor line in (b) show a more conventional tumor model, with a large tumor mass seen easily with MRI contrast enhancement.....	143
Figure 8.5. An example of a two region segmentation of a gadolinium enhanced T1-weighted image. In this example, the brain is segmented from the surrounding tissue.	144
Figure 8.6. A diagram outlining the procedure for homogeneous fitting. MR images were segmented into 2 regions: brain and surrounding tissue. Optical properties were then assigned based on literature values. Using these properties, a single pixel reconstruction provided a homogeneous fit of fluorescence yield to the measured data.....	145
Figure 8.7. Data-model mismatch for homogeneous fits of fluorescence yield plotted for individual subjects in the control (a), treated (b), and untreated [(c) and (d)] study arms.	146
Figure 8.8. Box-and-whisker plots show the median and inter-quartile of the fluorescence yield recovered using homogeneous fitting.....	147
Figure 8.9. Images of fluorescence yield recovered using two reconstruction techniques, namely two-region hard priors and no priors. Images are representative of the control (a), treated (b) and untreated (c) population arms.....	150
Figure 9.1. Using the fiducial markers as guides in Mimics software, lines were drawn connecting the inner surfaces of diametrically opposed fiducials (a). After four pairs were drawn, additional lines between and parallel to each existing pair are drawn. The outer lines may be removed to simplify the image and the intersection of the remaining lines identifies the center of the circular fiber array (b). Finally, the angle tool was used to locate the fiber contact points around the head (c).....	156
Figure 9.2. Simple segmentation using Mimics for the mouse head and brain regions (a). Region information was exported as a binary bitmap image (b).....	157

Figure 9.3. MRI coronal image series of a murine head bearing a large glioma grown from intracranial implantation of the U251 tumor line. Each column shows the same volume slice for different sequences: (a) T1-weighted TSE without contrast, (b) T1-weighted TSE with contrast, and (c) T2-weighted.	159
Figure 9.4. MRI coronal image series' of a murine head bearing a large glioma grown from intracranial implantation of the U251 tumor line. Each column shows the same volume slice for different sequences; (a) T1-weighted TSE without contrast, (b) T1-weighted TSE with contrast, and (c) T2-weighted.	160
Figure 9.5. Gd-enhanced coronal slices of the two tumor-bearing mice (a) and (c) were segmented into regions shown in (b) and (d), respectively. In (b), three regions delineate brain, edema, and all other tissue. In addition to those three regions, Gd enhancement in (c) was also segmented as a fourth region in (d).....	161
Figure 9.6. MR images (left) and homogeneously fit data (right) for the 6 control animals injected with IRDye [®] 800CW EGF Optical Probe.....	163
Figure 9.7. MR images and homogeneously fit data for two tumor-bearing mice. Data for each mouse is provided before, (a) and (b), and 48 hours after IRDye [®] 800CW EGF Optical Probe administration, (c) and (d).	165
Figure 9.8. Images for the tumor-bearing mice, only one of which showed Gd contrast in the fiber plane, reconstructed using three reconstruction techniques are shown next to the corresponding MR image used to provide spatial a priori guidance.	169
Figure 9.9. Images of fluorescence yield for the four control mice reconstructed using three different reconstruction approaches. For each mouse, the relevant MRI slice is shown (left) with the corresponding fluorescence images recovered using no prior, soft prior, and hard prior implementations.	171
Figure 9.10. Three regularization parameters were used for each of the three reconstruction techniques, resulting in a series of nine images for each mouse. Here the series for a tumor-bearing mouse is shown.	173
Figure 9.11. Three regularization parameters were used for each of the three reconstruction techniques, resulting in a series of nine images for each mouse. Here the image series for a control mouse is shown.	174
Figure 9.12. Ex-vivo fluorescence of EGF bound Li-Cor dye (a) in fresh sections of brain tissue. This mouse had a large Gd-enhanced region in the optical fiber plane, a region that showed high levels of fluorescence activity in FMT images (Figure 9.8, top row). Pathology slides (b) – (f) correspond roughly to the slices in (a) and show tumor regions matching the fluorescent enhancement.....	176
Figure 9.13. Higher magnification of the pathology slide in Figure 9.12(f) shows tumor and normal brain (a), tumor surrounding necrotic tissue and hemorrhaging	

(c), the boundary of malignant and necrotic cells (d), a closer view of hemorrhage (e), and a blood vessel supplying viable malignant cells (b).	178
Figure 9.14. Ex-vivo fluorescence of EGF bound Li-Cor dye (a) in fresh sections of brain tissue. This mouse had a large Gd-enhanced region outside of the optical fiber plane, likely corresponding to the top two images in (a). Pathology slides (b) – (f) correspond roughly to the slices in (a) and show tumor regions matching the fluorescent enhancement.	180
Figure 9.15. Magnified images of the murine brain histology slides shown in Figure 9.14. This mouse had a large Gd-enhanced region outside of the optical fiber plane, and an abnormal region of high T2 signal in the optical imaging plane. Images show normal tissue (a) in one hemisphere and extensive edema in the contra-lateral cortex [(b) and (c)], likely causing the crescent-shaped abnormality in the MR and FMT images.	181
Figure 10.1. The imaging test domain was derived from a T1-weighted coronal MR image of a human breast. Adipose and fibro-glandular regions were assigned clinically relevant values for endogenous chromophores. Note that HbO and dHb are in mM, water in percent and scattering parameters are dimensionless. A variety of exogenous distributions were used in this study.	187
Figure 10.2. Source-detector configuration for simulated data used in this study.	188
Figure 10.3. Two test domains for investigating perturbations caused by absorption and fluorescence exogenous contrast. In (a), exogenous contrast tumor specificity is assumed to be perfect, while in (b), the uptake profile is more realistic.	190
Figure 10.4. Perturbations in transmission amplitude and fluorescence amplitude, given different filtering efficiencies and quantum yield values, caused by a centrally located object with perfect drug uptake. Given these conditions, fluorescence signals appear to be more sensitive to the object.	191
Figure 10.5. Perturbations in transmission amplitude and fluorescence amplitude, given different filtering efficiencies and quantum yield values, caused by a centrally located object with imperfect drug uptake. For this lower drug contrast case, absorption measurements are more sensitive to the object than fluorescence emission, regardless of fluorescence quantum yield.	193
Figure 10.6. Threshold quantum yield values for excitation filtering efficiencies of 3 OD, 5 OD, 7 OD, and 100 OD [(a)-(d), respectively] over a range of contrasts and background concentration. These values represent the quantum yield value for which absorption and fluorescence measurements are equally sensitive to a centrally located tumor region.	195
Figure 10.7. Threshold quantum yield values plotted as a function of background drug concentration for a 5:1 tumor-to-background contrast (a). The quantum	

yield threshold curves delineate between experimental conditions which favor fluorescence and absorption measurements (b).	197
Figure 10.8. Changes in recovered values of fluorescence yield and absorption coefficient as a function of ICG concentration in a homogenous liquid phantom. Values were calculated relative to the recovered value at 10pM.....	198
Figure 11.1. Molar extinction spectra of hemoglobin, water, and LuTex are shown in (a). LuTex has a strong absorption peak at 735nm, which has a substantial impact on tissue absorption at concentrations of 300 nM, (b).	204
Figure 11.2. Target values of chromophore concentrations (mM) and scattering parameters for the simulated test domain (water is in percent). Lutex contrast is 3:1 for tumor-to-fatty layer and 2:1 for tumor-to-fibro-glandular layer.	206
Figure 11.3. Images of chromophore concentrations (mM), percent water, and scattering amplitude and power recovered using spectrally constrained absorption tomography with only the outer boundary as a spatial prior.....	207
Figure 11.4. Images of chromophore concentrations (mM), percent water, and scattering amplitude and power recovered using spectrally constrained absorption tomography of Lutex with hard priors of the internal tissue structure..	208
Figure 11.5. The spectrally constrained reconstruction technique applied to the domain containing ICG. The true values of chromophore concentrations (mM), percent water, and scattering amplitude and power provided in (a) were reconstructed without spatial priors (b) and with perfect hard priors (c).....	209
Figure 11.6. Quantification of Lutex concentration in homogeneous liquid phantoms using spectrally-constrained absorption tomography.	210
Figure 11.7. A method for using recovered chromophore concentrations and scattering parameters to reconstruct for fluorescence yield.....	212
Figure 11.8. An image of fluorescence yield recovered in the manner described in Figure 11.7 (b) seems to add little in terms of contrast quantification of ICG, as compared to the image of ICG concentration recovered using the spectrally constrained absorption reconstruction technique (a).	214
Figure 12.1. Photographs of phantoms used in this study. A liquid intralipid-based phantom (a) readily allows changing of the fluorophore concentration while gelatin phantoms containing TiO ₂ scatterer shown in (b) eliminate the need for an external container. Gelatin phantoms without scattering material were also used to assess the emission spectra without scatter (c).	218
Figure 12.2. Normalized LuTex fluorescence emission as measured in dilute concentration (2µg/ml) in deionized water.	219

Figure 12.3. Fluorescence emission of 5 uM LuTex measured in the multi-spectrometer system in phantoms composed of (a) gelatin and (b) De-ionized water. These spectra represent the non-turbid baselines since neither phantom contained significant scattering media.....	222
Figure 12.4. LuTex fluorescence emission experimentally measured at different source-detector distances in homogeneous scattering gelatin and intralipid based phantoms. The circular domain shown represents a cross-section of the cylindrical phantom, illustrating the input (red arrow) and output measurement sites (blue arrows). For illustration purposes, the intensity (shown as logarithm of intensity) of the diffuse excitation field is plotted in the circular region.	223
Figure 12.5. Fluorescence emission spectra through a liquid phantom of DI water and varying concentrations of intralipid are shown. Only spectra measured through intralipid concentrations of 0.1% and above are shown for the two detectors farthest from the source.	225
Figure 12.6. Absorption coefficients of 100% water and 300 nM LuTex is plotted for discrete wavelengths (green line with data points), with LuTex fluorescence emission (red dotted line) in dilute solution, indicating the overlap in absorption and emission at the shorter wavelengths from 700 to 750 nm.....	226
Figure 12.7. Diffusion based modeling of the fluorescence peak through a 60 mm diameter phantom, similar to Figure 12.4. The dilute emission spectrum of LuTex is shown as dotted lines, and the calculated emission spectrum from diffuse emission through the region is shown at discrete wavelengths (black circles). Experimental measurements are shown in blue for intralipid liquid phantoms. The circular domain shown represents a cross-section of the cylindrical phantom upon which the intensity (logarithm) of the excitation field calculated from the diffusion equation is plotted for illustration purposes.....	228
Figure 12.8. Extinction coefficients of chromophores used in the simulation are shown in (a). These are used to calculate tissue absorption coefficients at any wavelength within the NIR. The simulated domain contains contrasts in the various absorbing constituents, the spatial distributions of which are shown in (b).....	230
Figure 12.9. Fluorescence yield of LuTex is calculated from the drug concentration and the fluorescence quantum yield. Based on the concentration of LuTex assumed in Fig. 9, the target fluorescence yield is shown in (a). Reconstructing images from data collected with long-pass filtering can be an intractable problem as shown in (b), while resolving the emitted spectrum allows accurate recovery of the true fluorescence activity, as shown in (c). All images shown are in units of mm^{-1}	232
Figure 13.1. Examples of contrast-detail phantoms for chest x-ray ¹⁶² (a) and ultrasound ¹⁴⁷ (b) imaging. The ultrasound phantom contains a series of cones	

produced with different acoustic impedances. The diameter of the imaged object is varied by imaging different cross-sections of the cones.	237
Figure 13.2. Contrast detail curves used to compare two film-screen combinations for planar x-ray imaging, reproduce from Thompson and Faulkner ¹⁶⁴ . The y-axis represents true object contrast. Plotted curves represent the threshold for detecting an object of a given size and object. Objects above and to the right of the curve are considered detectable, while objects with sizes and contrasts below and to the left of the curve are undetectable.	238
Figure 13.3. 86 and 51 mm diameter test fields used in this study. A range of object sizes and contrasts are used to determine contrast-detail imaging limits.	241
Figure 13.4. Calculated contrast-to-noise (CNR) ratio for a range of object diameters and contrast levels in four circular test domains. (a) and (b) present data for objects near the edge and center, respectively, of a 51 mm test domain. (c) and (d), on the other hand, present data for objects near the edge and center, respectively, of an 86 mm test domain. In this analysis, objects which are reconstructed with a CNR value below 3.0 are thought to be undetectable by human perception, illustrating that there are regions of size and contrast which are not feasible to image with the algorithm.	243
Figure 13.5. Images of fluorescence yield for a range of object sizes located near the center of a 51mm diameter domain. CNR decreases with decreasing object diameter.	244
Figure 13.6. Contrast-detail curve showing the contrast-to-noise ratio (CNR) of 3 to approximate limits of detectable contrast and diameter for two anomaly positions in 51 mm (dashed lines) and 86 mm (solid lines) diameter test fields. In this analysis, objects above and to the right of each line are in the region where $CNR \geq 3$ and “detection” is considered possible.	245
Figure 13.7. Contrast accuracy plots provide the percentage (color-bar) of true contrast recovered in the image. (a) and (b) show data for objects near the edge and center, respectively, of a 51 mm test domain. (c) and (d) show data for objects near the edge and center, respectively, of an 86 mm test domain.	248
Figure 15.1. The proposed system combines the frequency domain Ti:Sapphire imaging system with the spectroscopy system.	256
Figure 15.2. A method for combining recovered chromophore concentration values and scattering parameters with images of fluorescence yield to reconstruct absolute quantum yield images.	261
Figure 15.3. Simulated test domain showing true values of chromophore concentrations (mM), scattering parameters and fluorescence quantum yield.	262

Figure 15.4. Recovered images of chromophore concentration, scattering parameters, fluorescence yield and fluorescence quantum yield. The outer boundary of the imaging domain was the only spatial information used in the reconstruction..... 263

Figure 15.5. Recovered images of chromophore concentration, scattering parameters, fluorescence yield and fluorescence quantum yield reconstructed using hard spatial priors..... 264

Chapter One: Introduction and Background

The primary objective of this thesis is to develop techniques to image the distribution and activity of exogenous optical contrast agents through centimeters of living tissue, facilitating diagnosis of disease and treatment monitoring for clinical applications, particularly in the human breast, and pre-clinical work in small animals. The imaging of exogenously administered agents is part of the expansive field of molecular imaging which encompasses a wide range of techniques to probe the molecular causes of disease using exogenous, endogenous and transgenic markers¹⁻⁶. Information on tissue function is derived from any number of mechanisms, including relatively simple blood flow kinetics, protein receptor expression, enzyme activation and chemical environment, though few of these more specific mechanism are used in clinical practice.

Unspecific exogenous contrast agents have been used in clinical applications for years. Injected, swallowed or inhaled drugs are commonly used in conventional medical imaging practice to enhance signal intensity and provide functional information of tissue physiology. Gadolinium enhanced magnetic resonance imaging (MRI) exams^{7, 8} and iodine or barium sulfate-based x-ray exams⁹, including computed tomography (CT), planar, and fluoroscopic modalities, are examples of standard contrast procedures. Most conventional contrast agents provide functional information derived only from mechanical kinetics such as blood flow, digestive tract dynamics, and pulmonary function. Prominent exceptions are targeted radiotracers used in positron emission tomography (PET) imaging, the most common being fluorodeoxyglucose (FDG), a

metabolic marker used in oncology to produce images of glucose uptake¹⁰. Though the specificity of FDG-PET provides very high diseased-to-normal tissue contrasts, images suffer from poor spatial resolution often making image interpretation difficult without co-registered information from highly resolved imaging modalities, usually CT scans. Exposure to ionizing radiation from the injected radio-nuclides and CT co-registration exams also elevates a patient's effective equivalent dose dramatically, increasing the risk of genetic damage leading to cancerous growth in later years. Furthermore, the short half-life radio-nuclides used in PET imaging must be produced in costly cyclotron facilities and injected within hours of production. Most institutions cannot maintain a cyclotron and outsource production and rapid delivery of the probes to a third party.

Optical techniques, on the other hand, can provide similar specificity to PET radiotracers without the dangerous ionizing radiation. One could reasonably assert that the gold standard in clinical tissue diagnosis is derived from optical exogenous contrast used in histopathology. Hematoxylin and Eosin (H&E) staining represents highly specific optical contrast based on light absorption in the visible regime. Many compounds also reemit absorbed optical energy in the form of fluorescence or phosphorescence which can further enhance the specificity of the measured signal. Fluorescence microscopy, a laboratory standard which provides specific, high contrast images of fluorescent markers is another example of optical exogenous contrast regularly used to reveal tissue physiology. Such specificity could enhance the diagnostic power of clinical imaging; however, translating these techniques to the clinic is inhibited by drug toxicity and the complexity of optical photon propagation despite a broad body of preliminary work exploring tissue diagnosis with endogenous and exogenous

fluorescence¹¹⁻¹⁸. To date, fluorescence contrast agents have made only modest inroads into clinical applications, the primary example being retinal and choroidal angiography using fluorescein and indocyanine green¹⁹⁻²³. Recently Stummer et al.²⁴ produced a compelling body of work which linked protoporphyrin IX fluorescence guided resection of brain tumors to clinical outcomes, leading to the adoption of the technique as the standard of care in Germany.

Broad efforts are underway to develop targeted, well tolerated optical probes for human and animal imaging⁵. However, even with the introduction of safe, specific molecules, non-invasive imaging of drug activity beyond several millimeters is a challenging problem due to restrictive levels of light attenuation, especially in the visible regime, and elastic scattering. The relatively low absorption in the near-infrared (NIR) allows measurable light penetration over 10 cm, though elastic scattering ensures most photons will change direction within 1 mm of entering the tissue. Photon propagation beyond this depth is diffuse, rendering impractical the application of standard x-ray imaging principles which depend on ballistic photon penetration. Imaging physiologically relevant endogenous and exogenous optical contrast in this regime requires model-based techniques which account for tissue derived photon scattering. The most popular approach, diffuse optical fluorescence tomography (DOFT), also known as fluorescence molecular tomography (FMT), produces low resolution images compared to standard clinical modalities such as x-ray CT and MRI due to the highly scattered photon fields and relatively sparse measurement sampling of the tissue volume. The reconstruction problem is ill-posed and often underdetermined. Furthermore, the tissue optical properties are heterogeneously distributed due to the complex tissue morphology.

These factors make the imaging recovery problem challenging. Sensitivity drops exponentially with increasing depth, resulting in a non-linear responsivity across the imaging field, and this effect can exceed the useful dynamic range of a measurement system for larger tissue volumes. Several preliminary studies in geometries resembling a human breast have examined this problem, with high fluorophore contrasts and simplified geometries²⁵⁻²⁷ and images of human breast using the non-targeted fluorophore indocyanine green (ICG) have very recently been published²⁸. Improving image resolution and contrast sensitivity is critical for identifying a clinical role for this emerging modality.

Fluorescence tomography is an extension of the more widely studied diffuse optical tomography (DOT), which has been developed for breast cancer imaging and treatment monitoring over the past decade²⁹⁻³⁴. Optical contrast is derived from the constituent endogenous chromophores, namely, oxygenated and deoxygenate hemoglobin, lipids, and water, as well as the size and distribution of sub-cellular structures that cause photon scattering in the NIR. Malignant-to-normal contrasts of hemoglobin can be as high as 200%³⁵. Even with this high endogenous contrast between diseased and normal tissue, standard DOT images often suffer from poor spatial and contrast resolutions. Methods to incorporate highly-resolved anatomical data obtained from standard clinical modalities have improved the ability to quantify images derived from optical contrast in tissue³⁶⁻⁴⁰. These hybrid approaches lead to a conceptually new application of optical tomography, one in which the highly resolved imaging system provides a structural template upon which volumetric optical spectroscopic images are constructed. This framework may be applied to either absorption and scatter

spectroscopy, or fluorescence spectroscopy. Additional challenges specific to the fluorescence case include lower signal intensity, excitation source contamination of the fluorescence emission measurements due to filter leakage, and complex tissue optical property effects on both the excitation and emission photon propagation. Applying spatial guidance techniques to the more complicated fluorescence problem may therefore yield even larger gains in imaging capability.

Another source of prior information used to improve DOT image recovery is knowledge of the extinction spectra of the dominant absorbing chromophores and tissue scattering behavior. This information may be used to constrain the imaging algorithm provided the availability of spectrally resolved constant-wave (CW)^{41, 42} or frequency domain (FD) data^{43, 44}. To date, spectrally-constrained imaging techniques have been applied to quantify endogenous tissue chromophore concentrations in the human breast^{29, 33, 43, 45}. A natural extension of this method is to include the extinction spectra of strongly absorbing contrast agents along with those of the endogenous absorbers, facilitating recovery of endogenous and exogenous chromophore concentration simultaneously.

This work seeks to improve fluorescence imaging of exogenous contrast agents by developing a sensitive, spectrally-resolved fluorescence tomography system designed to operate within the bore of a clinical MRI. The spatial resolution of simultaneously acquired MR images is exploited in the image recovery of fluorescence activity at a depth of several centimeters in tissue. The impact of this prior information is examined with simulated data as well as data acquired using tissue phantoms and tumor-bearing mice injected with targeted fluorescent molecular probes.

Towards the objectives of this work, the structure of the thesis is as follows:

Chapter two introduces the MRI-coupled multi-channel spectroscopic tomography system developed as part of this work⁴⁶. Basic system components are reviewed in the context of the design objectives.

Chapter three reviews the mathematical framework used for modeling photon fields and reconstructing images of tissue optical properties and fluorescence yield using the diffusion approximation. An alternative method to recover endogenous and exogenous tissue chromophore concentrations directly is also introduced. Additionally, two methods to incorporate tissue structural information from co-registered MR images are described.

Chapter four reviews the contrast agents used in this study and their photo-physical properties. The chapter also includes descriptions and recipes for all tissue simulating phantoms used throughout the study.

Chapter five presents data used to validate the performance of the experimental system introduced in *Chapter three*, ranging from basic verification of spectrometer function to analysis of the system's sensitivity to fluorophore concentrations in homogeneous phantoms. Data calibration procedures are also discussed.

In *Chapter six*, simulated and phantom data are used to examine the improvements in fluorescence activity image recovery provided by the spatial prior information from MRI.

Chapter seven is the first in a series of three chapters describing fluorescence tomography studies of gliomas in murine models. This chapter presents preliminary data for two mice.

Chapter eight describes an attempt to use fluorescence imaging to track the response of gliomas to a targeted therapy in murine models.

Chapter nine presents a successful imaging study of brain tumors in mice using a targeted molecular agent in a small number of mice.

Chapter ten re-examines an older issue originally addressed by Li et al.^{47, 48} and Sevick-Muraca et al.⁴⁹, comparing measurements derived from perturbations caused by optical absorption to those originating from fluorescence emission.

Chapter eleven discusses feasibility studies for using a spectrally-constrained imaging approach based on absorption, often referred to as the “spectral priors” approach, to recover values of endogenous and exogenous tissue chromophore concentrations directly.

In *Chapter twelve*, phantom and computer model data are used to examine the source and extent of fluorescence peak distortion in turbid media⁵⁰.

In *Chapter thirteen*, contrast-detail analysis is used to determine size and contrast limits of tumor detection for a variety of tissue geometries using simulated fluorescence tomography data.

Finally *Chapter fourteen* presents overall study conclusions and *Chapter fifteen* discusses short-term and long-term future directions and introduces a few new ideas for further research.

Chapter Two: Instrumentation

The multi-channel spectrometer-based detection system developed for imaging fluorescence yield in tissue is described in this chapter. The system operates in continuous wave (CW) mode using broadband detection which facilitates the use of unique spectral fitting pre-processing techniques to decouple the fluorescence emission from background contamination. The spectroscopic detection system couples directly into a Philips 3T magnet for simultaneous MRI and optical data acquisition. In this configuration, the highly resolved MR images are used as templates for imaging fluorescence yield from emission of an injected fluorophore. A custom-designed and manufactured rodent coil produced by Philips Research, Hamburg integrates the fiber optic array into a small-diameter RF pickup coil for imaging small animals in the 3T MRI.

This chapter provides a review of the system components in the context of the design objectives. A brief description of the multi-wavelength frequency domain system is also included since it was used extensively to acquire images of background optical properties for fluorescence imaging and to investigate spectrally-constrained absorption imaging of exogenous contrast, a technique described in Chapter 11. System validation, data calibration and imaging performance metrics are addressed in Chapter 5.

2.1 System Design

A primary goal of the project was the development of a multi-wavelength capable system with a wide spectral range to explore the limits of broadband spectroscopic tomography from within MRI scanners. The parallel spectrometer-based tomographic imaging system, depicted in Figure 2.1, couples into a Philips 3T MRI magnet and was developed to acquire spectrally resolved transmission, fluorescence emission, and bioluminescence spectra. Major system components described below include the spectrograph, detection array, fiber optic transmission of light to and from the tissue surface, the acquisition light source, and MRI coils which integrate the fiber optic patient interface. Photographs of the system are presented in Figure 2.2.

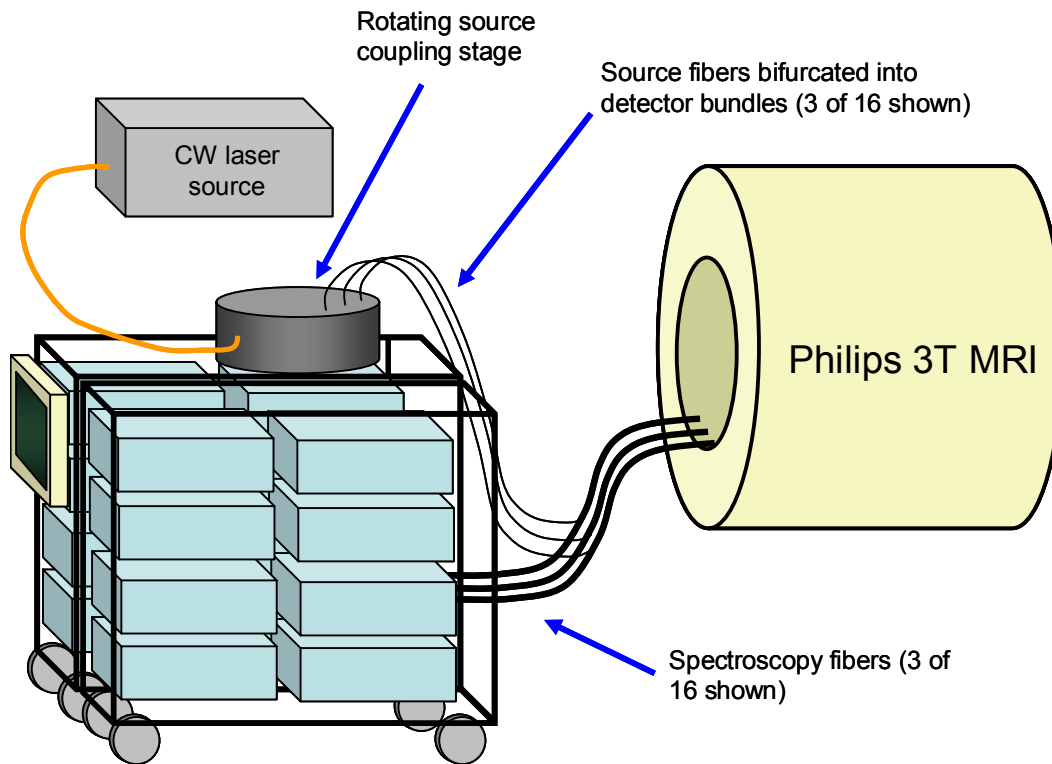


Figure 2.1. Diagram of the MRI-coupled 16 channel spectroscopy system for fluorescence tomography. Long, bifurcated spectroscopy fibers couple contact mode source-detection directly into the MRI bore.

2.1.1 Optical Detection System

The optical detection platform is composed of 16 Princeton Instruments/Acton Insight:400F Integrated Spectroscopy systems (Acton, MA) residing in two custom designed wheeled carts (8020, Columbia City, IN). The Insight 400F consists of a 0.3 m F3.9 imaging spectrograph and a low noise, front illuminated CCD (Pixis 400F) operating at -70 °C. The 1340 x 400 pixel CCD is binned vertically to maximize detector area/wavelength providing a binned detection area of 0.16 mm² for each horizontal pixel. Manufacturer specifications indicate a dark current of 0.0025 electrons/pixel/s and

quantum efficiencies of 0.45 at 750 nm and 0.20 at 950 nm. Each spectrograph contains a motorized grating turret holding 300 and 1200 l/mm gratings, which when coupled to the CCD, provide spectral ranges of 60 and 300 nm for a single grating position, respectively. Both gratings are blazed at 750 nm for maximum efficiency in the NIR.

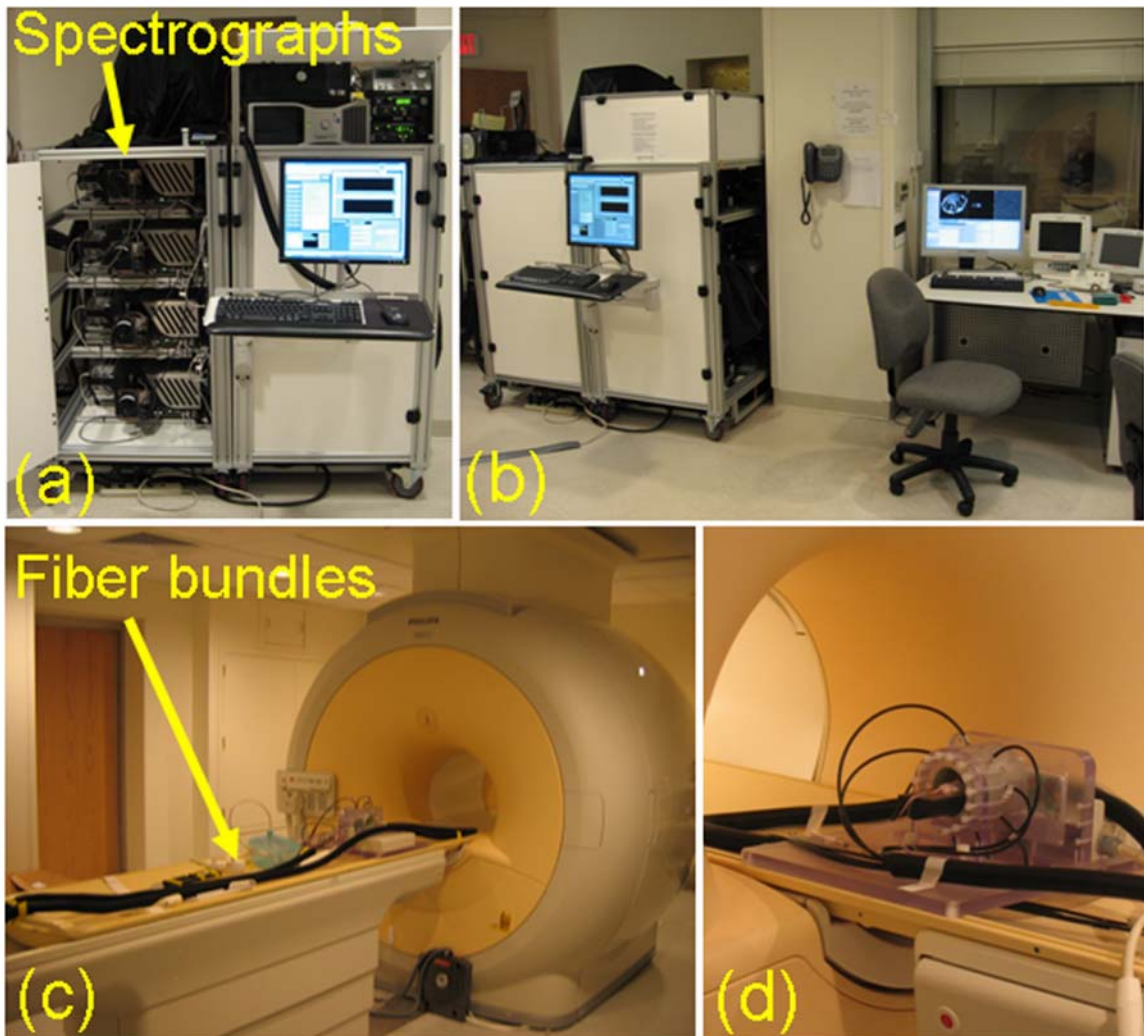


Figure 2.2. Top left: The spectroscopy system is built into carts which can be wheeled into the MRI control room [(a) and (b)]. Sixteen 13 meter long fiber bundles extend through ports in the wall and into the MRI bore [(c) and (d)].

2.1.2 Light collection and delivery

Sixteen custom designed bifurcated fiber bundles (Zlight, Latvia), diagramed in Figure 2.3, channel light to and from the imaging domain. Each fiber bundle is composed of eight 13 meter long and 400 μm diameter silica fibers which contact the tissue surface. Seven fibers from each bundle connect to the input system of each of the spectrographs while the eighth, known as a source fiber, branches off to the source coupling system. The light source is coupled sequentially into one of the sixteen fibers using a precision rotating stage (Velmex, Bloomfield, NY). Since each spectrograph is attached directly to one of the 16 detection fibers, this configuration requires no fiber-to-fiber coupling between the tissue surface and spectrometers and therefore provides parallel detection of full spectra for each source position without loss due to unnecessary coupling. The detector associated with the active source fiber is deactivated, resulting in 15 measurements for each 16 source positions, though this may be reduced for smaller domains. The motorized rotating stage unit also contains 15 frequency modulated PMTs in a configuration identical to that described elsewhere⁵¹. This design is part of an ongoing system expansion which will provide multi-wavelength frequency domain transmission mode acquisition through the source branch of the optical fibers and is addressed more thoroughly in section 15.1.3 of this document.

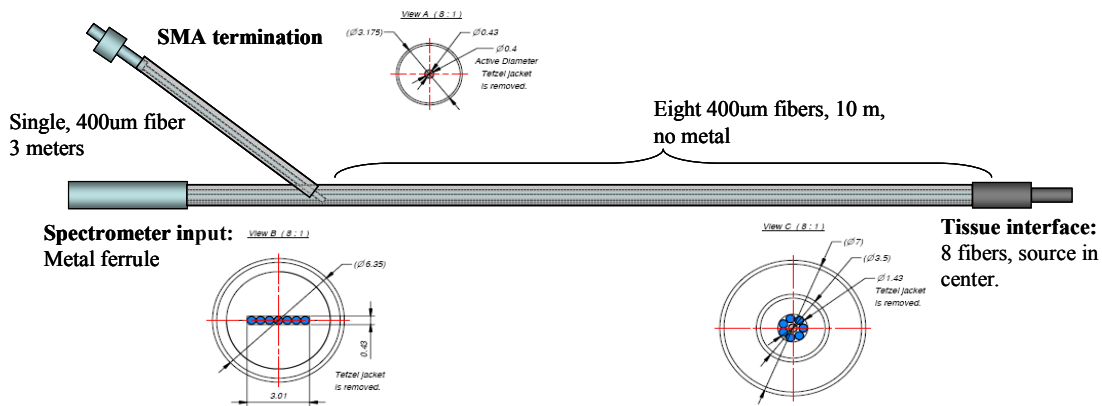


Figure 2.3. Diagram of the bifurcated spectroscopy fibers.

The terminal of the detection branch, labeled “Spectrometer input” in Figure 2.3, contains seven silica fibers arranged in a line to match the vertical entrance slit. This terminal is attached to custom designed and manufactured spectrometer entrance optics, depicted in Figure 2.4. Most of the light emitted from the $NA = 0.37$ fiber is collimated with an F1.4, 25 mm focal length digital camera lens (MegaPixel, Edmund Optics, Barrington, NJ), however since the $f\#$ of the fiber is less than 1.4 and it is a finite source, some light passes outside the lens aperture. The collimated light passes through a fully automated 6-position filter wheel containing two long pass interference filters, one with a 650 nm cut on and the other a 720 nm cut on (Omega, Brattleboro, VT), for fluorescence emission acquisition. Additionally, two neutral density (ND) filters (Thorlabs, Newton, NJ) reside in each filter wheel with optical densities (OD) of 1 and 2. Filter wheel positions are automatically adjusted during image acquisition. A 25 mm diameter, 60 mm focal length NIR achromat (Thorlabs, Newton, NJ) focuses the collimated and filtered light onto the input slit.

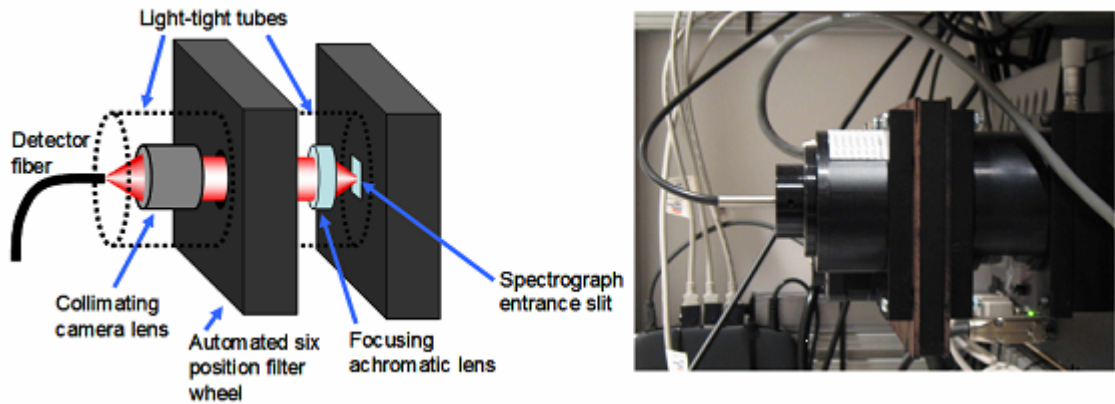


Figure 2.4. Diagram (left) and photograph (right) of the custom designed entrance optics. Lenses collimate the incoming light for filtering with selectable interference or ND filters and focus the light onto the spectrograph slit.

A simplified ray diagram of the optical system is presented in Figure 2.5 (Zemax) and illustrates the object-to-image magnification of the system, without consideration of aberrations. The calculation of magnification is simple for this case,

$$M = f_{\text{achromat}}/f_{\text{collimating_lens}} \quad 2.1$$

and the magnification of 2.4 produces a spot size of 7.2 mm by 0.96 mm focused on the spectrograph slit.

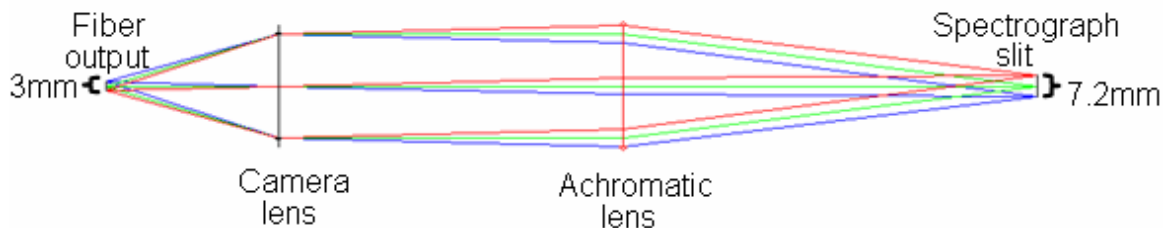


Figure 2.5. A ray diagram created using Zemax software illustrates the theoretical light path through the spectrograph coupling optics.

The entrance slits themselves are opened beyond the width of the fiber image to maximize photon collection. The magnified image of the fiber array at the slit plane defines an effective slit width approaching 1mm so that the system operates at a resolution of about 2.2 and 11.2 nm using the 1200 and 300 l/mm gratings, respectively. The spectral resolution can be increased at the cost of throughput by reducing the input slit width. An image of a fiber array focused on the CCD is shown in Figure 2.6.

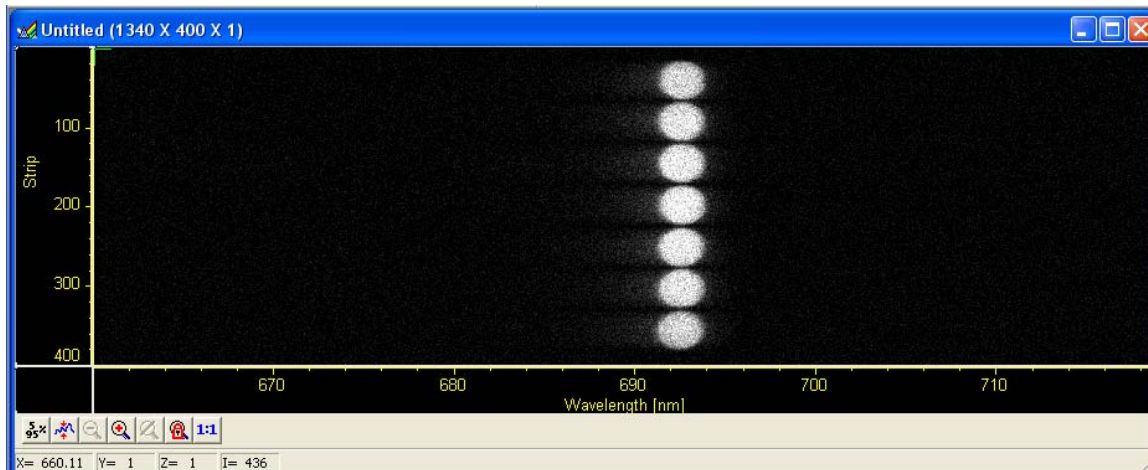


Figure 2.6. Image of the fiber array focused on the spectrometer CCD. An entrance optical system is considered aligned when this image is in focus, as above.

Usable dynamic range of the 16 bit CCD chip is over 2.8 orders of magnitude, assuming a minimum signal of 100 counts above background. Controlling the camera exposure times between 0.01 and 120 seconds adds an additional 4 orders for a total dynamic range approaching 7 orders of magnitude. This range is valid for fluorescence emission measurements which are pre-filtered using long-pass filters in the single-wheel automated filter selector described above. Since transmission mode measurements are not pre-filtering with the long pass filters, the ND filters may be used selectively to further enhance the detection performance, resulting in a total effective dynamic range of 9 orders of magnitude. Maximum camera exposure times are limited by the desired total acquisition time. If total acquisition time is not critical, the maximum camera exposure times may be increased to further extend the dynamic range.

2.1.3 Light sources

The imaging method for a given acquisition determines which light source to incorporate into the imaging sequence. Currently available sources include a high power tungsten white light source for broadband transmission tomography, a variety of laser diodes for transmission and fluorescence imaging, and a high power Mai Tai Ti:Sapphire laser (Spectra Physics, Irvine, CA) capable of automated wavelength tuning between 690 and 1020 nm. Bioluminescence mode imaging requires no external source. Since the focus of the work presented here is fluorescence imaging, most data for the presented examples were acquired using a 690 nm CW laser diode (Applied Optronics, South Plainfield, NJ) to excite the fluorophore.

2.1.4 Patient/animal interface

A unique MRI rodent coil designed in collaboration with Philips Research Europe (Hamburg, Germany) features sixteen access holes and nylon set screws to accommodate the spectroscopy fibers in a circular array. The following system details were drafted by Christoph Leussler and Peter Mazurkewitz at Philips Research ⁴⁶.

While small magnet bore animal systems are restricted to birdcage coil configurations, larger bore commercial clinical MR scanners allow the use of solenoid coil designs. The B_1 -field direction of this coil must be oriented orthogonal to the B_0 field axis of the magnet. For small animal imaging at 3T, the solenoid coil provides high B_1 sensitivity and good field of view coverage. Calculations of electromagnetic field and coil characteristics were performed from simulations using a commercially available EM program (FEKO), which is based on the method of moments (Figure 2.7).

The solenoid coil has an open inner diameter of 70 mm and is built from 8mm wide strip conductors wound around a fiberglass cylinder. The coil support cylinder is made of glass fiber and is mechanically fixed to a side wall. The parallel windings are connected as shown in Figure 2.8 and the gap between individual strip conductors is 8mm, providing space to accommodate the spectroscopy fibers. Circumscribing the fiberglass coil support cylinder is a removable polycarbonate cylinder containing nylon set screws to affix the spectroscopy fibers.

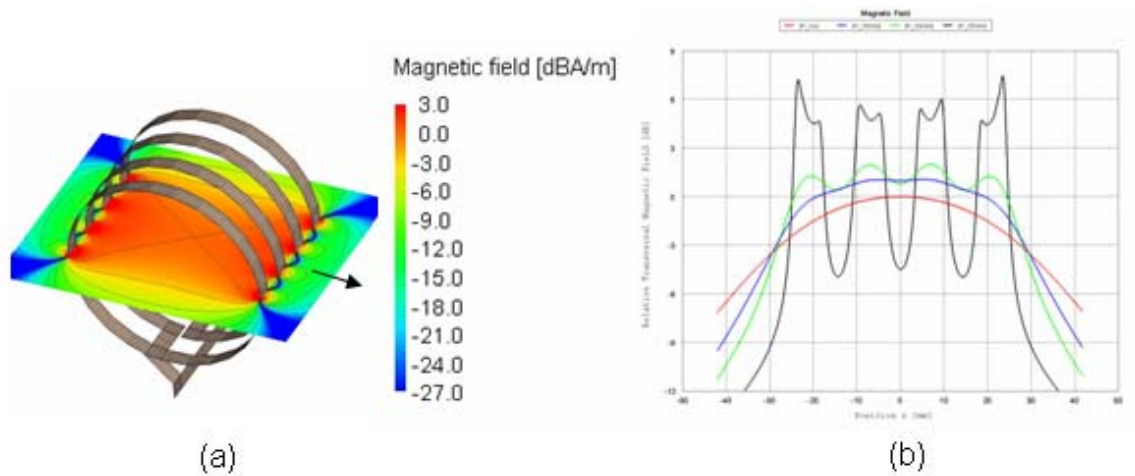


Figure 2.7. (a) Relative transversal magnetic field of the solenoid coil. The isocenter is set to 0 dB and the arrow shows the B_0 direction. (b) Sensitivity profiles along the coil axis (perpendicular to the main field, B_0) for different distances from the isocenter.

The overall inductance of the solenoid is $L_s = 1024 \mu\text{H}$ at 127 MHz. Sixteen equidistant splits with non magnetic capacitors (ATC 100B) are introduced along the conductor to avoid current inhomogeneities (propagation effects). During the transmit phase, the coil is detuned by 3 independent parallel detuning circuits distributed along the solenoid, which make the coil transparent for the B_1 transmit field. Optimized blocking radio frequency (RF) chokes prevent RF leakage and provide a high Q factor measured at $Q_L = 600$ for the unloaded coil. A low noise preamplifier is connected directly to the solenoid and optimal noise matching is performed via a low loss pi network.

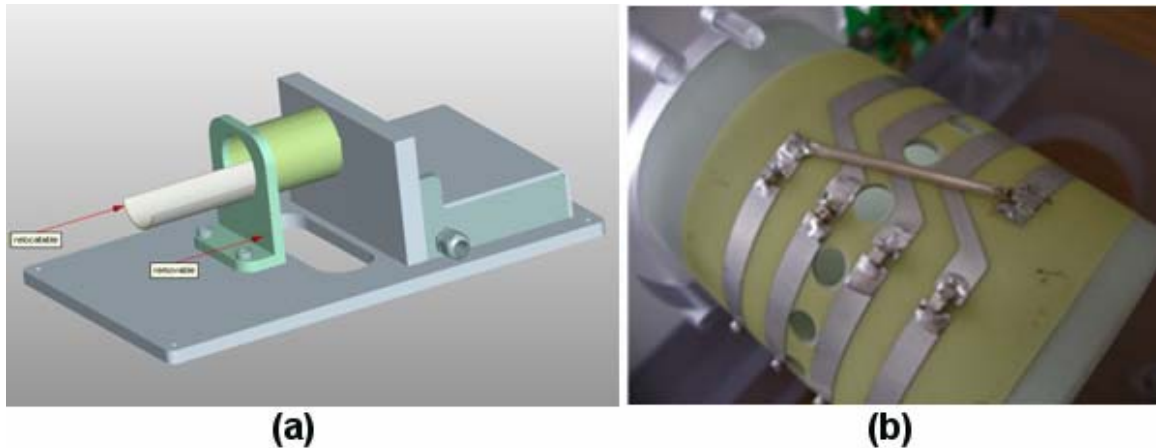


Figure 2.8. (a) CAD rendering of the Philips rodent coil. (b) Photograph of the coil layout showing connected strip conductors and holes to provide access for optical fibers.

A custom designed mouse head positioning system was developed for mouse brain imaging. Several iterations of the system were used for different studies reported in this thesis, each of which is detailed in the relevant section. The most evolved design is pictured in Figure 2.9 and consists of two concentric cylinders, made of black Delrin, which fit in the rodent coil. Eight fiber-accommodating thru-holes drilled radially through both cylinders circumscribe the subject. Importantly, the outer cylinder also contains circular divots half-way between each fiber thru-hole which snugly accommodate clinical copper sulfate MRI fiducials (IZI Medical Products, Baltimore, MD). These fiducials are critical references for locating fiber positions in the MR images.

The concentric cylinder design requires fabrication of a single outer cylinder while several inner cylinders may be manufactured with different inner bore diameters and canters to fit a variety of rodents or regions on rodents' bodies. Attaching a mouse bed to

the small cylinder also allows the animal to be positioned on the cylinder/bed apparatus outside of the large cylinder, and then inserted into the larger cylinder in the RF coil. Finally, the small cylinder may be replaced with cylindrical phantoms for system calibration and testing.

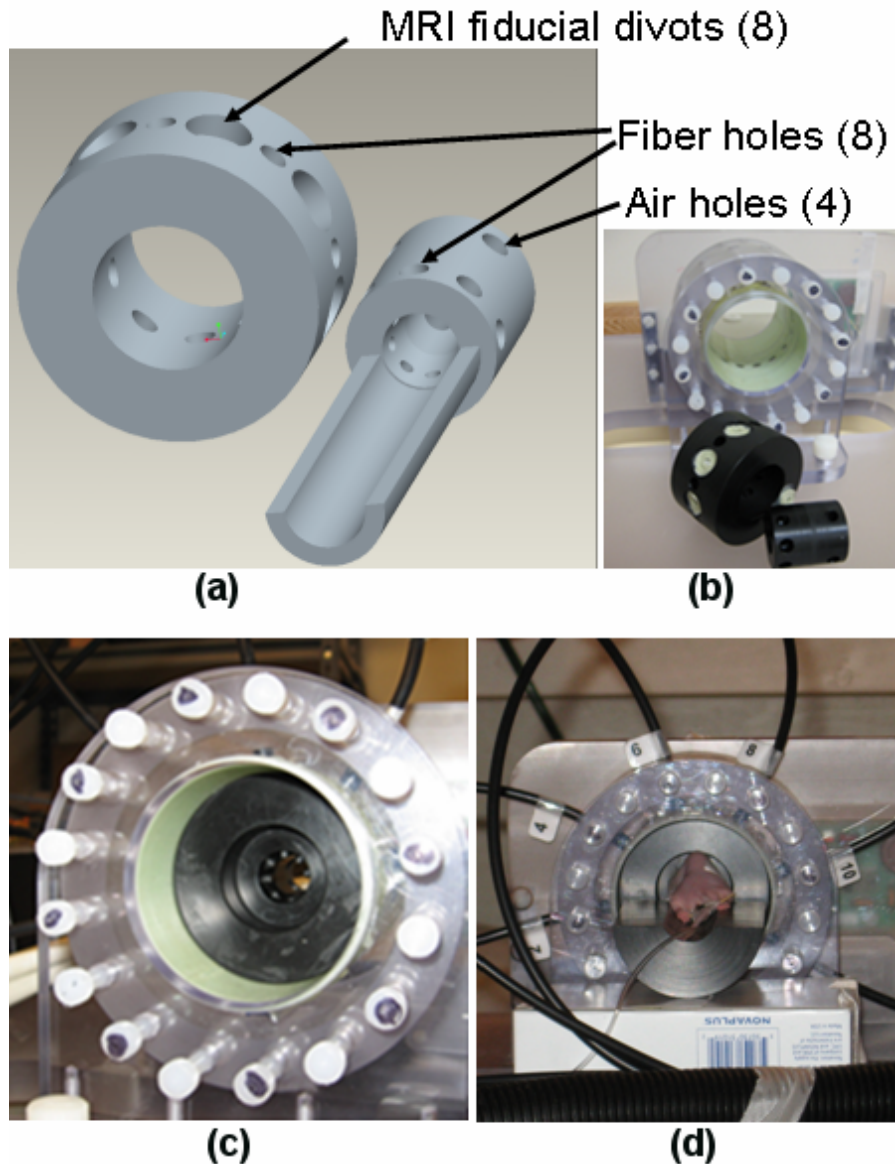


Figure 2.9. 3D CAD rendering, (a), and photographs of the latest generation fiber positioning system are shown. Two concentric cylinders, (b), fit snugly in the RF coil and accommodate eight optical fibers [(c) and (d)]. The outer cylinder also

houses eight MR sensitive fiducials in the plane of the fiber array positioned exactly between each fiber pair as shown in (b).

Larger volumes and patient breast imaging capabilities are provided by a fiber optic ring attached to a commercial 3T MRI breast coil (MRI Devices, Waukesha, WI), depicted in Figure 2.10. The current design requires manual fiber positioning using set screws, however, spiral ring and parallel plate geometries may be implemented for more reliable positioning.



Figure 2.10. The patient interface is a circular array of fibers that couples into a standard MRI breast coil (a), though parallel plate geometries are also under consideration (b).

2.1.5 Automated Acquisition

The system is operated using a Dell desktop PC running Windows XP Professional. Image acquisition is automated using custom programs written in Labview (National Instruments, Austin, TX) developed with the SIToolkit camera/spectrometer drivers produced by Rcubed, LLC (Lawrenceville, New Jersey). USB cables connect all

camera/spectrometer/filter wheel units to the computer, and the motorized source-coupling stage is connected via a serial cable. A screenshot of the primary acquisition control program is shown in Figure 2.11. The user interface is designed to minimize technician training. Imaging modes include Fluorescence Tomography, Transmission Tomography, Bioluminescence Tomography, Raw Data Only, System Calibration, and Basis Spectra Acquisition, and once a mode is selected, only relevant options pertaining to that imaging mode appear on the screen. Exposure times may be set manually by the user or automatically determined using an optimization routine which performs test exposures to calculate ideal exposure times for image acquisition. Additional options include real-time spectrum calibration and spectral fitting and automatic neutral density filtering to preferentially decrease filter OD as a function of source-detector distance for measurements not involving fluorescence emission. A user manual which includes instructions on how to use the software is located in Appendix A.

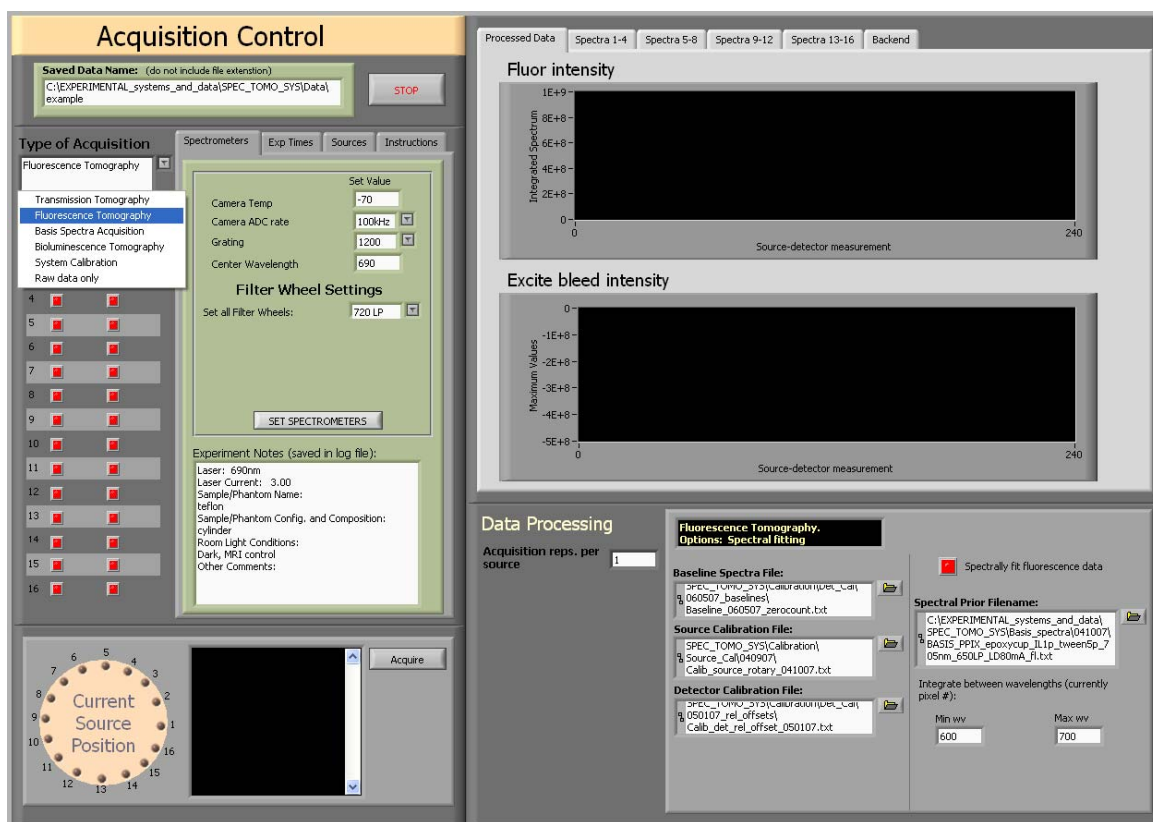


Figure 2.11. Front panel of the spectroscopy system’s image acquisition program, designed in Labview. The input controls are at left in the tab menu, and the output data can be observed at right as it is written to file. The window at the bottom left is updated continuously with acquisition status messages. Calibration filenames are provided at bottom right for real-time data calibration.

2.2 Frequency Domain Measurements

Tissue and tissue phantom absorption and scattering properties were determined using a parallel frequency domain (FD) system previously developed at Dartmouth (see Figure 2.12). System specifications and imaging performance data have been extensively reported^{29, 43, 51-55} and only a brief description is included here. Six laser diodes at 661, 761, 785, 808, 826, and 849 nm are modulated at 100 MHz and coupled sequentially into the tissue interface. Fiber bundles in contact with the tissue surface couple light leaving the tissue into photomultiplier tubes (PMT’s). The modulated signal is heterodyned

down to 500 Hz and amplitude and phase extracted for each source-detector pair. Once calibrated, these values are used to recover absorption and scattering properties of the interrogated tissue.

This system serves two critical roles in the work presented. Optical properties used in fluorescence tomography reconstructions of phantoms were measured using this system. This required transporting the phantom between the spectrometer-based fluorescence imager and the FD scanner. It also provides the platform to test and validate spectrally-constrained absorption imaging for extracting exogenous agent concentration, as described in section 11.1.

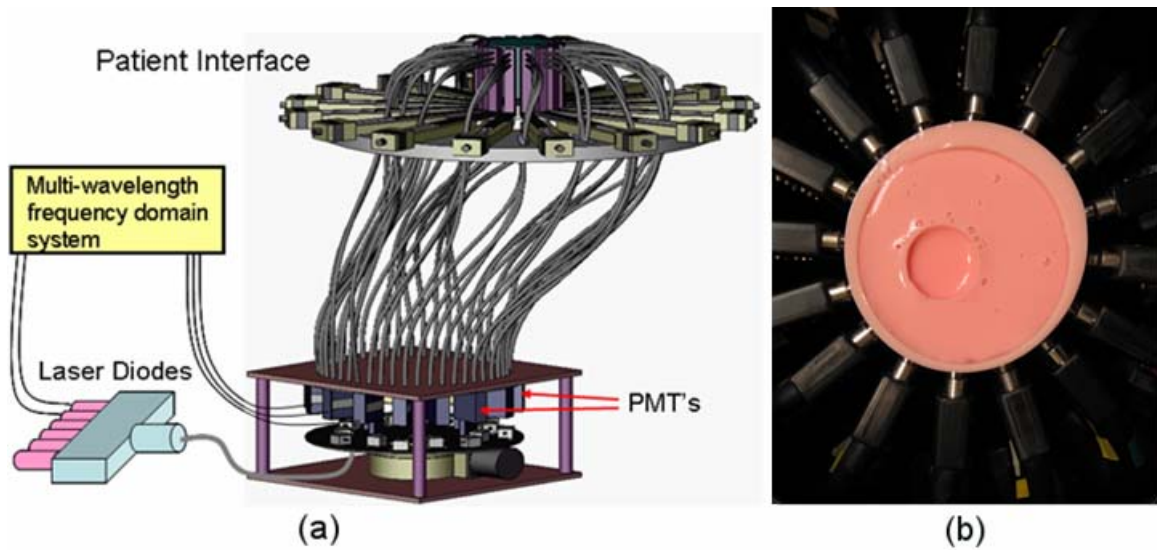


Figure 2.12. The three plane, 48 fiber frequency domain system which uses six laser diode sources and PMT detection is shown in (a). A photograph of the patient array holding a gelatin tissue phantom is shown in (b).

2.3 Summary

A spectrally-resolved MRI-coupled optical tomography system has been developed to image fluorescence yield in a variety of tissue volumes. This unique system

provides rich spectral information in a variety of diffuse optical imaging modes including broadband NIR transmission, fluorescence and bioluminescence. A unique rodent coil developed specifically for this system provides high resolution MR images of small animals which can be used to guide image reconstructions of the optical data. Calibration procedures and system performance figures will be discussed in Chapter 5, following the introduction of the theoretical imaging framework and phantom designs in Chapters 3 and 4.

Chapter Three: Modeling and image reconstruction techniques

This chapter introduces the modeling and computational framework for imaging exogenous contrast using fluorescence emission tomography. A spectrally constrained tomographic imaging technique based on the absorbing properties of endogenous and exogenous chromophores is also introduced. Finally, the implementation of spatial priors derived from MR information is described.

3.1 Fluorescence imaging

3.1.1 Modeling fluorescence fields

The mathematical approach for the fluorescence problem is well established⁵⁶⁻⁶⁰. The diffuse nature of near-infrared (NIR) photon propagation in biological tissue is the foundation of the model system used. In this regime, the initial excitation source (typically a laser delivered to the tissue) and the fluorescence emission photon field can be described by a system of coupled diffusion equations, here presented for a source modulated at frequency f , and written in terms of angular frequency $\omega = 2\pi f$,

$$-\nabla \cdot \kappa_x(r) \nabla \Phi_x(r, \omega) + [\mu_{ax}(r) + \frac{i\omega}{c(r)}] \Phi_x(r, \omega) = q_0(r, \omega) \quad 3.1$$

$$-\nabla \cdot \kappa_m(r) \nabla \Phi_{fl}(r, \omega) + [\mu_{am}(r) + \frac{i\omega}{c(r)}] \Phi_{fl}(r, \omega) = \Phi_x(r, \omega) \eta \mu_{of}(r) \frac{1 - i\omega\tau(r)}{1 + [\omega\tau(r)]^2} \quad 3.2$$

where subscripts x and m signify the excitation and emission wavelengths λ_x and λ_m , respectively, and fl indicates fluorescence emission at λ_m . The intrinsic optical parameters

$\mu_{ax,m}$ and $\mu_{sx,m}'$ are the absorption and reduced scattering coefficients respectively, $q_0(r, \omega)$ is an isotropic source, and $\Phi_{x,fl}(r, \omega)$ is the photon fluence rate at position r .

The diffusion coefficient is given by

$$\kappa_{x,m} = \frac{1}{3(\mu_{ax,m} + \mu_{sx,m}')} \quad 3.3$$

and $c(r)$ is the speed of light in the medium at any point, defined by $c_0/n(r)$, where $n(r)$ is the index of refraction and c_0 is the speed of light in a vacuum. The fluorophore parameters are the lifetime $\tau(r)$ and the fluorescence yield $\eta\mu_{af}(r)$, the latter a product of the fluorophore's quantum efficiency η and its absorption coefficient, $\mu_{af}(r)$. Imaging domains are discretized into meshes and modeled using the finite element method (FEM).

Type III boundary conditions (also known as Robin or mixed) are used to describe the fractional loss of photons at the tissue-air interface. The flux leaving the external boundary is described by:

$$\Phi_x(\xi) + 2A\hat{\mathbf{n}} \cdot \kappa_x(\xi)\nabla\Phi_x(\xi) = 0 \quad 3.4$$

written here for the excitation field. The coordinate ξ represents a point on the external boundary and A is derived from Fresnel's law and depends upon the relative refractive index (RI) mismatch between tissue and air;

$$A = \frac{2/(1 - R_0) - 1 + |\cos \theta_c|^3}{1 - |\cos \theta_c|^2} \quad 3.5$$

The critical angle, θ_c , is the angle at which propagation from within the domain undergoes total internal reflection at the boundary and

$$R_0 = \frac{(n_1 / n_{AIR} - 1)^2}{(n_1 / n_{AIR} + 1)^2} \quad 3.6$$

In this work, equations (3.1) and (3.2) are solved numerically on arbitrarily shaped domains using the FEM. In an extensive study on mesh resolutions, Yalavarthy et al. showed that breast sized meshes of approximately 2000 nodes provide an appropriate balance between mesh resolution and associated computation time for DOT imaging⁶¹. Thus, most studies in this work adopt this as a standard, examples of which are shown in Figure 3.1.

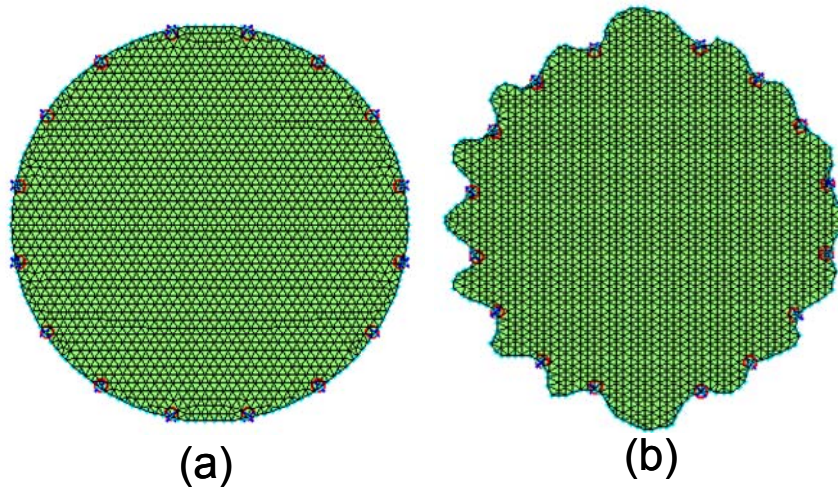


Figure 3.1. Circular, (a), and irregular, (b), 2-d FEM meshes composed of approximately 2000 nodes. The circular domain is 86 mm in diameter and the maximum diameter of the irregular domain is 108 mm. Red circles and blue x's mark the locations of 16 source-detectors.

Simulating data involves running the forward model in three stages: 1) frequency domain transmission at the excitation wavelength using Eq. 3.1, 2) frequency domain transmission at the emission wavelength also using Eq. 3.1 but with a laser source and optical properties at the emission wavelength, and finally 3) CW fluorescence emission using the excitation intensity field in the source term [Eq. (3.2)]. Since the experimental system operates in CW mode when acquiring fluorescence emission data, phase data is not considered in step 3. The internal distribution of the fluence fields are calculated for each step and boundary data extracted as shown pictorially in Figure 3.2. For simulation studies, a normal distribution of random noise may be added to the data, usually calculated as a percentage for amplitude data and degrees for phase data. Additionally, a percentage of the excitation intensity is added to the fluorescence emission measurements

to simulate excitation cross-talk in this signal arising from imperfect filtering efficiencies, an issue addressed in section 5.1.4.

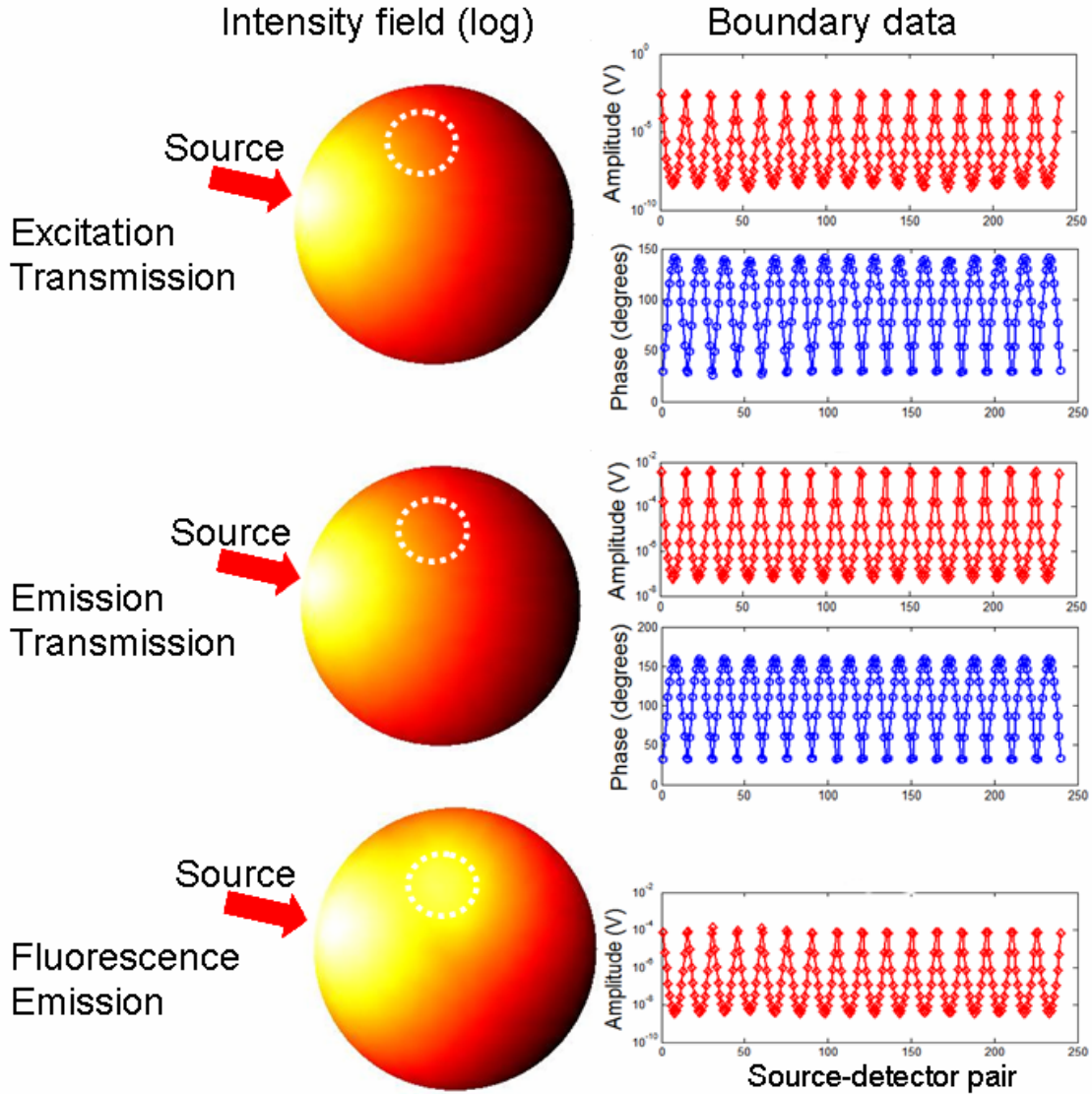


Figure 3.2. An illustration of the data produced by the fluorescence forward model used in this work is shown. The logarithm of the internal intensity field (left column) is plotted for a single source while the entire set of boundary data extracted for each source-detector pair is shown at left. Fluorophore contrast was assumed to be distributed homogeneously throughout the domain except for an elevated region marked by the white circle.

3.1.2 Fluorescence image reconstruction

Image reconstruction involves matching the measured boundary data to values calculated using the model by a non-linear iterative Newton-Raphson minimization. The computational approach is to minimize the difference between measured fluence, Φ^{Meas} , at the tissue surface and calculated data, Φ^C , from the model Eqs. (3.1) and (3.2). This is accomplished by adjusting the spatial distribution of the unknown parameters through minimization of the ‘objective’ function. The objective function for recovering the optical properties at the excitation wavelength, $\mu_x = (\mu_a, \kappa)_x$, is given by

$$\chi^2 = \sum_{i=1}^{NM} (\Phi_{x_i}^{Meas} - \Phi_{x_i}^C)^2 + \lambda \sum_{j=1}^{NN} (\mu_{x_j} - \mu_{x_0})^2 \quad 3.7$$

where NM is the total number of measurements given by the imaging system, NN is the number of parameters representing the optical property distribution which corresponds to the number of nodes in the reconstruction mesh, and I is an $NN \times NN$ identity matrix.

The general image reconstruction protocol is as follows:

- 1) Reconstruct for optical properties at the excitation wavelength, μ_{ax} and μ_{sx}' , with frequency domain data,
- 2) Reconstruct for optical properties at the emission wavelength, μ_{am} and μ_{sm}' , with frequency domain data collected using a laser source at the emission wavelength,
- 3) Use the reconstructed optical properties and fluorescence intensity (in CW) data to recover fluorescence yield.

This procedure is illustrated in a flow diagram in Figure 3.3, which follows the tracks of four separate data sets, producing one image of fluorescence yield. The same reconstruction algorithm was used to determine background optical properties in steps (1) and (2) and is based on previously reported work^{62, 63}. Following the Taylor series approach for deriving Newton's method, $\partial\chi^2/\partial\mu_x$ is evaluated at μ_x based on an expansion around a nearby point μ_{x_0} , where the second and higher order terms are ignored, leading to the iterative update equations:

$$\Delta\mu_{x,m} = \left[J_{x,m}^T J_{x,m} + \lambda I \right]^{-1} J_{x,m}^T \left(\Phi_{x,m}^{Meas} - \Phi_{x,m}^C \right) \quad 3.8$$

for the excitation and emission wavelength transmission measurements in the frequency domain and

$$\Delta\eta\mu_{af} = \left[J_{fl}^T J_{fl} + \lambda I \right]^{-1} J_{fl}^T \left(\Phi_{fl}^{Meas} - \Phi_{fl}^C \right) \quad 3.9$$

for the fluorescence yield update, where J is the Jacobian matrix, here calculated using the Adjoint method⁶⁴. In this work, I is the identity matrix, and λ is some fixed fraction multiplied by the maximum value on the diagonal of the Hessian matrix $J^T J$, and is therefore updated at each iteration. To arrive at Eqs. 3.8 and 3.9, the parameter penalty term which arises from the second term in Eq. 3.7 was ignored, as per the protocol reported in previous work⁶⁵.

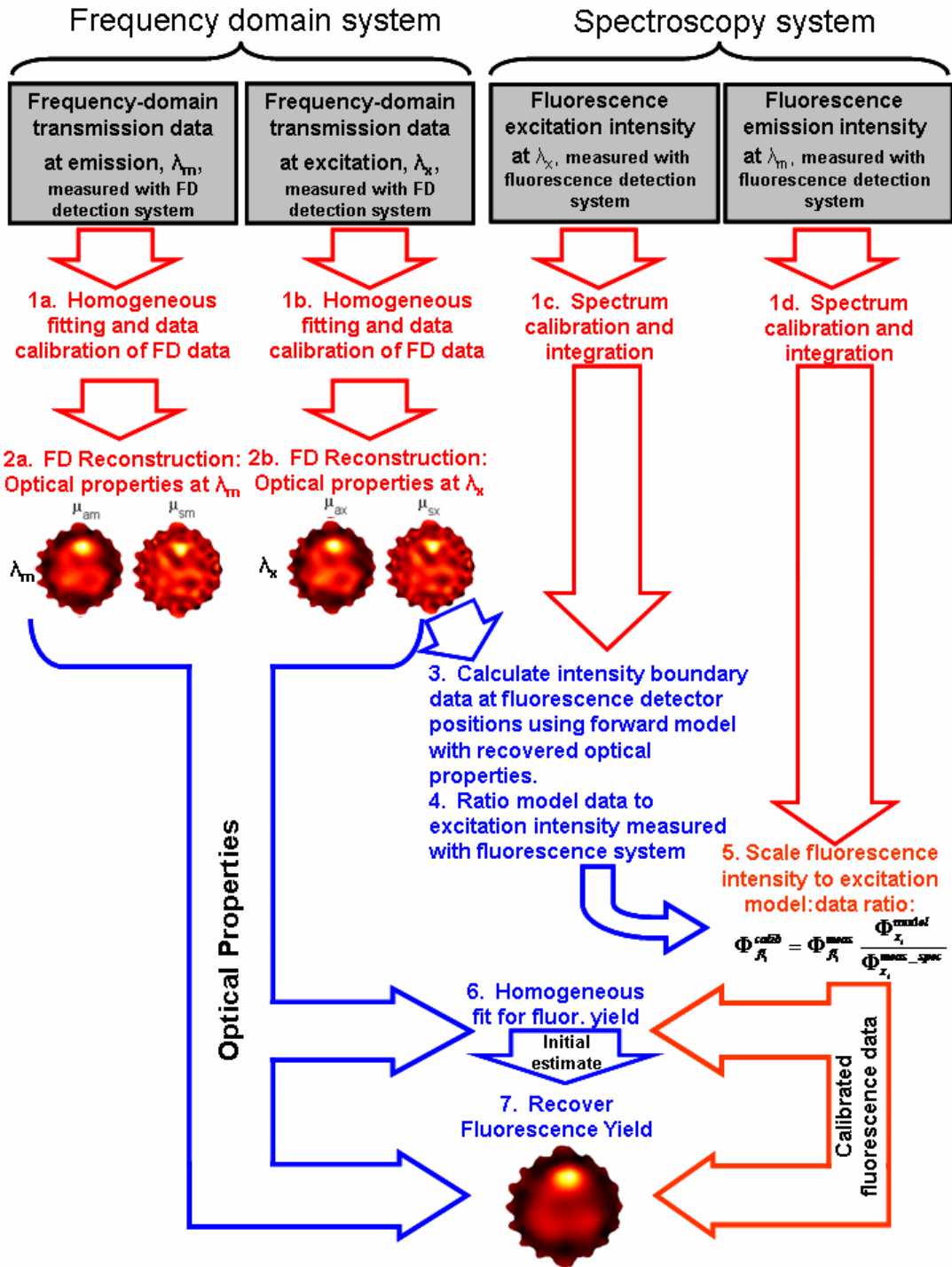


Figure 3.3. A full reconstruction from measured data is a complicated process involving four separate data sets, two from each tomography system. This flow diagram outlines the fluorescence recovery procedure, including calibration steps and homogeneous fitting algorithms.

The full reconstruction procedure outlined in Figure 3.3 was used for all simulated experiments presented throughout this thesis, though the unnecessary data calibration steps 3-5 were skipped since numerically generated data are perfectly calibrated to the model. An example of a set of reconstructed images from simulated data is presented in Figure 3.4. For most animal imaging experiments, optical properties were assigned to different tissue regions based on published values in the literature, in which case the process starts at step 3 in the figure. Approaches used for phantom data vary throughout the presented work, though in almost all cases, frequency domain data is used to calculate background optical properties at one or more wavelength(s) and these values are then used in steps 3-7. The approach used in a given experiment will be stated clearly in the description of each study.

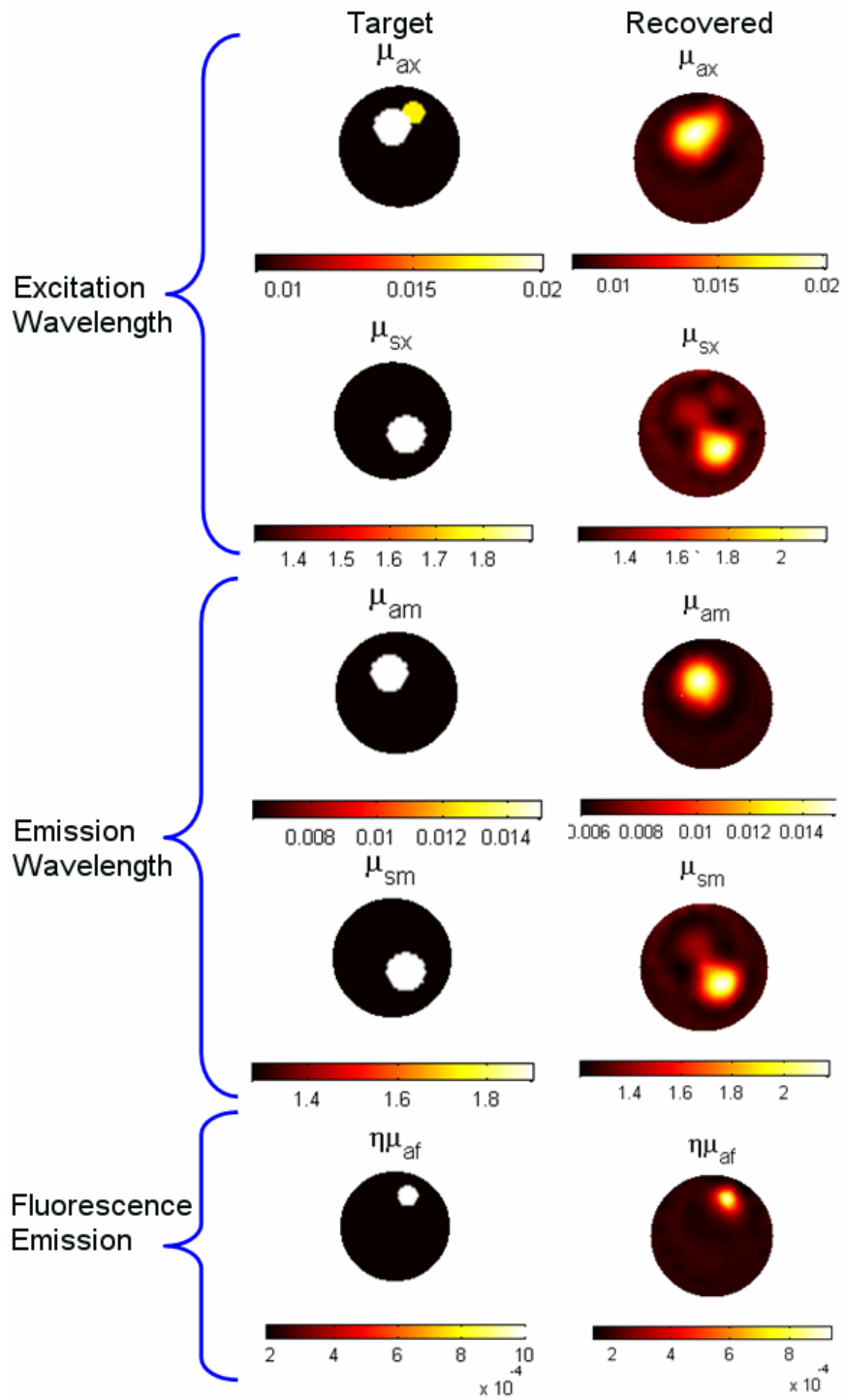


Figure 3.4. A simulated test domain for fluorescence image reconstruction is shown along with associated reconstructed images. The final image of fluorescence yield is the image of interest in most studies discussed throughout this thesis. All color-bars are in units of mm^{-1} .

3.2 Chromophore concentration recovery using spectral priors

Another approach to image administered optical contrast *in vivo* is to exploit the absorption characteristics of the exogenous agent to recover the spatial distribution of drug concentration. Spectrally-constrained reconstruction methods for diffuse optical tomography have been used to image endogenous tissue chromophore concentrations by incorporating prior knowledge of extinction spectra directly in the inversion formulation. This technique, first demonstrated by Corlu et al.⁴¹ and Li et al.⁴² for reconstructing continuous wave data, was expanded for frequency domain systems and shown to provide qualitatively and quantitatively accurate images of hemoglobin concentration, oxygen saturation, water content, and scattering amplitude and power^{29, 43}. The spectrally constrained approach may readily be generalized to include exogenous contrast agents by incorporating the extinction coefficient spectra of the administered dye in the imaging algorithm.

Since the optical contrast is derived from the absorbing and scattering properties only, equations (3.1) and (3.2) are simplified to ignore contribution of fluorescence emission and the problem is reduced to the familiar DOT diffusion equation, presented in the frequency domain,

$$-\nabla \cdot \kappa(r, \lambda, \omega) \nabla \Phi(r, \lambda, \omega) + (\mu_a(r, \lambda, \omega) + \frac{i\omega}{c}) \Phi(r, \lambda, \omega) = q_0(r, \lambda, \omega) \quad \mathbf{3.10}$$

The inversion is constrained by prior knowledge of the chromophore absorption spectra and application of Beer's law, $\mu_a(\lambda) = [\varepsilon(\lambda)]C$, as well as by an empirical

approximation to Mie Theory, $\mu'_s(\lambda) = a(\lambda)^{-b}$. Here, λ is wavelength, μ_a and μ'_s are the absorption and reduced scattering coefficients, ϵ is the extinction coefficient, C is the chromophore concentration, a is the scatter amplitude, and b the scatter power. Frequency domain data measured for a range of excitation light wavelengths can be coupled in the following manner $\partial\phi_\lambda = J_{c,\lambda}\partial c + J_{a,\lambda}\partial a + J_{b,\lambda}\partial b$ where $\partial\phi$ is the change in boundary data and

$$J_{c,\lambda} = \left. \frac{\partial\phi}{\partial\mu_a} \frac{\partial\mu_a}{\partial c} \right|_\lambda, J_{a,\lambda} = \left. \frac{\partial\phi}{\partial\kappa} \frac{\partial\kappa}{\partial a} \right|_\lambda, J_{b,\lambda} = \left. \frac{\partial\phi}{\partial\kappa} \frac{\partial\kappa}{\partial b} \right|_\lambda \quad 3.11$$

The system of equations is assembled as

$$\begin{pmatrix} \partial\phi_{\lambda_1} \\ \partial\phi_{\lambda_2} \\ \vdots \\ \partial\phi_{\lambda_n} \end{pmatrix} = \begin{bmatrix} J_{c1,\lambda_1} & J_{c2,\lambda_1} & J_{c3,\lambda_1} & J_{a,\lambda_1} & J_{b,\lambda_1} \\ J_{c1,\lambda_2} & J_{c2,\lambda_2} & J_{c3,\lambda_2} & J_{a,\lambda_2} & J_{b,\lambda_2} \\ \vdots & \vdots & \vdots & \vdots & \vdots \\ J_{c1,\lambda_n} & J_{c2,\lambda_n} & J_{c3,\lambda_n} & J_{a,\lambda_n} & J_{b,\lambda_n} \end{bmatrix} \begin{pmatrix} \partial c1 \\ \partial c2 \\ \partial c3 \\ \partial a \\ \partial b \end{pmatrix} \quad 3.12$$

where $c1$, $c2$, and $c3$ indicate endogenous chromophores (oxy- and deoxy-hemoglobin concentration and water content). An exogenous chromophore, $c4$, can be incorporated into the model system through the modification,

$$\begin{pmatrix} \partial\phi_{\lambda_1} \\ \partial\phi_{\lambda_2} \\ \vdots \\ \partial\phi_{\lambda_n} \end{pmatrix} = \begin{bmatrix} J_{c1,\lambda_1} & J_{c2,\lambda_1} & J_{c3,\lambda_1} & J_{c4,\lambda_1} & J_{a,\lambda_1} & J_{b,\lambda_1} \\ J_{c1,\lambda_2} & J_{c2,\lambda_2} & J_{c3,\lambda_2} & J_{c4,\lambda_2} & J_{a,\lambda_2} & J_{b,\lambda_2} \\ \vdots & \vdots & \vdots & \vdots & \vdots & \vdots \\ J_{c1,\lambda_n} & J_{c2,\lambda_n} & J_{c3,\lambda_n} & J_{c4,\lambda_n} & J_{a,\lambda_n} & J_{b,\lambda_n} \end{bmatrix} \begin{pmatrix} \partial c1 \\ \partial c2 \\ \partial c3 \\ \partial c4 \\ \partial a \\ \partial b \end{pmatrix} \quad 3.13$$

given that the extinction coefficient spectrum of the drug is known. In practice, contrast agents with large extinction coefficients are needed to ensure that the drug's spectral features contribute to the overall tissue absorption spectrum. An example of a simulated test domain and associated reconstructed images is shown in Figure 3.5. In this case, data from eight wavelengths were combined to produce the images, namely 661, 690, 735, 761, 785, 808, 826 and 849 nm.

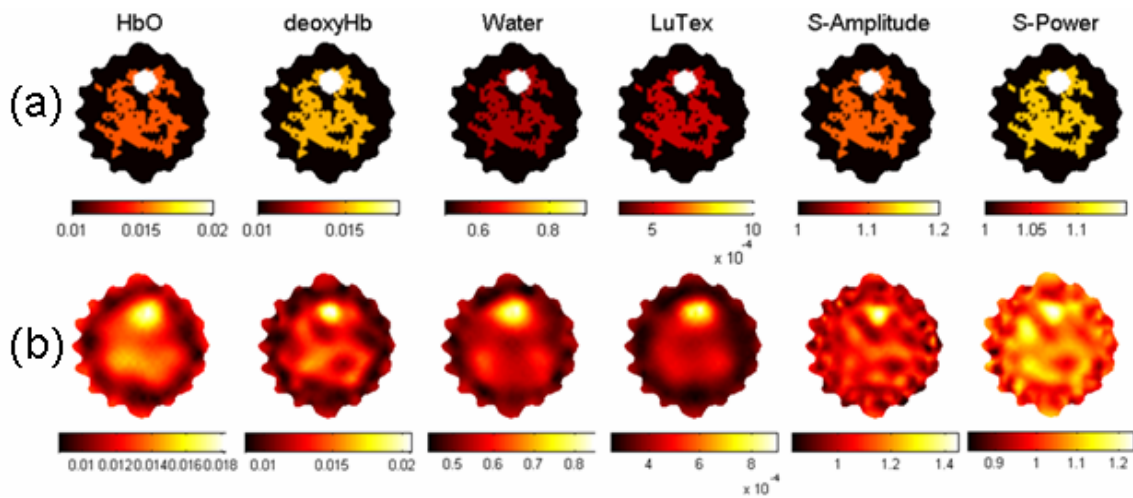


Figure 3.5. A simulated test domain for multi-wavelength spectrally-constrained image reconstruction is shown in (a). Associated reconstructed images, recovered simultaneously, are shown in (b). HbO, deoxyHb, and LuTex concentrations are in mM, water is in percent and scattering parameters are dimensionless.

3.3 Incorporating Spatial Priors

Two methods are used to incorporate tissue structural information derived from simultaneously acquired MR images into the optical tomography reconstruction algorithm. One approach defines the spatial relationship between the segmented MR image and optical parameters by encoding the segmented regions in the regularization

matrix. This is known as the soft priors approach since each node updates independently, allowing the recovery of tumor regions not explicitly segmented from the MR image. Alternatively, the hard priors approach divides the imaging domain into homogeneous regions segmented from the MR images, and is therefore unyielding in its application of spatial guidance.

Both implementations require spatial information obtained from high-resolution imaging modalities, such as MRI. The DOT imaging systems developed for this work are designed to couple into an MRI bore to provide simultaneous MR-DOT data acquisition. The reconstruction procedure is initiated by segmenting the MR image into major tissue types. This is followed by generating a problem specific FEM mesh from the outer boundary of the tissue volume and assigning region labels to appropriate nodes based on the MR segmentation. Both spatial priors techniques may be incorporated into any DOT algorithm presented previously.

3.3.1 Soft spatial priors

In the soft priors approach, spatial prior information is incorporated by assuming a ‘generalized Tikhonov’ penalty term and replacing the identity matrix in Eqs. (3.8) and (3.9) with a Laplacian-type matrix, demonstrated here for the excitation field associated with the fluorescence tomography reconstruction process^{37, 66, 67}:

$$\chi^2 = \sum_{i=1}^{NM} (\Phi_{x_i}^{Meas} - \Phi_{x_i}^C)^2 + \beta \sum_{j=1}^{NN} (L(\mu_{x_j} - \mu_{x_0}))^2 \tag{3.14}$$

where λ in Equation (3.7) has been replaced with the constant β . In this work, the dimensionless square matrix L encodes the spatial information from MR images acquired simultaneously with the optical data. After data acquisition, the MR images are segmented into regions representing major tissue types, such as adipose, fibro-glandular, and tumor tissues, identified by MR image intensity. The segmented image is then converted into an FE mesh compatible with the optical reconstruction software in a way that maintains the segmented tissue information. To construct the filter matrix, L , matrix elements associated with nodes in a given tissue region are assigned the same value. In this manner, the L-matrix represents an $NN \times NN$ Laplacian-type structure, the diagonal of which is $L_{i,i} = 1$ where i and j are nodal indices. If matrix elements are associated with nodes in the same tissue region (i.e., nodes i and j are in the same region) containing n nodes, $L_{i,j} = -1/n$. Elements associated with nodes that are not in the same tissue region are assigned $L_{i,j} = 0$. This structure allows sharp borders between tissue regions to be maintained during image reconstruction, while smoothing the image values in a given region. Following the same procedure as in the no-priors case, the parameter update is given by

$$\Delta\mu_{x,m} = \left[J_{x,m}^T J_{x,m} + \beta L^T L \right]^{-1} J_{x,m}^T \left(\Phi_{x,m}^{Meas} - \Phi_{x,m}^C \right) \quad 3.15$$

for the excitation and emission wavelength transmission measurements and

$$\Delta\eta\mu_{af} = \left[J_{fl}^T J_{fl} + \beta L^T L \right]^{-1} J_{fl}^T \left(\Phi_{fl}^{Meas} - \Phi_{fl}^C \right) \quad 3.16$$

for the fluorescence emission update. Much like λ in Eqs. (3.8) and (3.9), β is a fixed fraction multiplied by the maximum value on the diagonal of $\mathcal{J}^T J$. This update formulation may also be applied to the spectrally constrained implementation described above. Again, note that the penalty term has been omitted from Eqs. 3.15 and 3.16 just as in the no priors case ⁶⁵.

3.3.2 “Hard” spatial priors

The hard priors approach applies stricter constraints than the regularization-based implementation described previously. Nodal values are locked together by implicitly assuming segmented regions in the imaging domain are homogeneous. In practice, the Jacobian matrix is calculated on a fully resolved mesh at each iteration, but then collapsed into segmented regions for the inversion process,

$$\tilde{\mathcal{J}} = JK \tag{3.17}$$

where K is a matrix with dimensions $NN \times NR$, where NR is number of tissue regions in the spatial prior information. For regions 1 to N , K is written:

$$K = \begin{bmatrix} k_{1,1} & k_{1,2} & \cdots & k_{1,NR} \\ k_{2,1} & k_{2,2} & \cdots & k_{2,NR} \\ \vdots & \vdots & \ddots & \vdots \\ k_{NN,1} & k_{NN,2} & \cdots & k_{NN,NR} \end{bmatrix} \tag{3.18}$$

where

$$k_{j,n} = \begin{cases} 1, & j \in R_n \\ 0, & j \notin R_n \end{cases} \tag{3.19}$$

and R_n represents region n . This process drastically reduces the update parameter space from the product of number of nodes and number of unknown properties to the product of number of regions and number of unknown properties. In the spectrally constrained implementation, which may contain 2880 data points (240 phase and amplitude data points for each of six wavelengths) may reduce the parameter space 12000 unknowns (six parameters by 2000 nodes) to 18 unknowns (six parameters by 3 regions), making the inversion over-determined. Confidence in the segmentation is critical since regions are offered no spatial latitude. Indeed, the hard-priors approach is strictly a characterization-based implementation incapable of detection or uncovering false negatives, and therefore does not present as an image recovery problem *per se*.

3.3.3 A brief note on modeling and reconstruction software developed for this work

One component of this thesis was a revision of the NIRFAST software package originally authored by Hamid Dehghani. A full software manual was written for this version, dubbed NIRFAST_v2, and is included in Appendix B, while a brief description is provided here. The objective of the revision was to integrate separately developed tools, namely, the standard “single wavelength” frequency domain (FD) NIRFAST package, the multi-wavelength spectrally-constrained package, originally developed by Subha Srinivassan, the FLUORFAST package, developed by Hamid Dehghani and Scott Davis, and both hard and soft prior implementations for each of the preceding packages. The fundamental elements of the software, i.e. the mesh structure, FEM implementation, Jacobian calculations, etc., remained intact but were integrated into a new user

framework built around a database of extinction spectra of endogenous and exogenous chromophores and fluorophores. In this manner, users may choose to interact with the software only in terms of physiologically relevant parameters by using chromophore/fluorophore concentration values, Mie scattering parameters, and wavelengths of interest. Each mesh contains information about which chromophores/fluorophores are present and their spatial distributions throughout the mesh domain. Programs calculate/reconstruct data at wavelengths chosen by the user by consulting the chromophore spectra database. Thus, a single mesh loaded into the workspace may be used to calculate forward and inverse data of frequency domain transmission or fluorescence emission at any wavelength. This facilitates easy modeling of realistic domains, experimenting with different wavelength combinations for spectrally constrained absorption reconstructions, and more advanced usage, such as calculating the propagation of entire fluorescence emission spectra through tissue or combining spectrally-constrained absorption tomography and fluorescence emission tomography. A handful of parsing programs allows users to learn only a small set of commands which can activate any of these modeling approaches based on user input. Adding chromophores or fluorophores to the extinction coefficient database is simple and requires no programming modifications. Finally, hard and soft spatial prior implementations for almost all reconstruction approaches, i.e. single wavelength FD transmission, multi-wavelength spectrally constrained, and fluorescence, were included in the package. It should be noted that the “single wavelength” operation is built into the software as a legacy capability, able to recognize and convert pre-Version_2 meshes into the new format.

Chapter Four: Contrast Agents and Tissue Phantoms

This chapter reviews the contrast agents used throughout this work and outlines recipes for creating the most commonly used tissue simulating phantoms. Much of the data presented in this thesis was acquired using tissue phantoms rather than living tissue. Though each phantom formulation is in some way deficient in its ability to mimic tissue, phantoms are commonly used to validate an imaging system, decipher imaging limits, and identify data calibration procedures.

4.1 Exogenous Contrast Agents

Imaging performance in the context of the systems and techniques developed in this work cannot be de-coupled completely from the physical properties of the contrast agent used. Five contrast agents were used and are briefly described below. For many of these drugs, the relevant photochemical properties, such as quantum yield, emission spectrum, and extinction coefficient spectrum were measured directly to provide a foundation for understanding phenomena observed in deep tissue imaging.

4.1.1 Lutetium Texaphyrin and Gadolinium Texaphyrin

Lutetium Texaphyrin (LuTex), Pharmcyclics Inc. (Santa Barbara CA), a lutetium based photosensitizer, and Gadolinium Texaphyrin (GdTex), an identically structured molecule centered around Gadolinium and developed as an MR visible radio-sensitizer,

present similar optical behavior in the near-infrared region. Both have a strong absorption peak (Figure 4.1) corresponding to a dip in the absorption of deoxyHb and have shown some selectivity to malignant cells⁶⁸⁻⁷¹, making them candidates for spectrally constrained absorption imaging. They are also weakly fluorescent, providing a platform for direct experimental comparison of absorption and fluorescence imaging. Furthermore, GdTex is an MR sensitive probe which provides a mechanism to compare imaging sensitivity of optical tomography to MRI with simultaneously acquired data.

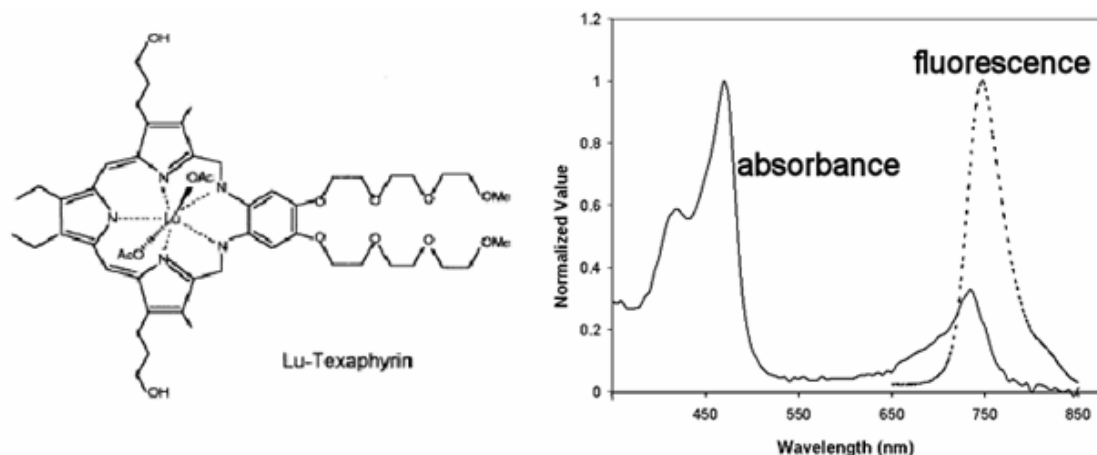


Figure 4.1. Chemical structure and normalized absorbance and fluorescence emission spectra of Lutetium Texaphyrin are shown.

4.1.2 Indocyanine Green

The most popular agent used for optical tomography of exogenous contrast is Indocyanine green (ICG), a relatively bright fluorophore used clinically for contrast-enhanced retinal and choroidal angiography^{19, 23, 72}. The photophysical properties of ICG under a variety of experimental and clinically relevant conditions have been studied extensively^{20, 23}. Upon injection, ICG binds completely to plasma proteins and therefore

is confined to the vasculature. ICG's strong optical absorption and high quantum yield make it an attractive drug for phantom studies and patient trials, however, it has no known tumor specificity beyond binding to albumin and therefore image contrast to characterize tumor regions obtains from blood pooling and hypervascularity only. Absorption and fluorescence spectra measured in our lab are included in Figure 4.2.

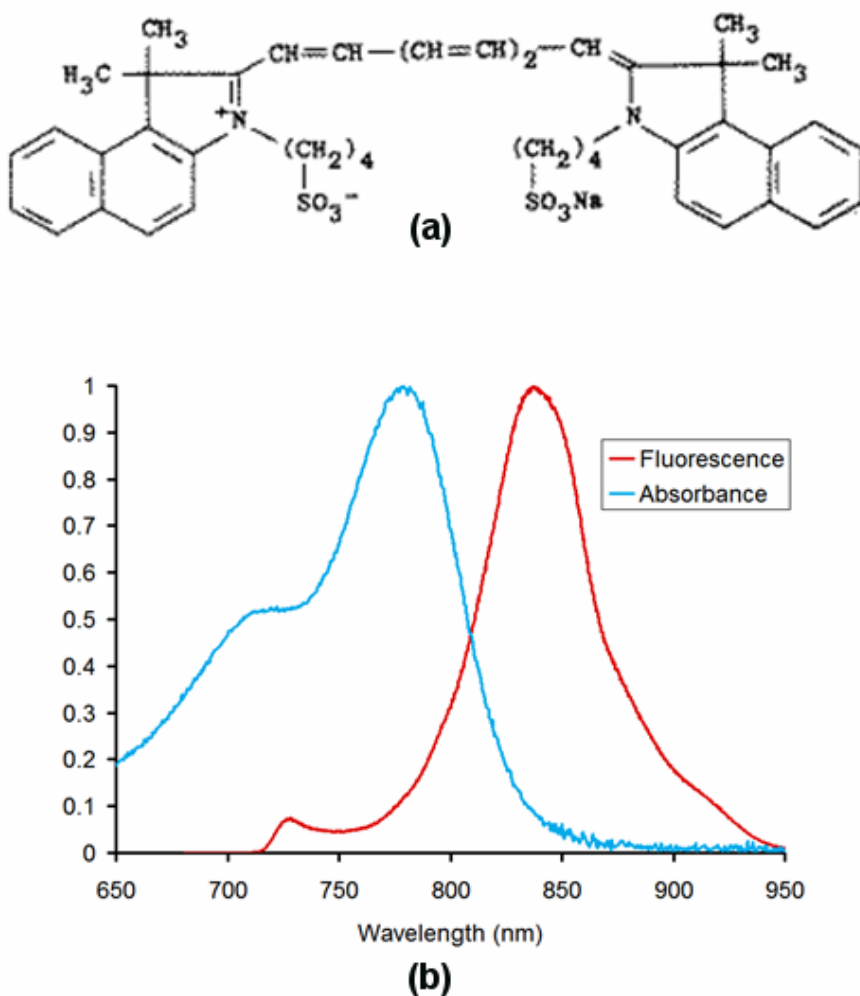


Figure 4.2. Chemical structure, (a), reproduced from Prahl ⁷³, and normalized absorbance and emission spectra of ICG (b). The fluorescence spectrum was measured in turbid medium (1% IL), and the secondary peak around 720-740 nm is contamination due to excitation cross-talk and auto-fluorescence.

4.1.3 IRDye 800CW EGF

Animal studies were completed with IRDye 800CW EGF Optical Probe (Li-Cor Biosciences Lincoln NE), an NIR fluorophore which targets epidermal growth factor receptor (EGFR). The EGFR is a tyrosine kinase receptor present on normal epithelial cells but commonly over-expressed in many types of cancer^{74, 75 76}. Increased EGFR activation is associated with suppression of programmed cell death and increased mitotic activity leading to proliferation, a result of a signaling pathway which begins with binding events between epidermal growth factor (EGF) and the EGFR on the cell membrane. Since the Li-Cor fluorophore IRDye 800CW is bound to EGF, images of fluorescence yield *in vivo* should correlate to the distribution of EGFR expression. Absorbance and emission spectra of the dye are shown in Figure 4.3.

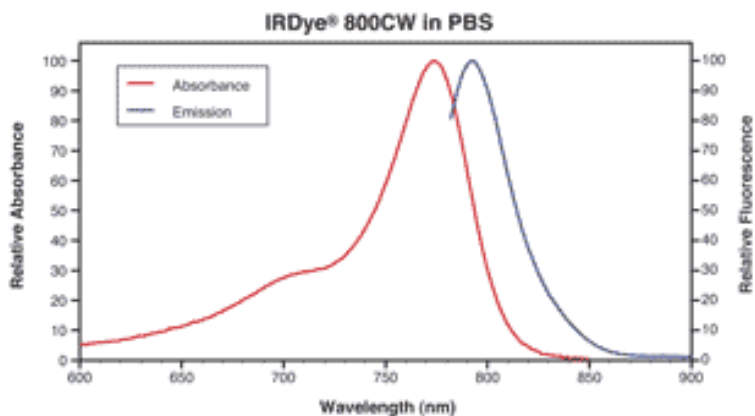


Figure 4.3. Normalized absorbance and emission spectra of IRDye 800CW EGF Optical Probe, reproduced from the Li-Cor website⁷⁷.

4.1.4 Protoporphyrin IX

An endogenous fluorophore and photosensitizer, Protoporphyrin IX (PPIX) has been studied for almost two decades for its therapeutic properties in photodynamic

therapy (PDT)^{78, 79}. Absorbance and emission spectra of PPIX are shown in Figure 4.4. PPIX is an intermediary product in the heme biosynthesis pathway, a process which can be overloaded upon the administration of exogenous 5 δ -Amino-Levulinic Acid (ALA) (Fisher Scientific Inc.), resulting in the buildup of PPIX in metabolically overactive cells, such as found in malignant pathologies. PDT with ALA-induced PPIX has been proven effective in treating cancerous and non-cancerous skin lesions⁸⁰⁻⁸², Barrett's esophagus and early stage esophageal carcinomas^{83, 84}, and has been investigated for treating tumors in other organs such as prostate⁸⁵ and ovary⁸⁶. ALA-induced PPIX fluorescence is highly specific in brain tumors, producing tumor-to-healthy tissue contrasts of up to 10:1. Stummer et al. showed that ALA-PPIX fluorescence guided resection of glioblastomas in humans improved surgical outcomes²⁴ to such an extent that the technique has become the standard of care in Germany. ALA-PPIX was used in this work to image gliomas in murine models.

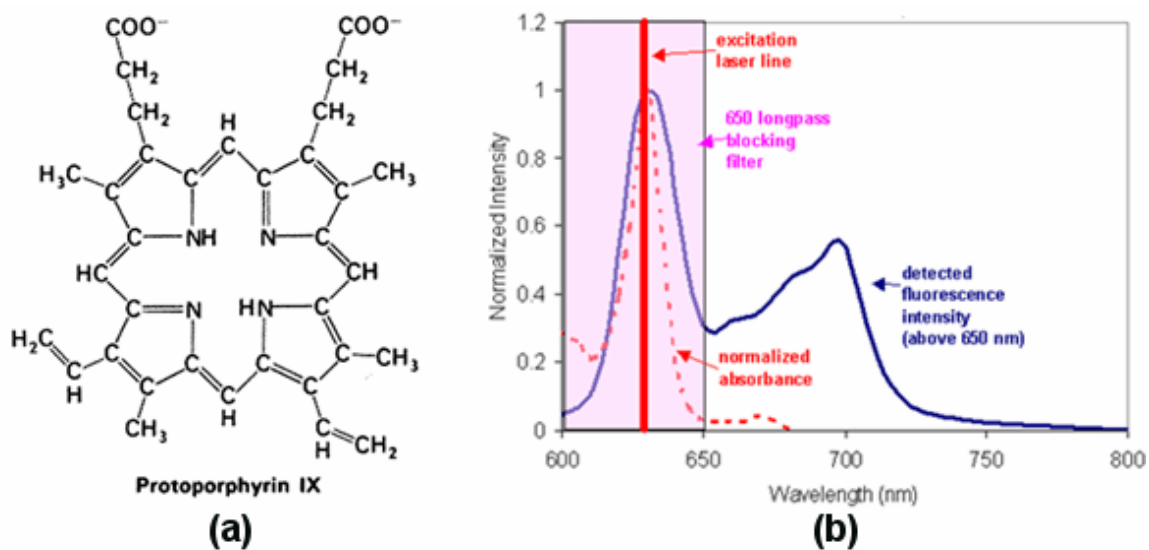


Figure 4.4. The chemical structure of PPIX, an intermediary in the Heme biosynthesis pathway, reproduced from Prahl⁸⁷. In (b), the normalized absorbance and fluorescence emission spectra are shown, along with a schematic of the excitation laser light wavelength and the filtering needed for effective emission detection.

4.2 Photophysical features of the probes

Values of fluorescence quantum yield may play a role in validating fluorescence tomography imaging. An approximate value for drug concentration can be derived from images of fluorescence yield if the quantum yield is known, providing a means of comparing the known drug concentration and therefore serving as a loose validation of the recovered fluorescence yield values. However, measurements of quantum yield are inherently difficult, even in controlled experiments, and the typically high sensitivity of quantum yield to solvent environment implies that only approximate values should be expected and will likely serve as an upper bound for expected yields in phantoms and animals^{23, 88, 89}. In addition, it is well known that the microenvironment around many fluorophores will affect their binding status and hence the fluorescence yield, by

changing the photophysical decay constants within the molecule. In this work, the comparative method introduced by Williams *et. al.*⁹⁰ was used to measure a quantum yield of 0.0046 for protoporphyrin IX in DMSO using a Kiton Red standard. This solvent provides the most monomeric form of PPIX, and therefore provides an upper bound on the fluorescent quantum yield which could be expected *in vivo*. The quantum yield of Lutex in de-ionized (DI) water was determined in a similar manner, resulting in a value of 0.0019. Since Lutex is highly soluble in an aqueous environment, this again provides a reasonable estimation of the maximum *in vivo* value. Quantum yield values for ICG in a variety of solvents are documented in the literature⁹¹, and can range from 0.0028 to 0.12.

Spectrally constrained absorption imaging of chromophore concentrations, as outlined in section 3.2, requires knowledge of the primary absorbers' extinction coefficient spectra. Of the agents presented in this work, LuTex, GdTex, and ICG are considered for this type of imaging approach given their strong absorption profiles in the NIR. The extinction spectra for these drugs were measured experimentally and are presented in Figure 4.5. along with Oxy/deoxyhemoglobin and water spectra obtained from existing published values⁸⁷. It is clear that these exogenous chromophores may impact the overall absorption spectra, even at a concentration 1/100th that of hemoglobin.

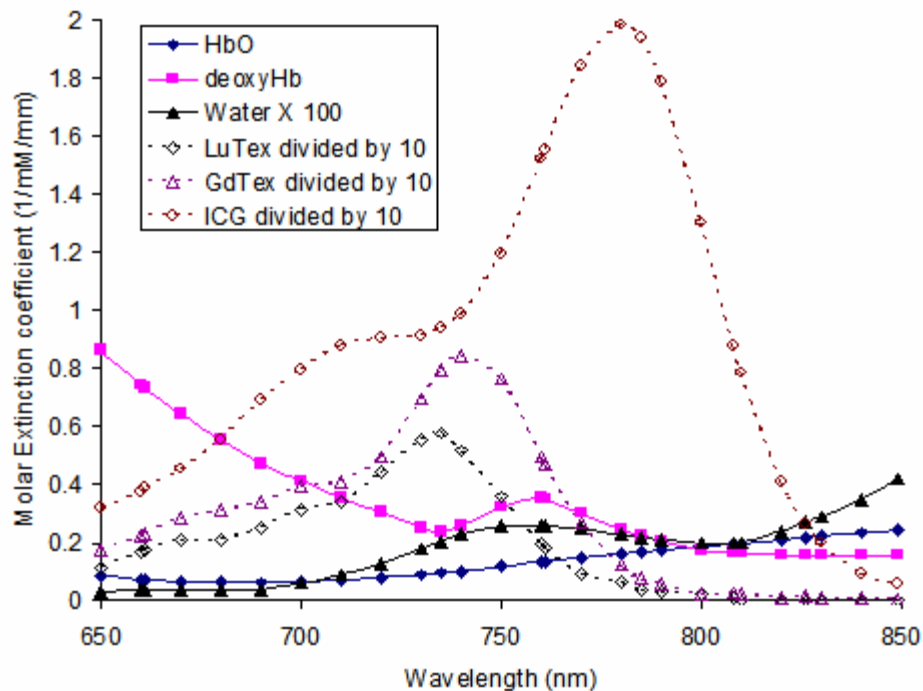


Figure 4.5. Extinction spectra measured for LuTex, GdTex, and ICG are shown. Values for endogenous chromophores are also shown, as compiled by Prahl⁸⁷, to illustrate the potential impact drugs such as ICG can have on the overall absorption profile of tissue.

4.3 Tissue Simulating Phantoms

A number of techniques to construct tissue phantoms which accurately simulate the optical behavior of near-infrared light *in vivo* have been developed over the past decade^{52, 65, 92, 93}. The additional consideration of exogenous fluorophores which photodegrade rapidly limits the range of phantoms available for fluorescence imaging, especially for cases of imperfect drug uptake. In these situations, the available options are restricted to single use phantoms which may last only a matter of hours.

Three types of phantoms are used in this thesis, all shown in Figure 4.6. Long lasting solid phantoms composed of epoxy resin, TiO₂ powder (for scattering), and India

ink are a mainstay for calibrating our legacy DOT systems. Though effective for single wavelength calibration, they do not match the absorption spectrum of blood, precluding their use as multi-spectral imaging test beds for spectrally constrained image reconstruction. Furthermore, they offer no means to introduce anything less than infinite fluorophore contrast. Liquid phantoms, pictured in Figure 4.6 (a), are composed of water (or phosphate buffered saline, PBS), intralipid, ink (or blood), and the exogenous drug and allow the use of background fluorescence but require liquid containers which introduce artificial boundaries, index of refraction mismatches, and light piping through container walls. Typically, liquid phantoms are composed of water or PBS with 1% intralipid for a reduced scattering coefficient of approximately 1mm^{-1} . India ink or blood is mixed in to provide the appropriate amount of optical absorption. Homogeneous test phantoms should be used to calibrate the appropriate ink concentration since each batch can have dramatically different absorption properties.

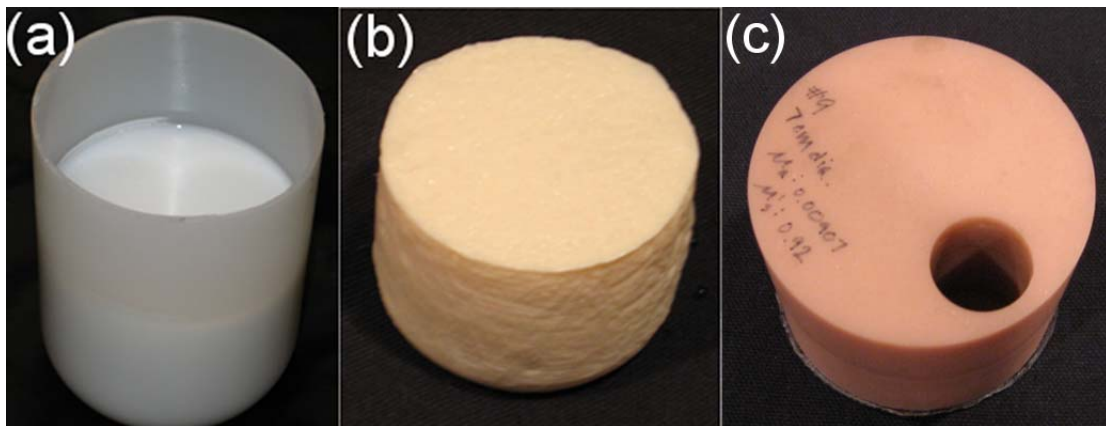


Figure 4.6. Examples of liquid (a), gelatin (b), and solid (c) tissue simulating phantoms.

Gelatin phantoms extracted from porcine skin (Sigma Aldrich), TiO_2 , blood and the exogenous contrast agent can be made to closely mimic heterogeneous tissue without artificial boundaries. Experiments confirm that Lutex and ICG mixed into gelatin prior to setting, but after being cooled to below 45 degrees C, will retain their fluorescent properties. It is expected that GdTex is also readily mixed into gelatin, though it is unlikely PPIX will behave similarly due to its strong tendency to aggregate in aqueous mixtures. Typical mixing procedure for a 300 ml gelatin phantom is as follows:

1. Prepare mold with Vaseline to ensure phantom can slide out easily.
2. Before mixing, weigh 0.8g of TiO_2 . "Sift" into a fine powder, usually by chopping larger chunks with a razor blade.
3. Using stir plate, slowly mix 30g gelatin into 300 ml of solvent. If using blood for absorption, be sure to use PBS or DPBS rather than water.
4. Once the gelatin looks fully dissolved, remove stir bar and heat to $< 40\text{C}$ in microwave (about 40 seconds).
5. Place back on the stir plate and slowly mix in TiO_2 .
6. Mix for about 30 – 45 minutes. TiO_2 should look almost completely dissolved.
7. When suspension thickens, mix in ink/blood and exogenous agents. This should be done as late as possible before the gelatin sets so it does not settle while cooling.
8. Pour into mold and refrigerate. Phantom should be ready in an hour.

Heterogeneous phantoms can be produced by making molds with complicated shapes to simulate different tissue types. After pouring the mixture into the outer mold, a second mold, lubricated with Vaseline, is inserted into the mixture displacing a portion of the phantom material and the entire phantom is refrigerated. Once the gelatin sets, the inner mold is removed, creating a shaped cavity in the gelatin. At this point, another mixture with different optical properties is poured into the cavity to simulate a second tissue type. This may be repeated to increase phantom complexity. Similar results are achieved by skipping the second mold altogether and simply scooping out material from cooled, set phantom material and then pouring the next unset gelatin mixture into the cavity. Again, this can be repeated several times. The most complex phantoms used in

this work contain three tissue layers: two gelatin and one liquid layer with higher fluorophore content, simulating a tumor, as shown in Figure 4.7.

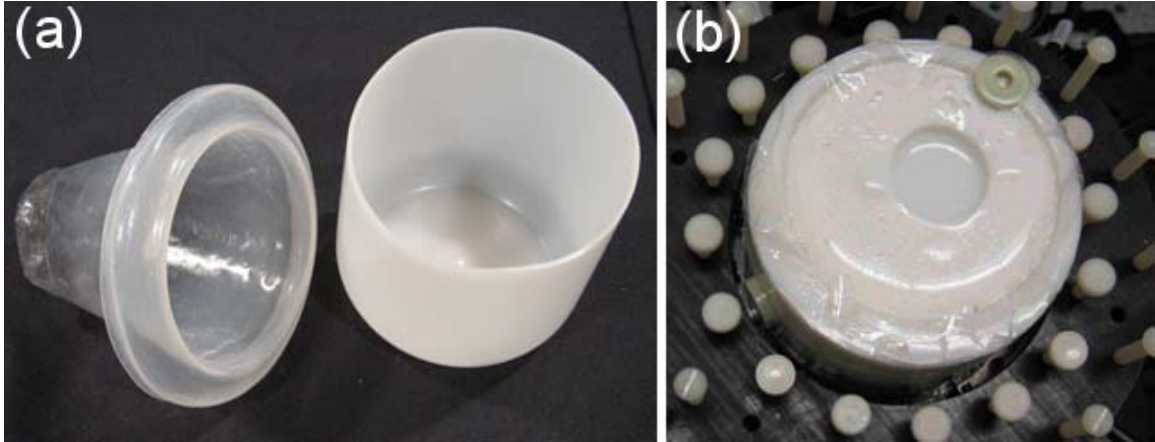


Figure 4.7. Multi-layer gelatin phantoms can be produced using a series of irregularly shaped molds (a). A three layer phantom is shown in (b).

Chapter Five: System Validation and Performance

This chapter reviews system validation experiments, presents data calibration procedures, and includes basic performance measures of the MR-coupled spectral tomography system introduced in Chapter 2, with a focus on fluorescence imaging. The reader should note that data calibration techniques evolved throughout the course of this work, and so for clarity, only the most effectively used approaches are described in this chapter. Descriptions of more specialized calibration procedures including relevant data processing tools are described in later chapters.

5.1 System validation

5.1.1 *Exposure time linearity*

A linear relationship between measured intensity and camera exposure time is critical for acquiring reliable measurements using the CCD/spectrometer systems. A simple experiment verified the performance of the shutter/exposure system for each camera. A series of spectra over a range of input exposure times were recorded with all spectrometers using the 690 nm CW laser on low power as a light source. The transmitted peak was integrated and plotted as function of exposure time. Results of this study for detectors 1-8 are presented in Figure 5.1 and demonstrate exceptionally reliable linear behavior as a function of exposure time. Similar results were observed for the remaining spectrometers (9-16), though are not shown here.

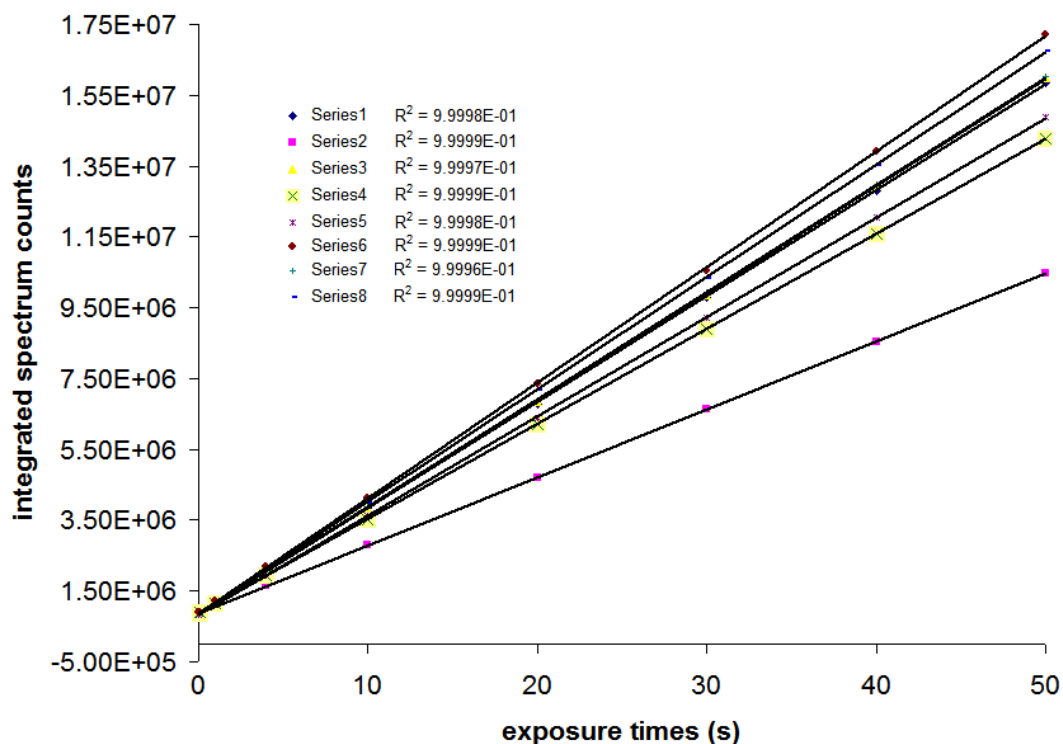


Figure 5.1. The linearity of measured intensity with exposure time was verified for all spectrometer systems. Only data for detectors 1-8 are shown here.

5.1.2 Wavelength accuracy

The Insight spectrometers are delivered pre-calibrated by the manufacturer and should be robust and accurate in terms of wavelength response. Errors in wavelength accuracy may arise from grating/camera/mirror misalignment in the spectrometer itself, incorrect software calibration, and dispersion-derived chromatic aberrations introduced by any of the optical components, such as the custom designed entrance optics added to

this system. These errors were measured for the spectral tomography system using neon emission lines.

The emission spectrum of a neon lamp is extensively catalogued and is a standard for wavelength calibration. In this experiment, the light from a neon lamp was coupled into an output fiber, the free end of which was fixed in a plastic tube facing the detection fiber of a given spectrometer. The measured spectrum was recorded using WinSpec software (Acton Research) which displays spectra that are wavelength calibrated according to the manufacturer. An example of a measured spectrum for one of the tomographic system's spectrometers (#14) is shown in Figure 5.2. The 1200 lp/mm ruled grating was used in this study for higher spectral resolution, however, entrance slits were left fully open to mimic the setup for tomographic acquisition, resulting in several nanometers of peak broadening, evident in Figure 5.2. Using this spectrum, the wavelengths of three known emission peaks in the NIR, 703.24127 nm, 724.51665 nm, and 743.88981 nm, were identified using the WinSpec manual cursor tools and recorded. This was repeated for each spectrometer, with the exception of spectrometer #2, which had technical difficulties at the time of testing.

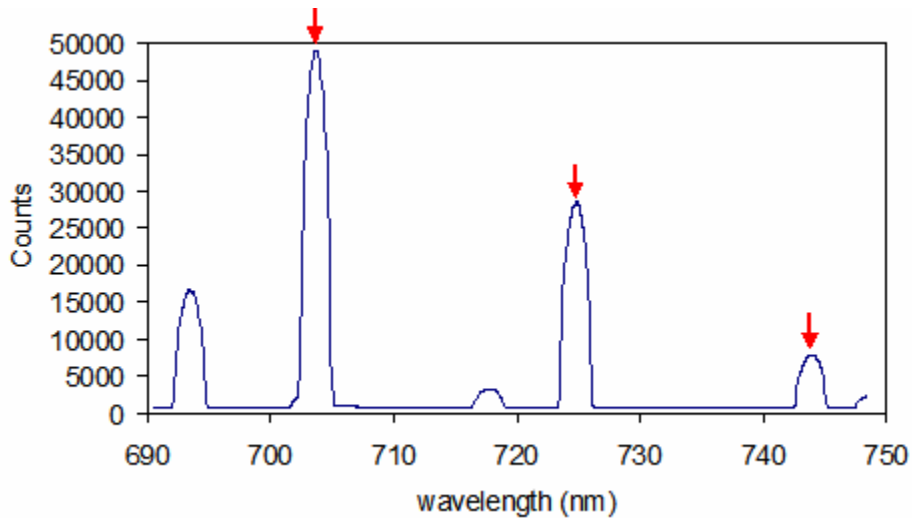


Figure 5.2. The emission spectrum of a neon lamp as measured by spectrometer #14 is shown. The red arrows indicate which emission peaks were used to calibrate the wavelength response of the cameras.

The tabulated results are presented in Table 5.1 and show only small deviations in wavelength from the actual emission line values. The maximum error between the literature values and those measured with the spectrometers for the 703 nm and 724 nm peaks is approximately 0.8 nm with an average error of around 0.30 nm. The maximum and average errors at the longer wavelength, 743 nm, is a bit higher at 1.1nm and 0.5nm, respectively, though this could be due to a magnified uncertainty in identifying the peak given the lower intensity of that emission line. These results indicate that the wavelength calibration of the spectrometers is more than adequate and the custom lens-based entrance optics did not introduce significant chromatic aberrations, especially when considered in the context of the data processing protocol. Specifically, the spectral fitting procedure based on pre-recorded basis spectra should be self-calibrating in terms of absolute wavelength accuracy and the subsequent integration of broad-peaked

fluorescence emission spectra also de-emphasize the effects of improper wavelength calibration. In this context, the numbers measured in this study decisively indicate that wavelength accuracy is not major source of error for fluorescence imaging.

Table 5.1. Neon lamp emission peak wavelengths in the NIR as measured with each spectrometer.

Actual emission line (nm)	703.24127		724.51665		743.88981	
	Measured peak (nm)	Error (absolute)	Measured peak (nm)	Error (absolute)	Measured peak (nm)	Error (absolute)
Spec. 1	703.26	0.01873	724.29	0.22665	743.43	0.45981
Spec. 2	NA	NA	NA	NA	NA	NA
Spec. 3	703.56	0.31873	724.59	0.07335	743.72	0.16981
Spec. 4	703.65	0.40873	724.76	0.24335	743.85	0.03981
Spec. 5	702.99	0.25127	724.03	0.48665	743.14	0.74981
Spec. 6	703.3	0.05873	724.42	0.09665	743.51	0.37981
Spec. 7	703.34	0.09873	724.55	0.03335	743.64	0.24981
Spec. 8	703.21	0.03127	724.29	0.22665	743.43	0.45981
Spec. 9	702.95	0.29127	724.16	0.35665	743.39	0.49981
Spec. 10	702.93	0.31127	723.9	0.61665	743.05	0.83981
Spec. 11	702.46	0.78127	723.69	0.82665	742.8	1.08981
Spec. 12	702.9	0.34127	723.99	0.52665	743.18	0.70981
Spec. 13	702.73	0.51127	723.9	0.61665	743.05	0.83981
Spec. 14	703.61	0.36873	724.76	0.24335	743.85	0.03981
Spec. 15	703.3	0.05873	724.33	0.18665	743.43	0.45981
Spec. 16	703.3	0.05873	724.42	0.09665	743.39	0.49981

5.1.3 Filter OD calculation

Each 6 position filter wheel contains two neutral density (ND) filter with OD's of 1 and 2 to extend the dynamic range of transmission mode measurements. In this configuration, OD filters reduce the intensity of light incident upon selected detectors as compared to the actual intensity collected at the tissue surface. If the OD is known, the collected intensity is easily extracted from the measurement. A practical configuration for imaging breast sized volumes in a circular geometry involves filtering the four

detector positions nearest the source with 2 OD filters while using 1 OD filters for the four next nearest detectors. In small animal imaging mode, it is common to use the 2 OD filters for all detector positions to acquire transmission measurements.

The manufacturer reported optical density of the filters is not a reliable measure of the true filtering capacity in a given optical system. All filters have wavelength-dependent responses and system alignment and manufacturing uncertainties can influence the achieved filtering efficiency. The non-flat spectral features are particularly critical for broadband transmission tomography which depends on accurate spectral measurement of light that has propagated through the tissue volume. However, this can be taken into account by measuring the OD spectra of each filter in the optical system.

To measure filter OD spectra, a cylindrical Teflon phantom was secured in the circular patient array, with all detector fibers contacting the phantom. A standard 400 μm fiber connected the output of a tungsten light source to an SMA connector attached to the center of the top of the phantom, as shown in Figure 5.3. The broadband source provided measurable intensities over the entire wavelength range of interest.

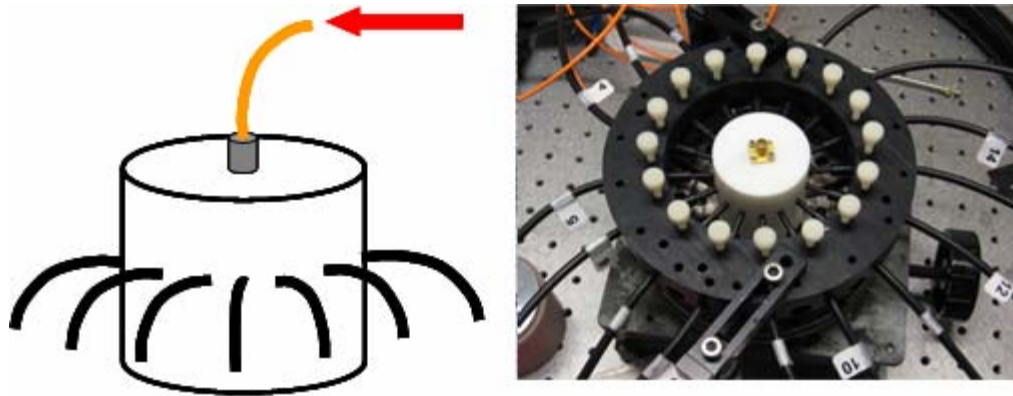


Figure 5.3. Diagram of the Teflon phantom configuration for measuring optical densities of ND filters used in the system (left) and corresponding photograph (right). A fiber transmitting light from a tungsten lamp is centered on the top of the cylinder which is encircled by detection fibers.

Each spectrometer system recorded spectra of unfiltered light as well as spectra of light that had passed through the 1 OD and 2 OD filters. Each measurement was repeated 10 times and averaged over the repetitions. The resulting relative intensities were used to calculate the OD at every pixel across the spectrum using,

$$OD(\lambda_i) = -\log\left(\frac{I_{filter}(\lambda_i)}{I_{no_filter}(\lambda_i)}\right) \quad 5.1$$

where I is a measured spectrum. This was repeated for different gratings centered at different wavelengths for each spectrometer and filter. Examples of calculated OD values are shown in Figure 5.4, demonstrating the dramatic dependence of optical density on wavelength. Values for a given grating and wavelength setting were compiled in a 1340 x 16 (number of pixels by number of spectrometers) matrix and stored in a text file.

Data calibration routines call these files to extract the actual intensity of light collected by the detection fiber:

$$I_0(\lambda) = \frac{I_{filter}(\lambda)}{10^{-OD(\lambda)}} \quad 5.2$$

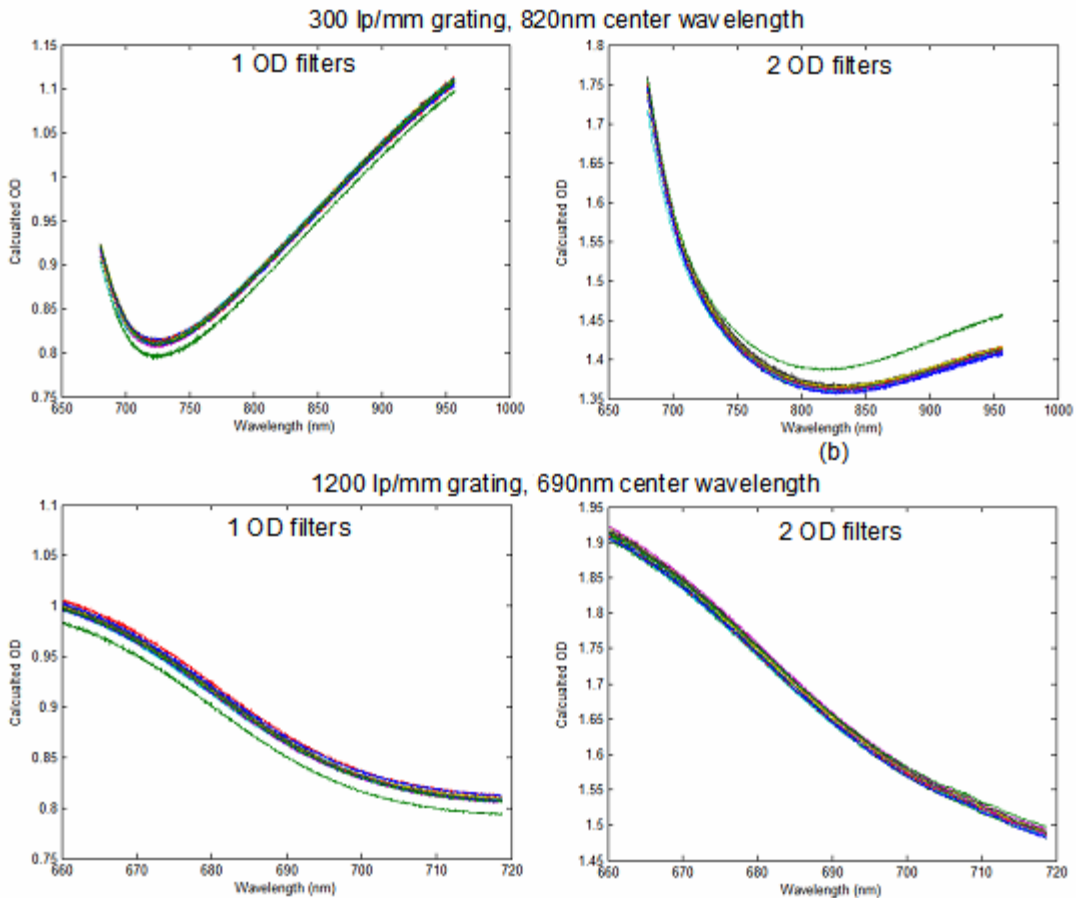


Figure 5.4. Wavelength dependent OD values calculated for 1 OD and 2 OD filters used in the spectral tomography system, each curve representing one spectrometer. Calculations were repeated for both gratings at a variety of center wavelength settings.

5.1.4 Excitation source rejection

A similar method was used to calculate the rejection efficiency of the laser peak using the fluorescence filters. Since this information is not used in the data processing procedures, cataloging this information is not as crucial as it was for the ND filters; however, it is important to understand how well the interference filters perform. In this study, only intensities in the filtered region were measured. The contaminating signal above the filter cut-on is discussed in the next section.

Light from the 690 nm CW laser diode was reflected off the inside of a Styrofoam cup and collected by a single detection fiber (spectrometer #15) located inside the cup. Filtered (720 nm long-pass) and unfiltered spectra were recorded and the peak intensity at the laser wavelength was used to calculate OD. The measured dynamic range was quite high and had to be controlled by adjusting the laser current and incorporating ND filters on the source side for the unfiltered measurement. These factors were incorporated into the calculation, which resulted in an OD of approximately 7, representing excellent excitation rejection. A similar measurement of the 650 nm long pass filters using a 635nm laser diode indicated an average OD rejection efficiency of 5.

5.1.5 Nature of the “bleed-through” signal

Figure 5.5 shows spectra measured at various locations around a cylindrical phantom composed of gelatin, water, and TiO₂ and illuminated by a 690 nm CW laser. Before entering a spectrograph, the light is filtered by the 720 nm long-pass interference filters. As expected, the laser peak at 690 nm is almost completely eliminated by the

filters, however, the residual light above the filter cut-on is confounding, especially given the absence of fluorophore in the phantom. Potential sources of this contamination include: 1) A tail from the laser gain curve, 2) Fluorescence from the phantom material, 3) Fluorescence from optical components such as emission filters, epoxy in the optical fibers, etc., or 4) Stray light inside the spectrograph. The validity of each possibility is discussed in the context of experimental evidence.

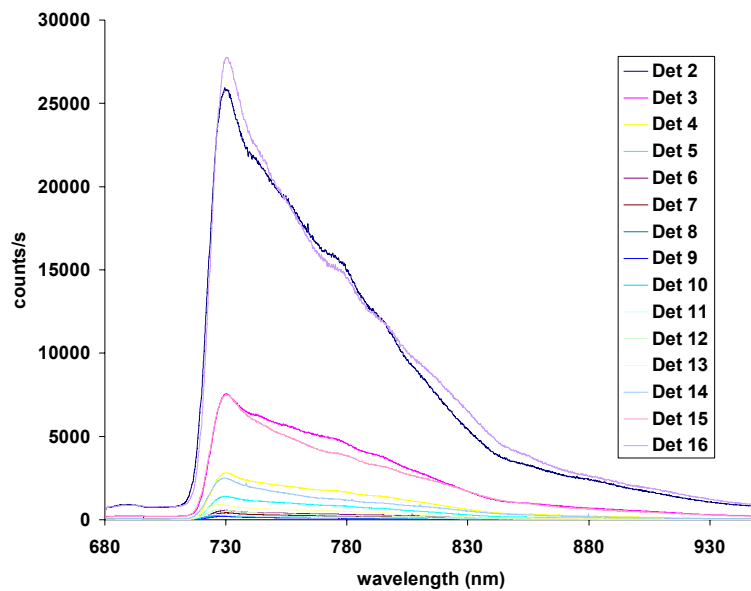


Figure 5.5. The measured spectra through a homogenous gelatin phantom show a residual signal above the 720 nm cutoff. This phantom was illuminated with a 690 nm laser diode.

Fluorescence downstream of the cutoff filter can be ruled out immediately by examining Figure 5.5. Clearly, the measured signal is filtered by the 720 nm long pass filter which resides in the entrance optical unit before entering the spectrograph. Fluorescence or stray light inside the spectrograph would not exhibit such wavelength

selectivity. Thus the fourth hypothesis involving stray light inside the spectrometer is also eliminated as a possible source of the contamination signal.

Consideration of hypothesis #1 is straightforward: If the contamination signal is simply a tail of the laser gain, it should be eliminated readily by proper filtering on the source side, before the light enters the tissue/phantom. Using collimating and focusing optics, a 680-700 nm band-pass interference filter (Omega, Brattleboro, VT) was incorporated into the optical light path between the source and phantom, as depicted in Figure 5.6.

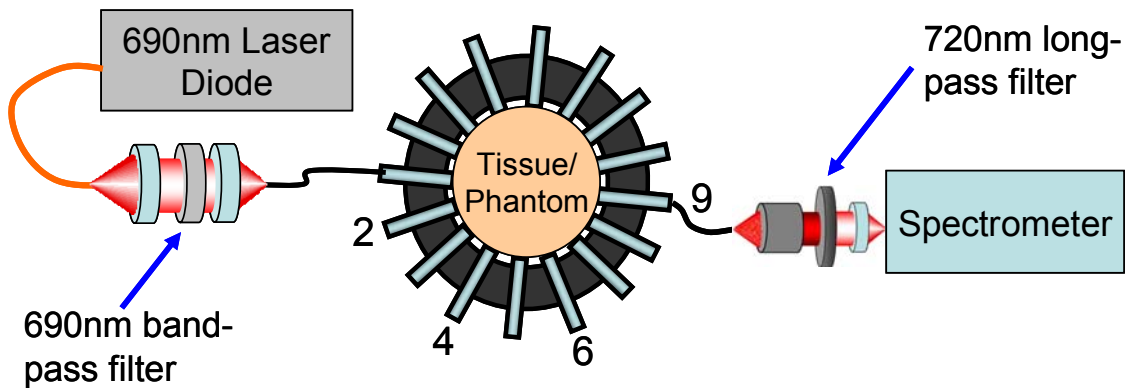


Figure 5.6. A simplified diagram of the source-to-detector light path shows the location of band-pass and long-pass filters in the optical system. One of 16 spectrometers is shown and detector positions are labeled with numbers.

Spectra were measured through a 60 mm cylindrical homogeneous liquid phantom containing 1% intralipid at a variety of detector positions around the phantom. These spectra are presented in Figure 5.7 along with spectra measured under identical conditions with an unfiltered laser source. The ratio between the filtered and unfiltered spectra, calculated pixel-by-pixel, are presented in Figure 5.8.

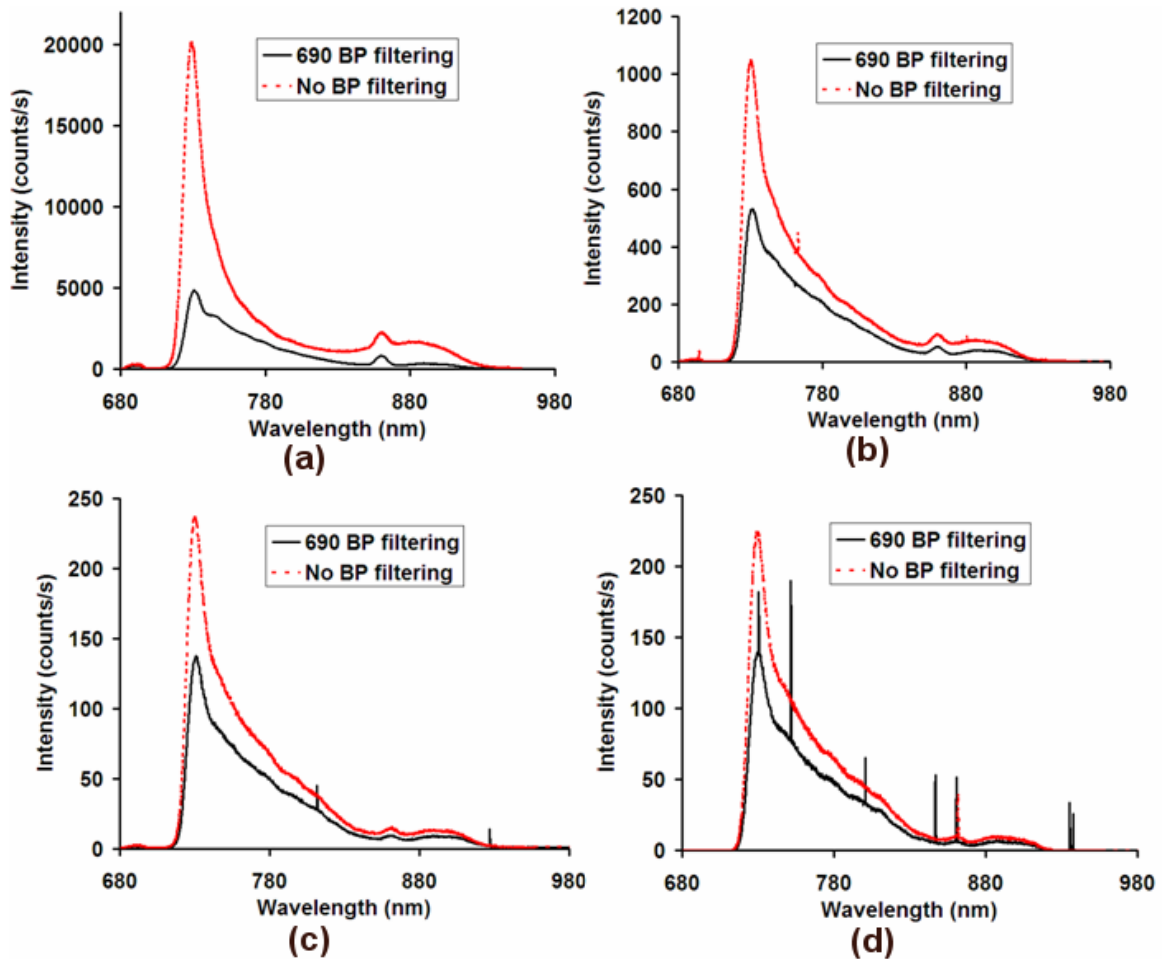


Figure 5.7. Contamination signal measured around a 60 mm diameter cylindrical phantom containing 1% intralipid in water. Data are shown for detectors positioned 1.1 mm (a), 3.3 mm (b), 4.9 mm (c), and 5.9 mm (d) from the source.

As is evident in both figures, the band-pass filter reduces the intensity of the contamination signal; however, the signal strength drops to no less than 20% of the unfiltered signal, much lower than the expected 4-5 OD. The lowest signal attenuation occurred at the detector nearest the source. Further from the source, the filtered to unfiltered ratio approaches 75%, close to the manufacturer reported value of 85% transmission in the pass-through band. It is clear that most of the loss in intensity at the

far-from-source detectors is due simply to the decrease in transmittance of the laser at the pass-through band. Thus, the signal is not being attenuated by the band-pass filter and is likely generated downstream the filter. Signals measured at detectors near the source appear to have some component of laser gain. The reduction of this signal at increasing source-detector separations may indicate preferential absorption of signal at shorter wavelengths as the light propagates through the tissue. These results indicate that a majority of the contamination signal arises from fluorescence generated between the band-pass filter components on the source side and long-pass filter on the detector side.

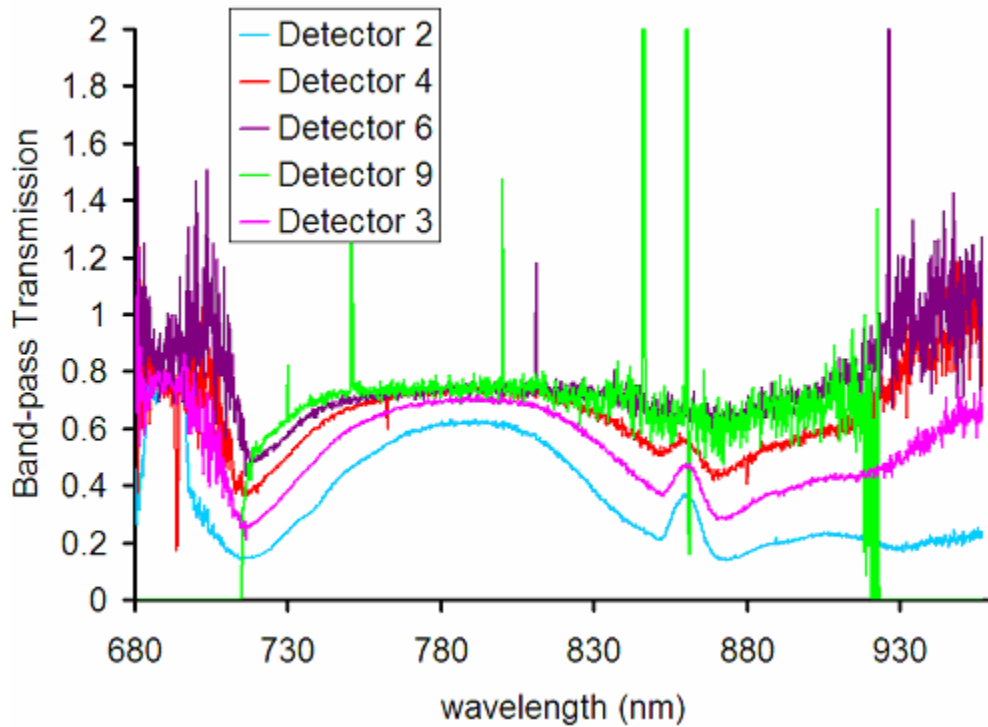


Figure 5.8. Ratios between the filtered and unfiltered spectra presented in Figure 5.7, calculated pixel-by-pixel. Spectra were measured at detectors located around a cylindrical phantom containing intralipid, as depicted in Figure 5.6.

To verify that this observation is not simply due to poor filtering on the source side, a Tungsten white light source was used to measure the filter rejection. For consistency, this was measured through a liquid phantom composed of 1% Intralipid and water. The measured spectrum, shown in Figure 5.9, indicates that the filter provides relative rejection up to the measurable dynamic range of the camera, or 2 orders of magnitude. Given manufacturer provided specifications, it is expected that the actual rejection should be greater than 5 orders; however, it is sufficient to note that even the 2 orders of magnitude recorded here is much higher than what was observed in Figure 5.7.

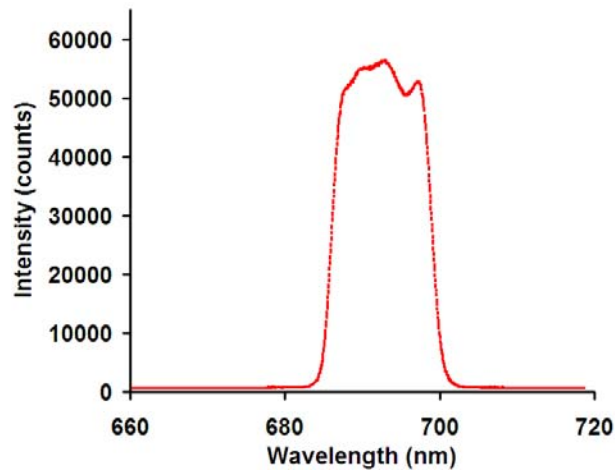


Figure 5.9. Light from a broadband Tungsten source filtered with the 690 nm band-pass filter.

A final filtering experiment provides further evidence that the signal does not originate from a tail in the laser gain curve. In this experiment, the 690 nm band-pass was removed and the 720 nm long-pass filter exchanged between the collimation/focusing filtering units depicted in Figure 5.6. Thus, a spectrum measured with the filter on the source side may be compared to one measured with the filter in front of the detector. Figure 5.10 shows both spectra on the same graph. These spectra were

measured at detector position 4 through a solid epoxy phantom containing ink and TiO₂. If the laser tail is responsible for the contamination signal, it should be present in both signals. Alternatively, if the signal is auto-fluorescence and the 720 nm long-pass filter is fixed in the source-side filter holder, the filter denies the downstream optical system excitation energy for fluorescence emission. This appears to be the case, as a significant drop in signal strength is observed when the filter is fixed in the source path.

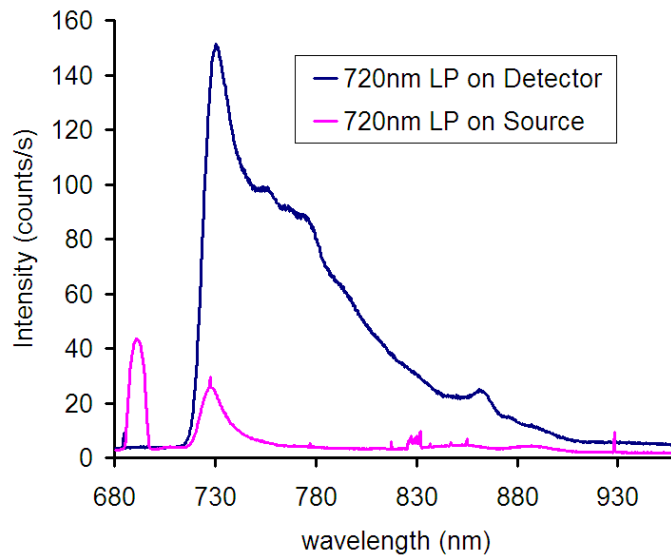


Figure 5.10. Spectra measured at detector 4 with the long-pass filter on the source side and detector side of the optical path.

Now that the signal has been identified as fluorescence, the source of this emission is considered. Specifically, it is important to determine whether the signal originates in the phantom or other optical components in the light path. Removing the phantom and measuring the light transmitted through air helps resolve this issue. The measured spectrum is shown in Figure 5.11 and is markedly different from those

measured through tissue phantoms, as well as in live animals, as will be discussed later in this work. Importantly, the laser peak is clearly seen in the filtered region and the relative intensity between laser peak and contamination signal is smaller than what is seen in phantoms. This indicates that the contamination signal is likely smaller through free space. The signal above 720 nm may originate from a variety of sources, including laser gain, fluorescence emission of optical components and even Raman scatter from the filters or other optical components. However, that the signal in general is much lower relative to the laser peak than that detected through the phantoms is compelling evidence that the phantom auto-fluorescence is responsible for most of the signal contamination (hypothesis #2).

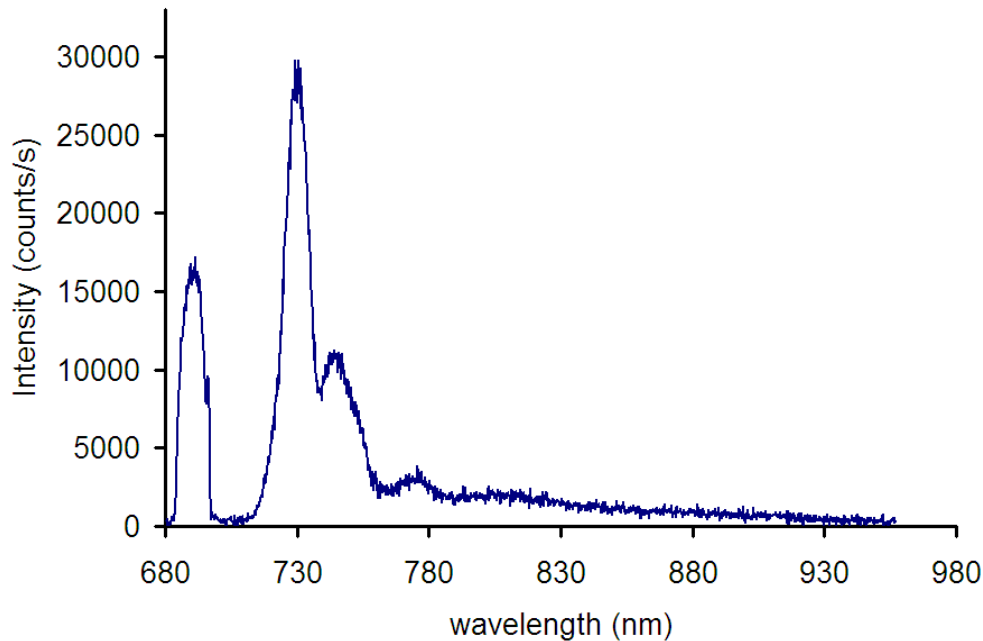


Figure 5.11. Spectrum measured through air between source and detector fibers.

The experimental evidence cited here indicates that the contamination signal is due primarily to phantom/tissue auto-fluorescence. This is an important result which

implies that better filtering cannot eliminate or dramatically reduce this signal, making alternative fluorescence de-coupling techniques critical for low-intensity emission measurements. Spectrally resolved measurements facilitate spectral fitting techniques to extract a fluorescence peak from the mixed fluorescence and auto-fluorescence signal. One approach developed for this work is described in the next section.

5.2 Optical Data Processing

The following section outlines the data processing procedures used for the optical data collected on the spectroscopy system (Sections 5.2.1 through 5.2.3) as well as additional calibration procedures for fluorescence emission measurements (Section 5.2.4). A second approach recently developed and used for some phantom and animal studies is included in section 5.2.5. Important data calibration programs for both approaches are catalogued in Appendix C.

5.2.1 Baseline/dark current correction

Each CCD displays a baseline offset for zero second acquisitions which must be subtracted from the raw spectra. Multiple repetitions of the baseline offset spectra were measured directly for each spectrometer. The median of the repetitions yields the baseline offset spectra to be subtracted, pixel-by-pixel (assuming vertical binning of the CCD chip), from each acquired spectrum. This is done for each spectrometer.

A similar method was used to correct for the dark current of the CCDs. Dark room acquisitions were recorded for a range of exposure times. Measured counts are proportional to exposure time. The counts per exposure time slope was determined per

binned pixel for each spectrometer and is used to subtract dark current from recorded spectra. After baseline and dark current correction, the spectra are converted to counts per second.

5.2.2 Detector calibration

A first order correction is applied to account for heterogeneity in throughput and wavelength dependence for all optical components between the tissue and CCD detector (ie. detection fibers, input optics, spectrometer optics, and CCD response). To collect the calibration values, detectors were arranged to circumscribe a 6 cm diameter cylindrical Teflon phantom, as depicted in Figure 5.3. An SMA connector was attached to one end of the homogeneous phantom and light from a high power tungsten white light source was focused into a fiber connected to the centrally located SMA connector. Spectra were recorded with all spectrometers (usually ten repetitions) and inter-detector calibration factors were calculated for every vertical pixel bin (total of 1340) for each spectrometer. This was done for each grating and grating position to be used in image acquisition. Calibration factors are stored in text files and used to scale detected signal in a wavelength dependent manner. An example of the normalized wavelength-dependent calibration factors is presented in Figure 5.12, which reveals an odd discrepancy between spectrometer systems in terms of spectral response. Incidentally, this pattern was repeatable and not influence by rotating the phantom in the fiber array, ruling out variations in the Teflon material itself and pointing towards actual variability in the spectral responses of the systems. Regardless of the source, the calibration procedure accounts for these systematic variations and provides a first order correction of overall

throughput variability between detector channels. A similar approach is used to correct for OD filtering as described in section 5.1.3.

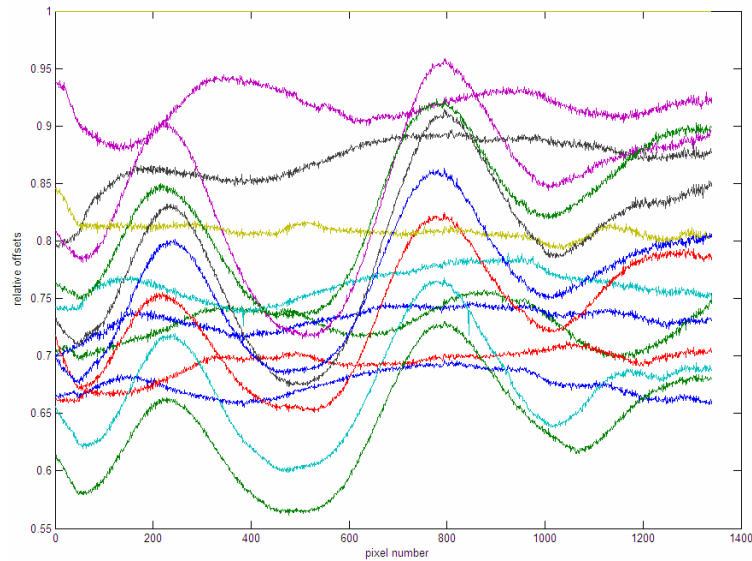


Figure 5.12. Inter-detector calibration factors as a function of pixel number. Light from a tungsten lamp propagated through a homogenous Teflon phantom and was measured by all 16 spectrometers (using the 300 l/mm grating centered at 820 nm) simultaneously. For each detector, the intensity at each pixel was normalized to the maximum intensity recorded by any detector at that pixel.

5.2.3 Source calibration

A first order inter-fiber source strength calibration was recorded by positioning a detector at the radial center of the Teflon cylinder, as illustrated in Figure 5.13. The detected signal from all 16 source fiber positions was then used to determine source scaling factors for future acquisition.

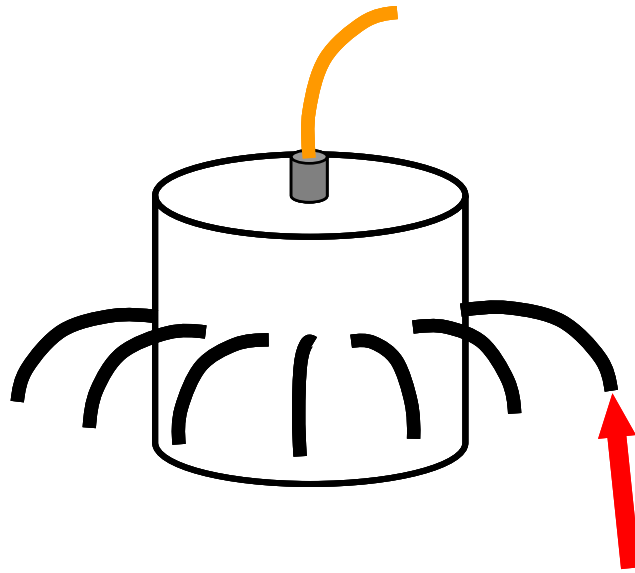


Figure 5.13. A first order source calibration was completed by measuring the intensity at a centrally located detector (orange) while illuminating the encircling fibers sequentially.

5.2.4 Fluorescence emission spectral fitting and data-model calibration

Fluorescence emission light is initially decoupled from the often much more intense excitation signal using long pass interference filters (optical densities between 5 and 7 depending on the filter set) and the wavelength selectivity of the spectrograph grating. Even with these components in place, light reaching the CCD retains residual signal not associated with fluorescence emission from the fluorophore target, which can be a significant component of the total signal, especially for cases in which the fluorophore has a low quantum yield or is at a low concentrations in the tissue. In order to decouple the true fluorescence signals further, previously recorded “basis spectra” of the residual non-fluorophore originating signal and the pure fluorescence signal are fit to

the data. Each spectrograph was used to record its own fluorescence emission basis spectra and residual excitation basis spectra in a controlled manner. All spectra were normalized to the maximum value. Fitting is accomplished by a linear least squares algorithm that minimizes the summation

$$S = \sum_{i=1}^N [y_i - (aF(\lambda_i) + bG(\lambda_i))]^2 \quad 5.3$$

with respect to a and b , where y_i is the measured intensity at a given wavelength pixel, F and G are the residual excitation and fluorescence basis spectra, a and b are the coefficients recovered in the minimization procedure, and N is the number of wavelength pixels per spectrum. The algorithm determines the amount of fluorescence emission and excitation cross-talk in the measured spectrum, the sum of which best fits the data in a least squares sense. This procedure is applied to each recorded fluorescence spectrum, a total of 240 spectra for a given acquisition. In some cases, the fluorescence peak has been observed to shift to longer wavelengths in large phantom volumes, an issue discussed in Chapter 12. To account for this, the minimization may incorporate the position of the peak as a free parameter by scanning the fluorescence curve over a range of wavelengths. At each wavelength position, the linear least squares algorithm determines the relative contributions of the fluorescence peak and excitation cross-talk and stores the sum of the residuals. Once the entire wavelength range has been scanned, the position which yielded the smallest residual is retained as the best fit. An example of fitted spectra along with the data fits is presented in Figure 5.14. More sophisticated

minimization techniques such as secant and bisection methods may be applied to decrease the computational burden, however, the overall computation time for all 16 sources and detectors is less than a minute and the simplicity of implementing the scanning technique makes it an acceptable choice.

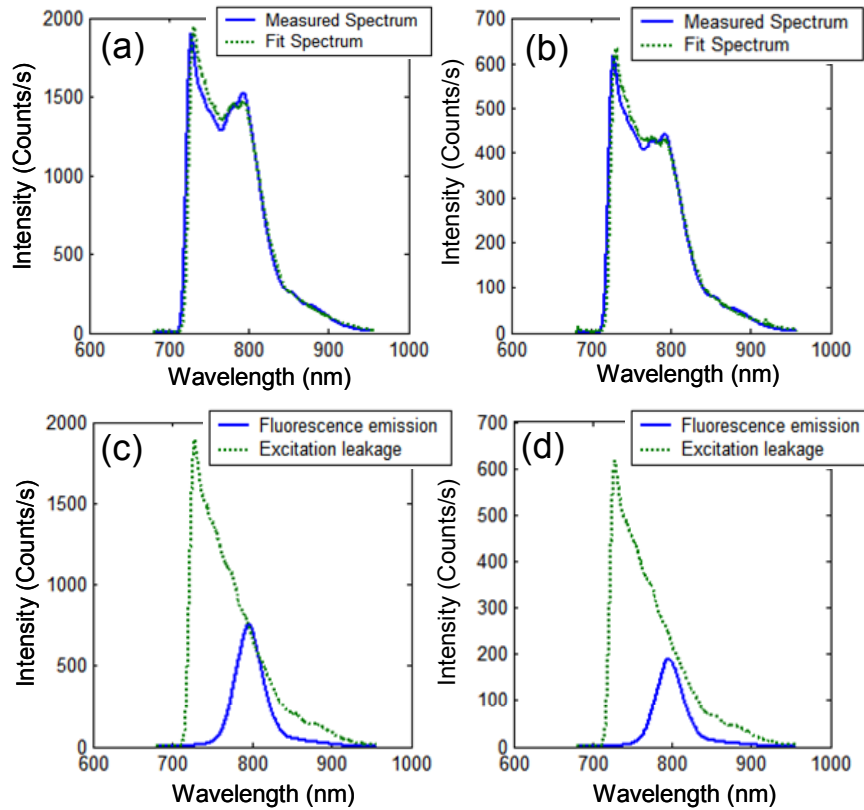


Figure 5.14. Each column represents an example of a single source-detector measurement and illustrates the spectral fitting routine used to decouple fluorescence spectra from the measured signal. The algorithm determines the relative contribution of the basis spectra [bottom row, (c) and (d)] which best fits the measured spectrum. The top row [(a) and (b)] shows the measured data (solid blue line) and the spectrum composed of the sum of the basis spectra (green dotted line). These examples are from a mouse injected with Li-Cor IRdye-800 EGF.

The fitting routine illustrated in Figure 5.14 minimizes the squared error based on the entire wavelength range; however, signals at shorter wavelengths are dominated by auto-fluorescence signal contamination and filter cut-on behavior. For fluorescence imaging, these shorter wavelength signals are of less interest than signals in the range of the fluorescence emission peak. Restricting the spectral fitting minimization to wavelengths above 740 nm, 20 nm above the filter cut-on wavelength, produces the results shown Figure 5.15, for the same data used in Figure 5.14. This procedure clearly produces more accurate data fits in the vicinity of the fluorescence peak, which is what is most important for fluorescence imaging.

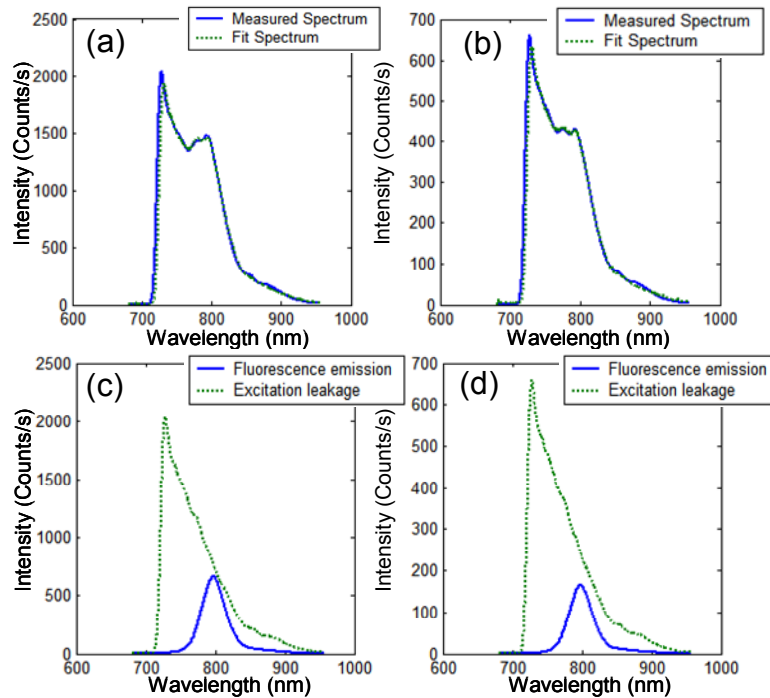


Figure 5.15. A more accurate minimization is produced when the spectral fitting wavelength range is restricted and does not include the filtered region. In this case, the same data presented in Figure 5.14 data is fit for the wavelength range only above 740 nm.

Once the fluorescence peak contribution has been decoupled from the measured signal, all or part of it may be integrated to provide a single value of fluorescence intensity for that source-detector position. Figure 5.16 shows the integrated fluorescence intensity of a single source and seven detectors from a tumor-bearing mouse head using data fit with the two spectral fitting techniques described above (one using the full wavelength range and the other using data only above 740 nm). The difference in terms of overall measured intensity is small, though noticeable. Importantly, data between source-detector pairs are not offset by a constant value, indicating that accuracy in spectral fitting may influence the relative perturbations which form the foundation of image reconstruction. For the remainder of this work, the more accurate spectral fitting procedure is used and the true influence of different fitting schemes on image formation is left untested.

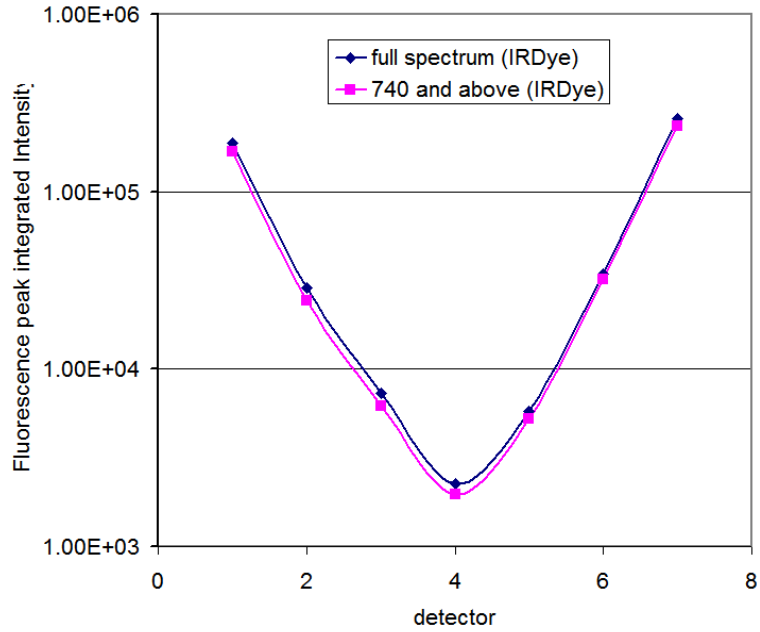


Figure 5.16. Calibrated intensity measured at seven detector positions (single source) around a murine head. Data was processed using two different spectral fitting routines.

Integrated fluorescence emission measurements are calibrated using the following equation,

$$\Phi_{fl_i}^{calib} = \Phi_{fl_i}^{meas} \frac{\Phi_{x_i}^C}{\Phi_{x_i}^{meas_spec}} \quad 5.4$$

where the index i indicates a single data point or source-detector pair. Φ_x^C is the intensity boundary data calculated from the images of μ_{ax} and μ_{sx} recovered using the frequency domain (FD) measurements from the PMT-based clinical system. This calculated, or “model”, boundary data must correspond to the spectrometer fiber positions, which do

not necessarily have to be identical to those used in the FD system. The quotient in Equation 5.4 essentially provides a scaling factor for the fluorescence measurements which accurately scales the fluorescence data to the FEM model and accounts for inter-detection channel throughput and fiber coupling discrepancies. An initial estimate for the iterative reconstruction algorithm is determined using a homogeneous fitting routine. This procedure uses the bisection method to minimize the data-model misfit assuming a homogeneous distribution of fluorescence yield.

5.2.5 Alternative data processing approach

The most recently acquired data was calibrated in a slightly different manner from what is described in sections 5.2.1 through 5.2.3. This modification does not affect the spectral fitting procedures outlined in section 5.2.4. In the alternative approach, the baseline/dark noise correction using pre-recorded data is abandoned in favor of a more direct baseline correction which calculates the offsets based on a small range of data within the measured spectrum. Spectra used to measure the excitation and fluorescence intensity both contain regions that should measure zero intensity. For excitation data, this region encompasses any wavelength range outside of the measured laser peak. For fluorescence spectra, a portion of the long-pass filtered region provides the baseline correction (for example, 700 – 710 nm for the 720 nm LP filter used with the 690 nm laser diode). In both cases, the median of intensity values covering the selected wavelength range is used to offset the entire spectrum. This provides a reliable and accurate correction, especially for low intensity data measured over long exposure times.

It should also be noted that relative intensity offsets of detector and source strengths, as outlined in 5.2.2 and 5.2.3, are unnecessary for fluorescence imaging due to the self-calibrating characteristics inherent in computing the fluorescence-to-transmittance ratio. Therefore, this alternative approach also omits these procedures as described above. However, the spectral response of each detector is important, and thus in this new approach, the relative detector offsets calculated in 5.2.3 are normalized individually to their own mean and the resulting spectrum corrections used in the same manner as in section 5.2.3.

5.3 Homogeneous Fitting

Fitting fluorescence intensity data measured through a tissue domain to data generated using the fluorescence diffusion-based model system provides a bulk measure of the fluorescence yield in the tissue. The recovered value may be used on its own, as a measure of total fluorescence activity in the interrogated tissue region, but for purposes of imaging, is used as an initial estimate in the full image reconstruction algorithm. Once the raw data has been processed as per the steps presented above, the calibrated data is used to generate a homogeneous estimate of the fluorescence activity in the domain. The imaged volume is assumed to have a homogenous distribution of fluorophore, (though the optical properties may be heterogeneous) and data generated using the numerical model is matched to the measured data. This is accomplished by minimizing the error between the measured data and model data while varying the homogeneous fluorescence yield inside the volume. The minimization routine developed here is a simple bisection method approach, which guarantees that the minimum will be determined as long as the

two initial estimates bracket the minimum. More sophisticated minimization techniques which converge faster may be used; however, the bisection method approach is not prohibitively time consuming for 2-D imaging and was used throughout this work. An example of calibrated boundary data is presented in Figure 5.17 which shows fluorescence intensity measured through a homogeneous phantom plotted with the homogeneous model data that best fits the measured data. In this case, the phantom contained ink, 1% Intralipid, and 10 nM ICG. Both sets of data are plotted as a function of source-detector pair where each parabola in Figure 5.17 represents a single source and multiple (13) detector positions. In this case, near-source detectors were ignored, and thus a total of 16×13 data points are shown.

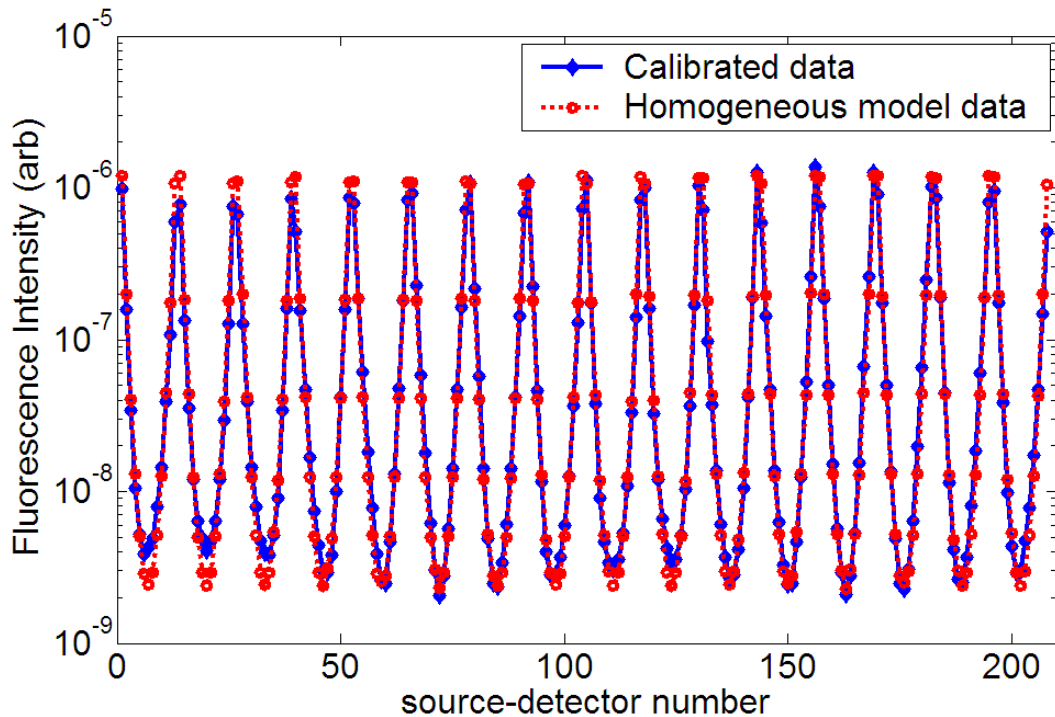


Figure 5.17. Calibrated data compared to homogeneous fit data for a homogeneous liquid phantom contain intralipid, ink and 10 nM of the fluorophore Indocyanin Green.

It is important to recognize that the fitting procedure requires knowledge of the optical properties at the excitation and emission wavelengths. In practice, these values will have been recovered using the frequency domain system described in section 2.2.

5.4 System Performance

5.4.1 Repeatability

An 8.6cm diameter homogeneous phantom composed of silicone, TiO₂ dioxide, and India ink was used to measure the repeatability of transmission mode measurements using the spectroscopy system. Optical properties of the phantom were 0.004 mm⁻¹ and 1.91 mm⁻¹ for the absorption and reduced scattering coefficients respectively. Measurements were repeated at each source-detector position using the 690 CW laser source. For a single vertically binned pixel array, the average and maximum standard errors at the laser peak are 1.4% and 1.8%, respectively, if fiber positions were not changed in between measurements. These increase to 18.3% and 19.5% with fiber repositioning, indicating that fiber coupling is the most significant source of error. If pixels are binned throughout the laser peak, the average and maximum standard errors change to 0.28% and 0.37% for fibers remaining in contact with the phantom and 14.8% and 16.3% for re-positioned fibers.

Determining measurement repeatability in fluorescence mode is less straightforward given the signal dependence on fluorophore concentration, absorption spectrum, and quantum yield. For this study, a 70 mm diameter liquid phantom containing DPBS, 1% intralipid, India ink, and 10 nM ICG was used to determine measurement repeatability. This measure was calculated in two ways, one considered

only the raw data for a given binned pixel array and resulted in a mean standard error of 0.7% and maximum standard error of 1.4% for the pixel array at the fluorescence peak. The second measure was determined based on the integrated intensity from the full calibration and spectral fitting routine, resulting in an average standard error of 0.6% and maximum standard error of 1.8%. It is clear that fiber positioning variability would dominate the data error for fluorescence measurements in this case. However, a calibration procedure unique to fluorescence measurements is used to correct for fiber coupling variability. This is accomplished by calibrating the fluorescence measurements to the transmission measurements acquired in the same geometry, as described in section 5.2.4. This provides inherent stability to systematic error, though is not unique to spectrometer-based detection which in and of itself does not necessarily provide an SNR advantage over more traditional detection schemes used for fluorescence tomography. The benefit of spectrometer based detection is improved separation of the fluorescence signal from background contamination, providing a more accurate fluorescence to transmittance ratio, especially for low concentrations of fluorophore.

5.4.2 Sensitivity

A 70 mm diameter liquid phantom containing DPBS, 1% intralipid and India ink was used to investigate the overall sensitivity of the system to ICG fluorescence. ICG dye dissolved in DI water was added to the solution to obtain solutions ranging from 10 pM to 1 μ M ICG. The optical properties of the intralipid/ink solution μ_a and μ_s' , were 0.006mm⁻¹ and 1.6mm⁻¹, respectively. Optical properties near the excitation and emission wavelengths were recovered for each concentration of ICG from data collected

using the clinical frequency domain system. Since the domain was known to be homogeneous, these properties were determined in a homogeneous fitting procedure only.

Fluorescence emission and excitation transmission measurements were recorded for each phantom, with a maximum allowed camera integration time of 120 seconds applied to the fluorescence measurements. The typical data measured across the emission spectrum are shown in Figure 5.18(a) for a strong fluorescence signal and Figure 5.18(c) for a weak signal. The spectral fitting procedure discussed in section 5.2.4 above was used to recover the true fluorescence signal and the non-specific background contributions, as shown in (b) and (d), respectively. Additionally, to quantitatively compare the spectral fitting procedure to more conventional means of fluorescence filtering, the measured, un-fitted spectra were integrated to simulate 720 nm long-pass filtering. In both cases, integrated values representing fluorescence emission intensities were calibrated following Equation (5.4) and used to determine homogeneous values of fluorescence yield.

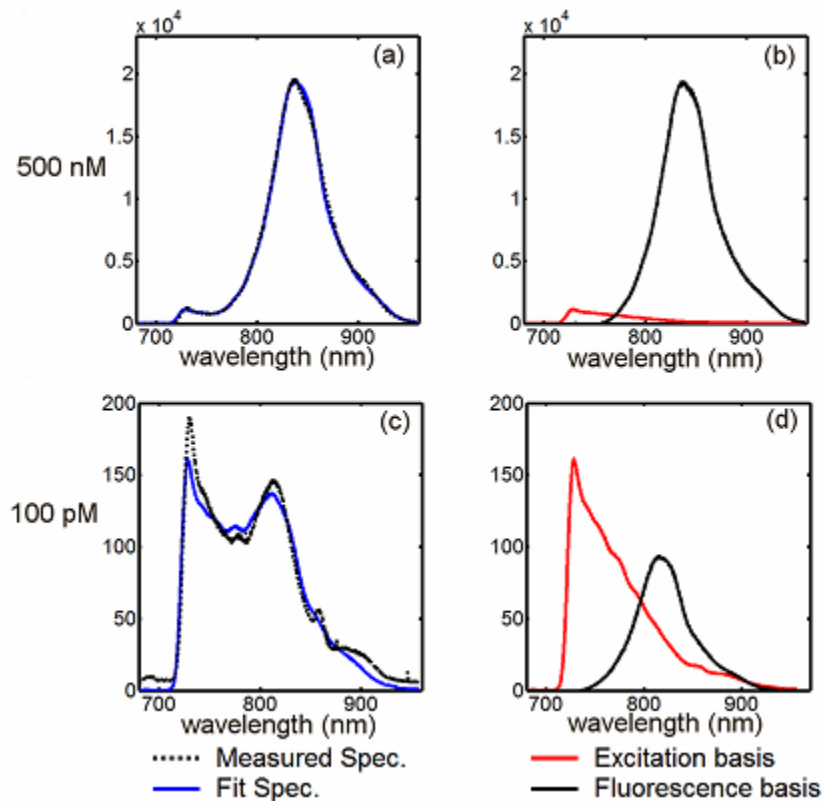


Figure 5.18. A spectral fitting routine is used to decouple fluorescence spectra from the measured signal. The spectral fitting algorithm determines the relative contribution of the basis spectra [right column, (b) and (d)] which best fits the measured spectrum. Two examples are presented above, both for a 70 mm diameter homogeneous phantom containing intralipid, ink and ICG [500 nM for graphs (a) and (b) and 100pM for graphs (c) and (d)].

Values of fluorescence yield recovered using the two data pre-processing techniques are plotted as a function of known ICG concentration in Figure 5.19. The linear fit shown in the figure was computed using the spectrally fit data with the y-intercept forced to zero and indicates a strong linear correlation of recovered fluorescence yield and ICG concentration ($R^2 = 0.99$). At concentrations above 1nM, the fluorescence yield values calculated using data that was filtered only, with no spectral fitting, closely matches the spectrally fit results. Fluorescence signals produced at these fluorophore

concentrations dominate the detected signal, a finding consistent with the data shown in Figure 5.14. However, fluorescence yield values recovered with spectrally fit data maintain the linear relationship at lower concentrations than those recovered using data without the spectral separation of background contamination. Clearly, the two techniques diverge at 1nM. At this concentration, the residuals between the recovered value of fluorescence yield and the linear approximation are 0.4% and 48% for the spectrally fit and filtering-only approaches, respectively. As the fluorophore concentration drops below 1nM, both techniques lose the consistent linear response observed at higher concentrations, though the filtered-only shows even less sensitivity to changes in fluorophore concentration. At 500 pM, the residuals increase to 57% and 192% for the spectrally fit and filtered-only data processing responses, respectively. Below this level, accurate quantification of fluorescence activity is unlikely in this phantom configuration, however, the spectrally fit data still shows a stronger response to changes in fluorophore concentration down to 10 pM. The residuals calculated at the lowest concentration measured were almost 5 times larger without spectral fitting, clearly indicating a more sensitive, if not accurate, response of the spectral pre-processing technique. It should be noted that since fluorophore quantum yield is not explicitly known in this solution, the calculated slope of the linear regression does not provide information on the actual relationship between true and recovered concentration, however, the linearity itself is a critical measure of system performance.

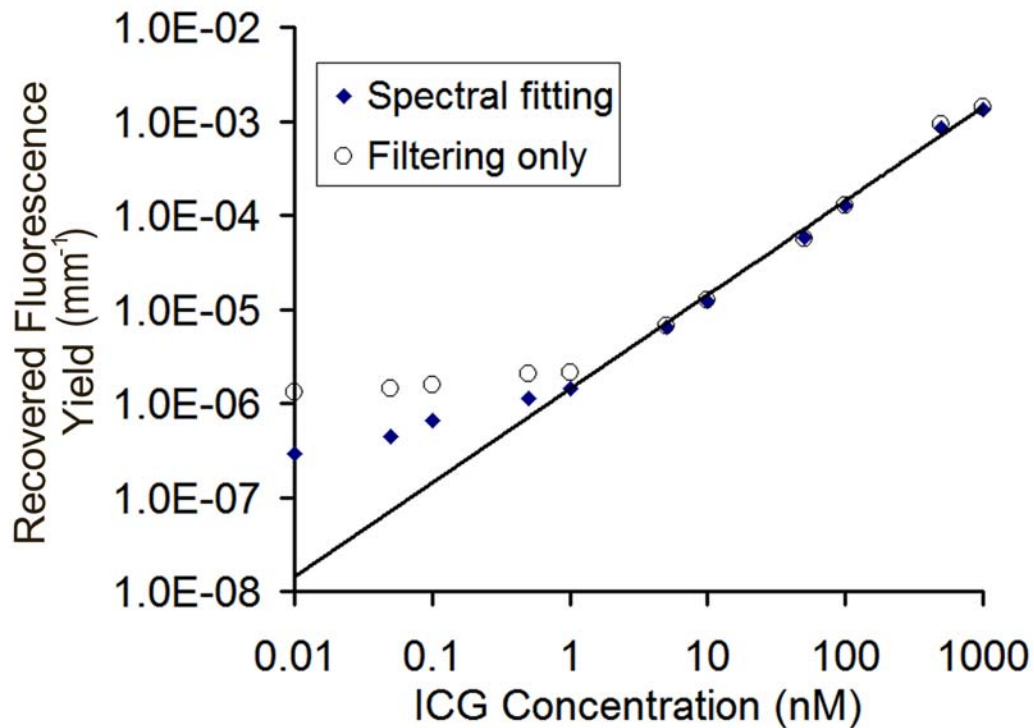


Figure 5.19. Recovered values of fluorescence yield as a function of ICG concentration in a 70 mm liquid phantom using two methods to process the recorded data. One method implements the spectral-fitting technique to decouple background contamination across the fluorescence emission spectrum while the other simply integrates the measured spectrum, as would be the case if the experimental system relied on long pass filtering alone. Values were determined using a homogeneous fitting algorithm for the background optical properties as well as the fluorescence yield.

5.5 Discussion and Summary

A system performance assessment for the MRI-coupled fluorescence tomography system has been presented. The system's high sensitivity, low noise CCD detectors were shown to be stable and provide repeatable measurements, the most significant error originating from fiber coupling errors. Fluorescence emission intensity may be scaled to the excitation laser transmitted intensity to account for these errors.

Characterizing the system's sensitivity to fluorophore concentration is complex given the dependence on concentration, absorption spectra, excitation filtering, and quantum yield. Sensitivity results of a commonly used fluorophore in a reasonably sized phantom were presented and demonstrated a linear response of the fluorescence yield fit to fluorophore concentration down to 1 nM using spectral fitting data pre-processing. Without spectral fitting, recovered values for 1 nM and below became inaccurate and the sensitivity slope began to flatten at these lower concentrations. This reduction in sensitivity was also observed for spectrally fit data, though the decrease in the response slope was less dramatic and did not show up until concentrations below 500 pM. Below this level, there is still a modest response to changing fluorophore concentrations, though recovered values are not linear. This was not caused by a drop in measurement SNR *per se*, as the measured signal even at 10 pM was strong and stable, but may have been due to systematic bias in the spectral fitting routine itself, inaccuracies in the basis spectra, or the presence of a contaminating signal with similar spectral characteristics to ICG,

The work presented here required the use of a separate frequency domain imaging system to obtain background optical properties and calibrate the fluorescence data to the algorithmic model. This is inconvenient at best and limits many of the advantages of the MRI-coupled imaging system. Importantly, the lack of FD imaging capabilities integrated into the imaging system requires re-positioning the subject to acquire background optical properties. Integrating PMT-based frequency domain detection into the spectroscopy system is underway, and described in section 15.1.3. The rotating source coupling stage was constructed with 15 PMT detectors in a design identical to that

reported elsewhere⁵¹. In this configuration, the source branch of the spectroscopy fibers will serve as both light delivery and pickup channels for the PMT's.

The system is capable of running in a variety of imaging modes. In fluorescence mode, the spectrograph system offers several advantages over filtered intensity measurements as spectrally resolved detection provides exceptional wavelength selectivity for excitation filtering. The excitation/auto-fluorescence contamination and non-specific background can be dramatically suppressed to improve the ability to quantify low level fluorescence, as was shown here. The system may also be used in the future to acquire emission data from multiple fluorophores simultaneously, contingent upon the individual fluorescence peaks being resolved well enough for the spectral fitting technique to extract the contribution from each fluorophore.

Chapter Six: Spatial prior implementations for fluorescence tomography

In this chapter, phantom and simulation studies are used to illustrate significant improvements in quantitative imaging and linearity of response with the spatial prior algorithms. In section 6.1, the spatial soft-prior algorithm is examined using simulated data in complex test fields and simple, infinite contrast phantoms of Lutetium Texaphyrin (LuTex). Tissue structural information, which can be determined from standard T1 and T2 MR images, is encoded as a spatial filter in the FMT reconstruction algorithm and used to guide the recovery of fluorescence activity, as described in Chapter 3. In this implementation, reconstruction parameters are grouped into regions based on tissue-type determined from the MR images but are permitted to update independently. A simulation study based on realistic geometries generated from MR images of a normal human breast serves as an initial illustration of expected improvements provided by the spatial priors approach in complex domains.

In section 6.2, soft and hard spatial prior implementations are examined using larger phantoms produced with low tumor-to-background contrasts. Indocyanine green replaces LuTex as the fluorescent contrast agent in these experiments. Images recovered using spatial guidance are compared to images recovered without this information,

demonstrating even further gains in image quantification in these more complex phantom geometries.

6.1 LuTex imaging using soft priors

6.1.1 Simulation studies

Test domains for simulation studies were derived from a T1 weighted MR image of a human female breast with a maximum diameter of 10.8 cm. A 2D slice of the breast volume was discretized into a finite element (FE) mesh of approximately 2000 nodes and MR image intensity thresholds were used to assign regions in the mesh as adipose and fibro-glandular tissue types. Figure 6.1 shows the original MR breast image and its associated discretized, region-labeled mesh. The MR image originated from a clinical exam with an MR coupled frequency domain NIR system⁹⁴ and therefore reveals an irregularly shaped breast boundary caused by the fiber optic array slightly compressing the breast at the contact positions. A simulated cancerous tumor region was added as a target anomaly or region of interest for these studies and is depicted in the figure. Additionally, a second test case with a tumor region located near the center of the domain was used to explore the nonlinear sensitivity of diffuse optical tomographic techniques. The source-detector positions were determined directly from the MR image and represent 16 optical fibers circumscribing the breast domain in a single plane. Light is detected at all non-source fiber positions providing a total of 240 source-detector combinations. This simulated configuration matches our experimental fluorescence tomography system.

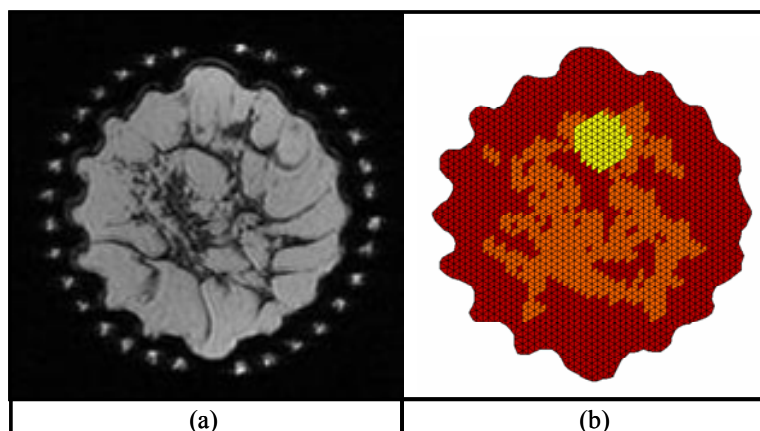


Figure 6.1 A coronal T1-weighted MRI slice of a human breast is shown in (a), from which the test domain for simulation studies was derived. Darker regions indicate fibro-glandular tissue imbedded in adipose tissue indicated by lighter values. The image was acquired during a clinical exam with an MR-coupled NIR tomography system and shows the indentations caused by the fiber optic probes. The test domain (b) was a discretization of the MR image coarsely thresholded into regions. The dark red region represents adipose tissue, the orange fibro-glandular tissue and the yellow circular anomaly region was added to simulate a tumor.

In this set of studies, regions were assigned values in terms of biologically relevant optical absorbing (HbO, dHb, Water, Lutetium Texaphyrin) as well as scattering parameters (Mie scattering amplitude and power). These values, provided in Table 6.1, represent typical known *in vivo* levels of endogenous chromophores and are consistent with previous clinical work ^{29, 62}. Though it is unknown exactly how Lutetium Texaphyrin (LuTex) will distribute in a human breast, the concentrations used are similar to those reported in *ex vivo* studies ⁶⁸ and at least represent a reasonably complex distribution for demonstrating recovery of fluorescence yield. Tissue chromophore concentrations were used to calculate total optical absorption and scattering values at the excitation and emission wavelengths based on experimentally determined values of molar extinction coefficients. Simulated noisy data was generated based on these optical

properties in the following manner: 1) frequency domain data for a light source at the excitation wavelength, 2) frequency domain data for a light source at the emission wavelength, and, 3) Continuous Wave (CW) fluorescence emission data at the emission wavelength. This represents a total of 3 data sets for a given imaging session: two frequency domain data sets for determining background optical properties and one CW fluorescence emission data set. CW fluorescence emission data was used to match the capabilities of our experimental system and results in a simplification of Equation (3.2) which can be handled by setting $\omega = 0$ rad/s.

Table 6.1. Chromophore concentrations and scattering parameter values assigned to the mesh regions in the simulation studies

	Oxy-hemoglobin (μM)	Deoxy-hemoglobin (μM)	Water (%)	Lutetium Texaphyrin (μM)	Scattering Amplitude	Scattering Power
Adipose	10	10	50	0.3	1.0	1.0
Fibro-glandular	15	15	60	0.5	1.1	1.1
Tumor	20	18	90	1.0	1.2	1.15

Given the modest Stoke's shift of LuTex, depicted in Figure 4.1, the choice of excitation wavelength has practical implications for experimental work. The difficulty in filtering the excitation signal precludes the use of LuTex's NIR absorption peak (about 735 nm) to excite the fluorophore. In this study, a 690 nm excitation wavelength was used for both simulated and experimental data acquisition. In addition to normally distributed random noise added to the frequency domain data (5% amplitude and 1 degree phase) and CW fluorescence emission (10% intensity), excitation signal leakage

through the filter was added to the CW fluorescence emission intensity to simulate a typical 7 OD rejection of the excitation intensity. This number comes directly from experimentally measured rejection estimates for the filters in the tomography system used in the experiments performed here (section 5.1.4).

The general image reconstruction protocol is listed in section 3.1. Initial estimates for all parameters were generated using homogenous fitting algorithms which enforce a single value for all nodes. The Jacobian matrix was calculated on a fine mesh of approximately 2000 nodes and interpolated onto a coarse reconstruction pixel basis for inversion. A 30 by 30 pixel reconstruction basis was used for the no-priors case. The spatial priors reconstruction used a semi-adaptive pixel basis that redistributes the pixels based on the region information. This method ensures that each region contains an adequate number of nodes to approximate the internal structure of the domain. Convergence was defined as less than a 2% change in projection error between successive iterations for the frequency domain optical properties algorithm and less than a 1% change in projection error between iterations for the fluorescence yield reconstruction. Similar algorithmic parameters were used for the phantom studies and are described in further detail below.

6.1.2 LuTex phantom studies: Perfect uptake

Lutetium Texaphyrin provided by Pharamcyclics was diluted in water and used as the imaging fluorophore. The test domain was a solid 5.5 cm diameter hardened epoxy phantom with scatterer and absorbers created by titanium dioxide powder and India ink, respectively^{53, 93}. The phantom had a 14 mm hole located approximately 12 mm from

the phantom center [similar to the phantom shown in Figure 4.6(c)]. The background optical properties were $\mu_{ax} = 0.005$ and $\mu_{s,x}' = 1.0 \text{ mm}^{-1}$, measured with a frequency domain system near the excitation wavelength. Unlike the simulation experiments, the optical properties were assumed constant throughout the domain in this experiment. These values were also used as the optical properties at the emission wavelength. The hole was filled with a solution of 1% Intralipid to match the scattering value of the background, and varying concentrations of LuTex (0.3125 μM to 5 μM) were added. This represents a simple test case for investigating the imaging response to varying concentrations of fluorophore. The excitation source was a 690 nm laser diode which matches the wavelength used in the simulation studies. Total acquisition time for the fluorescence emission was less than 4 minutes (a total of 240 CW data points).

Even after processing the collected light with a 720 nm long pass interference filter (Omega Optics, Brattleboro VT)) which provides 7 OD rejection of the excitation light as well as the filtering offered by the spectrograph grating, emission spectra recorded by the detector are composed of a sum of the pure fluorescence signal and contamination from phantom auto-fluorescence. Using the spectral fitting routine described in section 5.2.4, these signals were decoupled by fitting previously recorded “basis spectra” of the contamination signal and the pure fluorescence signal to the measured data. An example of the decoupling process for LuTex phantoms is presented in Figure 6.2 for one measurement at a single detector. The least squares algorithm operating on the basis spectra quantifies the amount of contamination and true fluorescence signal that exists in each spectral recording. Once fit, the fluorescence

signal was integrated and became the fluorescence emission intensity data for the reconstruction algorithm.

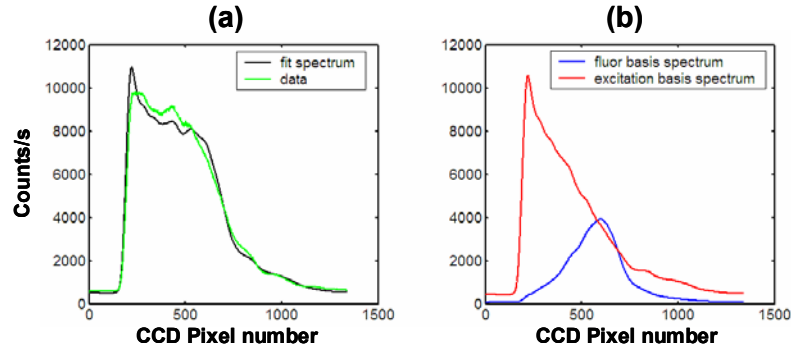


Figure 6.2. An example of a pair of basis spectra for the excitation and fluorescence light (in counts/s as a function of CCD pixel number) is shown in (b). These spectra were recorded for each detector prior to imaging. In practice, the basis spectra were used to perform a least squares fit to the spectrum measured for each source-detector pair to determine the relative contribution of the fluorescence and excitation light to the measured response.

To investigate the improved imaging capability of reconstructing data with spatial priors, each data set was reconstructed with and without spatial “soft” priors. Since the domain was easily characterized geometrically, spatial prior information was determined by direct manual measurement of the phantom. This information was encoded in the FE mesh used for reconstruction. Since background optical properties were previously determined with our frequency domain system, they were assumed known for image reconstruction. Convergence was defined as less than a 1 % change in projection error between iterations. All images were reconstructed using a 2GHz Centrino Duo laptop with 2GB RAM running Windows XP.

6.1.3 Simulation results

Figure 6.3 and Figure 6.4 display the target values of the two test cases along with images reconstructed using no priors and spatial soft prior information. Qualitatively, image recovery using spatial priors produces significantly more accurate images. Spatial priors preserve the general internal structure of the LuTex distribution, detail that is lost almost entirely in the no-priors case. Images of fluorescence yield show the most dramatic difference between the spatial priors and no priors reconstructions. Without spatial priors, the algorithm appears to have no ability to recover localized tumor-like regions of elevated fluorescence yield for these complicated cases. However, incorporating spatial priors results in images that qualitatively appear accurate and quantitatively are reasonably close to the true values. Figure 6.5 provides 1-D cross-sections near the y-axis of each domain. These plots confirm an inability of the no-priors imaging algorithm to recover the simulated fluorescent tumor in either test field. Alternatively, the spatial prior-based imaging algorithm not only picks out the objects of interest, but provides fairly accurate reproductions of the complicated structure of simulated fibro-glandular layers. Mean values for the simulated cancer region near the domain center are 79% and 51% of the true values for the spatial priors and no-priors reconstructions, respectively. These numbers change to 75% and 45% for the case with the cancer region closer to the edge of the domain. They represent a significant improvement in imaging performance; however, they alone do not illustrate the full impact of incorporating spatial priors. The cross-sectional plots indicate that the no-priors images contain virtually no spatial discrimination of the cancer regions. Regional

contrasts are depicted in Table 6.2 and further illustrate a dramatic overall improvement in cancer region quantification with spatial priors.

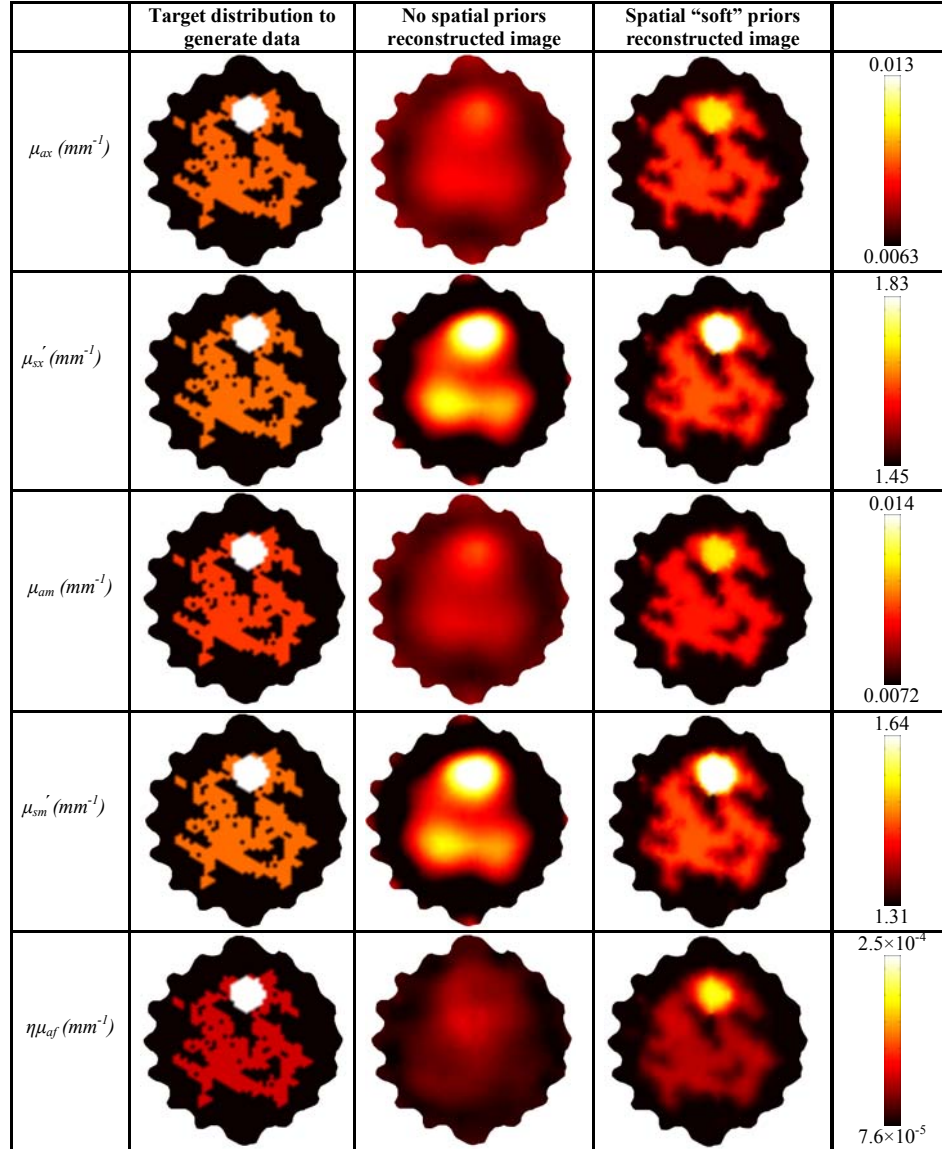


Figure 6.3. Target and recovered values of μ_{ax} , μ_{sx}' , μ_{am} , μ_{sm}' , and fluorescence yield, $\eta\mu_{af}$, for reconstruction implementations using no prior information and with spatial prior information. In this case, the simulated cancer region was near the edge, which is known to be easier to recover without spatial priors. The image scales are at right in units of mm^{-1} .

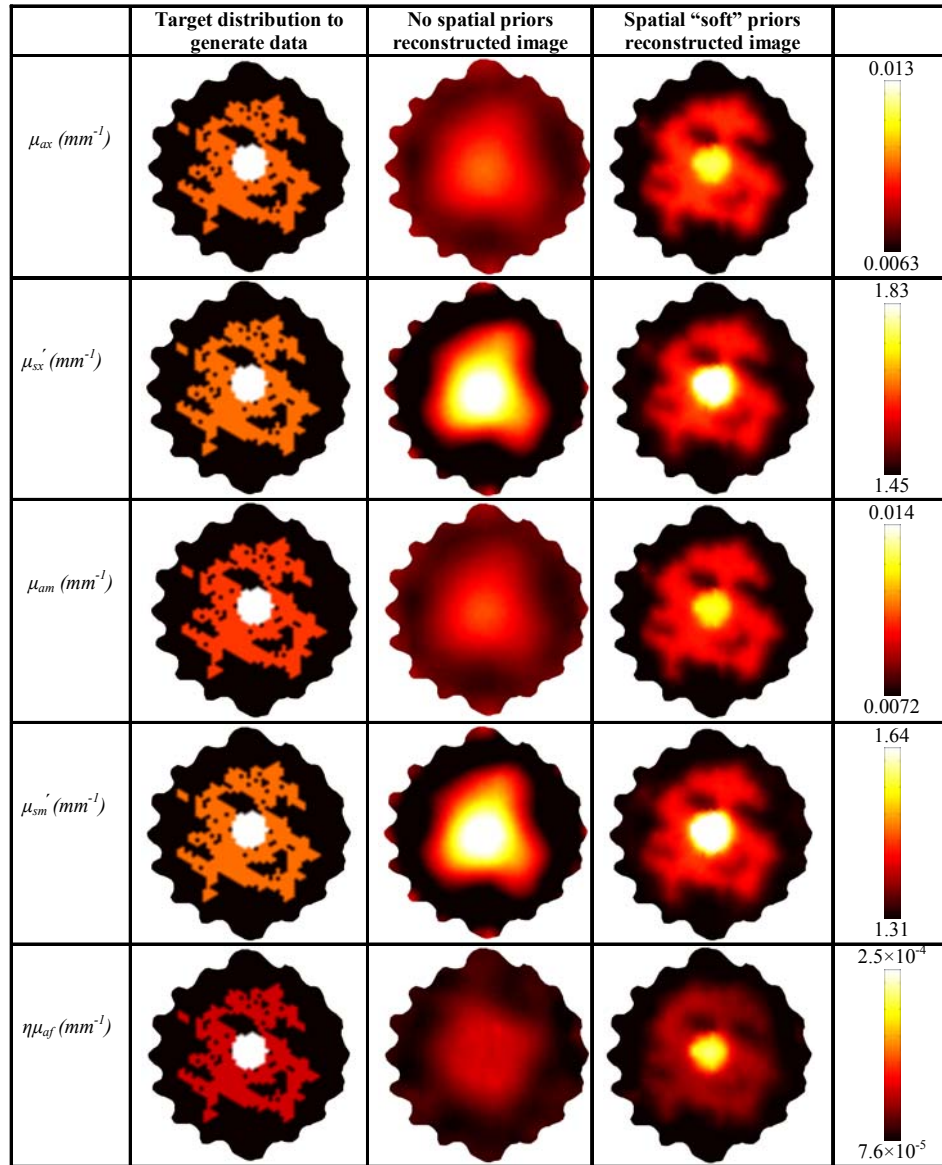


Figure 6.4. Target and recovered values of μ_{ax} , μ_{sx}' , μ_{am} , μ_{sm}' , and fluorescence yield, $\eta\mu_{af}$, for reconstruction implementations using no priors and spatial priors. In this case, the simulated tumor region was near the center of the imaging domain, which is known to be more difficult to recover accurately. Image scales are at right.

Table 6.2. Target and recovered fluorescence yield regional contrasts for the images in Figure 6.3 and Figure 6.44. Reported ratios were calculated using the mean values in each region.

Shallow tumor	Target Contrast	No spatial priors	Spatial “soft” priors
Tumor : fibro-glandular	2.0 : 1	1.1 : 1	1.6 : 1
Tumor : adipose	3.3 : 1	1.3 : 1	2.3 : 1
Deep tumor	Target Contrast	No spatial priors	Spatial “soft” priors
Tumor : fibro-glandular	2.0 : 1	1.2 : 1	1.8 : 1
Tumor : adipose	3.3 : 1	1.4 : 1	2.4 : 1

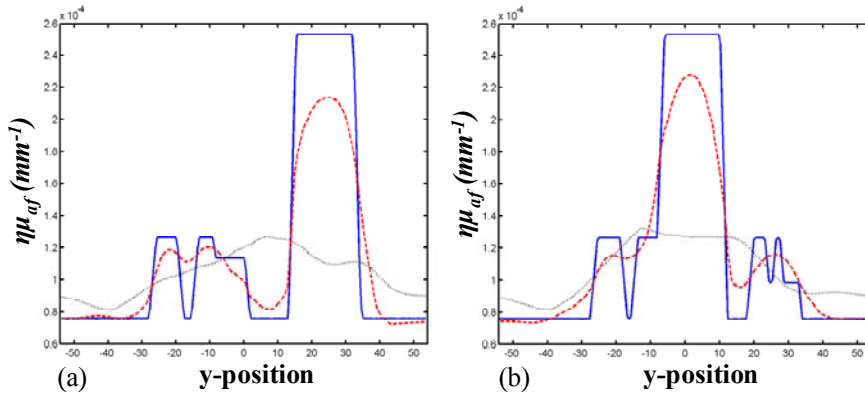


Figure 6.5. Cross sectional plots of fluorescence yield are shown for the simulated imaging domains in (a) the case with an object near the edge and (b) the case with an object near the center. In both cases, the cross section is in the y-direction just off center from $x = 0$. The solid line represents the target value, the small dotted line the recovered value using a no-priors based algorithm, and the dashed line the recovered value using spatially guided reconstruction.

In addition to improved qualitative and quantitative accuracy, the spatial prior algorithm reduced the reconstruction time significantly. The full reconstruction time for the no-priors case, including background optical property estimation, was just under 9

minutes for both the central and superficial tumor cases. These times were reduced to less than 3 minutes and 90 seconds using spatial priors. In both cases, structural information guided the algorithm to a convergent solution in fewer iterations than the no-priors cases.

6.1.4 LuTex phantom results: Perfect uptake

Figure 6.6 shows fluorescence yield images recovered from phantom data using both no-prior and spatial prior image reconstruction approaches. A qualitative assessment of the images reveals a dramatic benefit of the spatial prior on image formation. The fluorescent object's borders are more clearly defined for all concentrations of LuTex when using spatial priors. Furthermore, the values of fluorescence yield throughout the region of interest are more homogeneous, and therefore, more similar to the actual distribution for spatially guided reconstructions. Incorporating spatial priors also suppresses edge artifacts significantly. This is most apparent in images of phantoms with low LuTex concentration. Figure 6.7 shows a full scale image of the 0.3125 μM phantom. Artifacts near the boundary virtually dominate the no-priors image and represent the largest fluorescent yield values in that imaging domain. None of these artifacts exist in the spatially guided image generated from the same fluorescence emission data. The spatially guided image also includes an easily discernable fluorescent object at the correct location which is difficult to define in the no-priors case. These results indicate that for low fluorophore concentrations in this imaging domain, the correct fluorescent object would be identified only if prior structural information were incorporated in the reconstruction.

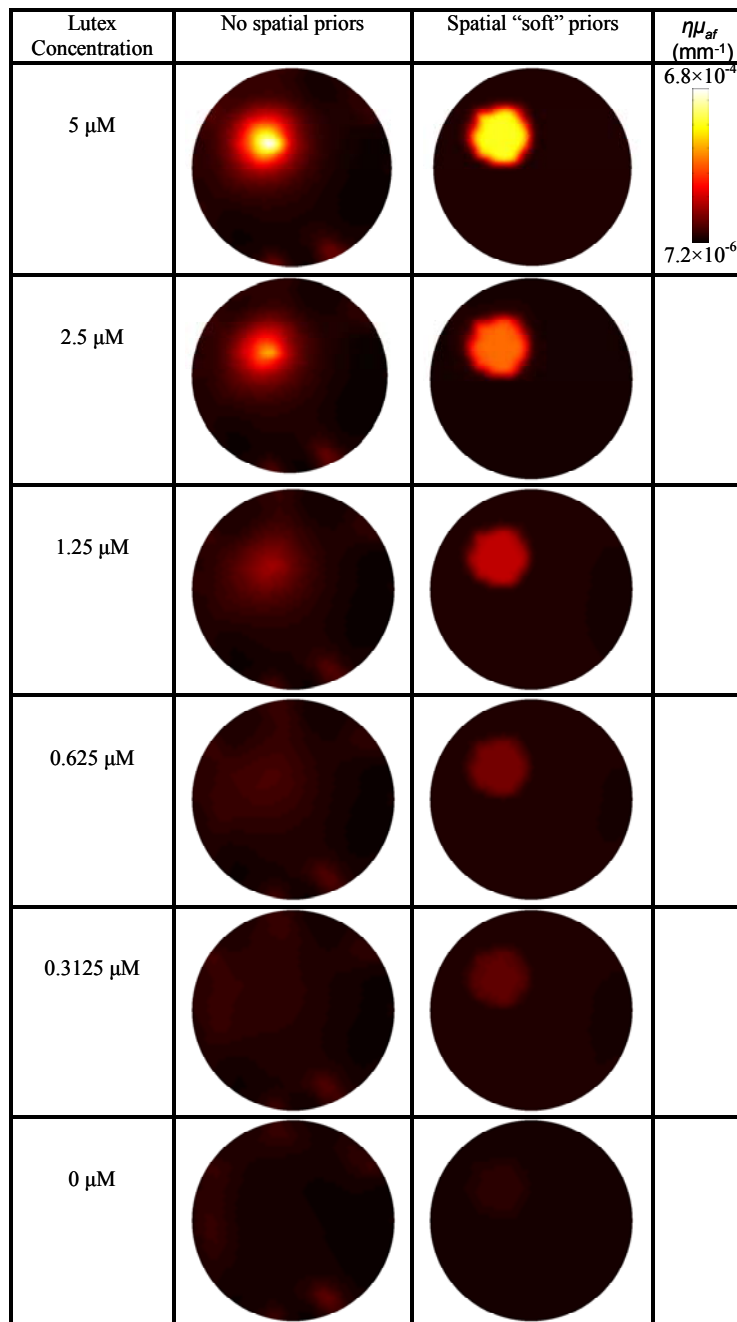


Figure 6.6. Recovered images of fluorescence yield are shown for varying concentrations of LuTex. The 14 mm diameter fluorescent inclusion was embedded in a 55 mm diameter solid epoxy tissue simulating phantom. Images were generated from the same data using algorithms based on no-priors and spatial soft prior implementations.

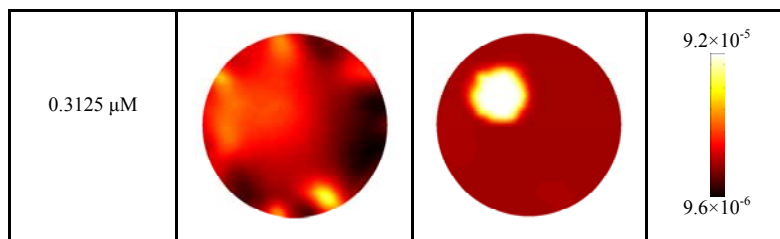


Figure 6.7. A narrower colorbar-scale version of the 0.3125 μM LuTex phantom images shown in Fig. 8 further illustrates the improvement in image accuracy, and removal of edge artifacts for the spatially guided algorithm. Images are of fluorescence yield in units of mm^{-1} .

6.1.5 Discussion

Both techniques suffer from a bias in the recovered fluorescence yield which results in a positive value in the region of interest for the case with no fluorophore. This is most likely caused by auto-fluorescence coupled with an imperfect spectral fitting technique and perhaps fluorescence peak distortion, addressed in Chapter 12, which results in positive values for fluorescence emission intensity even in phantoms containing no LuTex fluorophore.

In addition to improving image quality and fluorescence yield quantification, spatial prior-based reconstructions converged in substantially less time than the no-priors algorithms. Reconstruction times ranged from 50 – 90 seconds when not using spatial priors and approximately 22 seconds for spatially guided reconstructions, marking an improvement of just over 75% in some cases. These numbers represent only the fluorescence yield reconstructions and not the recovery of background optical properties since associated properties were assumed known from prior measurements. In cases requiring the recovery of background optical properties, the improvement in

reconstruction time is expected to be similar to that previously quoted in the simulation results.

Both phantom and simulation results demonstrated dramatic improvements in recovery and quantification of features in the fluorescence distribution. The results presented here show promise for this approach in all cases and tissue volumes considered. It is clear that incorporating anatomical features derived from MR images in DOFT image reconstruction will improve sensitivity to lower concentrations of fluorophore, qualitative accuracy, and fluorescence yield quantification in-vivo.

The phantom studies represented simple distributions of optical properties and fluorophore concentration and improvements in image quality were still substantial. It is expected that soft prior implementations will benefit imaging performance to an even greater extent in complex tissue domains, an assertion born out in the simulation studies and the ICG experiments described in the following section.

6.2 ICG phantom imaging: Imperfect drug uptake

6.2.1 Seventy millimeter pilot phantom

The perfect drug uptake experimental conditions used in the phantom study presented previously are unrealistic for clinical applications since most contrast agents, even targeted drugs, are expected to produce background signals in healthy tissue regions. More realistic conditions must include the presence of lower tumor-to-healthy tissue contrasts. A series of increasingly complex phantoms were used to investigate imaging of larger volume phantoms with imperfect tumor-to-background uptake. The first example is a 70 mm diameter cylindrical phantom composed of DPBS, 1% Intralipid

and India ink, resulting in background optical properties of $\mu_a = 0.005 \text{ mm}^{-1}$ and $\mu_s' = 1.4 \text{ mm}^{-1}$. ICG dissolved in DI water was added to the phantom volume to obtain a 300 nM ICG solution. A thin-walled plastic cylinder was positioned between the edge and center of the phantom to simulate a 2 cm diameter tumor region. The inclusion consisted of the same solution found in the phantom background, though the ICG concentration was elevated to 1 μM , providing a total contrast of just over 3.3:1. Background optical properties were determined by imaging the phantom in a separate frequency domain clinical system and calculated values for 785 nm were used for this experiment. The spectroscopy system was then used to acquire excitation intensity and fluorescence emission measurements. Integrated intensities were calibrated to the model as described earlier and images were reconstructed using an algorithm without spatial guidance as well as the soft spatial priors implementation. The resulting images are shown in Figure 6.8. Tumor-to-background contrast can be deciphered in both images, however, the spatially guided implementation provides a more accurate representation of the imaged domain. Inclusion borders are more clearly defined and the image represents substantially higher tumor-to-background contrast. Image contrasts based on the mean values of fluorescence yield in the tumor and background region are 1.68:1 for the spatial priors image and 1.14:1 for the no priors image.

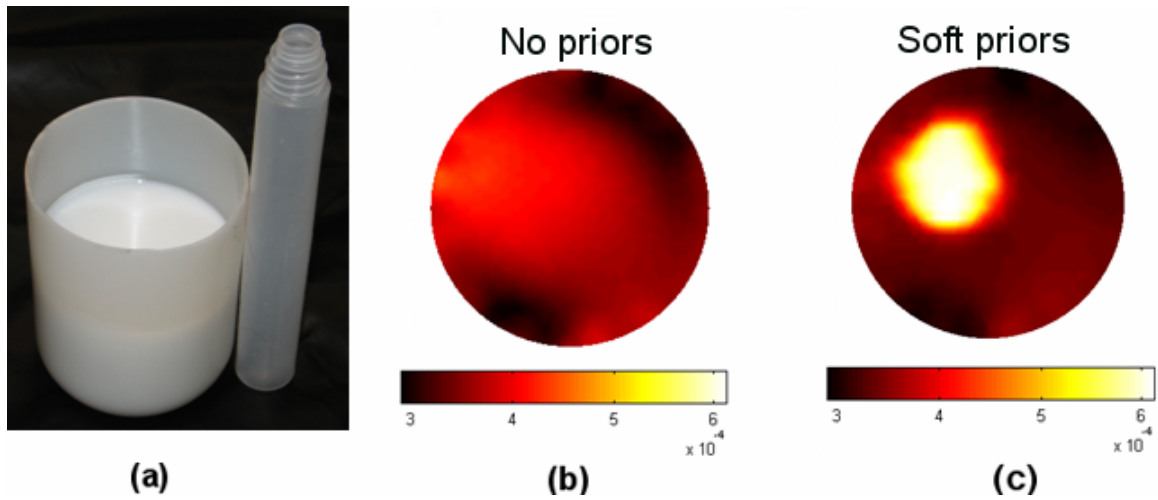


Figure 6.8. Containers shown in (a) were used to produce a 70 mm diameter liquid phantom containing an ICG heterogeneity. The ICG target-to-background concentration was 3.3:1. Images reconstructed using spatial soft priors, depicted in (c), are more accurate qualitatively and in terms of recovered contrast than images recovered without the spatial priors implementation (b).

6.2.2 Ninety millimeter, single-inclusion phantoms

6.2.2.1 Methods

A more comprehensive study was completed in larger, 92mm diameter cylindrical liquid phantoms composed of DPBS, 1% intralipid, and India ink. A 22mm diameter cylindrical plastic tube was suspended in the larger phantom volume to simulate a tumor region of elevated fluorophore concentration, as shown in Figure 6.9. The background liquid contained 300 nM of ICG while the tumor region was composed of the same intralipid solution but with varying concentrations of the fluorophore, to produce a range of tumor to background fluorophore concentrations between 1.5:1 to 6.6:1, or 50% to 560% contrast, respectively. Background optical properties of the intralipid/ink solution were determined using the separate frequency domain system at 785nm. These values, $\mu_a = 0.005 \text{ mm}^{-1}$ and $\mu_s' = 1.4 \text{ mm}^{-1}$, were assumed to be constant throughout the

wavelength range used here, though the absorption properties were adjusted based on the known ICG concentration and associated extinction spectrum at the excitation and emission wavelengths. The experiment was repeated for two inclusion positions, one near the edge of the phantom and one closer to the center, where the sensitivity to changes in fluorescence contrast is lowest. Data were calibrated in the manner described in section 5.2.5 and calibrated data was processed using the spectral fitting routine, from which homogeneous estimates were computed for each phantom configuration. Images were reconstructed using three approaches, two of which incorporate spatial prior: Soft spatial priors, hard spatial priors, and “no priors”.

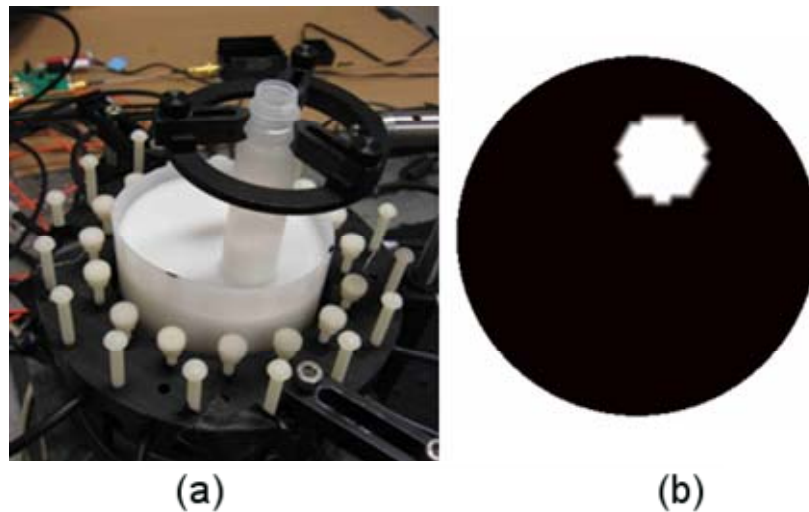


Figure 6.9. A photograph of the 92 mm diameter intralipid, ink, ICG phantom in the phantom fiber array is included in (a). The spatial prior information for an object near the edge is shown in (b).

6.2.2.2 Results and Discussion

Images for phantoms with the anomaly at the center and the edge are presented in Figure 6.10 and Figure 6.11, respectively. In both figures, each row represents (a) no

priors, (b) soft priors, and (c) hard priors implementations while columns represent different ICG concentrations in the tumor-simulating target. Images in each row are shown using the same color-bar scale, but this range may vary between rows.

It is clear that in this relatively large domain with imperfect drug uptake, images reconstructed without internal morphology information are qualitatively inaccurate and misleading, even at the higher contrast levels. On the other hand, both spatial prior techniques produced images that are qualitatively accurate and appear to show a more reasonable response to changing ICG concentration in the simulated tumor region. Close comparison of the two figures reveals a marked difference in image response between anomalies in the center and near the edge. Deep objects with very low fluorescence enhanced contrast are virtually invisible over the color bar ranges shown, even in images reconstructed using spatial guidance. Objects with identical characteristics near the edge are well resolved at even the lowest contrasts. The non-linear sensitivity of the diffuse imaging field is well known, expected, and clearly demonstrated here. This condition also afflicts spatially guided imaging, though to lesser extent than the unguided techniques.

Images recovered without the help of spatial priors provide the most pure expression of the measured boundary data content. Close examination of these images reveals a complete inability to localize the anomaly and return reasonable fluorescence yield image contrasts. Images for the deep target object show image intensities pulled to the right while image intensity actually decreases in the target region, likely due to increased absorption in the simulated tumor. Slightly improved localization is observed for objects near the edge of the tissue volume, though the maximum intensity is still well

outside the actual object location and image intensities do not seem to track well with increasing fluorophore concentration. The large centrally located structure, sometimes referred to as a ring artifact, is almost always a consequence of inaccurate data-model calibration, which arises for a number of reasons. Mismatch in this case may be caused by bias in the measured data or data processing, incorrect values of optical properties, a likely scenario given the assumptions made for these phantoms, or light tunneling issues prevalent when using liquid phantoms in plastic containers. Regardless of the source, this bias makes the no-priors imaging approach virtually intractable for the phantoms considered here.

Images recovered using the spatially guided approaches tell a more promising story. These implementations clearly prejudice the image recovery process, resulting in very reasonable images, from a qualitative perspective. While helpful in the situation presented here, this characteristic may be detrimental if MR segmentation and registration is inaccurate or simply does not correspond to the spatial distribution of fluorophore in the tissue volumes, possibly directing some of the data-model-mismatch-born image intensity into a target-object region inappropriately.

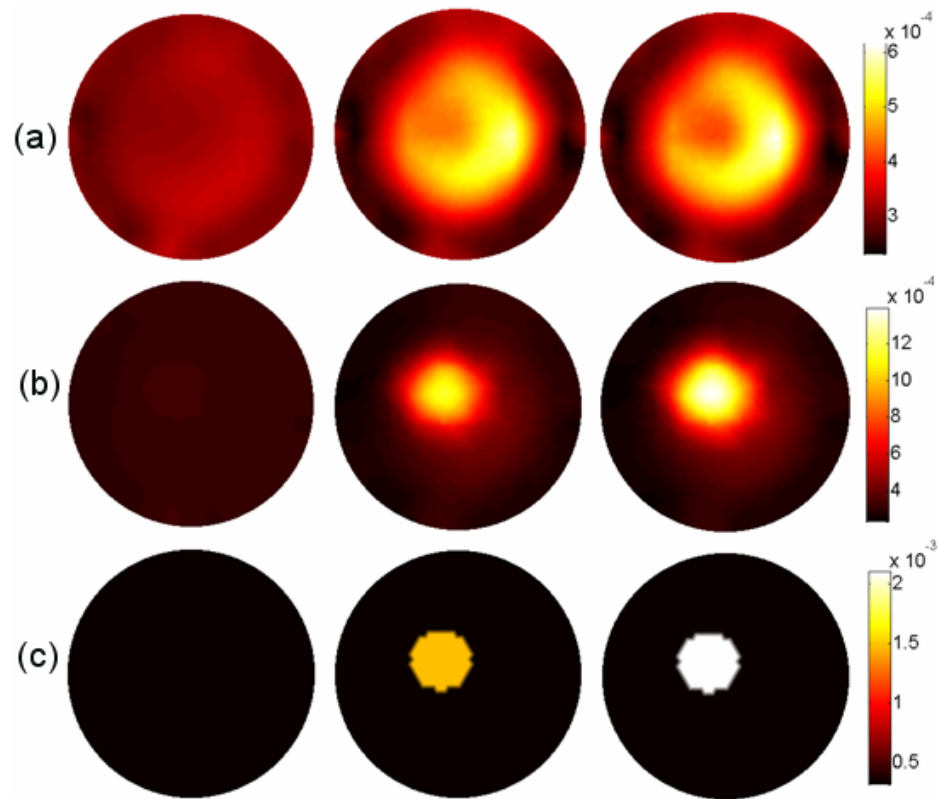


Figure 6.10. Reconstructed images of fluorescence yield for liquid phantoms containing intralipid, ink and ICG, using no spatial priors (a), soft priors (b), and hard priors (c). In this case, the simulated tumor region was just off center. Columns correspond to different tumor-to-background ICG contrasts, 1.5:1, 3.3:1, and 6.6:1 from left to right.

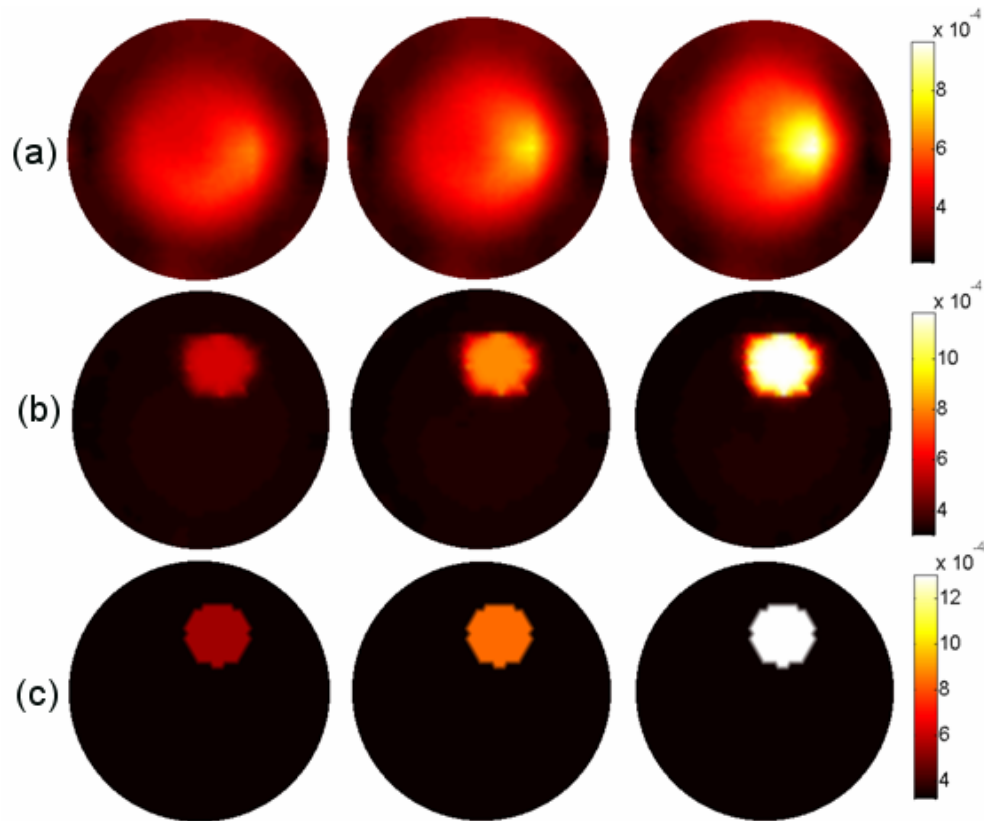


Figure 6.11. Reconstructed images of fluorescence yield for liquid phantoms containing intralipid, ink and ICG, using no spatial priors (a), soft priors (b) and hard priors (c). In this case, the simulated tumor region was close to the edge. Columns correspond to different tumor-to-background ICG contrasts, 1.5:1, 3.3:1, and 6.6:1 from left to right.

A more quantitative assessment reveals the extent to which spatial guidance impacts the imaging algorithm. Mean values of recovered fluorescence yield in the background and target regions are plotted as a function of target ICG concentration in Figure 6.12 for no priors, (a), soft priors, (b), and hard priors, (c), reconstructions. Values for both “center” and “edge” phantom configurations are plotted on each graph. The results in (a) confirm the poor quantification performance of unguided solutions.

Higher values of fluorescence yield in the anomaly are reported for both spatially guided techniques while background values remain fairly constant regardless of inclusion drug concentration. Both spatial prior implementations produce a large difference between recovered values for centrally located objects and objects near the edge. In the latter case, both techniques provide a reassuringly linear response to increasing concentration of ICG. Recovered values for deeper objects, on the other hand, are somewhat erratic with changing concentration. The data-model mismatch-derived bias is in part responsible for this behavior.

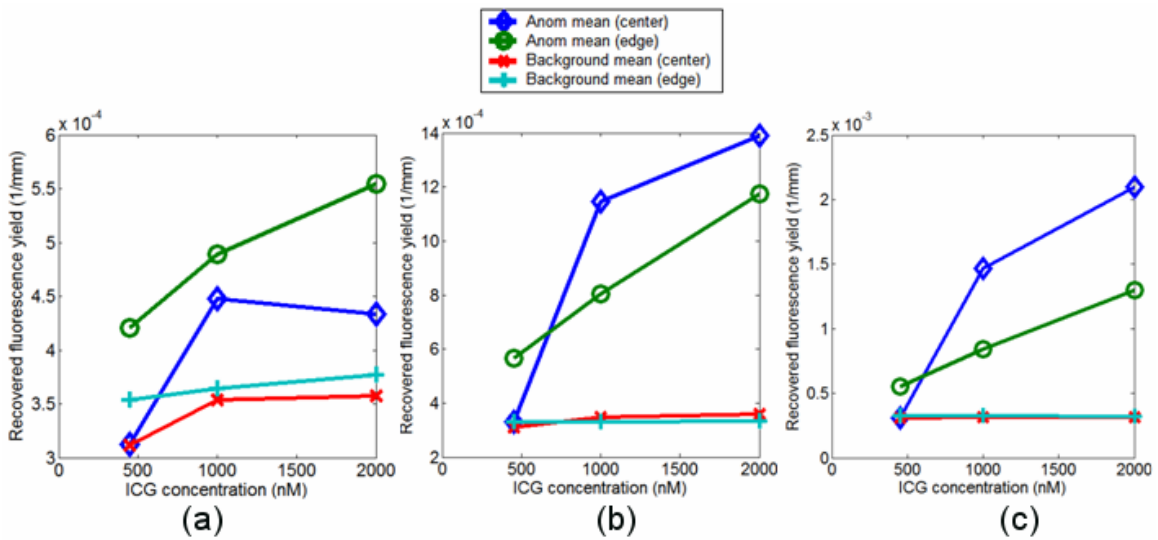


Figure 6.12. Mean values of recovered fluorescence yield in the anomaly (“Anom”) and background of the imaging domains for no priors (a), soft priors (b) and hard priors (c) reconstructions. Both phantom configurations are plotted on each graph, denoted in the legend by “(center)” and “(edge)”.

Recovered image contrast values calculated from the mean values provided in Figure 6.12 are plotted as a function of true contrast of ICG concentration in Figure 6.13, along with expected contrast values. The results produced with the no priors algorithm

are familiar. These images show insignificant recovered contrast compared to the true contrast based on ICG concentration [Figure 6.12(a)]. Image guidance improves the recovery of phantom contrast, but hard and soft prior implementations demonstrate different behaviors, especially when objects are deeply embedded. For objects near the edge, both spatial prior-based approaches provide a similar linear response in contrast recovery, though underestimate true contrast values based on ICG concentration. The erratic response to objects near the center is somewhat confounding and again is likely an artifact of data-model mismatch. This bias clearly has greater impact on imaging performance for objects located where imaging sensitivity is lowest.

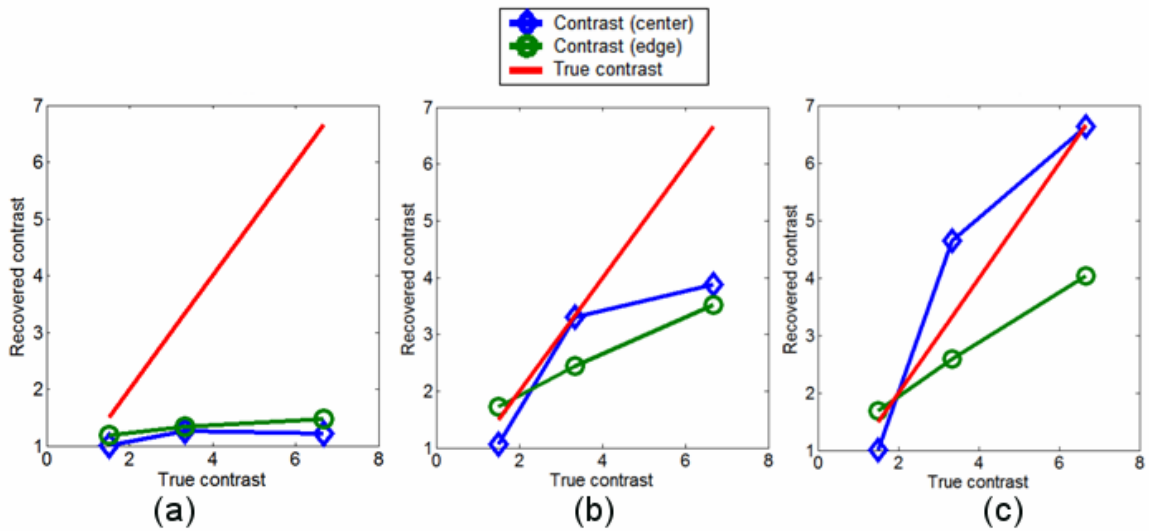


Figure 6.13. Calculated contrast determined using mean values of recovered fluorescence yield in the anomaly and background of the imaging domains for no priors (a), soft priors (b) and hard priors (c) reconstructions. Both phantom configurations are plotted on each graph, denoted in the legend by “(center)” and “(edge)”. True ICG concentration contrast is plotted in red.

6.2.3 Three layer phantom

6.2.3.1 Methods

Despite the complication of imaging imperfect drug uptake, the liquid phantoms' composition used previously is simple compared to the heterogeneous structure of breast tissue. In general, the organ is composed of a small number of optically significant tissue types; adipose tissue, fibro-glandular tissue, and suspect regions (benign and malignant tumors, cysts). Phantoms composed of similar multi-region structures provide the most clinically relevant testing platforms. Gelatin matrix phantoms, described in Chapter 4 can be used to produce these complex structures, a technique used in the experiments discussed here.

A 91mm diameter cylindrical phantom was composed of water, gelatin, TiO₂, and ICG. A photograph of the phantom is included in Figure 6.14 and shows three layers representing, from outside-in, adipose tissue, fibroglandular tissue, and a simulated tumor. ICG concentrations provide a tumor-to-adipose contrast of 10 to 1 (1 μM to 1 nM) and a tumor-to-fibroglandular contrast of around 3.3 to 1. Gadolinium was also added to the second layer so that each simulated tissue region would be discernable in an MRI scan for use as spatial prior information. MRI and optical data were collected separately and co-registered using MR sensitive fiducial markers. The MR segmentation is straightforward in this case, and images were segmented (Figure 6.14) to provide spatial guidance for the fluorescence reconstructions.

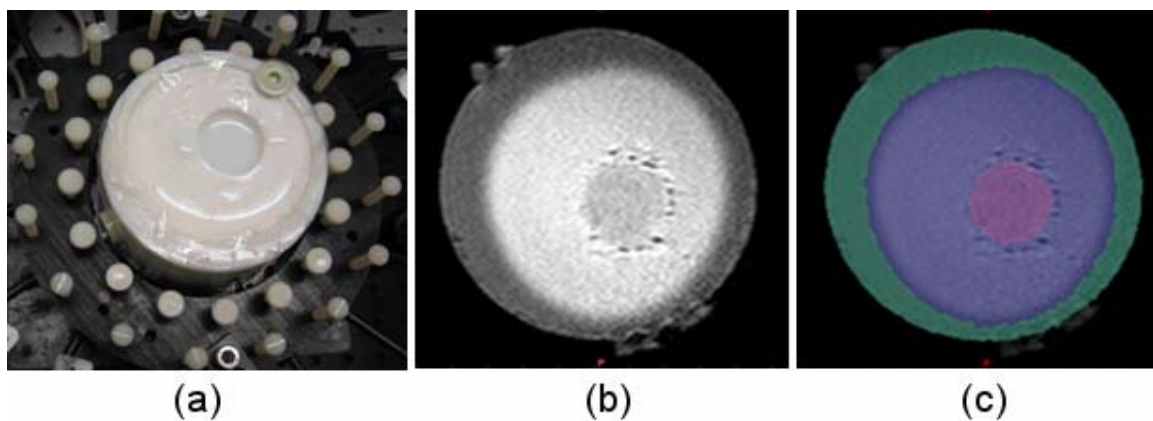


Figure 6.14. A photograph of the phantom in the optical fiber array is shown in (a). The second layer contained gadolinium, which provided MR image contrast, (b), for easy image segmentation using Mimics software (c).

6.2.3.2 Results and Discussion

Images of fluorescence yield recovered using all three algorithmic techniques are provided in Figure 6.15. While the images produced without spatial guidance moderately favor the true fluorescence distribution, boundary artifacts confound the image and overall quantification is poor. Importantly, spatially guided solutions report fluorescence contrast distributions in the correct locations and improve contrast quantification. In the best case, recovered tumor-to-fibro-glandular fluorescence yield contrast reaches about 50% of the actual value while tumor-to-adipose contrast reaches only 20% of true contrast. However, the large, low-contrast, complex phantom was a particularly challenging imaging domain and qualitative assessment of the images provides a promising outlook for image-guided reconstructions. Reducing tissue depth through mild compression in circular or parallel plate imaging geometries may readily improve contrast recovery significantly. The development of targeted fluorophores that produce

higher contrast between diseased and normal tissue should also enhance image quantification.

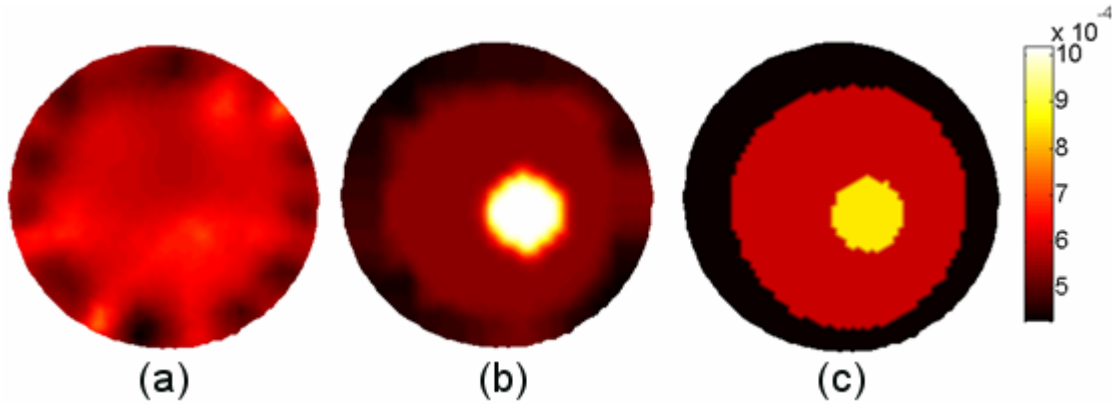


Figure 6.15. Fluorescence yield images of the three layer phantom reconstructed using no spatial guidance (a), soft-priors (b), and hard-priors (c). All images are plotted using the same color scale.

6.3 Summary

This study investigated an effective method to incorporate MR-derived tissue morphology for imaging fluorescence yield at depth in tissue. The conceptual assertion is that diffuse tomography will be more successful as an imaging modality when combined with pre-existing imaging systems which have higher spatial resolution, such as MRI. The algorithmic implementations essentially reduce the imaging problem from one of both localization and quantification to one of quantification only since the boundaries of the tumor are specified by the MR image. Simulation and phantom studies were used here to validate the method. Using data acquired in infinite contrast LuTex phantoms and much lower contrast ICG phantoms, the spatial prior implementations improved qualitative and quantitative imaging response of fluorescence yield. Prior information also suppressed image artifacts and more accurately represented the internal distribution

of fluorophore. In the no-priors case, edge or ring artifacts dominate the image for lower concentrations of fluorophore, and provide a misleading interpretation of the internal distribution of the fluorescent agent. Spatial priors information proved critical for discerning any fluorescence activity enhancement in large volumes with low fluorescence contrast. Imaging response in these cases was influenced dramatically by proximity of the tumor to the tissue surface, likely a consequence of bias in the calibrated data giving rise to data-model mismatch.

Even if data contains no data-model mismatch error, the impact of spatial guidance is dramatic. A simulated breast mesh derived directly from an MR image of a human breast served as the test bed for a complex tissue domain. The simulations demonstrated no ability to recover the internal distribution of the complicated domain without the use of spatially guided reconstructions. Qualitatively, fluorescence yield images generated without spatial priors had little resemblance to the target domain and completely disregarded the 18 mm simulated cancer region, as evidenced by 1D cross-sectional plots of fluorescence yield. Breakdown of the images in the no-priors case is likely due to poorly recovered background optical properties as well as the complexity of the fluorescence yield distribution itself. Certainly, part of the improvement in fluorescence yield image accuracy can be attributed to improved images of background optical properties.

In these studies, it was assumed that the fluorophore distribution correlates directly to the fatty, fibro-glandular, and tumor tissue layers, which themselves exhibit no significant intra-region heterogeneity, in a given imaging domain. While this assumption appears reasonable based upon the biology of the tissue for endogenous chromophores²⁹,

³⁴, fluorescent probes will have different characteristics in-vivo and further studies to determine a correlation between tissue type and fluorophore localization are necessary. Should this assumption prove to be unrealistic, the “soft” spatial prior approach offers some latitude in terms of correctly identifying structural prior information. The algorithmic implementation groups tissue regions together in a region-specific regularization and allows individual nodes in those regions to update independently. As opposed to “hard” prior approaches where nodal values in a given region are assumed homogenous, a soft prior technique may recover positive fluorescent objects not directly encoded in the spatial prior information. This is a subject of further investigation.

Spatially guided image reconstruction implementations based on prior knowledge of tissue morphology were shown to provide significant improvements in fluorescence yield recovery in complicated tissue volumes and to be highly beneficial for simple domains. Specifically, both phantom and simulation results demonstrated dramatic improvements in recovery and quantification of features in the fluorescence distribution. The structural guidance also reduced overall image reconstruction times substantially by limiting the number of required iterations to reach a solution. This was observed for both hard and soft prior implementations. The results presented here show promise for this approach in all cases and tissue volumes considered. Extensions of this study might include determining the effect of incorrectly identifying the structural prior, especially in cases where the MR images produce false negative or false positive readings⁹⁵. It is clear that incorporating anatomical features derived from MR images in fluorescence yield image reconstruction will improve sensitivity to lower concentrations of fluorophore, qualitative accuracy, and fluorescence yield quantification in-vivo.

Chapter Seven: Pilot MRI-FMT studies for imaging murine gliomas

This chapter describes two pilot MR-coupled fluorescence tomography case studies to image murine gliomas *in vivo*. It should be noted that the experiments presented in this chapter were originally designed by Summer Gibbs-Strauss for validation of bulk fluorescence spectroscopy without consideration of *in vivo* imaging; however, given the availability of the animals, a collaborative effort was initiated in which some subjects underwent simultaneous MRI-FMT acquisition. Summer Gibbs-Strauss also contributed most of the biologically-driven work, including animal handling, cell culture and implantation, drug delivery, and assistance in data acquisition. The evolution of the spectral fluorescence scanner is evident throughout the next three chapters (7 through 9) as the descriptions outline progress from relatively unsophisticated fiber coupling and software techniques used in small-scale pilot studies to more evolved approaches used for more ambitious studies.

7.1 Initial Attempts at Sparse Data Sampling and Loose Fiber Coupling in MRI-FMT

The first small animal imaging study attempted to image Aminoluvulinic Acid (ALA) induced Protoporphyrin IX fluorescence in 9-L glioma models in mice. At this stage of the system development, the mouse head and fiber array positioning system was quite primitive and only four optical fibers (Figure 7.1(a)) were used in this study without

a formal method for identifying and localizing fiber positions in the MR images. Data from one mouse was analyzed as an imaging subject, briefly discussed here.

The 9L tumor cells (10^6 cells in 10 μ L PBS) were implanted intra-cranially into the nude mouse. After 20 days of incubation, the mouse was imaged before and 2 hours after ALA (Sigma Aldrich) injection (at 100 mg/kg whole body dose). Ex-vivo studies in our lab have shown high tumor-to-normal brain tissue fluorescence contrast for this tumor line at this time point; however, fluorescence in the skin is also substantial after ALA injection⁹⁶. PPIX fluorescence was excited with a 635nm laser diode and the 1200l/mm grating was used to record the fluorescence emission spectrum, which peaks at around 705nm. The spectral fitting procedure described in section 5.2.4 was used to extract fluorescence emission from background contamination.

Gadolinium enhancement was quite strong for this tumor line, making tumor regions readily discernable in MR images. The large tumor region produces high image intensities in the MR image and shows an aggressive tumor bulk pushing against the skull. The MR images were segmented either using Mimics software, as described previously, or a Matlab GUI designed for work in breast imaging⁶⁵. The MR image and the corresponding 2-D mesh, made up of approximately 2100 nodes, are presented in Figure 7.1.

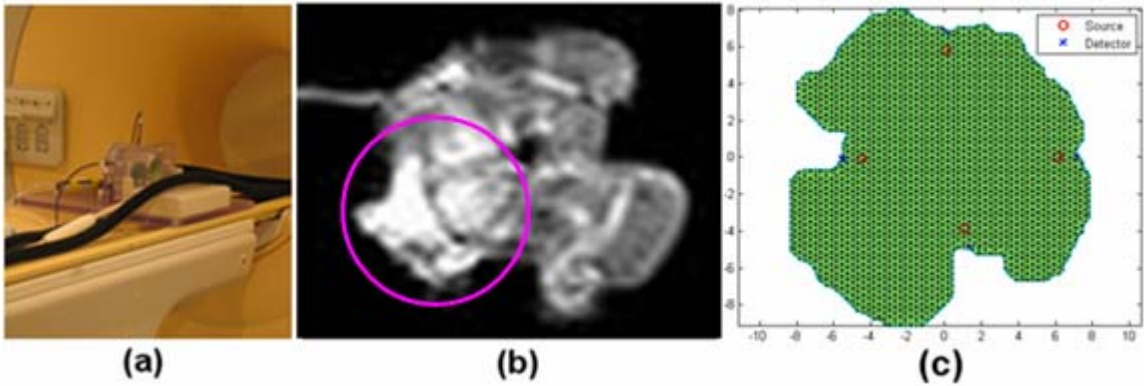


Figure 7.1. The small animal coil was used with four spectroscopy fibers for simultaneous MRI and fluorescence acquisition (a). A coronal slice of a Gd-enhanced MR image of a mouse head is shown in (b), from which an FEM mesh is generated (c). Fibers were located using the indents on the animal tissue surface (red circles show 1 scattering depth in from the locations identified).

7.1.1 Imaging endogenous PPIX fluorescence

7.1.1.1 Two region segmentation

Some malignant tumor cells produce PPIX at an accelerated rate without ALA administration, likely due to increased metabolic activity, and it may be possible to image malignant regions based on endogenous PPIX fluorescence alone. This hypothesis was tested by imaging a mouse before ALA injection. After the mesh was generated from the segmented MRI, homogenous values for optical properties, $\mu_{ax,am} = 0.01 \text{ mm}^{-1}$ and $\mu_{sx,sm} / = 1 \text{ mm}^{-1}$, were assigned throughout the two-dimensional domain. A homogeneous fitting routine produced a bulk value of fluorescence yield, used as the initial estimate in the image reconstruction algorithm.

The domain was segmented into two regions, one defined as tumor tissue based on the gadolinium enhancement, while the area outside of the tumor made up the second region. Images were formed using both soft and hard-priors implementations guided by

the two-region mesh. Resulting images are presented in Figure 7.3 and show very high tumor to background contrast in fluorescence activity: over 30:1 for the hard-priors image. These initial results are encouraging, indicating high production of PPIX in the tumor region compared to the surrounding tissue. Qualitatively, the two image formation techniques produce similar results; however, the recovered contrast based on the mean in each region is much lower for the soft-priors case, about 4.3:1. The soft-priors image also contains more subtle information on the fluorescence yield distribution. Specifically, the maximum of fluorescence activity, while still inside the tumor itself, is shown to be close to the center of the imaging domain. This information is lost in the hard-priors image.

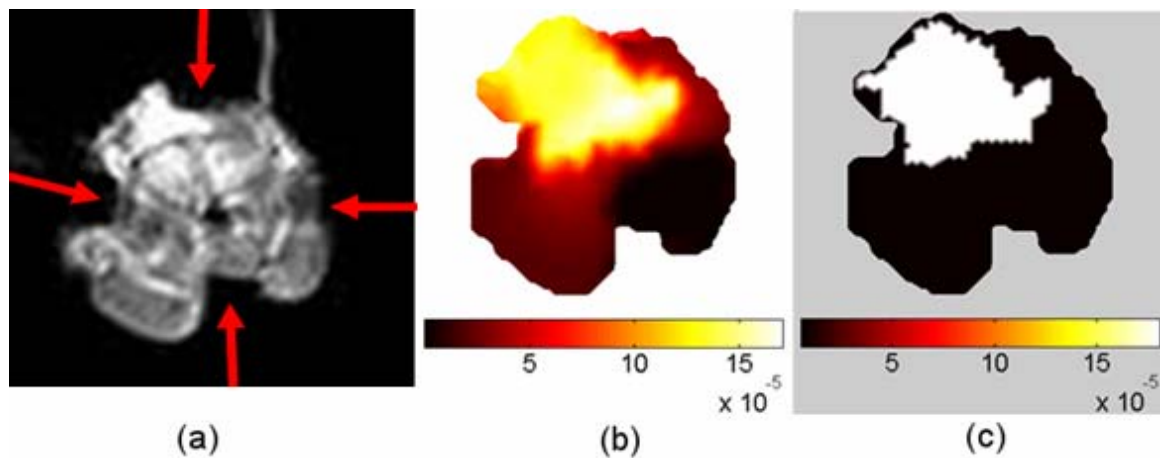


Figure 7.2. The MR image (a) and reconstructed fluorescence activity of PPIX fluorescence without ALA administration using soft priors (b) and hard priors (c).

7.1.1.2 Three region segmentation: False positive

The analysis was extended to incorporate a third region, outside the tumor area, as shown in Figure 7.3(a). The third region was placed randomly inside the domain,

providing an initial impression of the algorithm’s robustness to false region segmentation. Reconstructed images are shown in Figure 7.3 (b) and (c). The hard-priors imaging algorithm produced similar qualitative results to the two-region case, as the third region disappeared completely into the background; however, the image contrast climbed to near infinite, or the working precision of the computer. The soft-priors implementation, on the other hand, effectively pulled the image contrast out of the tumor region and into the large region which cuts through the center of the domain. This is not altogether inconsistent with the two region results, which showed the highest fluorescence activity in the tumor, but very close to the center of the domain. Fluorescence activity in the three-region implementation is shown to be lower in the tumor region as compared with the mid-section region, while the third “false” region plummeted to a positive constraint in the algorithm which prevents the fluorescence yield from dropping below 10^{-20} mm^{-1} .

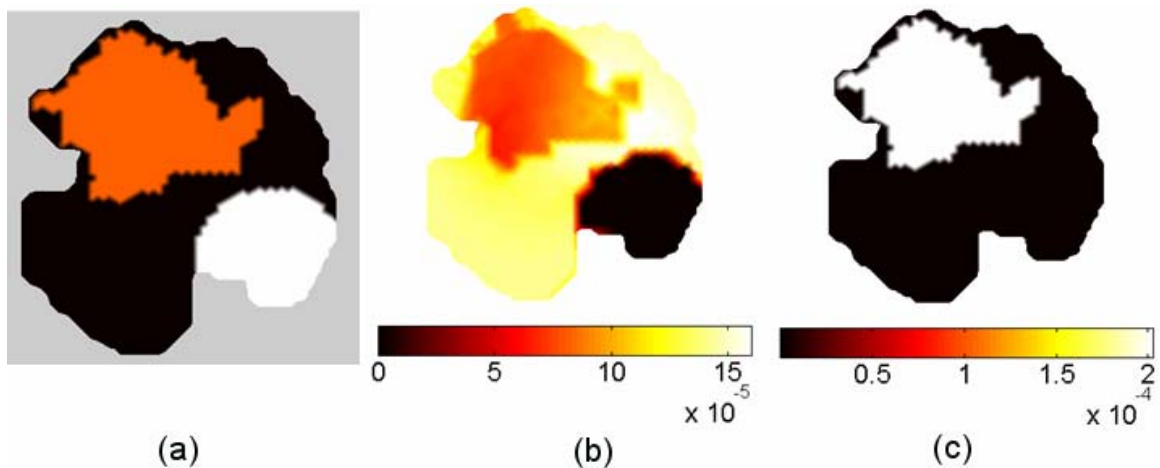


Figure 7.3. The same data was used to reconstruct images using spatial guidance based on a three-region segmentation. The regions are shown in (a), while the resulting images reconstructed using the soft and hard priors techniques are presented in (b) and (c) respectively.

The results associated with the three-region image formation protocol provide a relatively poor picture of imaging performance. Though we can only speculate, there are a number of fairly obvious reasons why the algorithm seems to break down in this case. Certainly the severe under-sampling of optical data resulting from using only four source-detector pairs makes the inversion problem particularly underdetermined. The hard-priors implementation addresses this to some extent by reducing the parameter space significantly; however, this does not change the non-uniform sensitivity inherent in the source-detector sampling on the boundary. Additionally, the foundation of the model system was rooted in assumptions of the optical property distribution. The homogeneous estimate may be inaccurate, in which case the model-based algorithm may not match the measured data under the best of circumstances. However, it is encouraging that the hard-priors implementation provided high tumor to background image contrast in the face of poor volume sampling, primitive fiber positioning, and perhaps inaccurate estimated optical properties.

7.1.2 Imaging ALA-induced PPIX fluorescence

Two hours after ALA administration, the same mouse was imaged in the MRI-FMT system. Meshes were generated following the pre-ALA administration procedure and the same homogeneous optical properties were assigned to the domain. Recovered images are presented in Figure 7.4 and do not show fluorescence enhancement in the tumor region. Fluorescence activity is shown to be elevated near the tissue surface in the soft-priors image and a large enhancement is seen well outside the tumor region. The tumor region itself is shown to have a negative contrast in fluorescence activity. The

strict enforcement of region information in the hard-priors image produces a similar general trend. Regions outside the tumor in this image are slightly elevated, while the tumor itself shows decreased fluorescence activity.

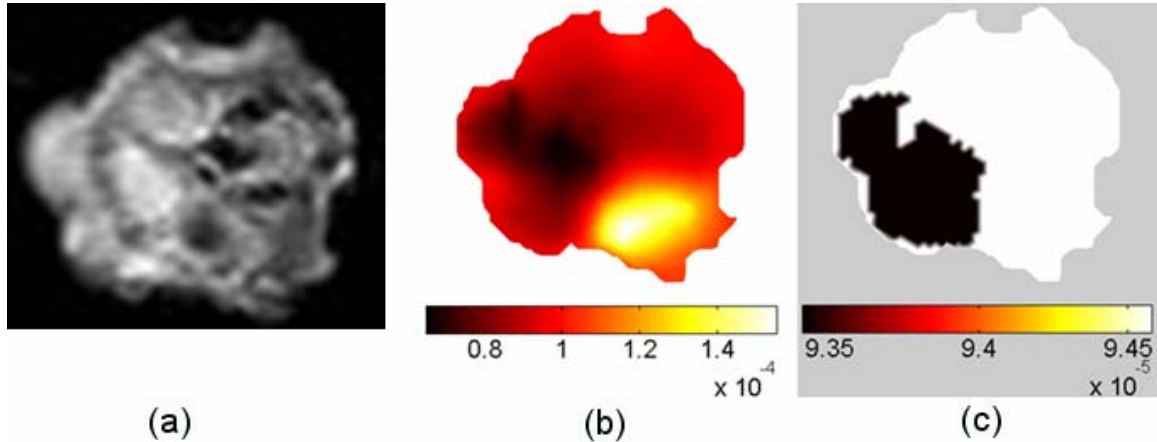


Figure 7.4. The MR image (a) and reconstructed fluorescence activity of PPIX fluorescence two hours after ALA administration using soft priors (b) and hard priors (c).

7.1.3 Summary

The potential deficiencies elucidated in section 7.1.1 for the endogenous PPIX fluorescence images apply in this case as well; however, images of ALA-induced PPIX fluorescence are less promising, though there may well be a biological explanation. Specifically, the results may indicate that the documented ALA-induced PPIX skin fluorescence dominates the image recovery. This is particularly clear in the soft-priors image, where elevated regions of fluorescence surround the interior of the tissue. It is unclear whether the skin is thick enough to impact the image recovery to the extent shown here. Indeed, PPIX skin fluorescence has been shown to influence the sensitivity of transmission fluorescence spectroscopy to murine glioma fluorescence, and skin photobleaching techniques have been developed to address this issue⁹⁶. Similar

techniques may be required for ALA-induced fluorescence tomography; however, this may only be determined after further studies with a more sophisticated imaging array and more confidence in the assignment of optical properties. Also requiring further study is the potential to image endogenous PPIX fluorescence in glioma tumors, as described above, a particularly intriguing and somewhat unexpected result coming out of this preliminary study. Additional PPIX studies were not completed as part of this thesis and therefore are left for future work.

7.2 EGFR imaging feasibility pilot study

The second pilot study is presented as a feasibility experiment to image epidermal growth factor (EGF) uptake in murine gliomas using Licor's IRDye[®] 800CW EGF Optical Probe. Ex-vivo work completed by Summer Gibbs-Strauss provided a convincing case that EGF- targeted dye uptake is high in U251 human glioma tumor cells while little fluorescence contrast is induced in 9-L tumor cells by the Licor probe. This likely indicates a difference in EGFR expression between cell lines.

7.2.1 Methods

The U251 line was selected for this study and 10^6 cells in 10 μ L PBS were implanted intra-cranially in six nude mice. The initial study parameters called for eight nude mice, including two controls; however, problems with the specialized rodent coil pushed back the imaging date and most mice had to be sacrificed due to tumor growth. This resulted in a three-mouse population consisting of one control, one fully developed

tumor visible in MR images, and one mouse with implanted U-251 cells, but no visible tumor in the MR images. Only data from the tumor-bearing mouse is discussed here.

A custom molded mouse bed which fit snugly in the small animal RF coil was designed and built by Summer Gibbs-Strauss and used in this study. Shown in Figure 7.5(b) the mouse bed contains fiber optic access holes to provide positioning of eight spectroscopy fibers around the mouse head.

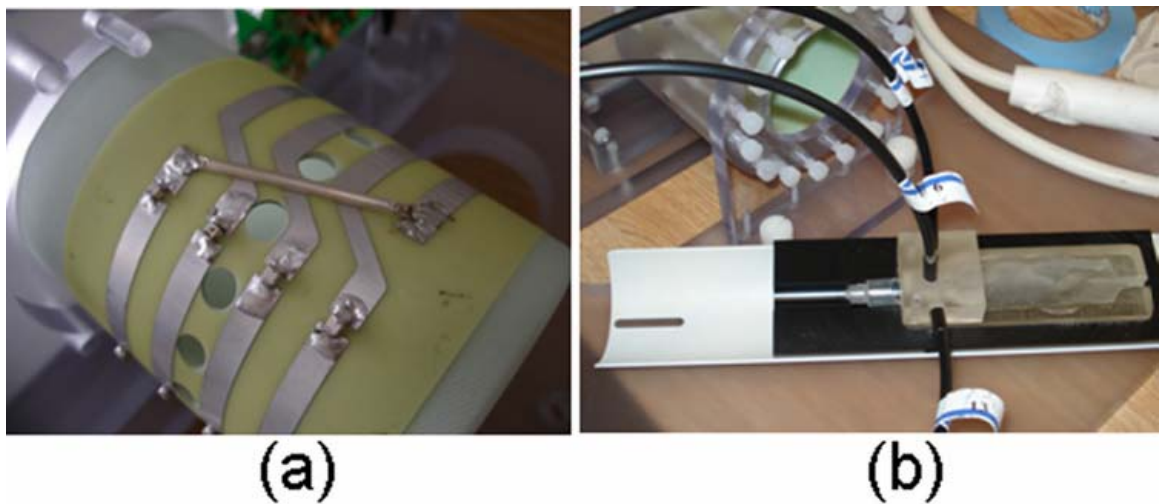


Figure 7.5. (a) Photograph of the coil layout showing access holes for the optical fibers. (b) The custom designed mouse bed accommodates the spectroscopy fiber bundles and fits into the rodent coil for simultaneous MRI and optical acquisition.

Simultaneous gadolinium enhanced MRI and fluorescence tomography acquisition of the population was completed 48 hours after IRDye[®] 800CW EGF Optical Probe injection. Fiber-tissue contact positions were determined from the MR images in reference to MR sensitive fiducials (IZI Medical Products) on the molded mouse bed. For each imaging session, a single coronal slice was segmented into regions using Materialize Mimics software. The example in Figure 7.6 shows an MR coronal slice of the tumor-visible mouse 48 hours after IRDye[®] 800CW EGF Optical Probe

administration and the resulting MR segmentation. The regionized mask was exported as a bitmap file from which a two-dimensional mesh with approximately 2000 nodes was generated for fluorescence reconstruction.

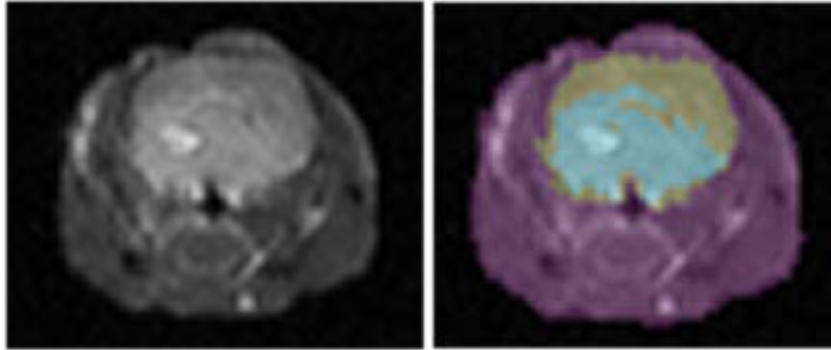


Figure 7.6. The coronal slice from gadolinium enhanced T1-weighted images of a tumor bearing mouse brain (left) is segmented into three regions using MIMICS software, identified by the blue, grey and purple colors in the image at right. The segmented image is used to generate an FEM mesh for spatially-guided fluorescence reconstruction.

7.2.2 Results

The spectral fitting technique described in section 5.2.4 was used to generate integrated intensity values of fluorescence emission from basis spectra of EGF optical probe fluorescence. Reconstructed images with and without the use of hard spatial priors are presented in Figure 7.7. The conventional diffuse tomography approach makes no use of the internal tissue structure, though the outer boundary of the domain is used in this case. Recovered values of fluorescence yield using this approach are highly surface weighted, showing an elevated region of fluorescence activity near the surface of the mouse head, well outside the actual location of the tumor. The diffuse, Gaussian shape of the elevated region is typical of fluorescent molecular tomography imaging without

spatial guidance⁹⁷⁻¹⁰⁴. The use of hard priors in three regions was implemented here. The tumor region outline was given by a region-growing threshold of the enhanced MR image and the fluorescence recovery algorithm estimated the fluorescence uptake in that pre-defined region. Recovered maps of fluorescence yield using the hard priors implementation show an elevated level of fluorescent activity in the tumor region.

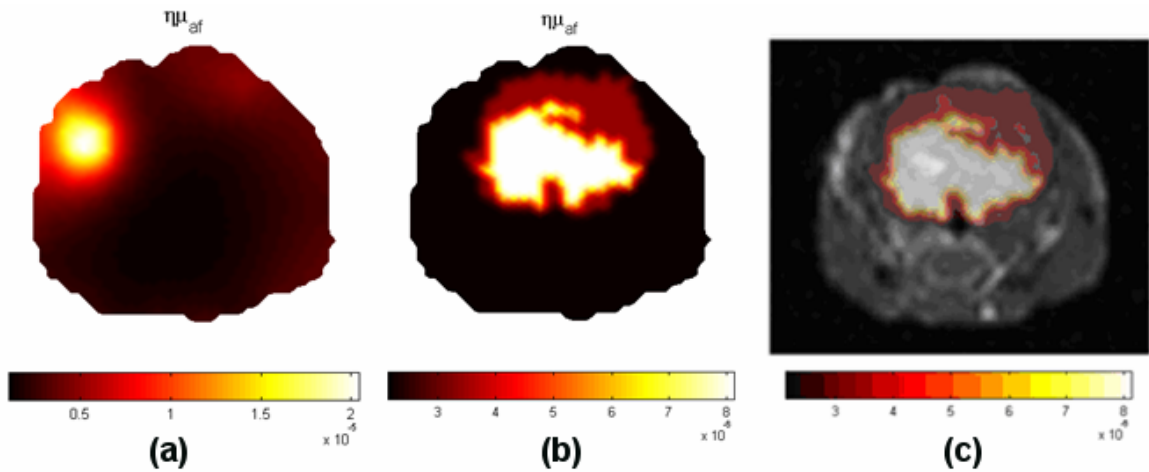


Figure 7.7. Images of fluorescence yield for a tumor-bearing mouse reconstructed using only the outer animal boundary as prior information, (a), and hard priors for the animal exterior, brain and tumor regions (b). An image overlay of (b) on the segmented MR image is shown in (c).

7.2.3 *Ex vivo validation*

Seventy-two hours after drug injection, and thus twenty-four hours after in-vivo imaging, the mouse was sacrificed for ex-vivo scanning. Fresh brain sections were imaged on a Li-COR Odyssey fluorescence scanner prior to fixation and histology preparation. Ex-vivo fluorescence scans and corresponding histology results are shown in Figure 7.8 and indicate a high tumor-to-background uptake of the targeted drug. Fluorescence activity did not correspond precisely to tumor regions of interest in H&E

slides, possibly because fresh slices used for emission scans were considerably thicker than the 4 μm slices used in histology and thus were susceptible to partial volume effects. However, the fluorescence image showing the slice which consisted predominantly of tumor cells (c) closely matched malignant morphology in the corresponding histology slide (f). The other two slices (middle and left) show the tumor mass located at the base of the mouse brain, similar to what was observed in the MR images. This tumor grew into the bone at the base of the brain and parts of it detached from the brain during the post-mortem surgical resection. Thus, comparing tumor-to-normal volumetric ratios determined from reconstructed images and ex-vivo analysis is difficult. However, general location and qualitative comparison of contrasts indicate that the imaging system is indeed sensitive to tissue targeted by the EGF probe.

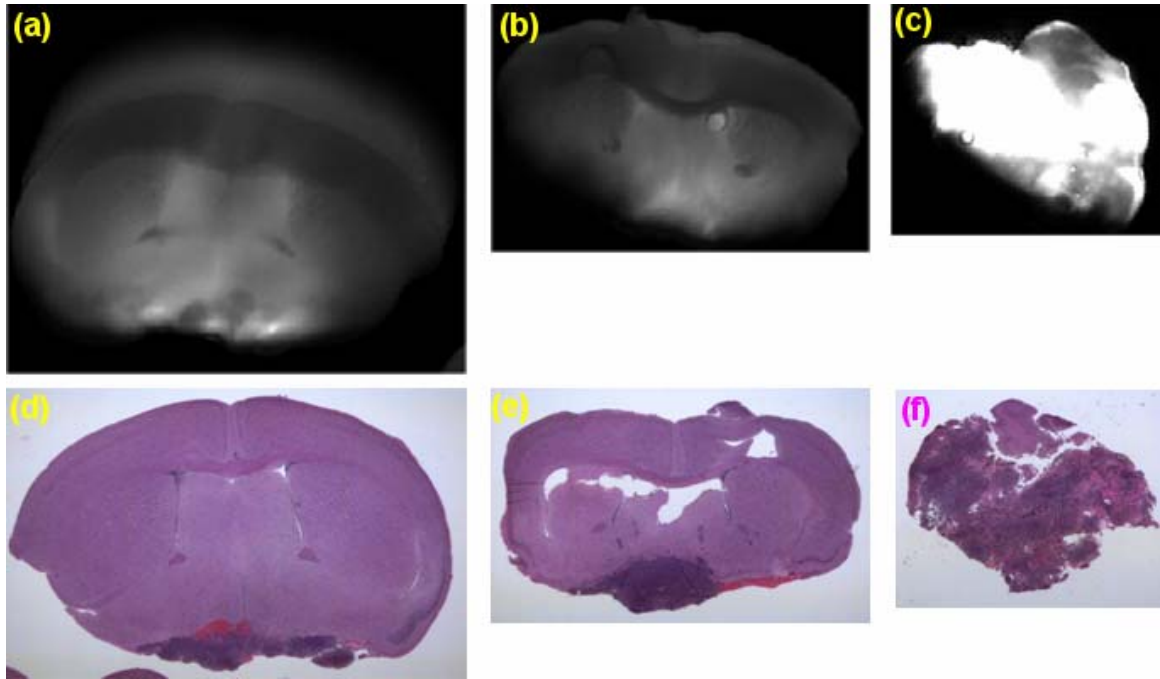


Figure 7.8. Ex-vivo fluorescence scans of fresh tissue sections from the mouse imaged in Figure 7.7 are shown in the top row. Histology slides correspond loosely with the fluorescence images and indicate tumor growth at the base of the brain [(d)-(f)].

7.2.4 Summary

The results of this feasibility study support several preliminary, yet promising conclusions. Ex-vivo and pathology data confirm that the U-251 tumor line yields high tumor-to-background uptake of the EGFR targeted dye. Though not explicitly proven, this implies that the tumor line over-expresses the EGF receptor. It was demonstrated that the emitted fluorescence measured at the boundary of the mouse head can be used to generate images of fluorescence activity *in vivo*, and to that end, MRI information was critical in recovering the accurate spatial distribution of fluorescence yield for this case. Again, this may imply that the system is able to image EGFR expression *in vivo*. To

provide a more substantial and quantitative validation, studies with larger mouse populations were initiated, described in the following chapters.

Chapter Eight: EGF-targeted fluorescence to monitor Erbitux treatment of gliomas in murine models

A treatment response study was designed to investigate the impact of EGFR targeted treatment on brain tumor uptake of IRDye[®] 800CW EGF Optical Probe and to validate the imaging performance of the MR-coupled tomography scanner in small animals. The treatment under investigation was Erbitux, a monoclonal antibody developed by ImClone as a therapeutic agent targeted to over-expression of EGFR. Erbitux molecules have a high affinity for EGF receptors, but upon binding to the receptors, do not catalyze the cell signaling chain leading to increased proliferation and suppressed apoptosis, processes characteristic of malignant cells. Several recent Binding events by EGF, on the other hand, are more likely to trigger this process. Acting as designed, the treatment should slow tumor growth, and make cells more susceptible to other, more toxic therapies^{74-76, 105}.

Based on the reported activation mechanism of the therapeutic molecule, we hypothesized that use of the treatment would reduce EGF probe fluorescence activity *in vivo* in two ways. First, competition for EGFR binding sites between the EGF fluorescent molecules and the monoclonal antibody should reduce the probe binding throughout the animal. Second, overall tumor volumes in treated subjects should be reduced as a consequence of therapeutic disruption of the signaling pathway. These

mechanisms should act together to produce smaller tumor volumes containing lower densities of fluorescent molecules.

Two complications were encountered in the course of this study that precluded a proper imaging validation. The fiber mouse positioning system fabricated for *in vivo* mouse brain imaging provided inadequate tissue-fiber contact and hindered locating the fiber probes in the MRI segmentation process. Additionally, GFP-transfection of the tumor cells altered the biology of the cell line, resulting in aggressive cells that grew diffusely throughout the brain and were not discernable in the MR images. These complications had serious implications for the imaging portion of the study; however, recovery of bulk fluorescence activity was still possible. This single-pixel reconstruction approach was applied to the murine population in this study and differences in recovered fluorescence yield between tumor and control mice were recorded.

8.1 Methods

8.1.1 Mouse preparation and study parameters

To facilitate post-mortem ex-vivo validation of the *in vivo* data, U251 tumor cells were transfected with green fluorescent protein (GFP) using the lipofection technique. This common procedure splices GFP producing DNA into the tumor line nuclei, but also selects for more robust cells which may have biological implications. Since the transfection occurs before the cancer cells are implanted, only tumor cells produce the fluorescent protein. Therefore, GFP fluorescence imaging is 100% specific to diseased areas. Since GFP fluorescence is in the visible wavelength range, light penetration is

poor, and *in vivo* imaging is impractical for all but subcutaneous tumors. However, *ex vivo* sections, such as used here, are easily imaged with commercial scanners.

Nineteen immuno-compromised mice (Charles River) survived to the endpoint of this study. The population was divided into three study arms: untreated, treated, and control. Mice in the untreated (6) and treated (5) arms were implanted with 10^6 GFP-transfected tumor cells (in 10 μ L PBS) via intracranial surgery. The control arm consisted of eight subjects, all of which had intracranial implantation of Phosphate Buffered Solution (PBS) in the same volume as that implanted in the tumor-bearing mice. Tumors were allowed to grow for 23 days before MRI/FMT images were acquired. During this period, mice were scanned in the MRI to check for tumor growth.

Subjects in the treatment arm received 1mg of Erbitux every four days¹⁰⁶ to maintain blood plasma concentration of the drug. Mice in the untreated and control arms received no Erbitux injection. Twenty-one days after tumors were implanted, Licor IRDye[®] 800CW EGF Optical Probe (1 nmole) was administered intravenously (IV) into the tail vein of the mice. The probe incubated for 48 hours before being imaged in the MRI/FMT system. As in the previously described experiment, eight sources and detectors were used for the optical imaging providing a total of 56 source-detector pairs for each animal.

8.1.2 Fiber positioning and MR image segmentation

Data analysis began by segmenting tissue regions and locating the fiber optic probe positions in the MR images using the Mimics software package. The mouse head fiber array introduced in section 7.2.1 and pictured in Figure 8.1 was used for data

acquisition in this study. A modification to the original design introduced four radial holes in the plane of the fiber to accommodate custom MR sensitive fiducial markers. In these studies, the sponge-like material found in commercially available copper sulfate MR fiducials (IZI, Medical Products, Baltimore, MD) was removed from the sealed packages and pressed into the fiducial channels in the mouse holder.

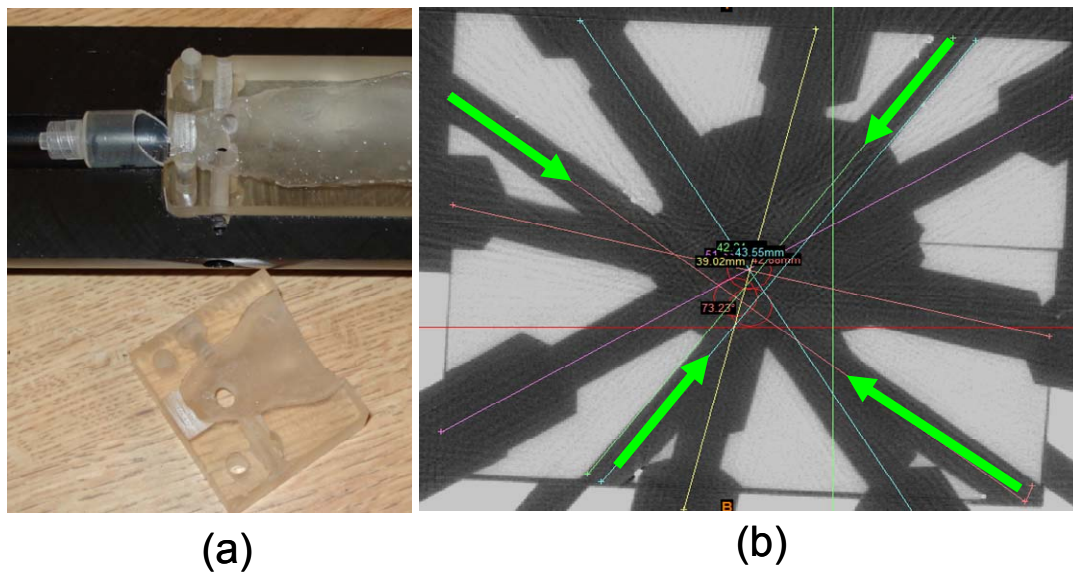


Figure 8.1. The mouse head holder shown in (a) was imaged using a micro-CT scanner, which provides strong contrast between epoxy resin and air (b). Green arrows mark the MRI fiducial channels while the other eight channels accommodate the optical fibers. Clearly, the point of conversion of the fiber array does not match the intersection of the fiducial channels.

The fiber array is arranged in a coronal plane circumscribing the mouse head, and thus the appropriate coronal MR slice was located by referencing the four fiducial branches emanating radially outward from the tissue, as seen in Figure 8.2 (a). These fiducial channels lie in the coronal slice of the fibers. The intersection of the lines drawn through the fiducial signals in the image provides a reference for the center of the circular

fiber array. Unfortunately, this intersection point does not coincide with the intersection of the fibers themselves and therefore, x and y direction translations are necessary to locate the center of the fiber array, a process shown in Figure 8.2 (b). These translations were determined prior to imaging using a micro-CT scan of the mouse holder, shown in Figure 8.1(b). Mimics angle tools were then used to triangulate fiber trajectories and ultimately, tissue contact points (Figure 8.2 (c)). The accuracy of this localizing procedure is questionable. The ill-defined borders of the fiducials make the initial identification of the fiducial intersection point somewhat uncertain, a problem that worsens over the course of an imaging session since the MR signal decreases as the fiducial material dries out. Multiple translations of reference points introduce additional uncertainty. Error in fiber positioning has critical implications for image recovery, an issue addressed in the follow-up to this study, in Chapter 9.

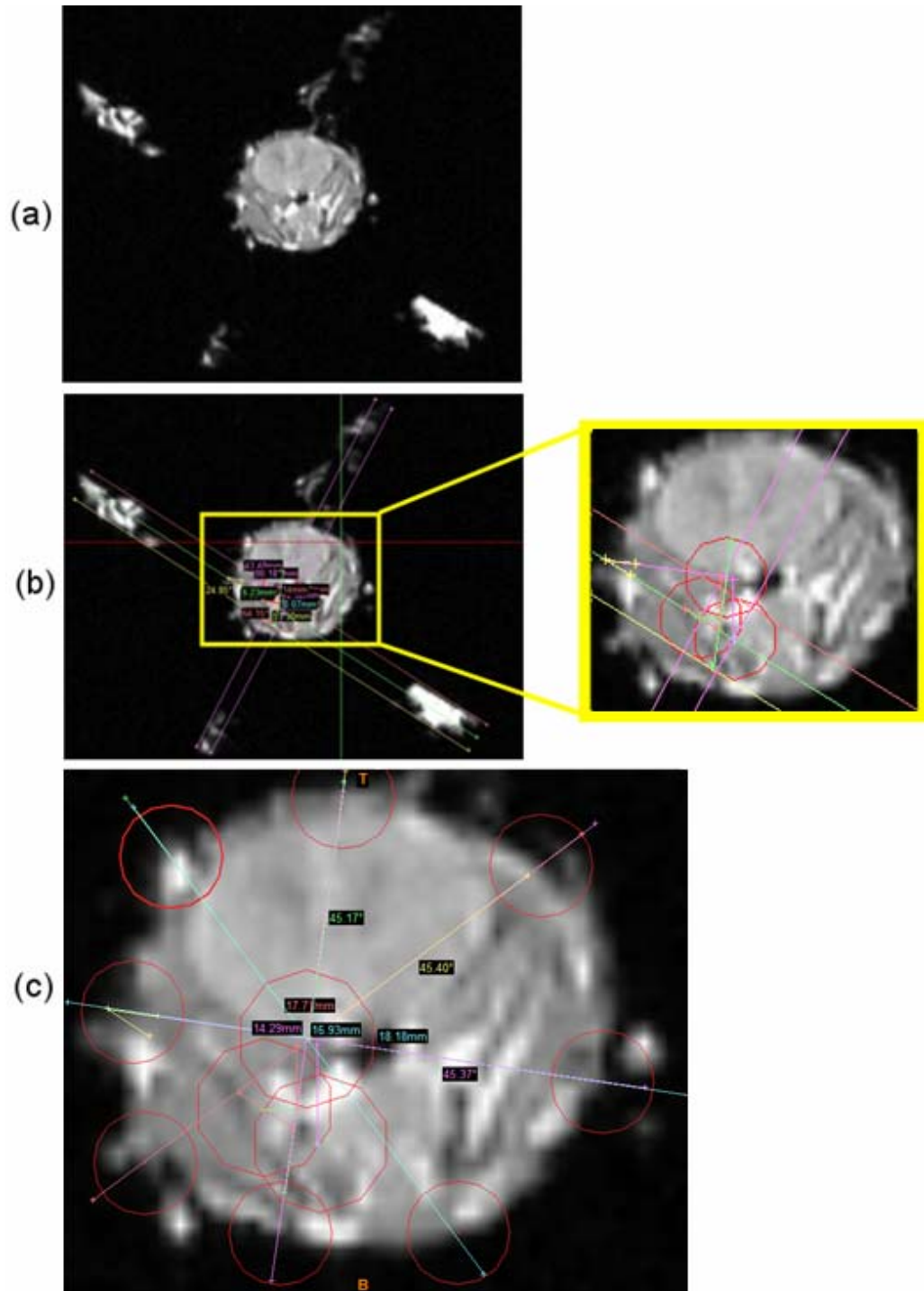


Figure 8.2. Fiber contact points were positioned with reference to MRI fiducial material (a). From the intersection of lines connecting the fiducial signals, linear translations localized the converging point of the optical fibers (b). Referencing this center point and fiducials, the Mimics angle tool was used to mark fiber contact points (c).

8.2 Results and Discussion

8.2.1.1 Absence of visible tumors in the MR images

Coronal MR images of a representative tumor-bearing mouse are presented in Figure 8.3, showing no visible tumor regions. Throughout the course of the study, it became increasingly evident that the physiology of the tumor line eluded imaging using conventional and unconventional MRI sequences. The subjects were observably ill, displaying classic signs of advanced brain cancer, discounting the possibility of unsuccessful intra-cranial surgeries. Previous experience with the U251 tumor line showed reliable enhancement with gadolinium contrast, a trait not observed in this study. Figure 8.3 presents T1 weighted, T2 FLAIR, T1 inversion recovery and T1 weighted contrast enhanced images, none of which provide any evidence of an abnormal mass. Other slices throughout the brain show similar results. Swelling of the ventricles in some of the subjects was the only noticeable abnormality. This could indicate tumor growth in the ventricle space or blockage in the ventricular drainage duct due to tumor growth.

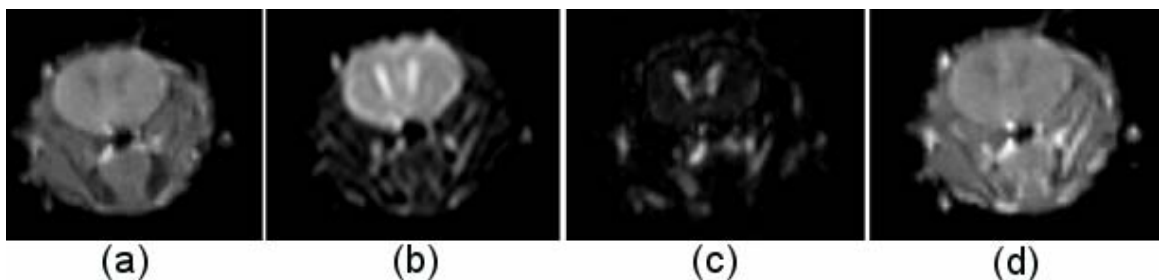


Figure 8.3. Representative coronal MR images of a mouse brain implanted with GFP-transfected U251 tumor cells. Images acquired using the following pulse sequences are shown: T1-weighted turbo spin echo (a), T2 FLAIR (b), T1 inversion recovery (c), and gadolinium enhanced T1 turbo spin echo (c). Some swelling in the ventricles is noted, but no discernable tumor mass.

Ex-vivo analysis of one of the mice shows tumor cells infiltrating the brain, growing in a highly diffuse pattern. Figure 8.4 compares MRI and ex-vivo results for two tumor cell lines. Images for the GFP-transfected U251 line used in this study are provided in (a) and illustrate the diffuse infiltrative nature of the tumor line. GFP fluorescence corresponds to the tumor cells identified in the histology slides. Importantly the tumor region is not identifiable in the MR image, even with the aid of ex-vivo slides. The GFP-transfected 9-L tumor line, on the other hand, produces large tumor masses easily visualized with MRI contrast. Though improbable, it is possible that the blood-brain barrier remains intact with this U251 tumor line, blocking penetration of the relatively large gadolinium delivery molecule. Another possibility is that the absence of a bulk tumor mass limits the per image volumetric concentration of the contrast agent to a regime below MR sensitivity. Other MR sequences, such as diffusion weighted imaging, have been used to try to identify the tumor, with little success. For the purposes of this analysis, the absence of MRI identifiable tumor masses in this mouse population facilitated a re-assessment of the study aims.

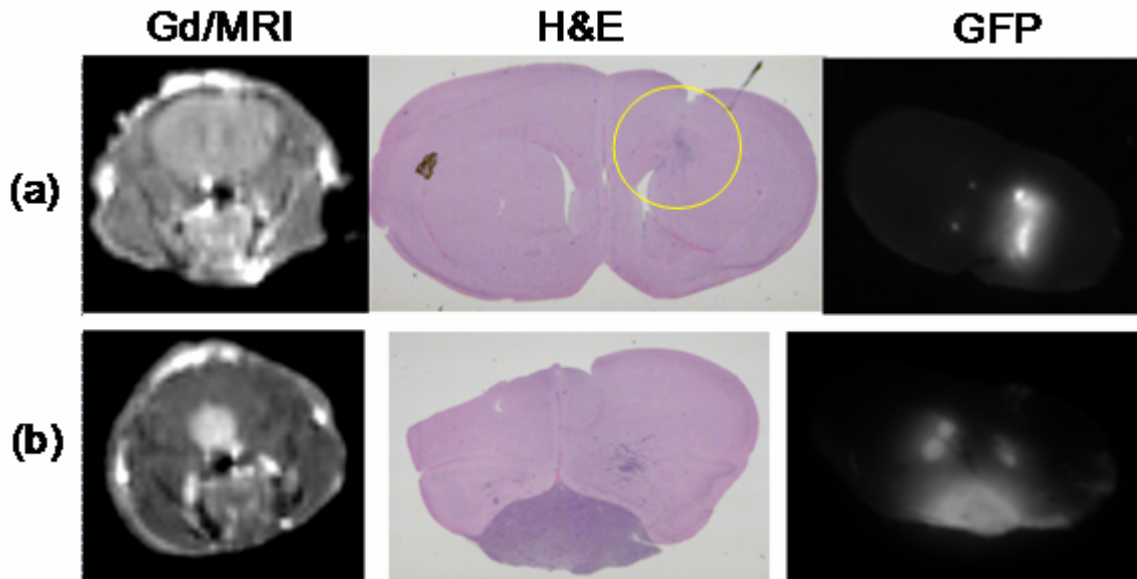


Figure 8.4. Gadolinium enhanced MRI, histology and *ex vivo* GFP fluorescence of two tumor lines. In (a), GFP-transfected tumors used in this study present no MRI enhancement and show up in the histology slides as diffuse, infiltrative sites throughout the brain. For comparison, images for the GFP-transfected 9-L tumor line in (b) show a more conventional tumor model, with a large tumor mass seen easily with MRI contrast enhancement.

An inability to identify tumor regions in the MR image has serious implications for the image guided fluorescence tomography technique under investigation. The objectives of the study were adapted to this reality, and a new focus on image guided bulk fluorescence extraction was adopted. In this approach, the mouse population was analyzed based on results from the homogeneous fitting procedure alone. The procedure still require FEM meshes from the MR images and thus a coronal image of each mouse was segmented into two regions, brain and surrounding tissue, as shown in Figure 8.5. These meshes were then used to produce homogeneous values of fluorescence yield, as described presently.

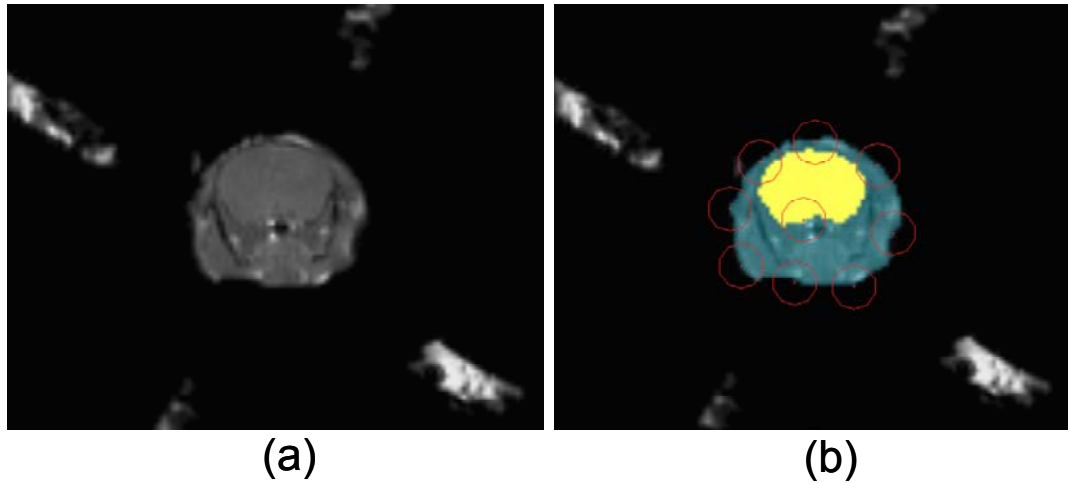


Figure 8.5. An example of a two region segmentation of a gadolinium enhanced T1-weighted image. In this example, the brain is segmented from the surrounding tissue.

8.2.2 Homogeneous fitting

The fluorescence homogeneous fitting routine described in section 5.3 was used to determine bulk values of fluorescence yield in the volume sampled by the optical probes. After the MR images were segmented and transformed into NIRFAST-compatible meshes, tissue optical property values were assigned based on a compiled list of murine tissue properties by van der Zee¹⁰⁷. The brain and suspected tumor regions were all assigned $\mu_{ax} = 0.03 \text{ mm}^{-1}$, $\mu_{sx}' = 2.25 \text{ mm}^{-1}$ at the excitation wavelength and $\mu_{am} = 0.03 \text{ mm}^{-1}$, $\mu_{sm}' = 2.75 \text{ mm}^{-1}$ at the emission wavelength. All other tissue types were assumed homogenous and assigned $\mu_{ax,m} = 0.01 \text{ mm}^{-1}$ and $\mu_{sx,m}' = 1 \text{ mm}^{-1}$ at the exciting and emitting wavelengths. In this manner, the model incorporated heterogeneous optical properties while fluorescence activity was assumed to be homogeneous. The approach is outlined in Figure 8.6.

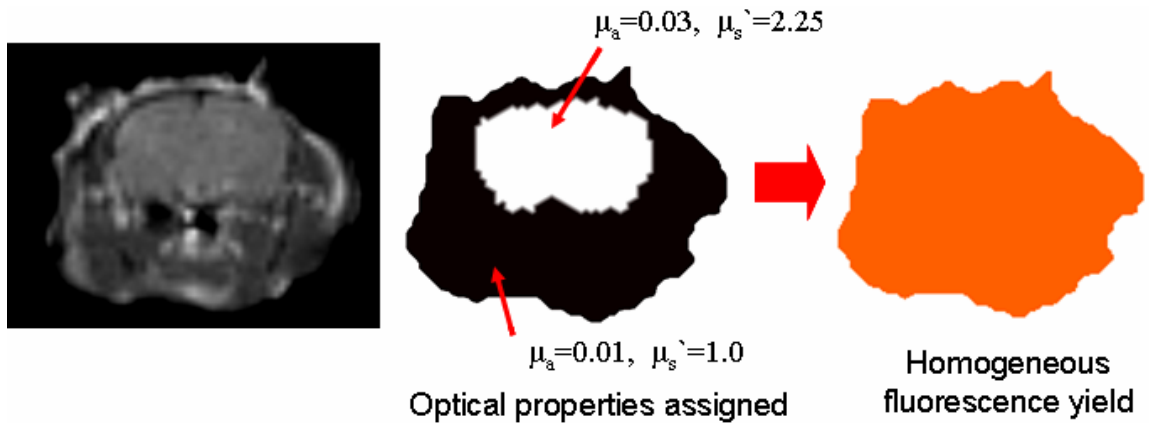


Figure 8.6. A diagram outlining the procedure for homogeneous fitting. MR images were segmented into 2 regions: brain and surrounding tissue. Optical properties were then assigned based on literature values. Using these properties, a single pixel reconstruction provided a homogeneous fit of fluorescence yield to the measured data.

Examples of the data-model mismatch for homogeneous fits are presented in Figure 8.7 for mice in the control (a), treated (b), and untreated [(c) and (d)] arms of the study. These graphs show the measured data as well as data generated using the model for a homogeneous value of fluorescence activity, as determined by the fitting algorithm. These values were analyzed with common statistical tools to compare fluorescence activity between study arms.

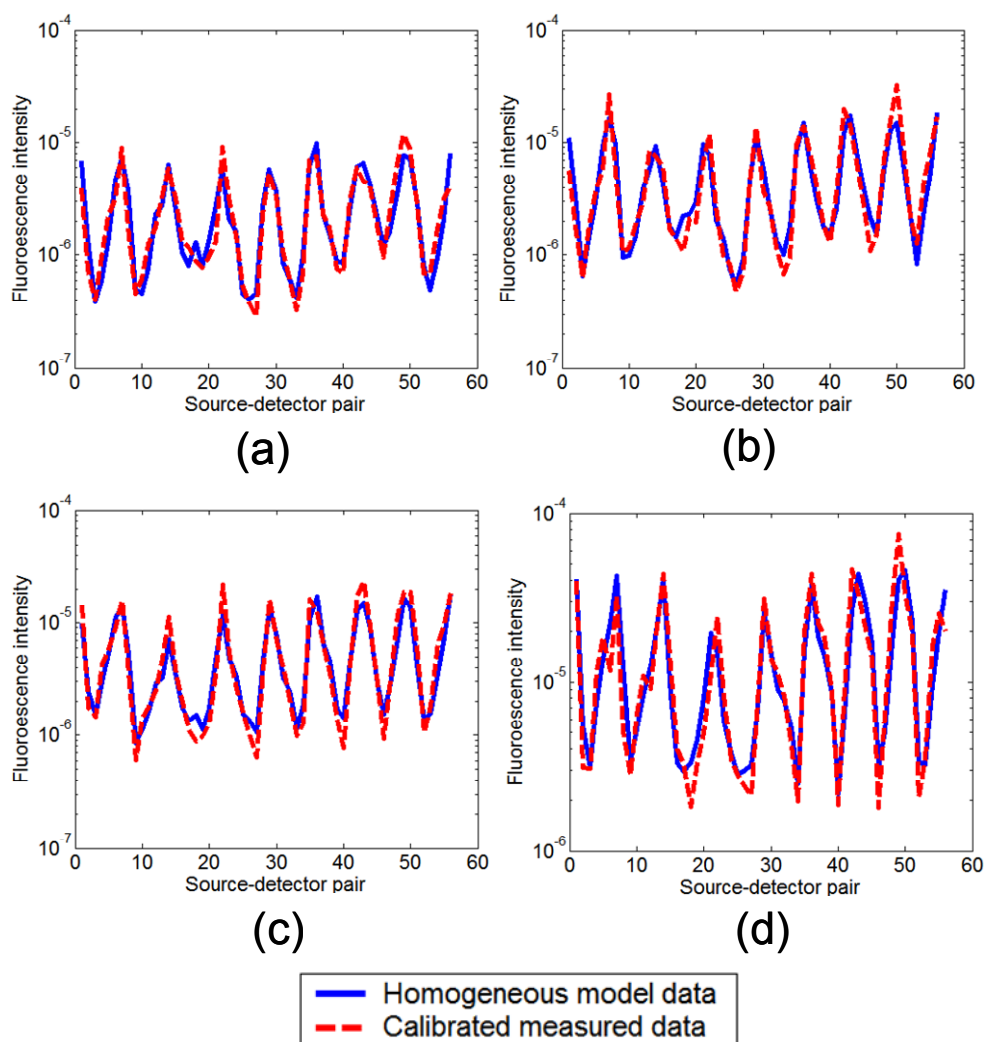


Figure 8.7. Data-model mismatch for homogeneous fits of fluorescence yield plotted for individual subjects in the control (a), treated (b), and untreated [(c) and (d)] study arms.

Bulk values of fluorescence yield for the entire mouse population are presented in Figure 8.8. These results show a clear difference between the medians of the control and tumor-bearing subjects. A difference between treated and untreated arms is less obvious. Interestingly, the variability between subjects is higher for tumor-bearing mice, particularly untreated animals, than controls. This may be due to biological variability,

either in tumor growth or drug uptake. Additionally, fiber array positioning with respect to the malignant cells may also be a factor contributing to the larger data spread in the untreated arm. Since malignant regions could not be identified in the MR images, the fiber array could not be positioned to ensure the optically sampled volume included tumor tissue. The location of fluorescent tissue with respect to the fiber array has a significant influence on the measured intensity, and therefore recovered fluorescence yield. This clearly is not an issue for cancer-free control arm subjects which, not coincidentally, show much lower inter-subject variance. The large differences in variance impacts the statistical significance of the differences between arms.

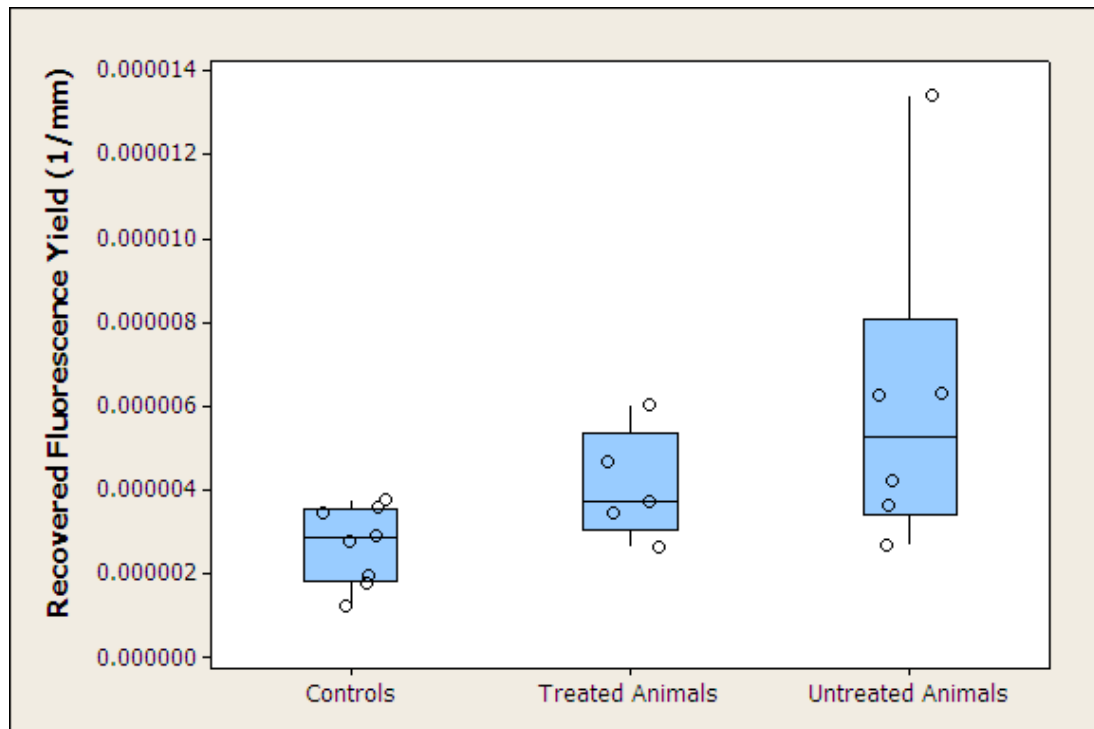


Figure 8.8. Box-and-whisker plots show the median and inter-quartile of the fluorescence yield recovered using homogeneous fitting.

Fluorescence yield results were compared between study arms using the one-tailed heteroscedastic Student's t-test. These values are reported in Table 8.1 and show statistical significance between any and all arms vs. the control group. This is an important result, confirming that the EGF probe is specific to malignant cells *in vivo* and demonstrating that the system is sensitive to the drug uptake, even for bulk fluorescence measurements. That the p-value is lower between the control vs. treated than control vs. untreated groups is a result of the higher variance among the untreated subjects.

Table 8.1. Student's t-tests between population arms. *Statistical significance is reported for $p < 0.05$.

Population Arms	p-value
Control / Untreated	0.042 *
Control / Treated	0.037 *
Treated / Untreated	0.140
All tumor bearing / Control	0.012 *

The variance in the untreated group may also have contributed to the failure to achieve a statistical difference between treated and untreated arms, though this will only be confirmed with larger population studies. Certainly, biological explanations cannot be ruled out. Possibilities include ineffective treatment, non-specific antibody binding, or more complicated biological processes. A binding event triggers receptor internalization of itself and the bound molecule. It is unclear whether the receptor remains in the cell or is recycled to the cell surface^{74, 108, 109}. The latter possibilities would mitigate expected

decreases in fluorescence activity due to treatment. Future studies may examine these more complex possibilities.

8.2.3 Image reconstruction

Despite problems with the optical fiber array and identification of tumor masses in the MR images, a more extensive analysis of the optical data's content was accomplished by reconstructing images with the available data. Data for all subjects were reconstructed using a two-region spatial-hard-priors approach as well as a no-prior approach, save for the outer boundary. The two-region fit can be thought of as a step up from the single-region fit described above. Presuming imaging geometry is correct and tumor fluorescence is localized in the brain, one would expect positive image contrast of fluorescence yield between the brain and surrounding tissue area. Given the strict application of the spatial information, the quantitative value will be averaged over the region's area; however, brain-to-background contrast would be a promising sign that the data contains some tumor localization information. If that were true, the corresponding images reconstructed with the no priors approach should show similar trends of elevated fluorescence activity toward the top of the mouse head.

Representative images for mice in the control (a), treated (b) and untreated (c) arms are presented in Figure 8.9 and show no propensity toward elevated fluorescence activity in the brain region. This discouraging result is not entirely unexpected, given the issues involving fiber contact reported earlier. The hard priors images show higher levels of fluorescence yield outside of the brain while full reconstructions indicate a consistent pull to the lower-right of the imaging domain. This was observed in most subjects

analyzed. Interestingly, the maximum image intensity is highest for the untreated mouse, but the lack of localization in the brain region undermines any confidence that the data contains spatially relevant information.

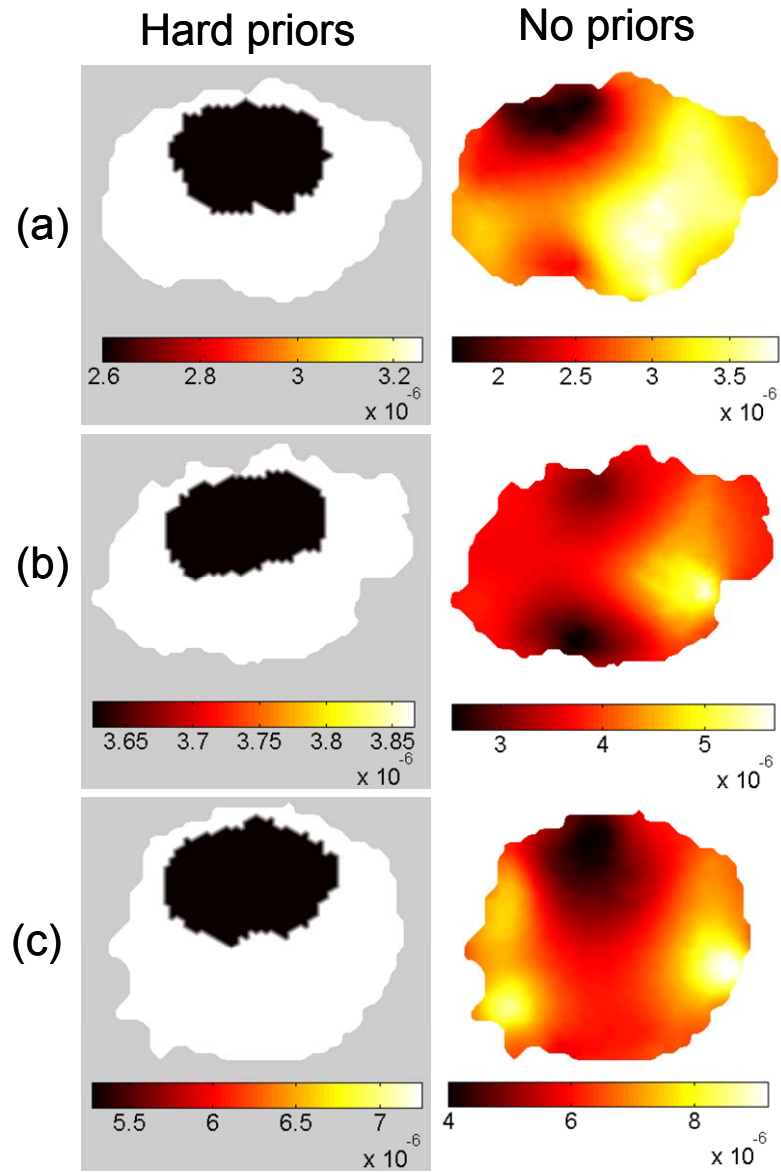


Figure 8.9. Images of fluorescence yield recovered using two reconstruction techniques, namely two-region hard priors and no priors. Images are representative of the control (a), treated (b) and untreated (c) population arms.

Hot spots near the edge of the image usually indicate fiber coupling errors. The consistency of these artifacts between subjects suggests that baseline readings from control mice might be used to account for these errors during calibration. To explain this, mean values for each source-detector pair recorded on the control mice were subtracted from each data set using,

$$\phi_{calibII} = \ln(\phi_{het}) - \ln(\phi_{contr_mean}) + \ln(\phi_{model_homog}) \quad \mathbf{8.1}$$

Several other formulations were attempted; however, little improvement was observed in the resulting images. Images of tumor-bearing mice continued to show higher fluorescence activity outside of the brain region with hard-prior reconstructions, while edge artifacts were common in the no-priors images. It is clear from these results that a new approach to fiber coupling is critical for successful small animal imaging.

8.3 Summary

Image guided single-pixel fluorescence spectroscopy of U251 gliomas using the EGF targeted probe and MR-FMT system proved sensitive to the presence of malignant tissue *in vivo*. The calculated p-value between tumor and control mice was 0.012 when all tumor-bearing mice were group together. These values decreased when individual arms were compared to one another, though both treated and untreated arms were significantly different from controls. Statistical differences were not found between treated and untreated arms, though it is unclear if this is due to system uncertainty or biological mechanisms.

The imaging component of the study was unsuccessful. An inadequate fiber array made fiber-tissue contact questionable. Gaps between fiber probes and the tissue surface

provide favorable conditions for stray light contamination in detection channels and introduce large data-model misfit errors since free-space propagation is not part of the model system. Poorly integrated MR fiducial references introduced significant uncertainty when localizing fiber positions in the MR image.

The biological transformation of U251 cells which led to MR invisibility further confounded the study objectives. It is possible that the GFP lipofection process, which inherently selects for more hearty cells, produced a more aggressive cell line with infiltrative growth characteristics. To address this, a simpler imaging validation study using the parent tumor line was initiated.

Chapter Nine: Imaging of MR-detectable U-251 tumors using fluorescent EGF Probe

Results from the large scale Erbitux study revealed two impediments to a successful imaging experiment, one biological and the other mechanical, both of which are addressed directly in this follow-up validation study. GFP-transfection of the U251 tumor line altered the physiology of the cells, producing a phenotype not readily detectable with conventional MR. This in itself is an intriguing result which was investigated further as part of Summer Gibbs-Strauss' thesis¹¹⁰; however, the unconventional behavior of the tumor model impeded the validation of the MRI-guided fluorescence tomography scanner *in vivo*. For the current study, this issue was designed out of the experimental protocol by using the parent U251 tumor cell line, which is known to grow in large masses which enhance readily with Gd-MRI contrast. Another addressable concern involved the hardware design of the animal interface. It became increasingly clear that the molded mouse bed was inadequate for imaging purposes due to uncertainty in fiber-tissue contact and difficulty locating fiber positions in the corresponding MR images. A full re-design of the fiber positioning system was completed for the current study. Unlike the previous animal experiments, the study presented here was designed specifically for the validation of the system as an imaging apparatus.

9.1 Methods

9.1.1 Mouse preparation

Fourteen nude mice were prepared for this study, six controls and eight tumor-bearing mice. One million cells in 10 μ L PBS U251 cells were implanted intra-cranially in the eight tumor mice, while sham surgeries were performed on all controls. Based on past experience, the imaging sessions were scheduled for 23 days after surgery; however, five tumor-bearing mice past away several days before the scheduled imaging session due to advanced disease. This unfortunate miscalculation reduced the diseased population to three mice, one of which showed no sign of tumor mass in MRI scans. Therefore, only two tumor-bearing mice were included in the analysis here.

Except in one case, all mice received IV injection of the EGF dye (1 nmole) 48 hours before image acquisition, the exception being an imaging session for each of the tumor-bearing mice before drug administration. Optical acquisition time was around 15 minutes, and fit easily into the 30 to 40 minute MRI acquisition procedure. In some cases, mice were re-positioned after a scout scan to ensure tumor and brain regions were sampled properly with the fiber array, extending total acquisition time slightly.

9.1.2 Fiber positioning and MR Image segmentation

The annulus-shaped fiducials provided a reliable reference for positioning fibers in the MR image. The coronal slice corresponding to the fiber plane was easily identified by determining which slice showed the largest gap between the visible sides of each fiducial. Indents in the tissue also helped locate the appropriate plane. If necessary,

software may be used to re-slice image stacks, however, this was avoided by carefully orienting MR image slices during the acquisition protocol.

After selecting the proper plane, geometric tools part of the Mimics software package were used to position the fiber contact points. The first step was to locate the center of the fiber optic array, accomplished by drawing lines connecting the inner annuli of diametrically opposed fiducials, as shown in Figure 9.1(a). Lines were then drawn between each existing pair of lines. The intersection of these lines represents the center of the circular fiber array. Angular spacing between each fiber bundle is exactly 22.5 degrees from the center of the fiducial. The geometrical angle tool in Mimics was used to position the fiber-tissue contact points.

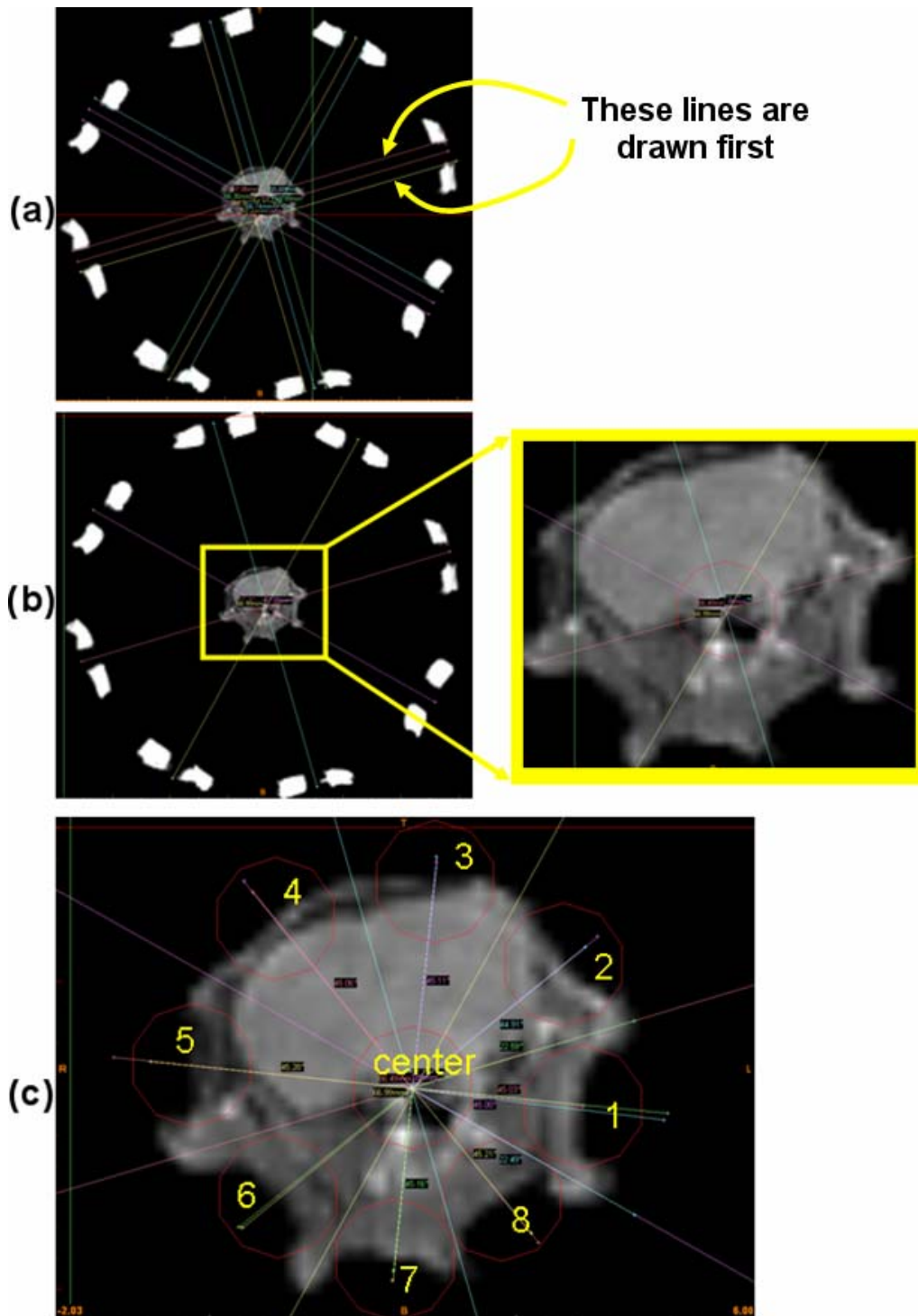


Figure 9.1. Using the fiducial markers as guides in Mimics software, lines were drawn connecting the inner surfaces of diametrically opposed fiducials (a). After four pairs were drawn, additional lines between and parallel to each existing pair are drawn. The outer lines may be removed to simplify the image and the

intersection of the remaining lines identifies the center of the circular fiber array (b). Finally, the angle tool was used to locate the fiber contact points around the head (c).

Once fiber positions were located and exported, the problem of segmenting tissue regions was addressed. Mimics software offers several automatic and manual tools for segmenting imported images. Typically, the first region was defined using a threshold and was adjusted to include the entire tissue domain. Given the variation in intensity within the imaged tissue, manual manipulation of the segmented region was required. Next, region growing tools were used to determine brain and tumor regions, again with manual adjustments to the region. Upon completing the image segmentation process, the viewing style was changed to a binary mask and exported as a bitmap image, shown in Figure 9.2. If the mask had more than three regions, Boolean operations were used to ensure all regions were visible in the bitmap image.

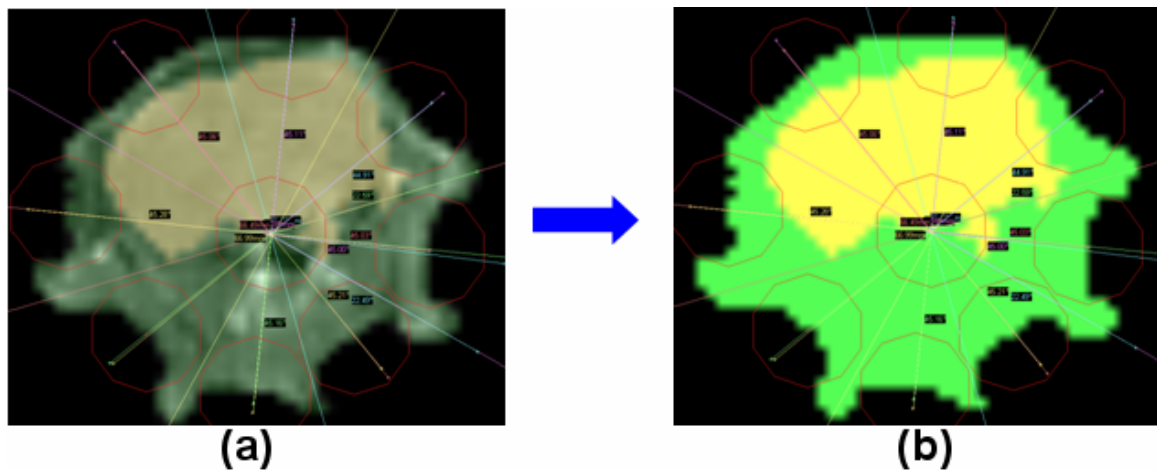


Figure 9.2. Simple segmentation using Mimics for the mouse head and brain regions (a). Region information was exported as a binary bitmap image (b).

9.1.3 Confirmation of tumor-detection in MR images

Two tumor-bearing mice survived through the imaging date and were imaged with MRI-FMT before dye administration and 48 h after the IV injection. Survey scans were used to ensure a suspicious area was in the plane of the fiber array, often requiring re-positioning the mouse in the fiber array. T1-weighted coronal images with (a) and without (b) gadolinium contrast as well as T2-weighted images (c) for one mouse are shown in Figure 9.3. Each row represents images from different MRI sequences of the same volume. Slice thickness and spacing were identical for all scans shown. The plane of the fiber array is boxed in blue. Gadolinium circulated between 5 and 10 minutes before the contrast enhanced sequence was initiated. The dark region in the T1 weighted images corresponds to high image intensity in the T2 weighted images, likely indicating edema. Gadolinium enhancement is seen near the center of the brain in the first three anterior images (b), however, this region is clearly beyond the plane of the fiber array.

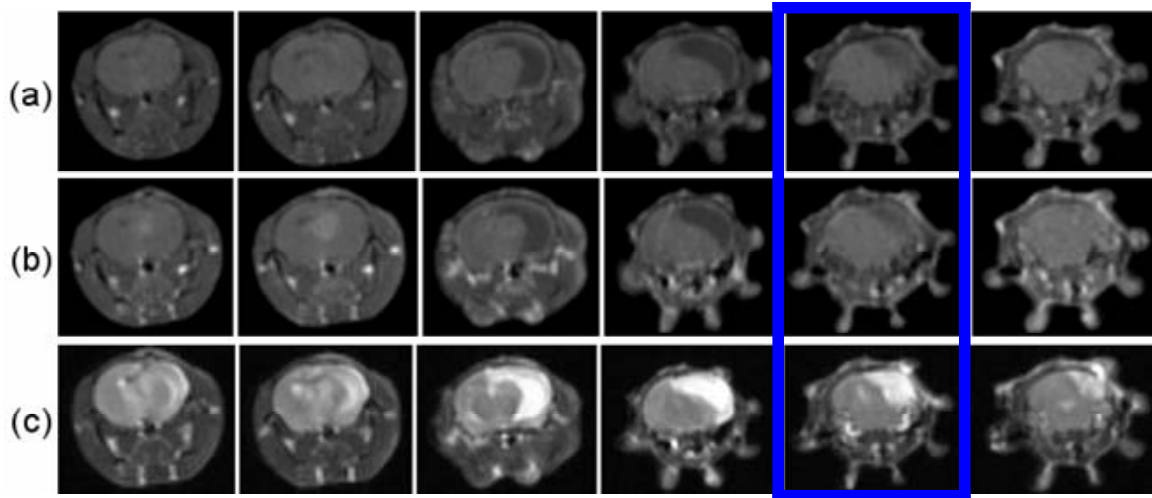


Figure 9.3. MRI coronal image series of a murine head bearing a large glioma grown from intracranial implantation of the U251 tumor line. Each column shows the same volume slice for different sequences: (a) T1-weighted TSE without contrast, (b) T1-weighted TSE with contrast, and (c) T2-weighted.

A similar collection of images for the second tumor-bearing mouse is presented in Figure 9.4. The T1-weighted images without contrast, (a), show a similar dark region of possible edema corresponding to high T2 signal. However, gadolinium penetration in this mouse was far more extensive and the classic ring enhancement is obvious. This pattern typically indicates severe blood-brain barrier breakdown with leaky vessels encircling a poorly perfused, possibly necrotic mass. Significantly, the fiber plane intersects both enhanced and dark areas in the MR image. These regions were segmented into separate regions for optical image reconstruction.

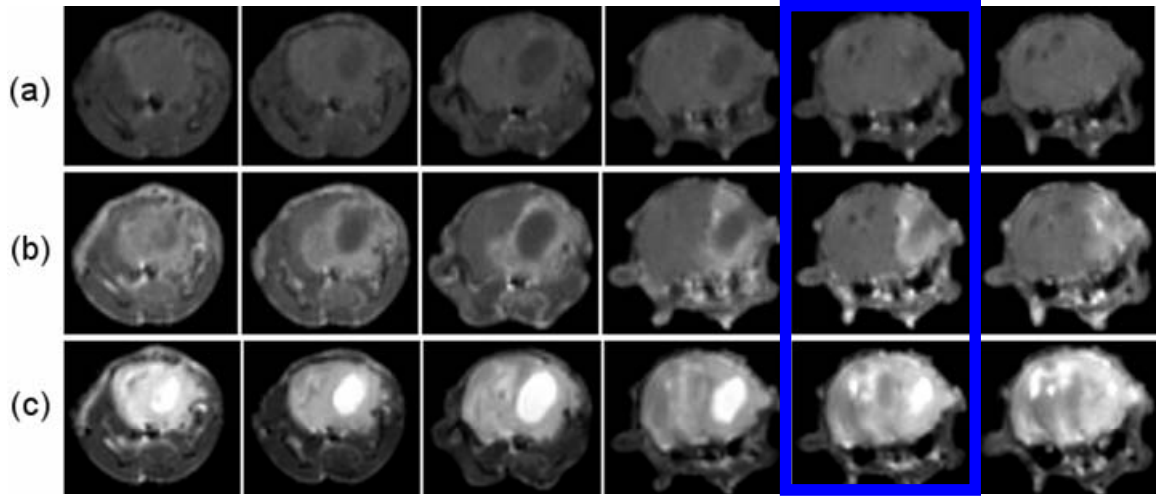


Figure 9.4. MRI coronal image series' of a murine head bearing a large glioma grown from intracranial implantation of the U251 tumor line. Each column shows the same volume slice for different sequences; (a) T1-weighted TSE without contrast, (b) T1-weighted TSE with contrast, and (c) T2-weighted.

For each mouse, the Gd-enhanced MR image in the fiber plane was segmented into three or four regions as defined from MR image contrast: 1) normal brain, 2) suspected necrosis or edema, 3) suspected malignant region/Gd-contrast enhancement (if visible in image), and 4) all other tissue. Coronal images and corresponding segmentations are shown in Figure 9.5. Once segmented, 2100 node meshes compatible with the NIRFAST software were generated. Optical property values were assigned from a compiled list of optical properties by van der Zee¹⁰⁷. In this case, the brain and suspected tumor regions were all assigned $\mu_{ax} = 0.03 \text{ mm}^{-1}$, $\mu_{sx}' = 2.25 \text{ mm}^{-1}$ at the excitation wavelength and $\mu_{am} = 0.03 \text{ mm}^{-1}$, $\mu_{sm}' = 2.75 \text{ mm}^{-1}$ at the emission wavelength. All other tissue types were assumed homogenous and assigned $\mu_{ax,m} = 0.01 \text{ mm}^{-1}$ and $\mu_{sx,m}' = 1 \text{ mm}^{-1}$ at the exciting and emitting wavelengths. Homogeneous

estimates of fluorescence yield were determined using the bisection method outlined in section 5.3.

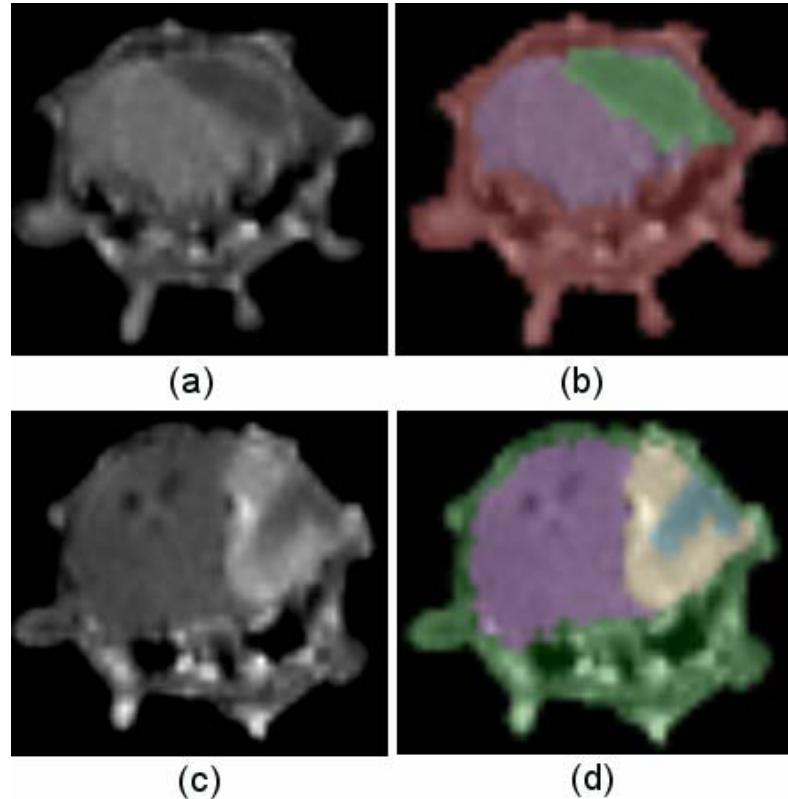


Figure 9.5. Gd-enhanced coronal slices of the two tumor-bearing mice (a) and (c) were segmented into regions shown in (b) and (d), respectively. In (b), three regions delineate brain, edema, and all other tissue. In addition to those three regions, Gd enhancement in (c) was also segmented as a fourth region in (d).

9.2 Results

9.2.1 Homogenous fitting results and discussion

After segmentation and source-detector position files were exported, Matlab routines were used to generate a 2-D mesh for image reconstruction, calibrate the fluorescence data, and compute a homogeneous fit of the fluorescence yield that best fit the calibrated data. Figure 9.6 shows MR images of the control mice and the

corresponding homogeneous fits of the data. It is clear that the calibrated data matches the homogeneous model data well for mice that survived and remained in the RF coil positioning system. Marked deviations from the homogeneous fits were observed for two mice, one of which moved during data acquisition and one of which did not survive the image acquisition.

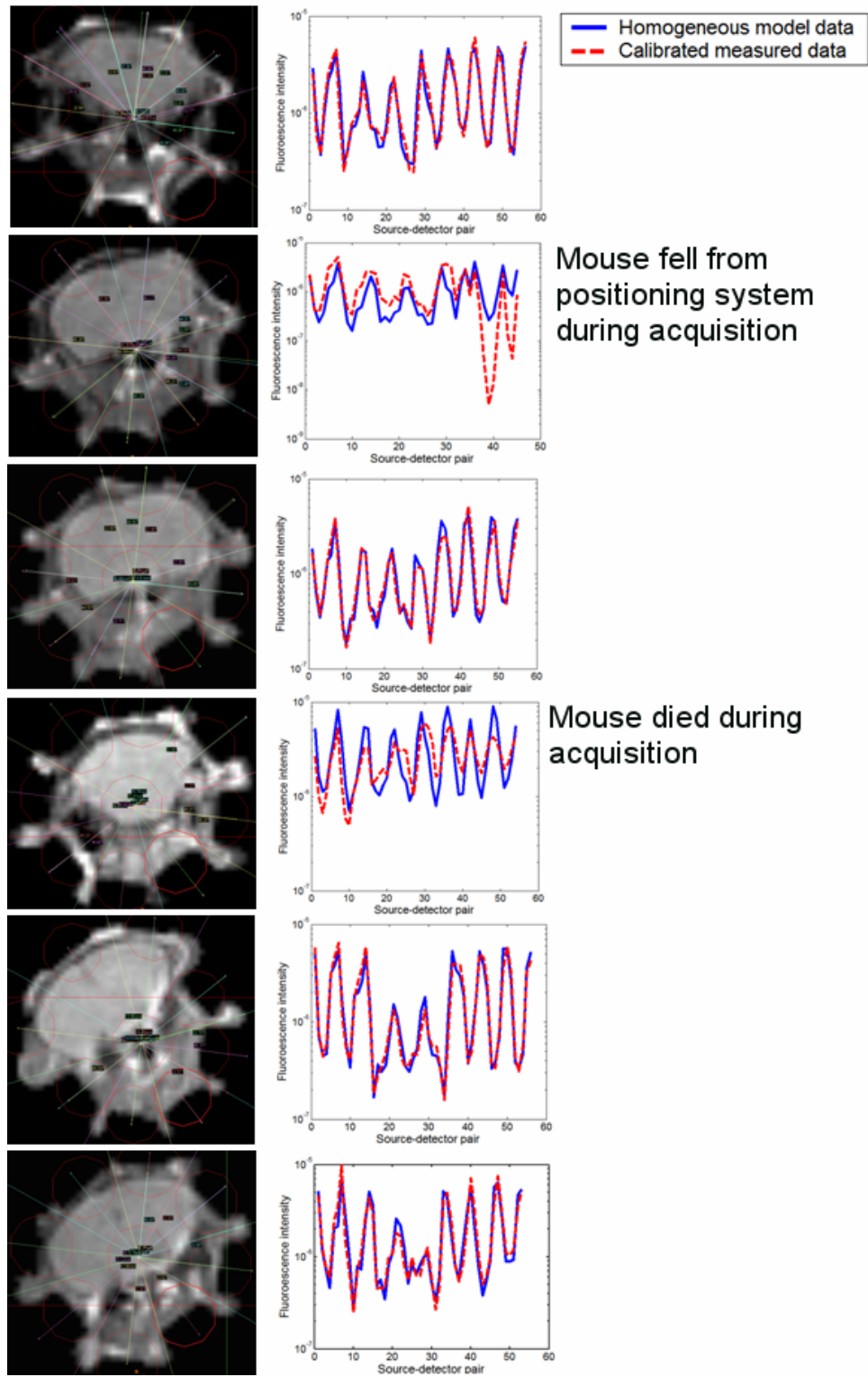


Figure 9.6. MR images (left) and homogeneously fit data (right) for the 6 control animals injected with IRDye[®] 800CW EGF Optical Probe.

Homogeneous fits of the data for the tumor-bearing mice are shown in Figure 9.7. The two mice were imaged prior to optical probe administration (a) and (b), and 48 hours after injection (c) and (d). Besides auto-fluorescence, little to no evidence of a fluorescent peak could be discerned in data acquired prior to probe administration. In many cases, a slight negative fluorescence peak provided the best fit to the spectral data based on the spectral fitting routine. These data points imply a lack of fluorescent signal and should not be ignored. In this case, negative fluorescence intensity values were assumed to indicate negligible fluorescence and a value of 10^{-20} counts/s was assigned to these data points. This clearly influences the homogeneous fitting routine, facilitating particularly poor fits. Data measured at the 48 h post-injection time point, on the other hand, portray much higher levels of fluorescence intensity and the homogeneous fit data matches the real data reasonably well.

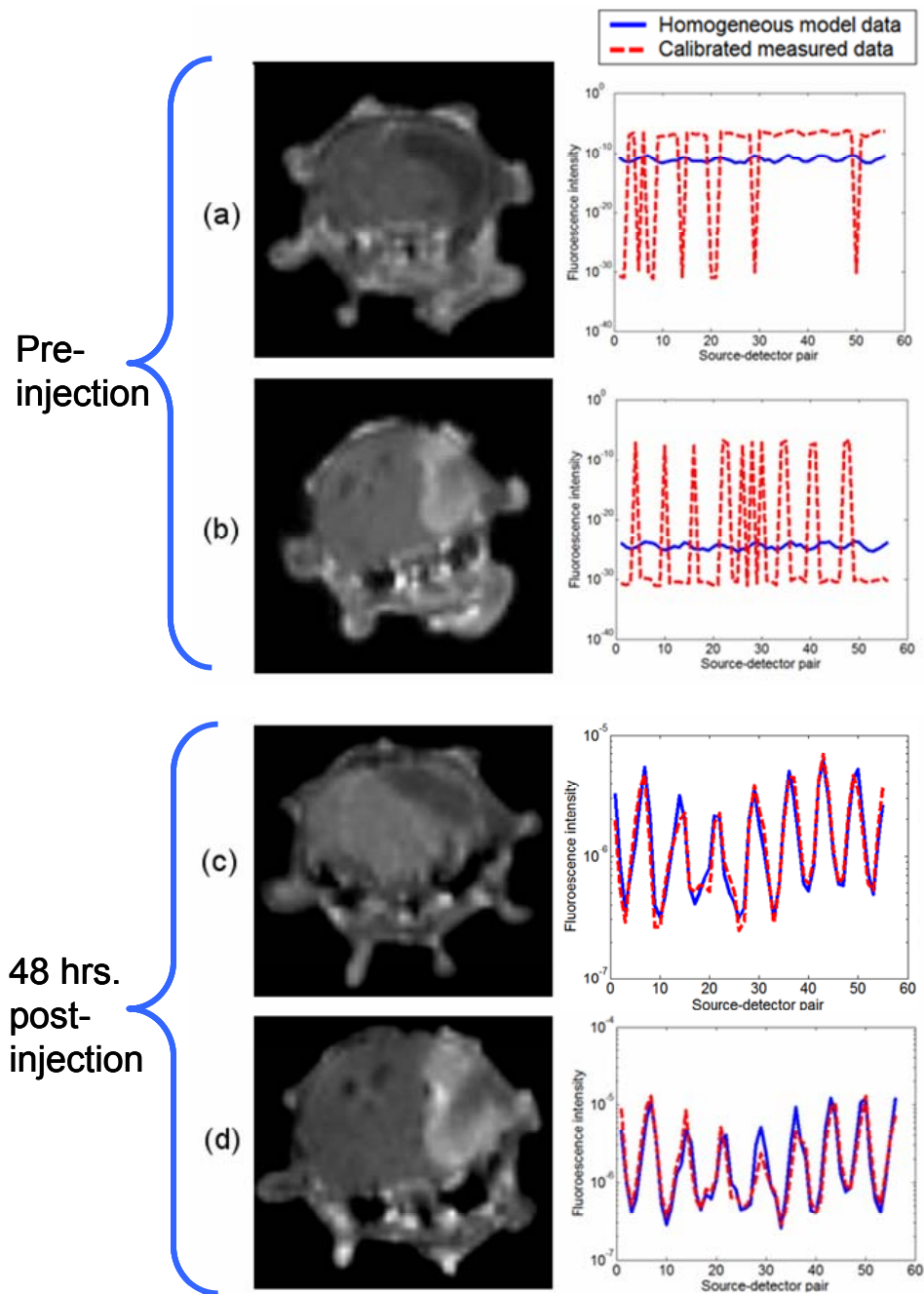


Figure 9.7. MR images and homogeneously fit data for two tumor-bearing mice. Data for each mouse is provided before, (a) and (b), and 48 hours after IRDye[®] 800CW EGF Optical Probe administration, (c) and (d).

Examining the homogeneous fit values and the data-model mismatch error between calibrated and model data generated for a homogeneous value of fluorescence yield, presented in Table 9.1, reveals interesting and promising trends. Data-model mismatch was calculated as the sum of the squared error between calibrated data and homogeneous model data. Given the small number of mice in the tumor group, few concrete conclusions can be drawn beyond anecdotal observations. These observations are, however, consistent with expectations. Fits for mice not injected with the optical probe are well below values for all other cases, for reasons discussed above. These values may eventually prove to be diagnostic contingent upon the results of a larger population mouse study, but for now, these results are noted, but excluded from the present discussion.

Data associated with two control mice produce relatively high data-model mismatch error, as shown in red in Table 5.1. Both anomalies are easily explained; one mouse died during image acquisition and the other fell from the mouse positioning system. Both data sets were therefore excluded from further analysis. Interestingly, the errors for all other control mice show relatively little variance (14% of mean) and are consistently under 3.1, while data for the mouse with a large Gd-MRI enhanced tumor visible in the plane of the fiber array deviate more substantially from the associated homogeneous fit, with an error of 8.5. Ignoring data for mice not injected with the optical probe, this mouse produced the highest mismatch error, as would be expected. The homogeneous fit to this data was also 90% higher than the next highest homogeneous fluorescence yield calculation. The tumor-bearing mouse which contained Gd-MRI enhancement outside the fiber plane produced a homogeneous fit value well

within the range of the control mice, though at 3.4, the error of the fit was slightly larger than the control mice. Despite the small populations, diagnostic information appears to reside in the homogeneous fit values and the associated data-model mismatch error. Larger mouse populations may eventually confirm this initial impression. For now, we will consider the imaging problem; whether recovered images of fluorescence yield are reasonable and provide additional contrast between mouse populations in this study.

Table 9.1. Homogeneous fit values of fluorescence yield

Population Arm	Homogeneous Fit Fluorescence Yield (10^{-6} mm^{-1})	Data-model mismatch error	Comments
Control Mice (Dye injected)	1.61×10^{-6}	2.79	
	1.25×10^{-6}	66.82	Fell from mouse bed during acquisition
	1.37×10^{-6}	2.28	
	2.91×10^{-6}	12.67	Died during acquisition
	1.71×10^{-6}	2.34	
Tumor-bearing mice (Dye injected)	2.32×10^{-6}	3.09	
	1.91×10^{-6}	3.39	No Gd. Enhancement in fiber plane
	4.42×10^{-6}	8.54	Gd. enhancement in fiber plane
Tumor-bearing mice (No dye injected)	1.46×10^{-11}	2.55×10^4	
	6.83×10^{-25}	3.07×10^4	

9.2.2 Image recovery results and discussion

Homogeneous values of fluorescence yield reported in Table 9.1 provided the initial estimate for fluorescence yield image reconstructions. Images were recovered using three algorithmic approaches which incorporate the MRI information: Soft spatial priors, hard spatial priors, and “no priors”, the latter indicating that no internal anatomical information was used to guide the fluorescence reconstruction, though the outer boundary was known from the MR image. Each image was reconstructed using three values of the

regularization parameter, specifically 1, 10, and 50. As described earlier, these values were scaled to the maximum of the diagonal of the inversion matrix, $J^T J$. Except where noted, all images shown were reconstructed with the highest regularization value.

Fluorescence yield images for the two tumor-bearing mice are shown in Figure 9.8, along with the associated gadolinium-enhanced MRI slice. The optical fiber array encircled a gadolinium enhanced tumor region in only one of the mice and these images are provided in the top row. The enhanced region segmented out of the MRI image shows elevated fluorescence activity in all three images. In particular, the two images generated with internal spatial priors show very strong contrast in the gadolinium enhanced region surrounding a region of low fluorescence activity corresponding to the darkened area in the MR image. In both cases, enhanced tumor region-to-normal brain tissue contrast approaches 9:1. The no priors image shows a diffuse elevation in fluorescence yield, though the subtleties of the spatial distribution of fluorescence yield are lost given the low spatial resolution. The maximum recovered value and overall contrast are substantially lower, most likely due to the under-determined inversion ‘spreading’ the image intensity across the imaging field, a common phenomenon observed in simulation and phantom studies conducted previously.

The bottom row shows images for the mouse with an obvious abnormality composed of an extensive dark region and gadolinium enhancement outside of the fiber plane. Spatial priors were introduced as a three region mask, normal brain, dark region, and all other tissue. The spatially guided images show very slight differences between normal brain and surrounding tissue, 16% according to the hard priors image, but a significant negative contrast in the region corresponding to the dark abnormality in the

MR image. This region presents with T2 and T1 signatures similar to the dark region in the previous mouse, i.e. high fluid content and absence of gadolinium enhancement. The possibility that these regions are composed of necrotic and/or edematous tissue is encouraging, as such pathologies are expected to show little to no contrast of a targeting fluorophore. The no priors image also shows negative contrast in the abnormal region, though, as expected, returns diffuse, poorly resolved images. However, images reconstructed without spatial guidance produce the most pure expression of the information content in the data, and it is reassuring, if not necessary, that their general trends match those recovered in the guided images. This is an important concept which when applicable, instills confidence that spatial guidance does not dominate image recovery.

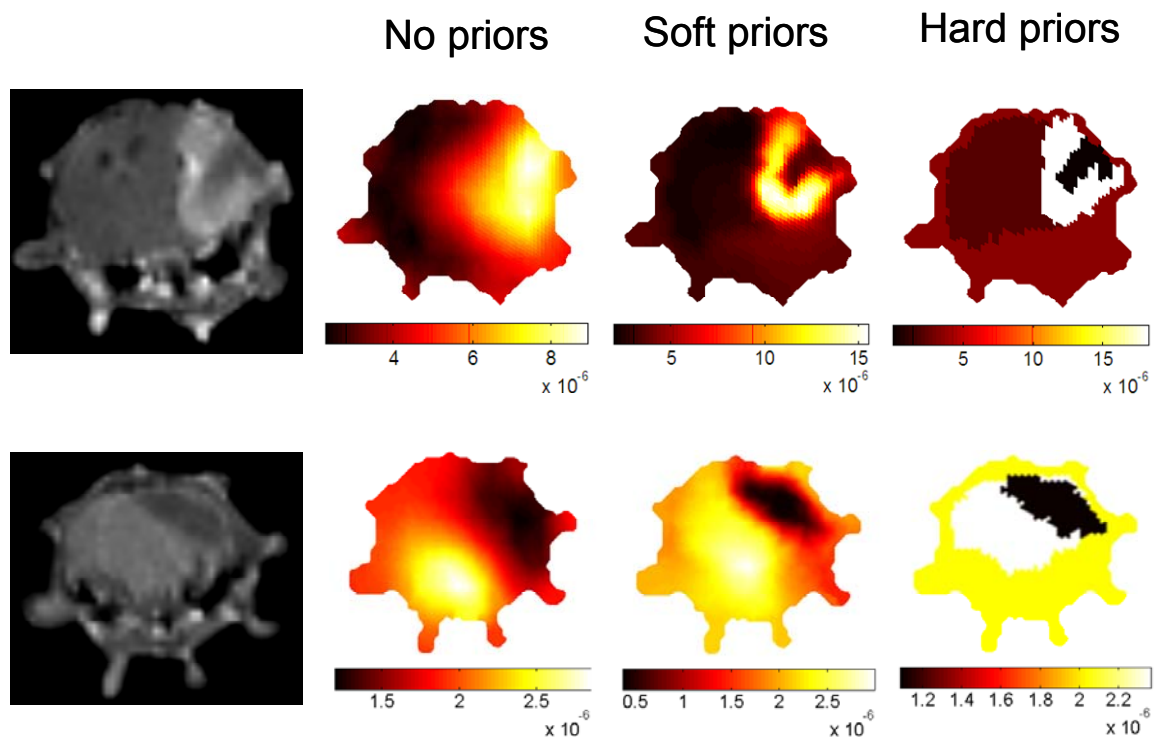


Figure 9.8. Images for the tumor-bearing mice, only one of which showed Gd contrast in the fiber plane, reconstructed using three reconstruction techniques are

shown next to the corresponding MR image used to provide spatial a priori guidance.

Images for the control population are shown in Figure 9.9. The control mice underwent sham surgeries only, and therefore the spatial guidance was introduced as a two region problem; brain and surrounding tissue. Most images show elevated levels of fluorescence activity outside of the brain region, an initial indication that a strongly fluorescent mass does not reside in the brain region. Overall image contrasts are modest, especially compared to the fluorescence enhanced tumor in Figure 9.8 (top row). Importantly, the maximum reconstructed value of fluorescence yield for all reconstruction techniques is highest in the mouse with a gadolinium enhanced mass sampled by the fiber optic array. Considering only the hard-priors images, this value is around tenfold higher than the maximum values recovered in three of the control mice and approximately six times higher than the fourth control mouse. A similar comparison between the tumor-bearing mice in Figure 9.8 indicates a 7.5 times increase in maximum fluorescence yield.

Overall, the maximum value of recovered fluorescence yield in the mouse with a gadolinium-enhanced mass sampled by the fiber optic array is over six times higher than the maximum recovered values in all other subjects. It is unfortunate that the tumor-mouse population was so small. A larger population might support the identification of image intensity thresholds to help facilitate characterization and quantification of fluorescence activity *in vivo*.

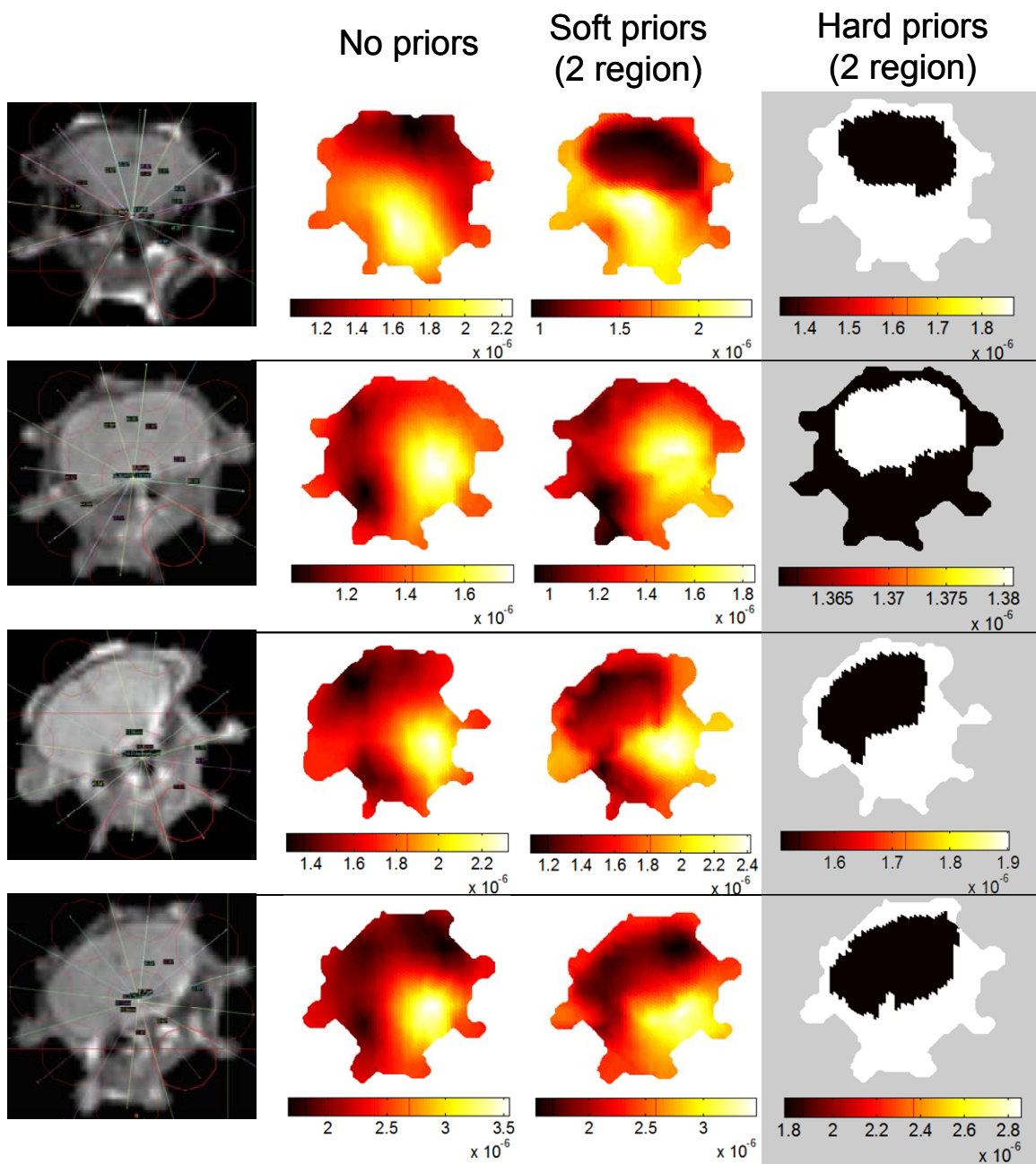


Figure 9.9. Images of fluorescence yield for the four control mice reconstructed using three different reconstruction approaches. For each mouse, the relevant MRI slice is shown (left) with the corresponding fluorescence images recovered using no prior, soft prior, and hard prior implementations.

9.2.2.1 A brief note on regularization

Samples of reconstructed images for a tumor-bearing mouse and a control mouse presented in Figure 9.10 and Figure 9.11 demonstrate the effect of the regularization parameter, termed λ for the no priors and hard priors cases and β for the soft priors implementation, on recovered images. Reconstruction approaches which allow all nodes to update independently, the no priors and soft priors approaches, are particularly sensitive to changes in regularization. Fluorescence contrast localization and recovered values are inconsistent as regularization changes in these images. However, the hard-priors technique, which collapses the parameter space of the imaging problem, is virtually insensitive to adjustments in regularization. This robustness is an encouraging result which may guide the choice of regularization parameter for the other reconstruction techniques. For example, the soft and hard prior images correspond most closely for $\beta = 50$, an observation that led to the choice of displayed images in Figure 9.8 and Figure 9.9.

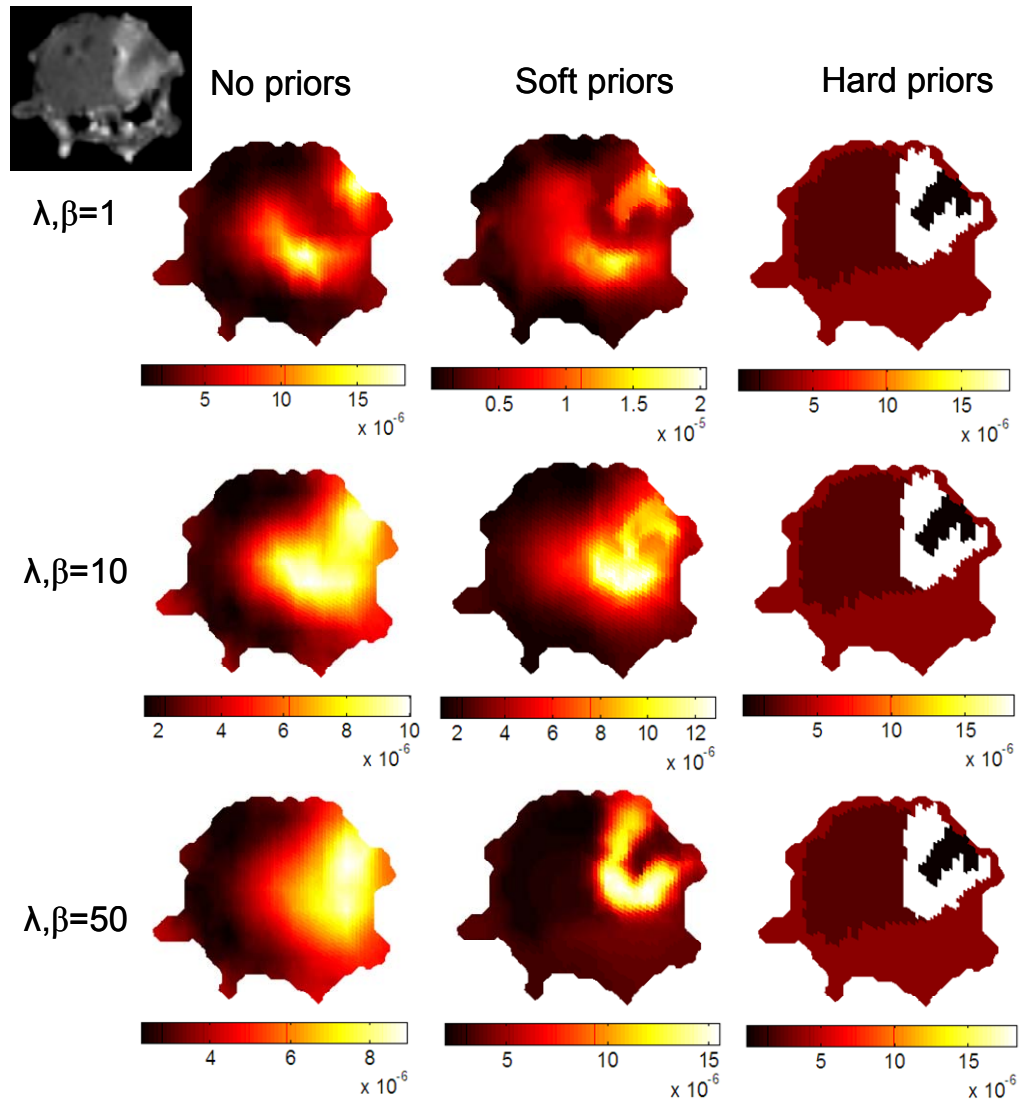


Figure 9.10. Three regularization parameters were used for each of the three reconstruction techniques, resulting in a series of nine images for each mouse. Here the series for a tumor-bearing mouse is shown.

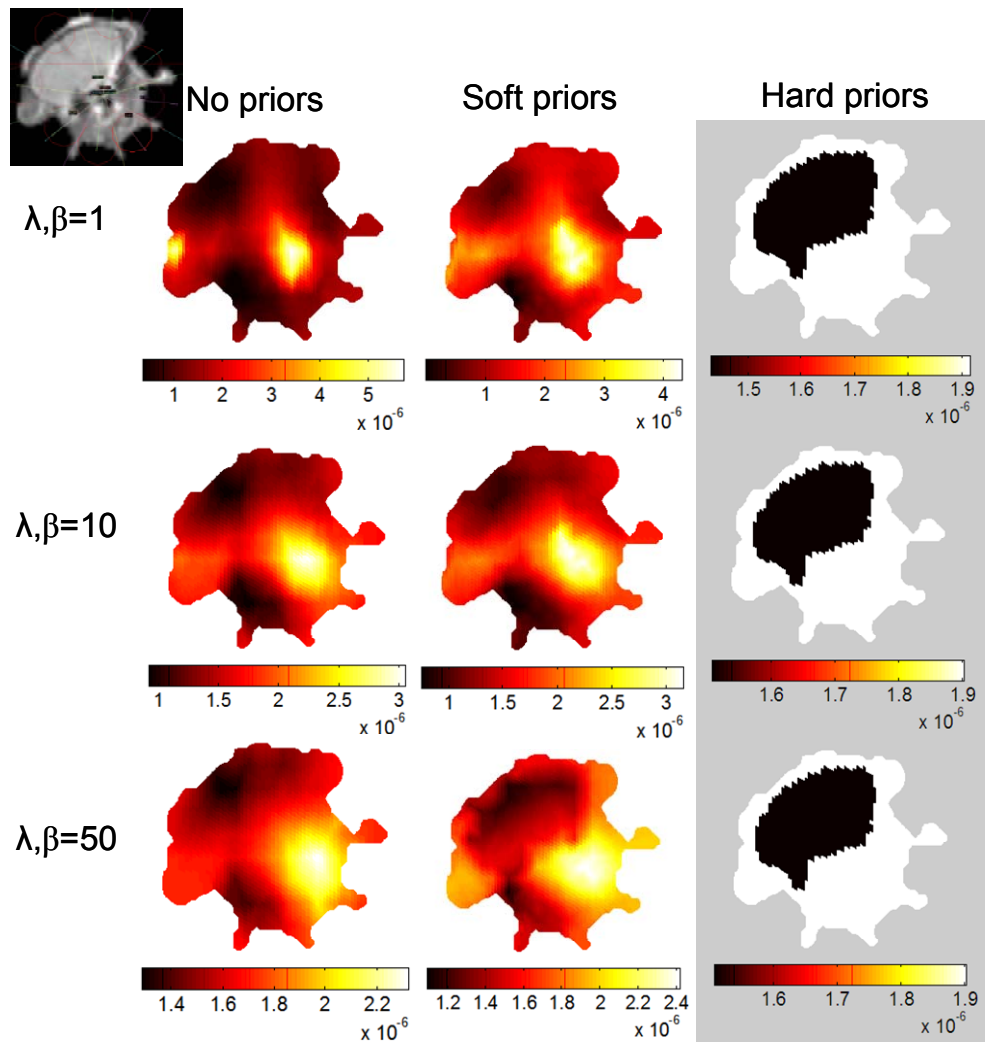


Figure 9.11. Three regularization parameters were used for each of the three reconstruction techniques, resulting in a series of nine images for each mouse. Here the image series for a control mouse is shown.

9.2.3 *Ex-vivo validation of tumor-bearing subjects*

Immediately after MRI-FMT imaging, tumor-bearing mice were sacrificed and the brain surgically removed and sectioned into slices imaged on the Li-Cor Odyssey scanner. Sections were then preserved and fixed for histology staining. Here, we consider the subject with a large glioma which showed strong Gd enhancement in the

plane of the fiber (subject shown in Figure 9.8 and Figure 9.10). Ex-vivo slices and photographs of H&E slides are provided in Figure 9.12. The tissue volumes sampled for the ex-vivo fluorescence and H&E slides do not match precisely due to slice thickness and variability in orientation, however, it can be stated with some confidence that fluorescence activity corresponds to malignant regions identified by histology. Though the Li-Cor scanner provided particularly low dynamic range, requiring narrow windowing of the image, it is clear that the fluorescence contrast between tumor and normal tissue is quite high. This is certainly a partial validation of the FMT images presented in Figure 9.8; however, the images may contain more subtle information regarding the tissue physiology. Specifically, the dark region surrounded by the strong fluorescence contrast may indicate sensitivity to necrotic or edematous tissue.

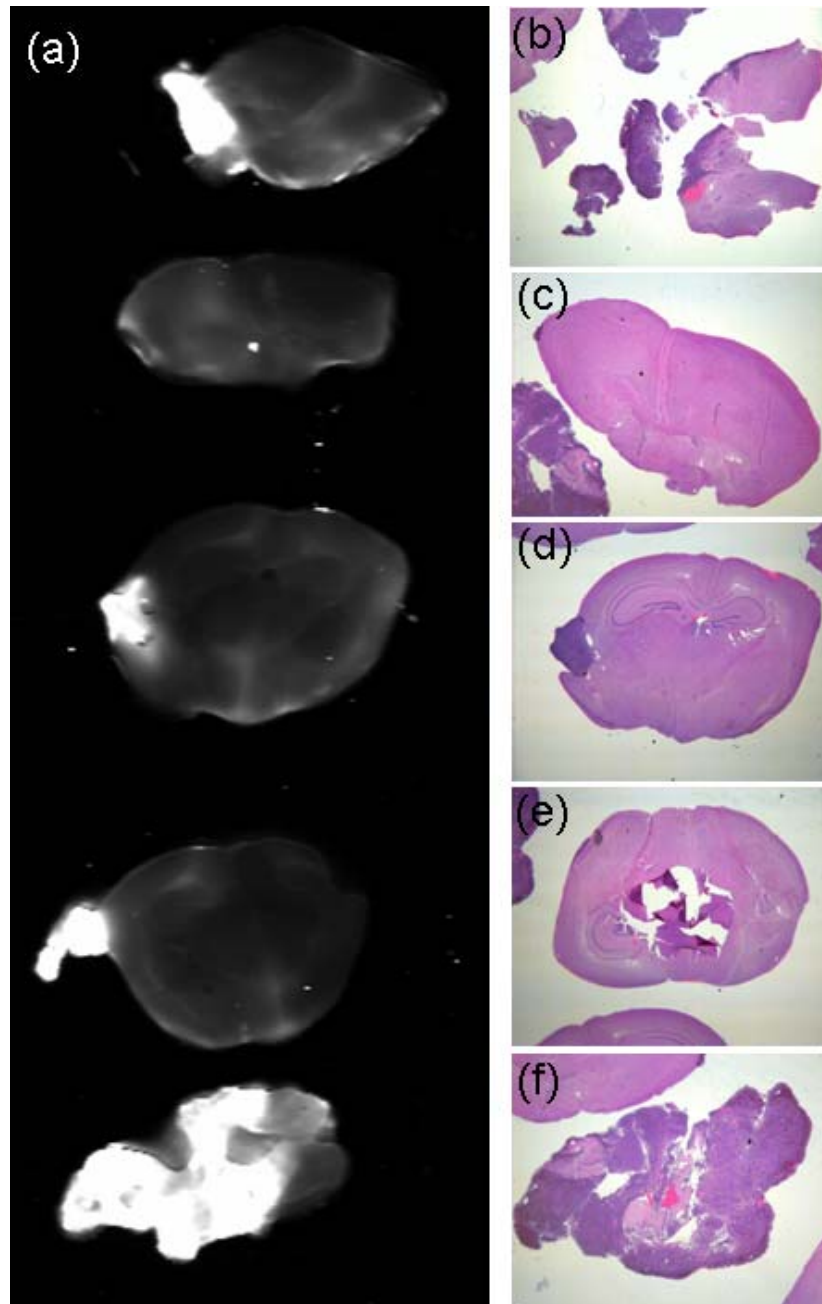


Figure 9.12. Ex-vivo fluorescence of EGF bound Li-Cor dye (a) in fresh sections of brain tissue. This mouse had a large Gd-enhanced region in the optical fiber plane, a region that showed high levels of fluorescence activity in FMT images (Figure 9.8, top row). Pathology slides (b) – (f) correspond roughly to the slices in (a) and show tumor regions matching the fluorescent enhancement.

Closer inspection of the histology slide in Figure 9.12 (f), the slice containing the bulk of the tumor, provides further validation of the FMT images for this mouse. Evidence of a necrotic or edematous region surrounded by active tumor cells would go a long way to substantiating the FMT images reported in Figure 9.8. Figure 9.13 shows different magnifications of the slide, highlighting some of the critical cellular changes in and around the tumor. Widespread tumor cell (purple regions) infiltration into normal brain tissue is seen in Figure 9.13 (a) while (c) reveals malignant cells surrounding a large necrotic core (light pink). The boundary between viable cancer and necrotic cells is seen clearly in (d). Darker pink regions in (c) may be the result of hemorrhage, a suspicion confirmed at 40X magnification in (e). The higher magnification also reveals active cell mitosis indicating a growing, aggressive tumor. Finally, blood vessels like those in (b) were noted throughout viable tumor regions.

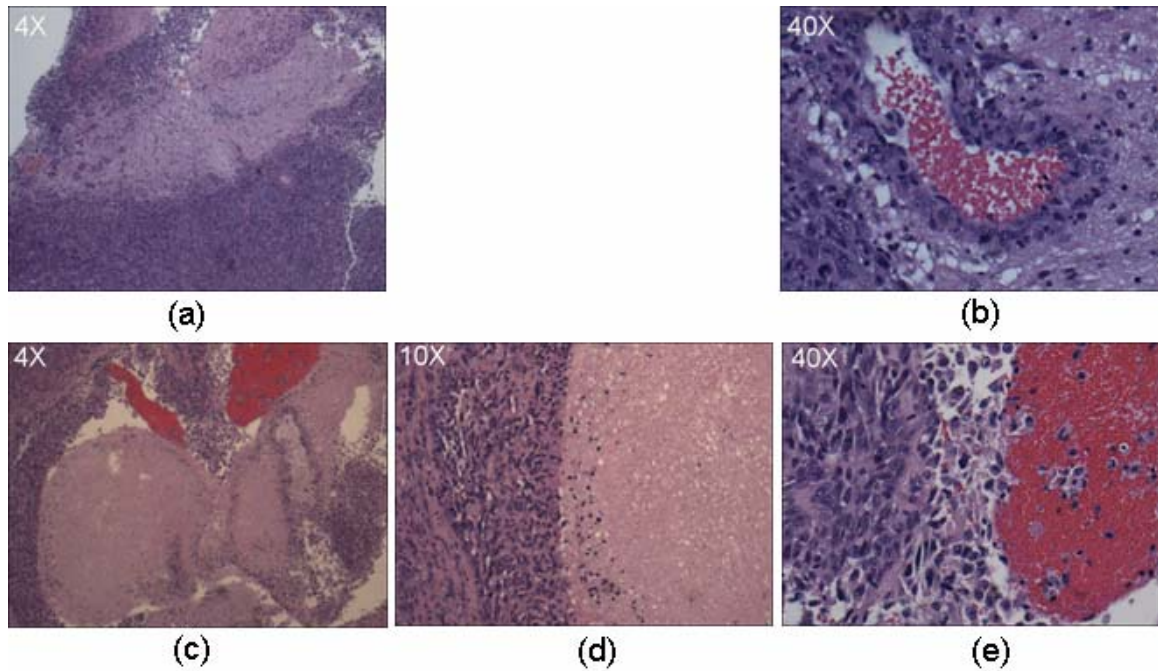


Figure 9.13. Higher magnification of the pathology slide in Figure 9.12(f) shows tumor and normal brain (a), tumor surrounding necrotic tissue and hemorrhaging (c), the boundary of malignant and necrotic cells (d), a closer view of hemorrhage (e), and a blood vessel supplying viable malignant cells (b).

The overall pathological picture is one of an aggressive malignant tumor, well supplied with blood, surrounding a necrotic core, likely associated with edematous tissue, and indications of extensive hemorrhaging. This is entirely consistent with both MRI and FMT images measured *in vivo*. T2 weighted enhancement corresponded exactly to dark regions in T1 weighted gadolinium contrast images, usually indicating fluid pooling, surrounded by a strong gadolinium enhanced region. Clearly, this corresponds to the malignant tissue, a region that also produced high fluorescence activity in the FMT images. The necrotic region presented as a dark region with little fluorescence activity, an expected result given the absence of a blood supply and viable cells lined with EGFR.

MR images of the second tumor-bearing mouse showed gadolinium contrast enhancement only outside of the fiber plane. However, the large dark abnormality in the T1 images presented as negative contrast in fluorescence activity in the FMT images. This would be consistent with necrosis or edema, as described above. Figure 9.14 shows ex-vivo fluorescence and H&E slides of brain sections. As in the mouse previously described, fluorescence activity matches the tumor regions defined by histology. Close inspection of the two middle sections (oriented opposite to one another) in (a) reveals a large, dark crescent shape, which may well correspond to the dark region in the T1 weighted and FMT images.

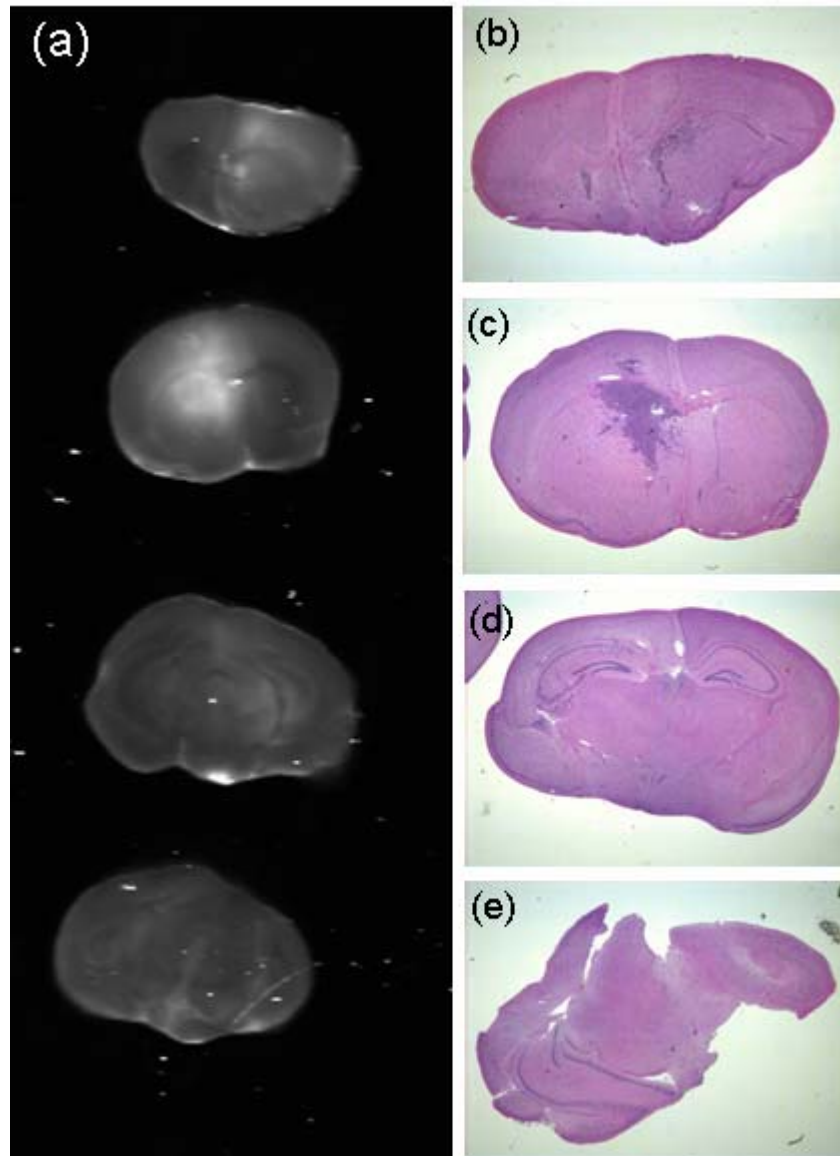


Figure 9.14. Ex-vivo fluorescence of EGF bound Li-Cor dye (a) in fresh sections of brain tissue. This mouse had a large Gd-enhanced region outside of the optical fiber plane, likely corresponding to the top two images in (a). Pathology slides (b) – (f) correspond roughly to the slices in (a) and show tumor regions matching the fluorescent enhancement.

The bulk structure of the brain itself indicates abnormal physiology. Normal brain hemispheres should be symmetric, but slices (b), (c), and (d) show dramatic midline shift in the brain structure, an indication of substantial swelling in one of the brain

hemispheres. Inspection of magnified images in Figure 9.15 confirms the presence of extensive edema running along the cortex of one hemisphere (b), with no evidence of edema on the contra-lateral side. Further magnification in (c) shows a clear boundary between mid-brain and edematous cortex tissue. There is no evidence of necrosis.

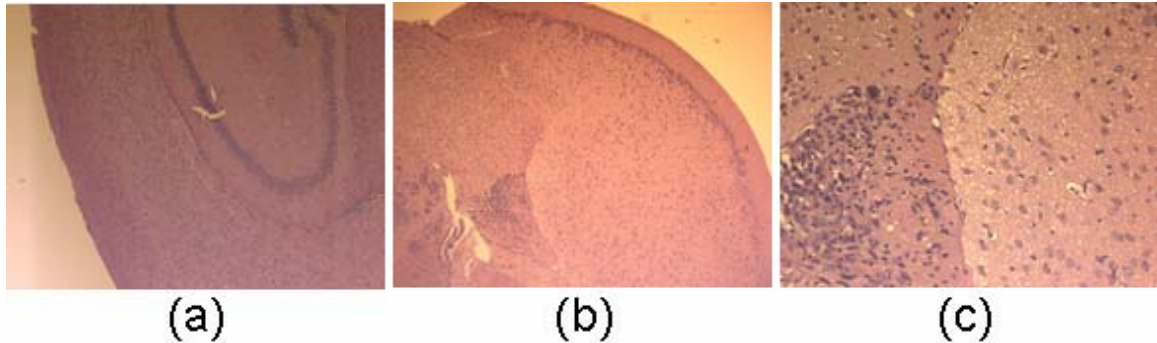


Figure 9.15. Magnified images of the murine brain histology slides shown in Figure 9.14. This mouse had a large Gd-enhanced region outside of the optical fiber plane, and an abnormal region of high T2 signal in the optical imaging plane. Images show normal tissue (a) in one hemisphere and extensive edema in the contra-lateral cortex [(b) and (c)], likely causing the crescent-shaped abnormality in the MR and FMT images.

Tissue slices showing the greatest extent of edema are outside of the coronal plane of the bulk tumor, consistent with the Gd-MR images. The extensive swelling was likely a result of back-pressure due to blockages in the venous return, perhaps due to tumor growth or inflammatory response. Indeed, the presence of lymphocytes indicates an immune response. Overall, these slides confirm the in-vivo imaging results. With reasonable certainty, we can conclude that the edematous tissue evident in the histology slides caused decreased T1 signal, increased T2 signal, and decreased fluorescence activity. This is consistent with expectations.

9.3 Summary

A newly designed fiber position system with integrated MR fiducial references provides substantial improvement in locating and positioning tissue-fiber contact points in the MR images, a critical process for tomographic image recovery. The concentric cylinder system is an evolved design, appropriate for imaging a variety of regions on nude or shaved mice. Beyond the hardware developments, it was clear the U251-GFP line in the Erbitux study (Chapter 8) had a different phenotype which made tumors difficult, if not impossible, to routinely detect in the MRI images. Extensive analysis of this issue was completed as part of Summer Gibbs-Strauss' PhD Thesis¹¹⁰. In the current study, U251 parent line tumors were clearly delineated with standard Gd-MRI contrast. These images facilitated easy segmentation for spatial prior guidance in optical image reconstructions.

The imaging results presented in this study are encouraging for the prospects of targeted glioma imaging *in vivo* using the MR-coupled system, though the surviving rodent population was too small for statistical conclusions to be drawn. It is critical that the tumor region intersect the plane of the imaging fibers, and scout MR images should be used to verify mouse positioning before full MRI-FMT image acquisition begins. Images of the only mouse which had MRI contrast enhancement in the plane of the fiber array showed high levels of fluorescence yield, corresponding to the MR-enhanced region, surrounding very low values of fluorescence activity in what turned out to be a necrotic core with hemorrhage. Maximum recovered values of fluorescence yield were six to ten times higher in this mouse than all other subjects. Images of the other tumor-bearing mouse also presented a region of low level fluorescence activity which seemed to

correspond to edematous tissue as determined by T2 enhancement and histology. Larger mouse populations must be studied to confirm this anecdotal case and extract diagnostic thresholds, work that is ongoing presently.

Chapter Ten: Comparing sensitivity of fluorescence and absorption-based measurements for diffuse optical tomography

Though the primary objectives of this thesis involve imaging fluorescence activity of exogenous contrast using luminescent signals, fluorescence emission is inextricably linked to the absorption properties of the fluorophore. By definition, any fluorescing agent must possess the capability to absorb photons in order to transition to higher energy states, from which fluorescence photons are emitted through the radiative relaxation process. The technical challenges associated with imaging fluorescence activity in larger tissue volumes include filtering the fluorescence excitation light from an emission signal often orders of magnitude lower and deciphering the impact of optical property heterogeneity on the fluorescence yield images. Meeting these challenges requires high sensitivity detection, exceptional optical filtering, and the capability to image, or accurately estimate, the background optical properties of the imaging field. However, the technical requirements may be simplified if the spatial distribution of the drug concentration is the primary imaging objective and the absorption properties of the exogenous agent alone are enough to provide adequate optical contrast.

Imaging exogenous contrast based on drug absorption is a clinical protocol routinely used with conventional modalities. Radiographic contrast agents, for example, are composed of high Z-number materials which absorb x-rays at clinically relevant

energies. These contrast drugs are used to enhance x-ray image contrast and consist either of barium sulfate, used for digestive track imaging, or iodine, which is administered intravenously for imaging blood pharmacokinetics. Compounds that absorb optical energy are also commonly used in clinical practice, though mostly in ex-vivo analysis. Indeed, the gold standard in clinical tissue diagnosis is derived from optical exogenous contrast used in histopathology. Hematoxylin and Eosin (H&E) staining represents highly specific optical contrast based on light absorption in the visible regime.

Translating the specificity of these optical agents into human imaging is challenging due to the chemical toxicity of these compounds. To date, indocyanine green (ICG) remains the most widely available fluorophore approved for human use. Though ICG is an unspecific agent, Gurfinkel et al. demonstrated that ICG provides tumor-to-normal contrast if imaged as a blood pool agent ¹¹¹. It also absorbs strongly in the NIR and has been studied for years as a dynamic contrast agent for diffuse optical imaging and spectroscopy in small animals ¹¹²⁻¹¹⁴ and the human breast ¹¹⁵⁻¹¹⁷.

This work naturally raises the question of which optical contrast mechanism provides the best opportunity for exogenous contrast imaging. This question was addressed directly in a comprehensive study by Li, et al. which compared detection limits for fluorescent and absorbing contrast using analytical frequency domain data ⁴⁷. The study showed that fluorescence measurements are more sensitive to smaller objects than absorption-based measurements for a quantum yield value of 0.1 and perfect excitation filtering. However, some fluorophores in development have much lower quantum yields, such as lutetium texaphyrin, for which a value of 0.0019 was measured as part of this work (section 4.2). Determining the most favorable imaging approach clearly depends on

the drug's quantum yield, among other parameters, and theoretical values of quantum yield for which measurements using absorption and fluorescence are equally sensitive exist.

This study seeks to determine the experimental conditions under which fluorescence measurements offer more sensitivity than measurements based on absorption in breast-sized volumes. Simulated data was used to produce quantum yield values representing the transition between fluorescence and absorption-favored conditions for a simulated drug with optical absorption mimicking that of LuTex. Parameters explored included tumor-to-background contrast, background concentration, and filtering efficiency. Experimental data were also used to compare recovered values of absorption coefficient and fluorescence yield in homogeneous liquid phantoms.

10.1 Methods

10.1.1 Simulations

The imaging test field for the simulation component of this study was comprised of a breast-shaped test mesh generated from a segmented T1-weighted coronal MR image of a 2D human breast, identical to that used in section 6.1.1, The “background” domain contained no tumor region and presented endogenous chromophore contrast only between the fatty and fibro-glandular regions, as shown in Figure 10.3. A variety of exogenous contrast distributions were used in this study and are specified for each experiment. In all cases, the exogenous absorption and fluorescence contrast were introduced as a simulated drug with the absorbing properties of LuTex. Quantum yield was varied as an independent variable for the fluorescence emission measurements.

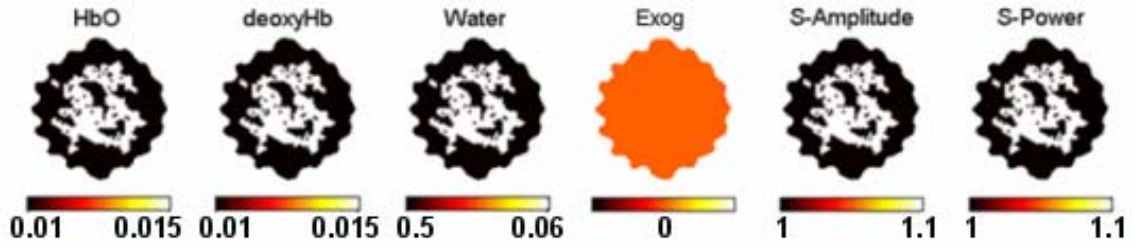


Figure 10.1. The imaging test domain was derived from a T1-weighted coronal MR image of a human breast. Adipose and fibro-glandular regions were assigned clinically relevant values for endogenous chromophores. Note that HbO and dHb are in mM, water in percent and scattering parameters are dimensionless. A variety of exogenous distributions were used in this study.

The parameter of interest in this study is the relative perturbation in boundary data intensity caused by a drug-enhanced tumor, defined as

$$P = \frac{|I_{\text{detector}}^{\text{anom}} - I_{\text{detector}}^{\text{background}}|}{I_{\text{detector}}^{\text{background}}} \quad (10.1)$$

where I is the intensity measured at the boundary for a given source-detector pair. Determining P , also known as detectability, involves running the forward model with (denoted as *anom*) and without (denoted as *background*) the exogenous anomaly, extracting the appropriate boundary data, I , and using Equation (10.1). Data from perturbations caused only by exogenous *absorption* are termed “transmission” measurements, for which 735 nm was used as the laser source wavelength, this being the peak of the LuTex absorption band in the NIR. Fluorescence data was generated for excitation and emission wavelengths of 690 and 761 nm and the fluorescence emission perturbation was recorded for excitation filtering efficiencies of 3 OD, 5 OD, 7 OD and

in some cases, 100 OD. Perturbation values were calculated for a variety of detector positions relative to a single source, as shown in Figure 10.2, for both transmission and fluorescence measurements. No additional noise was added to the simulated data beyond that derived from imperfect excitation filtering.

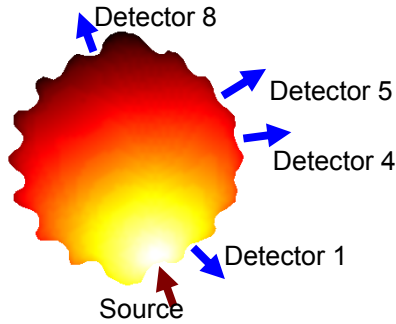


Figure 10.2. Source-detector configuration for simulated data used in this study.

10.1.2 Phantom studies

The phantom component of this study made use of data measured during the fluorescence ICG sensitivity analyses in section 5.4.2 to compare the relative change in recovered values of the absorption coefficient and the fluorescence yield arising from increasing drug concentration. Briefly, ICG dye dissolved in DI water was added to a 70 mm diameter homogeneous liquid phantom containing DPBS, 1% intralipid and India ink. The optical properties of the intralipid/ink solution μ_a and μ_s' , were 0.006mm^{-1} and 1.6mm^{-1} , respectively, before the introduction of ICG. At each ICG concentration, the clinical frequency domain system described in section 2.2 was used to determine optical properties near the excitation and emission wavelengths via the homogeneous fitting

procedure. Optical properties at 785 nm were also recovered since this corresponds to the absorption peak of ICG monomers.

Fluorescence was excited using a 690 nm CW laser, and emission and excitation transmission measurements were recorded for each phantom using the spectral tomography system, with a maximum allowed camera integration time of 120 s applied to the fluorescence measurements. After data spectral fitting and integration of the fluorescence peak, the homogeneous fitting algorithm was used to estimate the fluorescence yield in the phantom volume using the optical properties recovered with the FD system.

10.2 Results

10.2.1 Simulation studies

10.2.1.1 Perturbations as a function of Quantum Yield

The first set of simulation experiments considered transmission and fluorescence perturbations caused by a centrally located tumor region in two different tumor-to-normal tissue drug uptake situations: One an idealized case with infinite contrast (Figure 10.3(a)), and the other a more realistic drug uptake case with finite drug concentration contrast ranging from 2:1 to 3:1 (Figure 10.3(b)). The exogenous contrast concentration was assumed to be 300 nM, 500 nM, and 1000 nM for adipose, fibro-glandular, and tumor regions, respectively. Though this distribution is not necessarily expected *in vivo*, it represents a sufficiently heterogeneous and complex case for the purposes of this study.

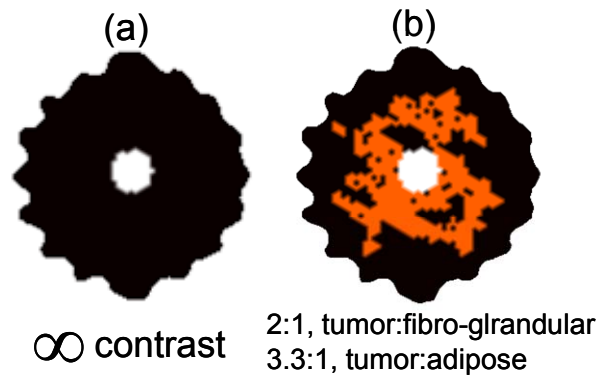


Figure 10.3. Two test domains for investigating perturbations caused by absorption and fluorescence exogenous contrast. In (a), exogenous contrast tumor specificity is assumed to be perfect, while in (b), the uptake profile is more realistic.

Figure 10.4 presents graphs of relative intensity perturbation as a function of fluorescence quantum yield at three detector positions for infinite exogenous agent contrast, corresponding to the test domain in Figure 10.3(a). The graphs include perturbations of transmission intensity resulting only from an increase in the concentration of the exogenous agent, as well as fluorescence emission intensity degraded by different amounts of excitation bleed-through. The perturbation caused by absorption is unaffected by quantum yield, as expected, while perturbations in fluorescence signals are proportional to quantum yield. The seemingly anomalous dip in perturbation for the 3OD fluorescence case is easily explained. First, it should be noted that for plotting purposes, the perturbation was calculated as an absolute value and all perturbation values to the left of the minimum are actually negative. It is apparent from Equation (10.1) that negative perturbation values indicate that there is a stronger fluorescence signal without a fluorophore in the tissue than if the tissue contains a fluorescent anomaly. This is due to the combination of low quantum yield and low filter

efficiency. When there is no fluorescent anomaly present in the field, excitation bleed-through accounts for the entire fluorescence signal. The presence of the fluorescent inclusion introduces absorption to the tissue along with the fluorescence activity, reducing the transmitted excitation signal slightly, and therefore reducing the bleed-through signal. If the fluorescence emission is not strong enough to make up for this loss in bleed-through emission, the perturbation will be negative. In short, more excitation cross-talk signal is lost than light is gained by fluorescence emission in this bleed-through-dominated regime. Although this effect can be eliminated with better filtering, it should be considered when using low-quantum yield fluorophores.

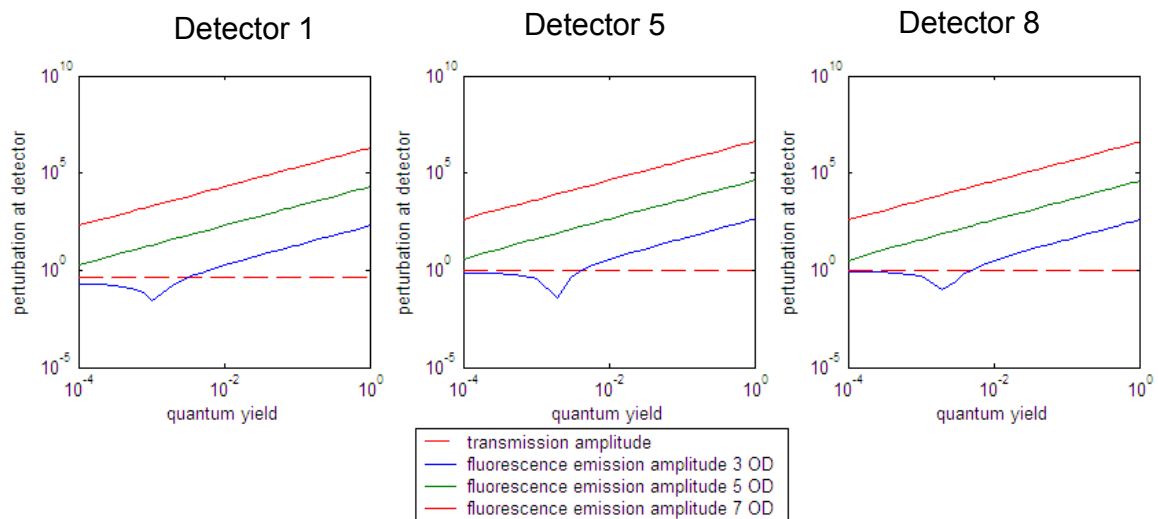


Figure 10.4. Perturbations in transmission amplitude and fluorescence amplitude, given different filtering efficiencies and quantum yield values, caused by a centrally located object with perfect drug uptake. Given these conditions, fluorescence signals appear to be more sensitive to the object.

It is clear from Figure 10.4 that the fluorescence signal is more sensitive to the presence of an anomaly if the tissue contains infinite tumor-to-background contrast of the exogenous agent. This is consistent for all source-detector pairs and filtering efficiencies of 5 OD and higher, given quantum yields of 0.0001 and above. If the filtering efficiency drops to an experimentally poor 3 OD, a quantum yield of around 0.1 is required for the fluorescence sensitivity to match that achieved with absorption-based transmission perturbations, though this depends on which source-detector pair is considered. This intersection defines a quantum yield threshold for a given imaging situation. Thus, contrast agents with quantum yield values higher than this threshold favor fluorescence measurements, while transmission perturbations are greater for those with lower quantum yields. This finding applies to tissue volumes with infinite tumor-to-background contrast.

Figure 10.5 provides results for the case with drug uptake of 2:1 for tumor-to-fibro-glandular tissue layer and 3:1 for tumor-to-fatty tissue. For this case, the absorption perturbation is more significant for all values of quantum yield and filtering efficiencies tested. The characteristic dip indicating negative perturbations due to dominance of the bleed-through signal is now seen for higher filtering efficiencies. Furthermore, if enough filtering is applied, fluorescence perturbations asymptote to values independent of quantum yield and additional excitation filtering. These values represent the maximum expected perturbation for fluorescent anomalies and are significantly lower than perturbations caused by the absorption profile of the exogenous drug. These results clearly indicate that background concentration and tumor-to-background contrast help determine which signal provides the most sensitive measurement, a finding consistent with data provided in Li, et al.⁴⁷ This is addressed directly in the next experiment.

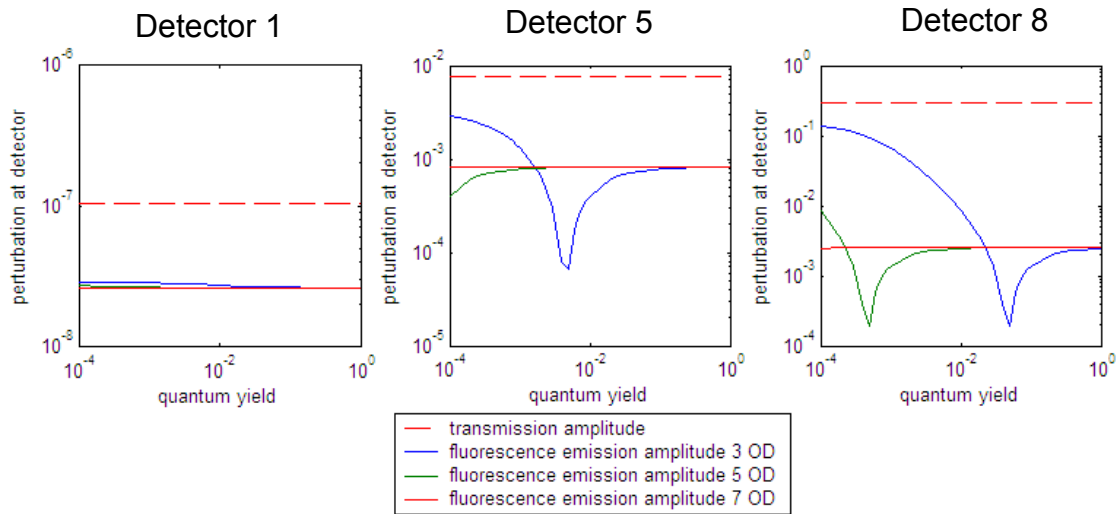


Figure 10.5. Perturbations in transmission amplitude and fluorescence amplitude, given different filtering efficiencies and quantum yield values, caused by a centrally located object with imperfect drug uptake. For this lower drug contrast case, absorption measurements are more sensitive to the object than fluorescence emission, regardless of fluorescence quantum yield.

10.2.1.2 Quantum Yield Threshold

In this component of the study, the quantum yield value at which fluorescence and transmission perturbations intersect, i.e. the quantum yield threshold, was determined for drug contrasts ranging from 1.1:1 to 10:1, and background concentrations ranging from 10 nM to 1000 nM. The secant root finding method, initialized with the output of a bisection method algorithm, was used to determine the quantum yield value which minimizes the difference between fluorescence and transmission perturbations over the range $\eta = 10^{-6}$ to $\eta = 1$ for each combination of contrast and background concentration. The exogenous contrast distribution was assumed to be homogeneous except for the tumor region and only detector #4 was considered for this experiment.

The values of quantum yield at which fluorescence and transmission perturbations are equal are plotted in Figure 10.6 for a range of background drug concentrations and target-to-background contrasts. These values represent the transition between regimes in which absorption-based measurements are more sensitive than fluorescence measurements, given a drug with a similar absorption profile to LuTex. Figure 10.6 [(a) – (d)] provides threshold quantum yield values for excitation filtering efficiencies of 3 OD, 5 OD, 7 OD, and 100 OD, respectively. The lower limit of the colorbar values in (c) and (d) is 10^{-6} , indicating that fluorescence perturbations are larger than absorption perturbations as long as the quantum yield is greater than 10^{-6} . The white regions marked “ $\eta > 1$ ” indicate regimes for which absorption perturbations are always larger than fluorescence perturbations, regardless of quantum yield value. The leftmost edge of this region, at 200 nM, represents a hard upper limit for background drug concentrations above which transmission perturbations are always more sensitive. This limit does not seem sensitive to the object contrast, at least for the data sampling used here.

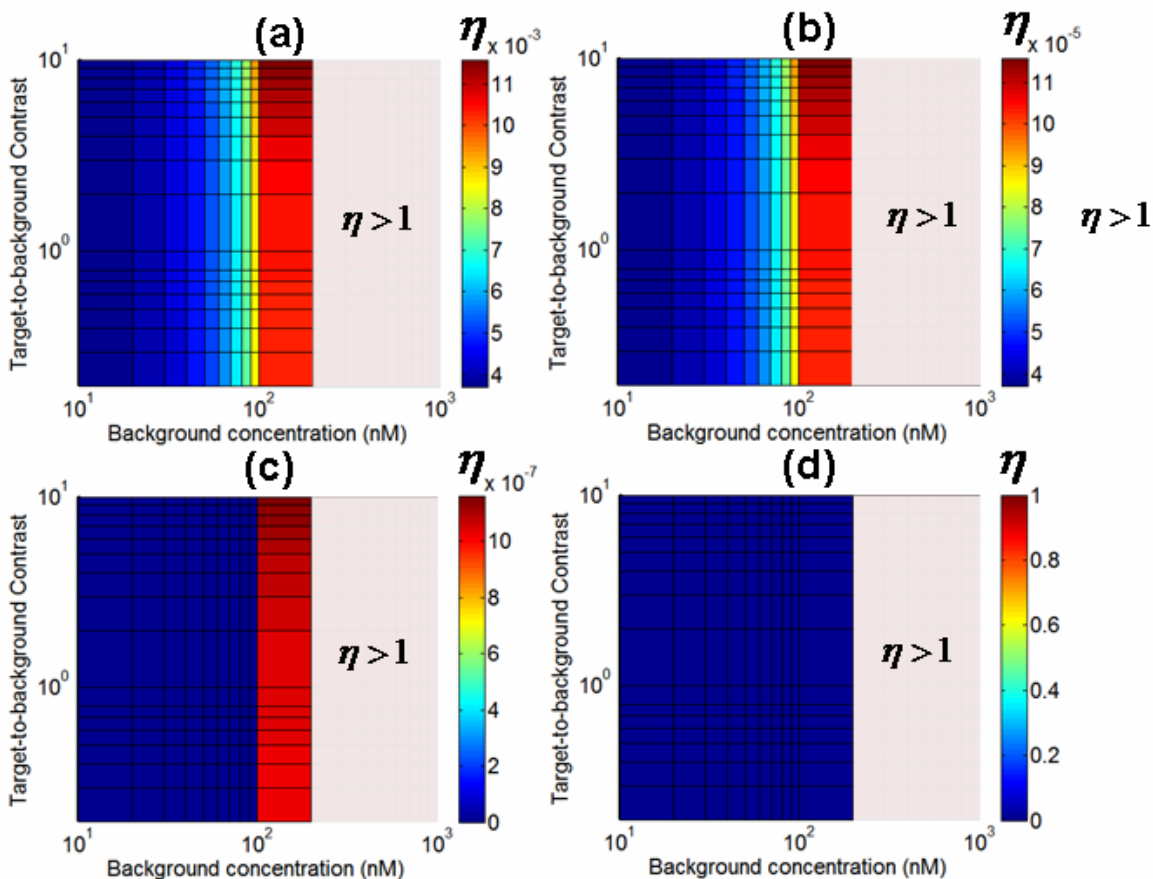


Figure 10.6. Threshold quantum yield values for excitation filtering efficiencies of 3 OD, 5 OD, 7 OD, and 100 OD [(a)-(d), respectively] over a range of contrasts and background concentration. These values represent the quantum yield value for which absorption and fluorescence measurements are equally sensitive to a centrally located tumor region.

To visualize the influence of background drug concentration on the threshold quantum yield values, cross-sectional plots along a single contrast value (5:1 in this case), are presented in Figure 10.7. Since data sampling near the absorption-fluorescence limit was rather sparse for data presented in Figure 10.6, the data was re-sampled to produce the curves shown in Figure 10.7. These curves represent the minimum value of quantum yield required to ensure fluorescence measurements are more sensitive to the tumor

region than transmission measurements for a range of excitation filtering efficiencies. In this manner, regimes may be defined based on contrast agent quantum yield and expected background concentration. Regions above and to the left of a given curve represent a “fluorescence sensitive” regime while background/quantum yield combinations below and to the right of each curve can be considered “absorption sensitive”, assuming a 5:1 target-to-background contrast. This is illustrated in Figure 10.7 (b) for the 7 OD filter results. Furthermore, the more highly sampled data better illustrates the asymptotic behavior near the hard limit between fluorescence and absorption sensitivity in Figure 10.7. Conditions clearly favor transmission measurements when background drug concentration approaches 150 nM, regardless of filtering efficiency. On the lower concentration side of this hard limit, excitation filtering efficiency has a large impact on threshold quantum yield values. As filtering efficiency degrades, higher and higher quantum yields are required to produce meaningful fluorescence perturbations at the tissue boundary.

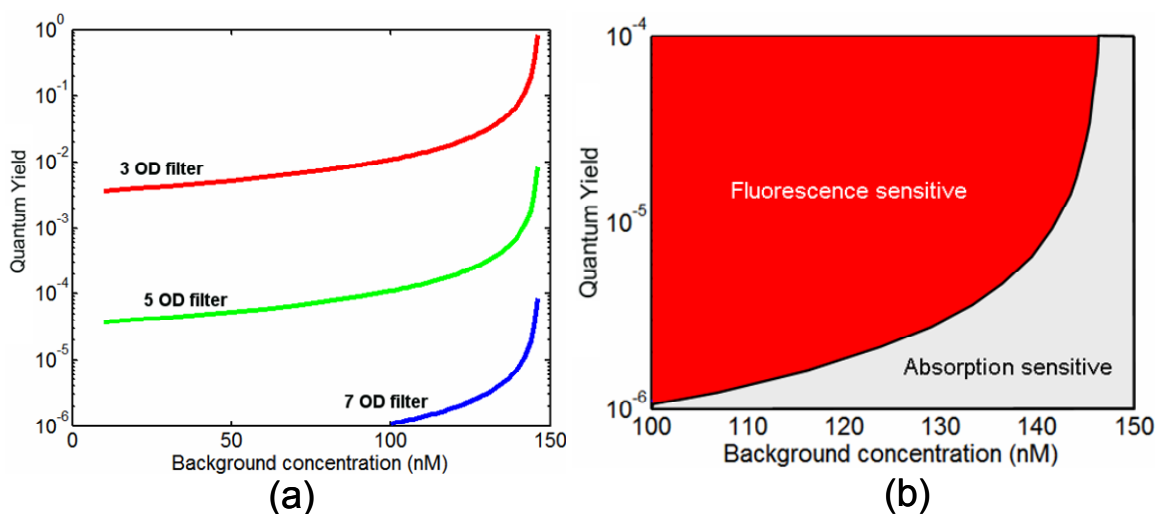


Figure 10.7. Threshold quantum yield values plotted as a function of background drug concentration for a 5:1 tumor-to-background contrast (a). The quantum yield threshold curves delineate between experimental conditions which favor fluorescence and absorption measurements (b).

10.2.2 Phantom results

Recovered values of the absorption coefficient at 785 nm and fluorescence yield were compared for a range of ICG concentrations in a homogeneous liquid phantom. Changes relative to values recovered at 10 pM are plotted in Figure 10.8 for both data sets. It is immediately apparent that relative changes in the fluorescence yield caused by increasing fluorophore concentration are orders of magnitude higher than changes in the absorption coefficient, indicating substantially higher sensitivity to changes in drug concentration. At lower concentrations, particularly below 0.5nM, absorption sensitivity seems to levels off; while fluorescence yield values still show dramatic changes to concentration.

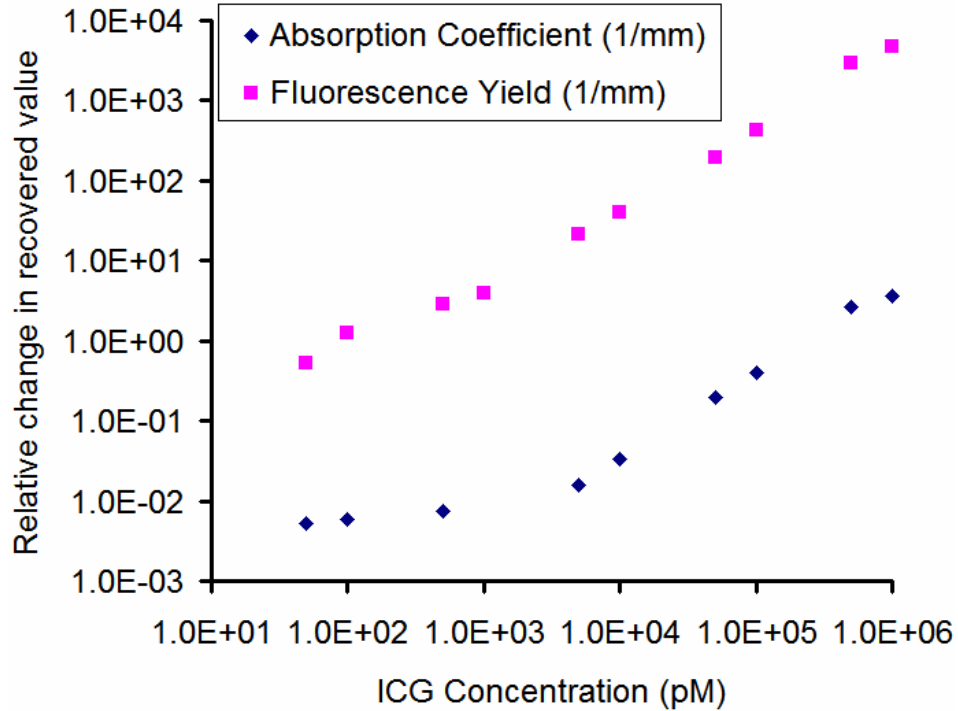


Figure 10.8. Changes in recovered values of fluorescence yield and absorption coefficient as a function of ICG concentration in a homogenous liquid phantom. Values were calculated relative to the recovered value at 10pM.

10.3 Discussion and summary

The initial results for the tissue volume with infinite tumor contrast substantiate the conventional belief favoring fluorescence imaging; however, many contrast agents, including all optical agents currently approved for *in vivo* human use, will not provide infinite specificity. Thus, imperfect uptake must be considered. As shown here, when the contrast agent is present in the background, perturbations in boundary data caused by the fluorescing tumor region are not necessarily larger than those introduced by absorption properties of the drug. Results for these more realistic cases indicate that background drug concentration is the primary factor determining at what quantum yield value fluorescence perturbations equal perturbations arising from the corresponding

contrast in absorption for a given filtering efficiency. These values can be used to define a threshold quantum yield curve, or surface, above which fluorescence measurements are more sensitive and below which absorption provides the larger change in boundary data for a given excitation filtering efficiency.

Regardless of filtering efficiency, all quantum yield threshold curves asymptote at a certain drug background concentration, representing a hard limit for conditions favoring fluorescence measurements. Significantly, the limit determined here, 150 nM, is clinically relevant for ICG imaging *in vivo*. On the low concentration side of the hard limit, proper filtering becomes the major factor influencing the quantum yield threshold curves. In this regime, conditions favor fluorescence if the quantum yield is approximately an order lower than the inverse of the filter OD, at least for 5:1 contrasts. For example, threshold quantum yield values are around 10^{-2} for 3 OD filtering. If the general trends presented here apply consistently to different fluorophores, this may serve as a simple rule of thumb, provided an estimate of expected contrast is in hand.

Since the simulation studies considered only the idealized detection case, no consideration of detector signal-to-noise (SNR) was included beyond excitation contamination of the fluorescence signal. Thus, Figure 10.6 and Figure 10.7 provide no information on object detectability. However, if the noise behavior of both detection channels is similar, the results presented here will be unchanged, since, by definition, the reported thresholds represent quantum yield values at which transmission and fluorescence perturbations are equal. Analysis of detection thresholds between transmission and fluorescence measurements has been studied extensively by Li et al.⁴⁷

Other factors that will most certainly impact the results of this study include the presence of auto-fluorescence in the imaged volume, absorption spectra of the drug, and imaging wavelengths used. In these studies, transmission data perturbations were calculated at the absorption peak of the drug rather than at the excitation wavelength itself. This approach was used to maximize the photon absorption due to the drug, thus mimicking likely experimental conditions. On the other hand, the fluorescence excitation wavelength used was far short of the absorption peak, again to simulate experimental systems which often sacrifice optical absorption cross-section for reduced excitation contamination in the emission signal. The optimal excitation wavelength may readily be determined using studies similar to this one.

Phantom experiments inherently account for the technical challenges unique to each imaging system and thus provide an optimal method for comparing sensitivity to the two optical contrast phenomena. The homogeneous case considered in this study showed a clear advantage for fluorescence emission imaging. Results from these studies are not readily compared to the numerical results due to the difference in absorption profiles of the theoretical and real drugs used. However, simulated data for homogeneous test domains (not shown here) produced trends similar to those observed for the infinite contrast case shown in Figure 10.4. Thus, the general conclusion that fluorescence perturbations are higher than those introduced by changes in absorption in homogeneous domains is consistent between numerical and experimental results. Whether numerical results agree with experimental data acquired using heterogeneous phantoms with different background concentrations remains to be explored.

This study has broad implications for a variety of imaging approaches. *In vivo* drug concentrations of targeted contrast agents and molecular probes, such as receptor targeted probes, which incubate for several hours or even days are expected to be fairly low given the long clearance times. In these cases, fluorescence imaging is likely the most appropriate approach. On the other hand, imaging drug pharmacokinetics, such as has been done with ICG^{28, 113, 115-117}, is often performed within minutes of large systemic doses resulting in relatively high background concentrations. In these cases, it is less clear whether fluorescence emission would be the most effective imaging approach, provided drug concentration, and not fluorescence activity, is the imaging parameter of interest. Simulation studies similar to those presented here can be repeated for any contrast agent and imaging geometry, facilitating a more informed approach to *in vivo* imaging.

An important issue not addressed in this study is the problem of distinguishing the absorption arising from the exogenous agent from endogenous absorption. This is not an issue for dynamic imaging, where changes in tissue absorption are measured; however, in the single-wavelength approach discussed here, static quantification of *in vivo* optical absorption offers no information on whether the source of the absorption is endogenous or exogenous. This leads to one of the undeniable advantages of fluorescence imaging; the measured signal is often produced entirely by the administered agent, provided appropriate excitation filtering and auto-fluorescence corrections are in place. However, multi-spectral approaches which use endogenous and exogenous extinction spectra as spectral prior information may be able to recover chromophore concentrations directly. This technique was developed as part of this thesis and is discussed in the next chapter.

Chapter Eleven: Direct recovery of contrast agent concentration using spectrally constrained image reconstruction: A feasibility study

Chapter 10 showed that diffuse measurements on the tissue surface may be more sensitive to changes in absorption than fluorescence in tissue volumes with high fluorophore concentrations. Despite the advantage in sensitivity, transmission measurements that are not resolved in time or wavelength contain no information on whether the source of the absorption derives from endogenous or exogenous chromophores. Thus, single wavelength absorption and scattering tomography of optical properties is not useful in this context without data measured before and after drug administration¹¹⁷. It is reasonable to assume that incubation times of more specifically targeted optical probes will exceed constraints on imaging session time with the subject immobilized, precluding pre and post contrast administration data acquisition. However, spectral priors-based image reconstruction algorithms that exploit the known extinction spectrum of the exogenous and endogenous chromophores may be capable of quantifying drug concentration without pre and post-injection image differencing.

The mathematical framework for spectrally-constrained imaging of multiple tissue chromophores was introduced and developed in Chapter 3. Briefly, prior knowledge of the molar extinction coefficients for the constituent tissue chromophores,

including any exogenous agent, as well as prior approximations about the photon scattering behavior are incorporated into the inversion formulation. Thus, values of concentration for all chromophores as well as scattering parameter values are recovered simultaneously, constrained by the extinction spectra and empirical Mie scattering relationship.

In practice, contrast agents with large extinction coefficients are needed to ensure that the drug's spectral features contribute to the overall tissue absorption spectrum. Extinction coefficient values for LuTex are shown in Figure 11.1(a) along with the absorption spectra of endogenous chromophores. Figure 11.1(b) demonstrates how the overall tissue absorption properties change with the introduction of LuTex at a concentration of 300 nM, assuming endogenous tissue consists of 0.01 mM oxy- and deoxyhemoglobin and 50% water. Scatter amplitude and power are each assumed to be 1. The strong absorption peak of LuTex at 735 nm has a substantial impact on overall tissue absorption at this concentration and therefore may be suitable for spectrally constrained imaging. Similarly, the same concentration of ICG also impacts tissue absorption due to its large extinction coefficient, peaked at 785nm, making it another candidate for the imaging technique.

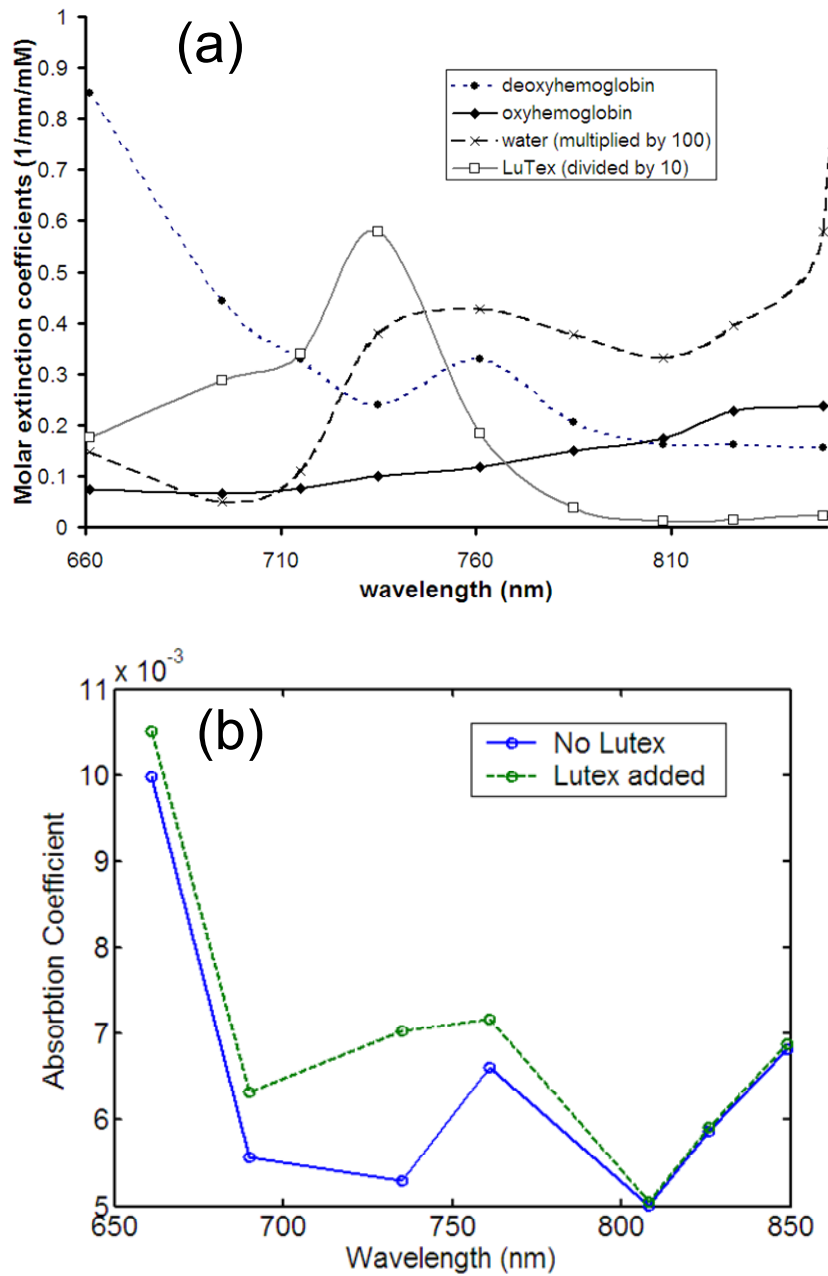


Figure 11.1. Molar extinction spectra of hemoglobin, water, and LuTex are shown in (a). LuTex has a strong absorption peak at 735nm, which has a substantial impact on tissue absorption at concentrations of 300 nM, (b).

In this pilot study, simulated data generated from realistic 2D breast tissue domains were used to demonstrate the simultaneous recovery of images of endogenous

and exogenous chromophore concentrations, and scattering parameters using LuTex and ICG as exogenous agents. Frequency domain data measured through tissue phantoms were also used to determine whether this approach can be used to extract LuTex concentration. Finally, a method to combine the multi-spectral absorption data with fluorescence emission data to produce images of both ICG concentration and fluorescence activity is introduced and discussed.

11.1 Chromophore recovery using spectrally constrained reconstruction

11.1.1 Methods

11.1.1.1 Simulations: LuTex and ICG imaging

The test geometries were derived from an axial MR image of a human breast identical to that used in section 6.1.1. An abnormality was artificially added to simulate a malignancy within the fibro-glandular layer. Figure 11.2 provides the test field parameters or “true values” used in the LuTex example, including endogenous chromophores, scattering parameters, and an estimated concentration of Lutex ranging from 300 nM to 1 μ M. Simulated frequency domain transmission data was generated for eight wavelengths in the near-infrared, namely 661, 690, 735, 761, 785, 808, 826 and 849 nm and five percent amplitude and 1° phase normally distributed noise was added to the data at each wavelength.

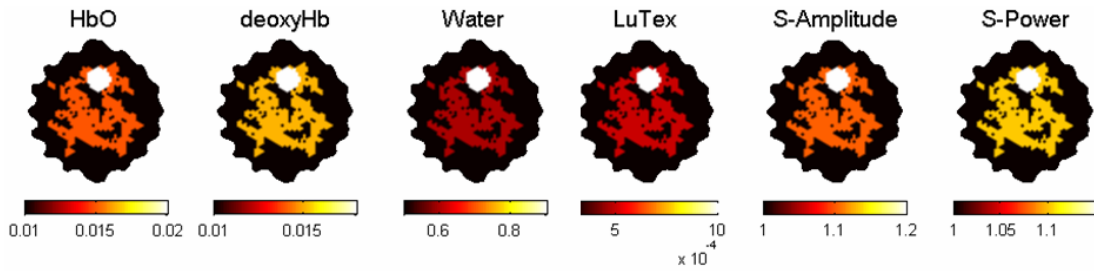


Figure 11.2. Target values of chromophore concentrations (mM) and scattering parameters for the simulated test domain (water is in percent). Lutex contrast is 3:1 for tumor-to-fatty layer and 2:1 for tumor-to-fibro-glandular layer.

A similar domain containing ICG in place of LuTex was also tested with the same noise parameters though different wavelengths. The target field for the simulated ICG phantom is provided in the results section alongside the associated reconstructed images.

11.1.1.2 Phantom data

The test phantom was a 91mm diameter homogeneous intralipid (1%) phantom containing oxygenated blood, at approximately 0.02mM, and different concentrations of Lutex, ranging from 50 nM to 1000 nM. Data was acquired using the PMT-based clinical frequency domain system described in section 2.2 using a tunable Ti:Sapphire laser source. Measurements of phase and amplitude at the 80 mHz laser pulse frequency were collected for 14 wavelengths: 690, 710, 730, 735, 750, 761, 770, 785, 790, 800, 808, 820, 826, 830, 835 and 849nm. Data-model fitting routines provide homogeneous fits for concentrations of the constituent chromophores as well as homogeneous estimates of scatter power and amplitude.

11.1.2 Results

11.1.2.1 Simulation results

Images reconstructed using data from all wavelengths simultaneously without spatial prior information (save for the outer boundary of the domain) are shown in Figure 11.5. The images are qualitatively reasonable, though betray the relatively low resolution characteristic of diffuse tomography. The fibro-glandular and tumor regions are readily discernable in all chromophore images and values for the endogenous chromophore concentrations are quantitatively typical and acceptable for this imaging approach. The recovered distribution of the contrast agent, Lutex, is also reasonable and overall image contrast is encouraging.

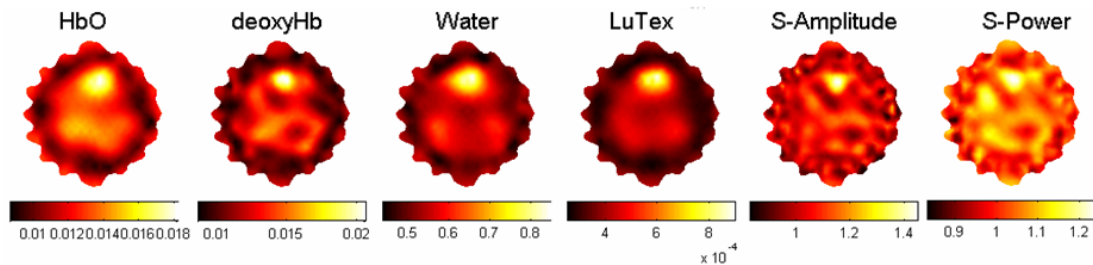


Figure 11.3. Images of chromophore concentrations (mM), percent water, and scattering amplitude and power recovered using spectrally constrained absorption tomography with only the outer boundary as a spatial prior.

The qualitative and quantitative accuracy of the images may be improved by incorporating interior tissue structural information in the reconstruction process. The spatial hard priors implementation collapses the reconstruction parameter space into homogeneous regions defined by the MR image segmentation, as described in 3.3.2. In this case, three regions exactly matching the true distribution were used. Reconstructed

images for the hard-priors algorithm are presented in Figure 11.4 and demonstrate precise recovery of most unknown parameters.

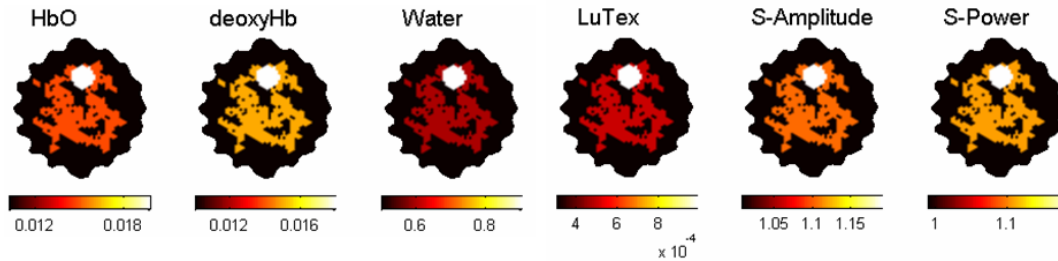


Figure 11.4. Images of chromophore concentrations (mM), percent water, and scattering amplitude and power recovered using spectrally constrained absorption tomography of Lutex with hard priors of the internal tissue structure.

A similar analysis was performed using ICG as the exogenous absorbing agent, results of which are presented in Figure 11.5. Assigned chromophore values vary slightly from the Lutex example, though are still in the range of reported *in vivo* concentrations. The wavelength range for this study was 690, 700, 730, 750, 770, 800, 820, 830 and 849 nm.

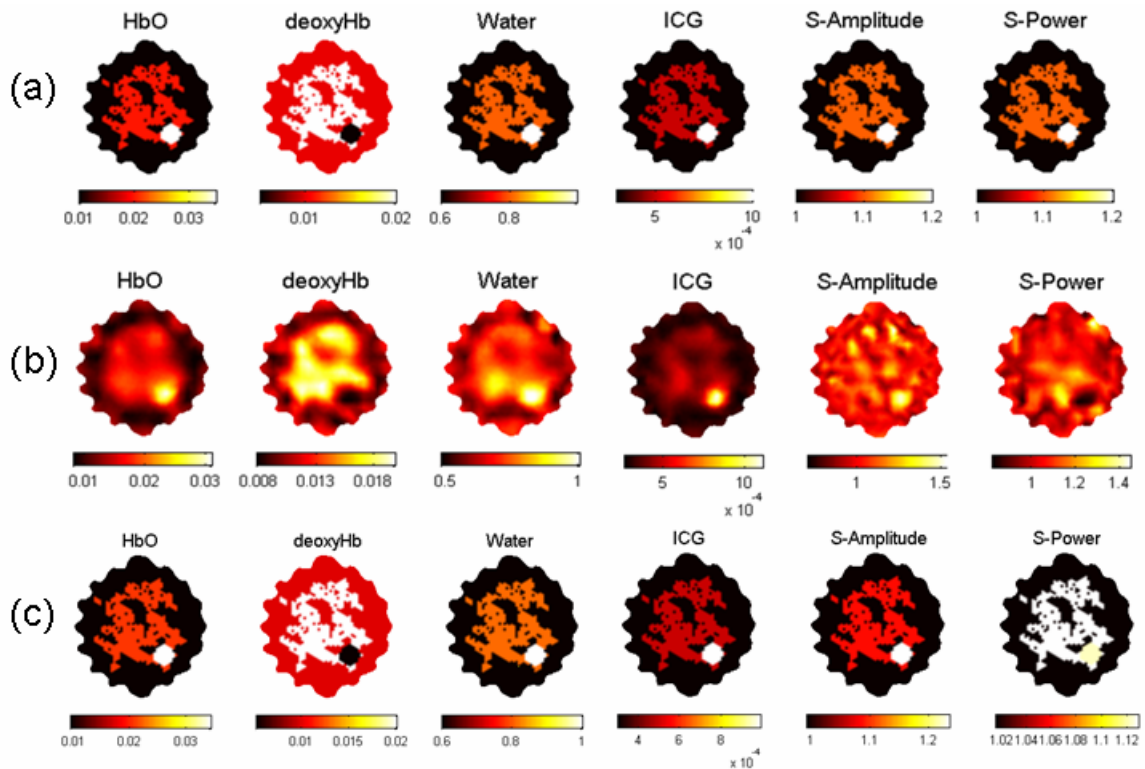


Figure 11.5. The spectrally constrained reconstruction technique applied to the domain containing ICG. The true values of chromophore concentrations (mM), percent water, and scattering amplitude and power provided in (a) were reconstructed without spatial priors (b) and with perfect hard priors (c).

11.1.2.2 Phantom results

Homogeneous fitting to the data collected at 14 wavelengths produced accurate values for Lutex concentrations above 100 nM, as shown in Figure 11.6. The calculated slope of the system response to Lutex concentration is 17.6% higher than the true slope, with an R^2 value of 0.99. Sensitivity to changes in concentration is questionable below 100 nM.

Intralipid, blood, Lutex

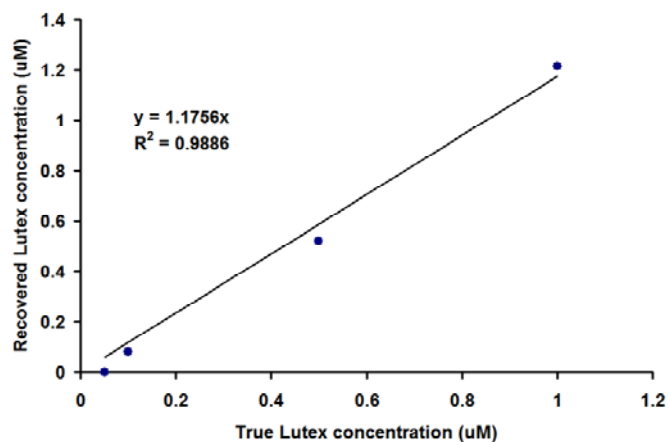
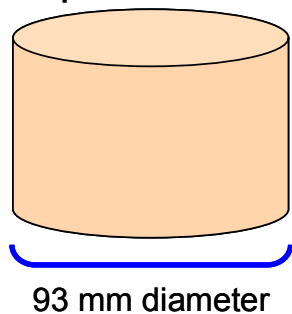


Figure 11.6. Quantification of Lutex concentration in homogeneous liquid phantoms using spectrally-constrained absorption tomography.

11.1.3 Discussion

Reconstructions of simulated noisy data at multiple wavelengths provided excellent image recovery of chromophore concentrations using the spectrally constrained technique, especially when hard prior tissue information was incorporated into the imaging algorithm. This was applied to both LuTex and ICG images for concentrations ranging from 300 to 1000 nM. Extrapolating these results to expected *in vivo* performance is difficult, though sensitivity studies in homogeneous phantoms is an appropriate first step. The phantom results shown here are encouraging for quantifying LuTex concentrations above 100 nM in large tissue volumes but provide little information on the imaging performance of this approach in heterogeneous volumes.

Though frequency domain data was used here, the technique may also be applied to CW or combined CW/FD data and wavelength optimization studies, such as completed by Corlu et al.⁴⁵, may be beneficial to the development of an optimized imaging protocol. In particular, proper recovery of water content is often challenging given the lack of PMT

sensitivity above 850 nm, where water is the dominant absorber. Preliminary studies in our lab indicate that including a single wavelength of CW intensity around 900 nm with the FD data set improves image recovery of water content for endogenous chromophore reconstructions. Presumably, this would also benefit cases in which exogenous absorbers are considered.

Further analysis is required to validate the approach and determine under what circumstances it may be useful. Imaging heterogeneous gelatin-blood phantoms with different background concentrations and inclusion contrasts will be critical for proper validation. The hard limits of measurement sensitivity between fluorescence and transmission detection determined in Chapter 10 will come into play when defining a potential clinical role for this approach.

11.2 . Future directions: Combining recovered chromophore concentrations and fluorescence data to reconstruct fluorescence yield

A natural extension of the approach described in the previous section is to use the recovered values of chromophore concentration to reconstruct images of fluorescence yield. Figure 11.7 schematically outlines a procedure to use the results of spectrally resolved absorption tomography in fluorescence tomography reconstructions. In short, recovered chromophore concentration and scattering parameter values are used to calculate the excitation and emission tissue optical properties, and the recovered concentration of the exogenous contrast agent is used as the initial estimate for the fluorescence reconstruction.

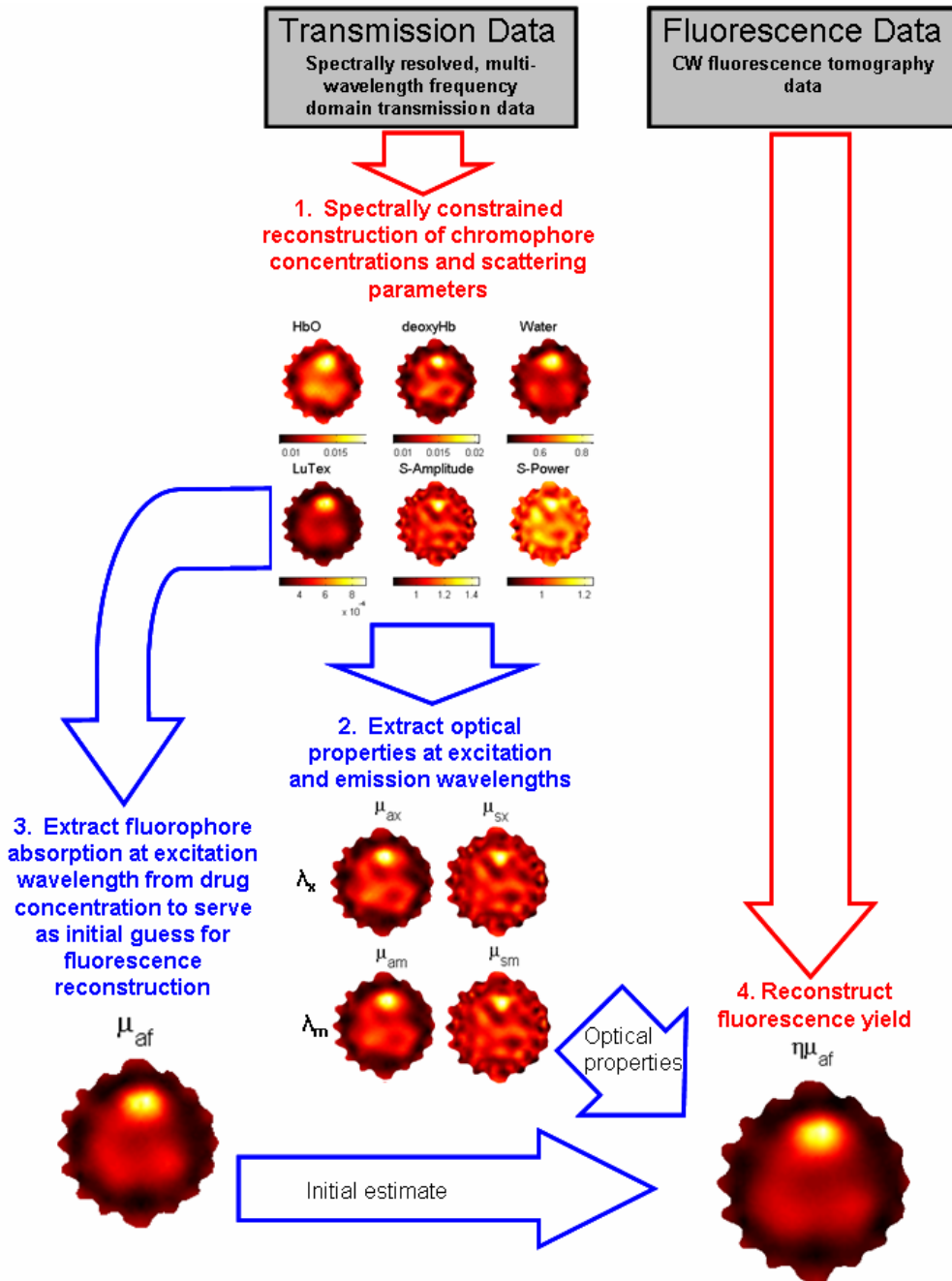


Figure 11.7. A method for using recovered chromophore concentrations and scattering parameters to reconstruct for fluorescence yield.

Following the procedure outlined in Figure 11.7 and using the recovered values of chromophore concentration in Figure 11.5(b) to determine the background optical properties and fluorescence yield initial estimate, an image of fluorescence yield was reconstructed and presented in Figure 11.8 along with cross sectional plots of the true and recovered values. For comparison, the image of ICG concentration determined directly from the spectrally resolved image reconstruction approach is also shown. These results indicate that little is gained from adding fluorescence imaging if drug concentration is the primary imaging objective. Similar results obtain for hard priors based reconstruction following the same procedure. Values of drug concentration are so precise in the hard-priors implementation, the subsequent fluorescence reconstruction does not improve the quantification of drug concentration in this case. Alternatively, if fluorescence activity is the critical imaging parameter, spectrally constrained reconstruction of the chromophore concentration can improve the fluorescence yield images over algorithms that use only the excitation and emission wavelengths for image recovery. This anecdotal evidence must be confirmed in a systematic study, most appropriately accompanied by a methodical comparison of absorption and fluorescence imaging. These studies are left for future work.

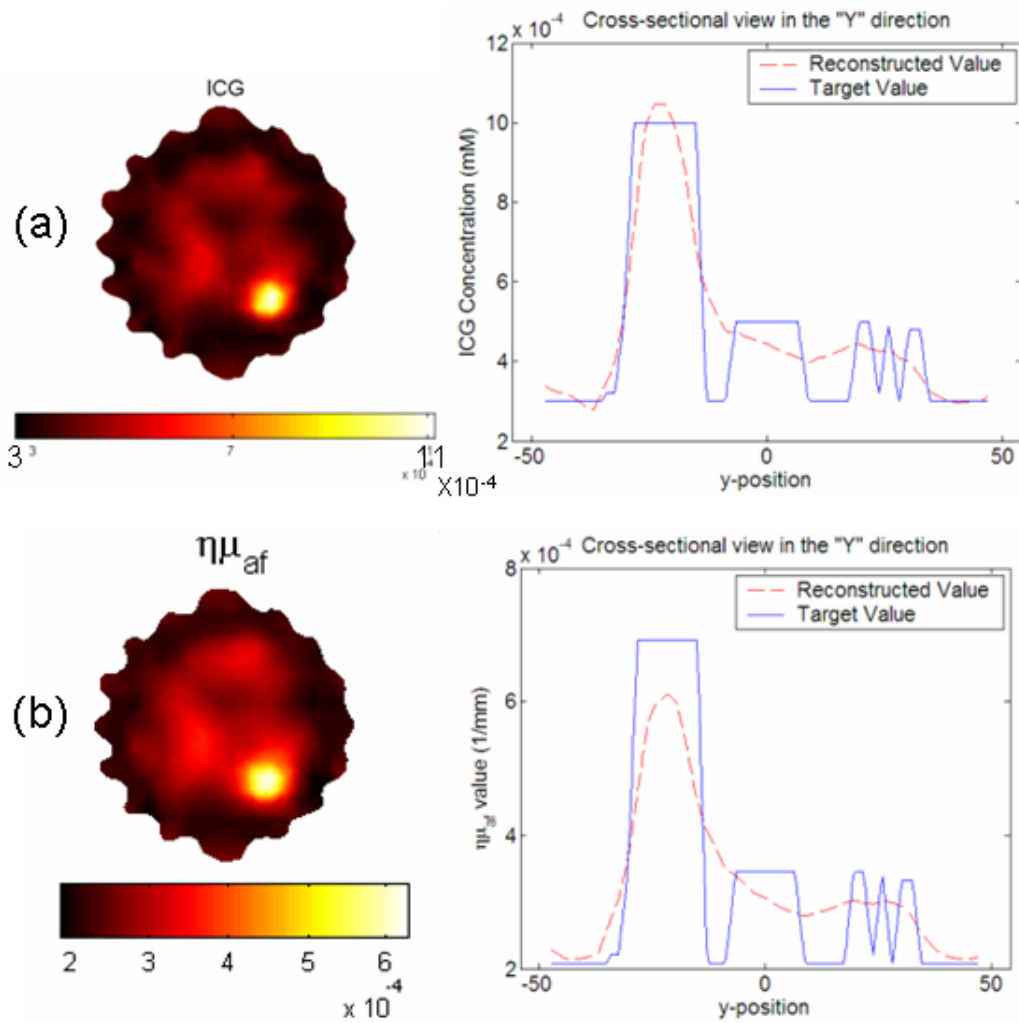


Figure 11.8. An image of fluorescence yield recovered in the manner described in Figure 11.7 (b) seems to add little in terms of contrast quantification of ICG, as compared to the image of ICG concentration recovered using the spectrally constrained absorption reconstruction technique (a).

Chapter Twelve: The Beam Softening Effect: Spectral Distortion of Luminescence in Tissue

In this chapter, the influence of tissue optical properties on the shape of near-infrared (NIR) fluorescence emission spectra propagating through multiple centimeters of tissue is investigated. Experimentally measured fluorescence emission spectra measured in 6 cm homogeneous tissue phantoms shows dramatic spectral distortion which results in emission peak shifts of up to 60 nm in wavelength. Measured spectral shapes are highly dependent on the photon path-length and the highly scattered photon field in the NIR amplifies the wavelength-dependent absorption of the fluorescence spectra. Simulations of the peak propagation using diffusion modeling describe the experimental observations and confirm the path-length dependence of fluorescence emission. Spectral changes are largest for longer path-length measurements, and this will be most dominant in human tomography studies in the NIR. Spectrally resolved or multi-wavelength band-pass measurements are required to detect these changes, and may be essential to interpret such effects, which would otherwise be attributed to erroneous intensity measurement. This phenomenon is analogous to beam hardening in x-ray tomography, which can lead to image artifacts without appropriate compensation. The peak shift toward longer wavelengths, and therefore lower energy photons, observed for NIR luminescent signals propagating through tissue may readily be described as a “beam softening” phenomenon.

12.1 Introduction

While fluorescence molecular imaging and spectroscopy systems for use in small animals^{46, 103, 118-122} have evolved to the point of commercial availability and clinical trials in humans are underway²⁸, some of the more subtle complexities of the signal acquisition remain to be examined. One important consideration that has not been investigated in detail, especially in the near-infrared (NIR), is the interaction between the remission spectrum of the reporter and the intervening tissue through which the light transport occurs prior to detection. In particular, changes in spectral emission can be detected which are intimately linked to the tissue optical properties and the path-length of signal travel involved. In this study, a systematic evaluation of NIR spectral shift has been completed using simulations and tissue phantoms.

As interest in fluorescence spectroscopy for tissue diagnosis grew^{16, 18, 123-125}, researchers began to develop methods to compensate for spectral distortion due to tissue optical properties in order to recover intrinsic fluorescence spectra. Original work reported by Wu et al.¹²⁶, Durkin et al.¹²⁷ and Richards-Kortum et al.¹²⁸, examined photon migration, Kubelka-Munk and exponential models, respectively, to extract intrinsic autofluorescence signal from the measured distorted spectrum emitted from tissue. In 1996, Durkin et al.¹²⁹ compared several modeling approaches and determined that a partial least squares method yielded an accurate spectral correction. Analytical expressions derived by Gardner et al.¹¹ were used to extract spectra measured through tissue samples on the order of 1 cm. In 2001, Müller et al.¹² provided a comprehensive investigation of the effects of absorption and scattering on intrinsic fluorescence extraction based on a photon migration model.

All of these efforts were focused on tissue spectroscopy in the visible spectrum where autofluorescence is high and the significant photon absorption restricts the distances over which light signals can be measured to a few centimeters. However, path-lengths of measurable signal through tissue are significantly longer in the NIR due to the lower absorption and higher scattering properties. While Patterson and Pogue¹³ developed a general construct for modeling fluorescence propagation through homogeneous tissues based on diffusion theory, they did not consider the spectral distortion in the detected emission directly. Some investigators^{130, 131} have recognized the inherent depth information contained in the spectral distortion and have demonstrated the ability to localize fluorescent layers in tissue simulating phantoms by calculating the ratio of emitted intensity at different wavelengths.

Most experimental fluorescence tomography systems employ one or more band-pass or long-pass filters to separate the excitation signal from the fluorescence emission. Rarely are these systems developed with the capability to resolve the full fluorescence emission spectrum. Ignoring the spectral changes in deep tissue imaging may have implications for quantitative accuracy of the recovered images, especially for systems that use relatively large emission wavelength ranges. Since wavelength-dependent attenuation of the fluorescence emission increasingly distorts the measured spectrum as photon path-length increases, the effect is expected to become more pronounced when imaging through larger tissue domains, such as the human breast.

This chapter investigates NIR fluorescence emission distortion using homogeneous turbid phantoms and diffusion based modeling. Here, the model system is extended to calculate spectrally resolved emission spectra at discrete wavelengths based

on fluorescence spectra of dilute solutions and wavelength-dependent optical properties of tissue. Experimentally measured spectra are compared with spectra generated using the model system. Phantom geometries used are representative of the dimensions to be encountered in tomographic imaging of fluorescence activity *in vivo* and the potential implications that spectral distortion has for fluorescence tomography are discussed.

12.2 Experimental Details

12.2.1 Phantom design

Liquid and gelatin phantoms, described in Chapter 4 were used for this study. Liquid phantoms contained 1% intralipid in water and 5 μM Lutetium Texaphyrin while gelatin phantoms were produced following the protocol outlined in Chapter 4. In both cases, no additional absorbers were added. Photographs of liquid and gelatin phantoms used in this study are shown in Figure 12.1.

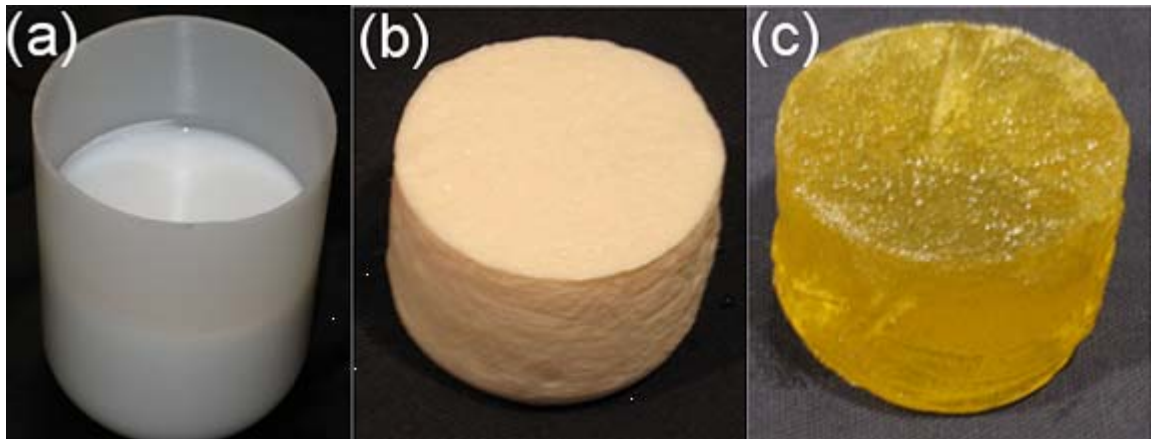


Figure 12.1. Photographs of phantoms used in this study. A liquid intralipid-based phantom (a) readily allows changing of the fluorophore concentration while gelatin phantoms containing TiO_2 scatterer shown in (b) eliminate the need for an external container. Gelatin phantoms without scattering material were also used to assess the emission spectra without scatter (c).

The fluorescent drug used in this study was Lutetium Texaphyrin (LuTex), a water soluble dye developed as a photodynamic therapeutic sensitizer. It is a texaphyrin based molecule with lutetium in the center to induce a large triplet state splitting⁶⁸. The absorbance and fluorescence emission peaks in dilute solution occur at approximately 735 nm and 750 nm, respectively, as shown in Figure 4.1. Figure 12.2 shows a normalized fluorescence emission spectrum of LuTex in a dilute solution of DI (deionized) water measured by a standard fluorometer (Yvon Jobin).

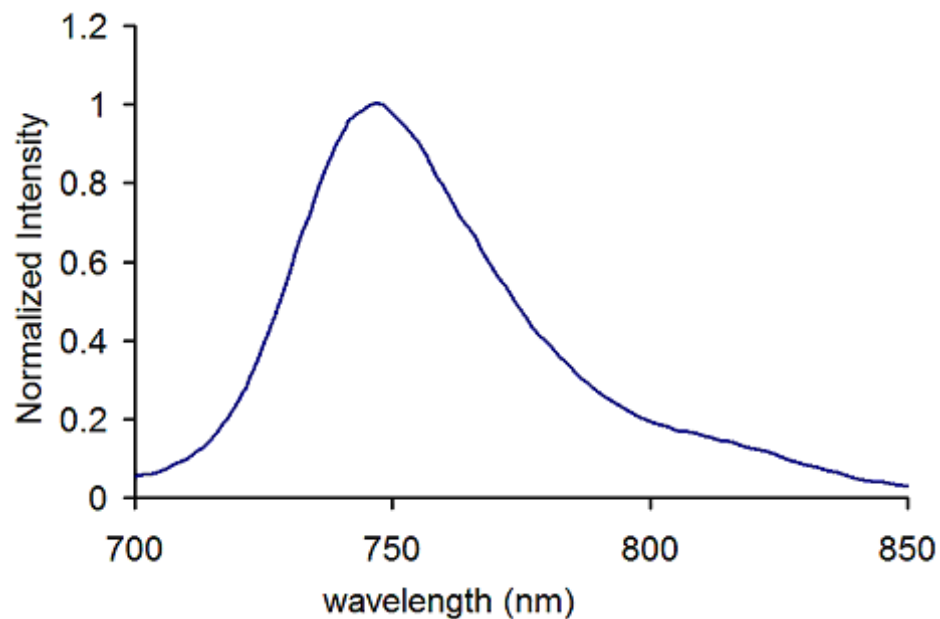


Figure 12.2. Normalized LuTex fluorescence emission as measured in dilute concentration (2 μ g/ml) in deionized water.

12.2.2 Modeling Light Propagation

Extending the FEM system to model spectral changes of luminescence emission is rather straightforward. Here, the coupled system of diffusion equations presented

earlier are re-written for the continuous wave case, matching the instrument's CW capability:

$$-\nabla \cdot \kappa_x(r, \lambda_x) \nabla \Phi_x(r, \lambda_x) + (\mu_{ax}(r, \lambda_x)) \Phi_x(r, \lambda_x) = q_0(r, \lambda_x) \quad 12.1$$

$$-\nabla \cdot \kappa_m(r, \lambda_m^i) \nabla \Phi_{fl}(r, \lambda_m^i) + (\mu_{am}(r, \lambda_m^i)) \Phi_{fl}(r, \lambda_m^i) = \Phi_x(r) \eta(\lambda_m^i) \mu_{af}(r) \quad 12.2$$

Unlike the excitation field, which is assumed to arise from a light source at a single excitation wavelength, the emission spectrum of the fluorophore can cover several hundred nanometers. To account for this spectral bandwidth in the numerical model, Equation (12.2) is discretized over a wavelength range indicated by the index i . Though the excitation field and fluorophore absorption coefficient in the source term of Equation (12.2) do not depend on emission wavelength, the fluorescence source strength varies with wavelength based on the shape of the emission spectrum of the fluorophore which is introduced into the model through a wavelength-dependent fluorescence quantum yield, $\eta(\lambda_m)$. The fluorescence emission then propagates through the tissue subject to wavelength-dependent optical properties, $\mu_{am}(r, \lambda_m)$ and $\mu_{sm}'(r, \lambda_m)$, which must be modeled to accurately describe the fluorescence spectrum measured at the tissue surface. In practice, this is accomplished by first calculating the excitation field in Equation (12.1), and then solving for the emission field in Equation (12.2) at wavelength λ_m^i for each i .

In this study, the emission spectrum of LuTex was modeled from 700 nm to 850 nm in intervals of at least 10 nm. Some intervals were smaller given the availability of information at additional wavelengths. The extinction spectrum of LuTex was measured directly using a Cary 50 UV-Vis spectrophotometer (Varian, Inc., Palo Alto CA). Absorption coefficients at each wavelength were calculated as a sum of the constituent

chromophores, usually oxygenated and deoxygenated hemoglobin, water, and the exogenous agent of interest, however, since whole blood was not used in the phantom experiments, only water and LuTex were considered in the numerical portion of the study. Published values for the extinction spectrum of water, compiled by Prahl⁷³, were used to calculate the absorbing contribution of water. Scattering properties of tissue in the NIR were modeled using an empirical approximation integrated into the NIRFAST software, as described in Chapter 3 and elsewhere⁴⁴.

12.3 Results and Discussion

12.3.1 Phantom results

Emission spectra measured through homogeneous gelatin and water phantoms containing 5 μM LuTex and no scattering media are presented in Figure 12.3. The phantoms were 60 mm diameter cylindrical shapes with sources and detectors around the outer surface in one plane. Data presented are for different source-detector positions on the boundary. As the photon path-length increases, the influence of the media changes the emission spectra modestly, however, in general the emission peak is not significantly distorted when measured through these phantoms.

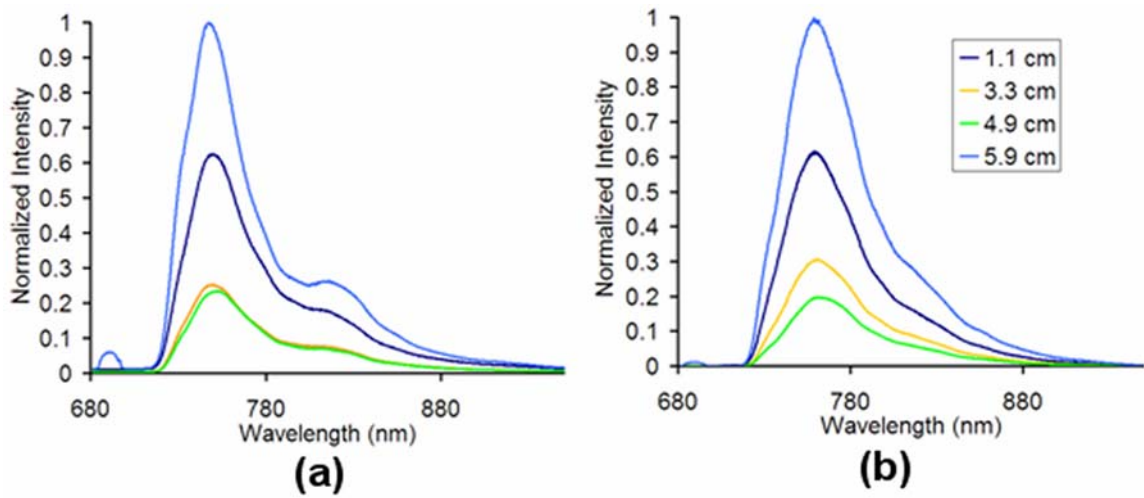


Figure 12.3. Fluorescence emission of 5 uM LuTex measured in the multi-spectrometer system in phantoms composed of (a) gelatin and (b) De-ionized water. These spectra represent the non-turbid baselines since neither phantom contained significant scattering media.

In turbid phantoms of the same size, the emission spectra changes dramatically. LuTex emission spectra measured for a range of source-to-detector distances around a cylindrical turbid phantom are presented in Figure 12.4. Data for spectra measured through both gelatin and liquid phantoms are shown and illustrate the significance of the peak distortion through several centimeters of turbid media. Source-detector distances are approximately 1.1, 3.3, 4.9, and 5.9 cm for the spectra included in the figure. Within 1 cm, the measured fluorescence spectrum is similar to the dilute sample, though a secondary peak is evident around 800 nm in both phantoms. As the source-detector distance increases, the spectra are changed more dramatically. The secondary peak becomes increasingly prominent and as the propagation distance increases, the entire spectrum settles to a single peak at around 820 nm.

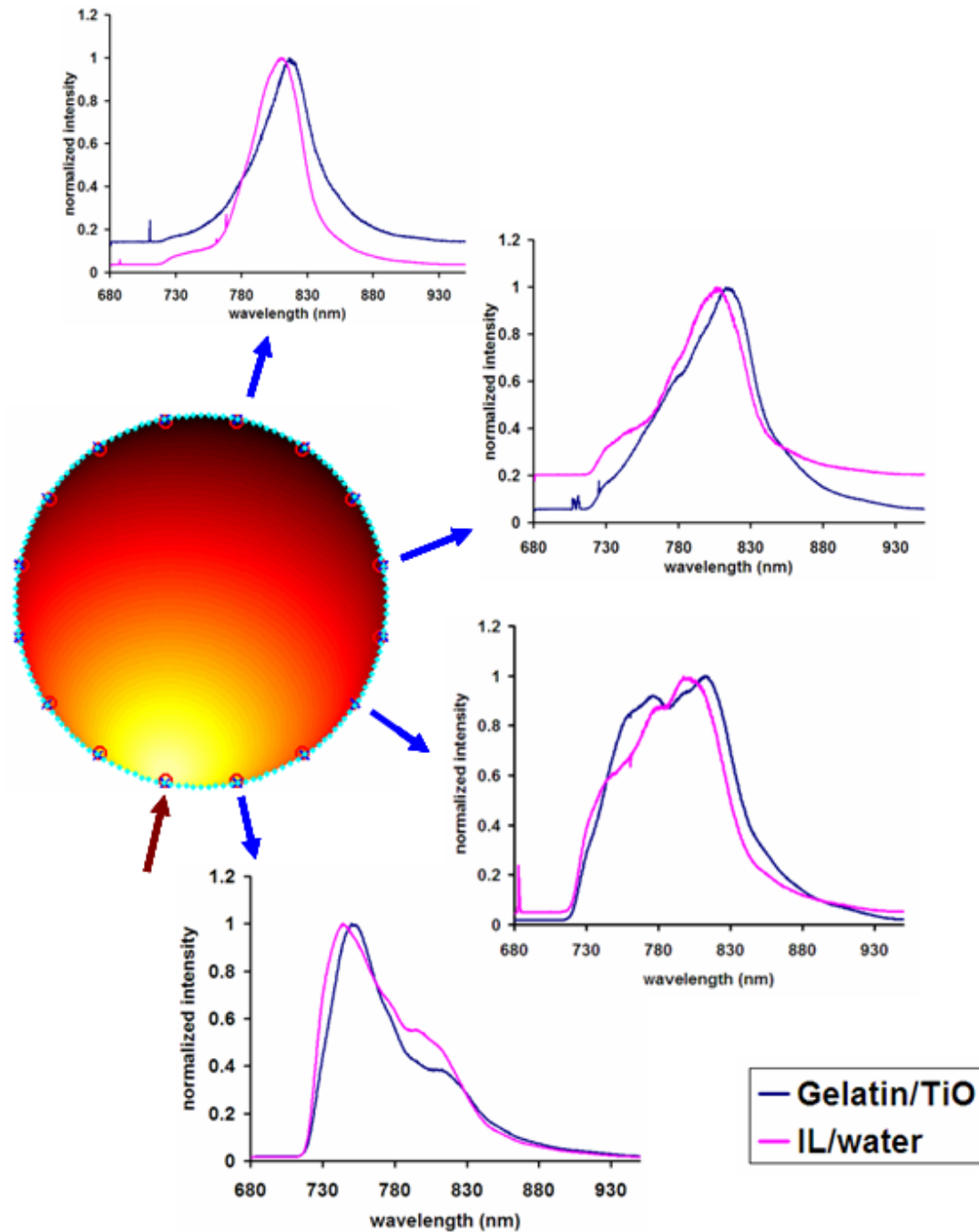


Figure 12.4. LuTex fluorescence emission experimentally measured at different source-detector distances in homogeneous scattering gelatin and intralipid based phantoms. The circular domain shown represents a cross-section of the cylindrical phantom, illustrating the input (red arrow) and output measurement sites (blue arrows). For illustration purposes, the intensity (shown as logarithm of intensity) of the diffuse excitation field is plotted in the circular region.

Photon path-length may be altered by source-detector geometry or by changes in scattering properties. Figure 12.5 demonstrates the influence of intralipid concentration on the measured emission spectrum. The spectral changes observed as result of increasing intralipid concentration are similar to those observed when source-detector distance is increased, as expected.

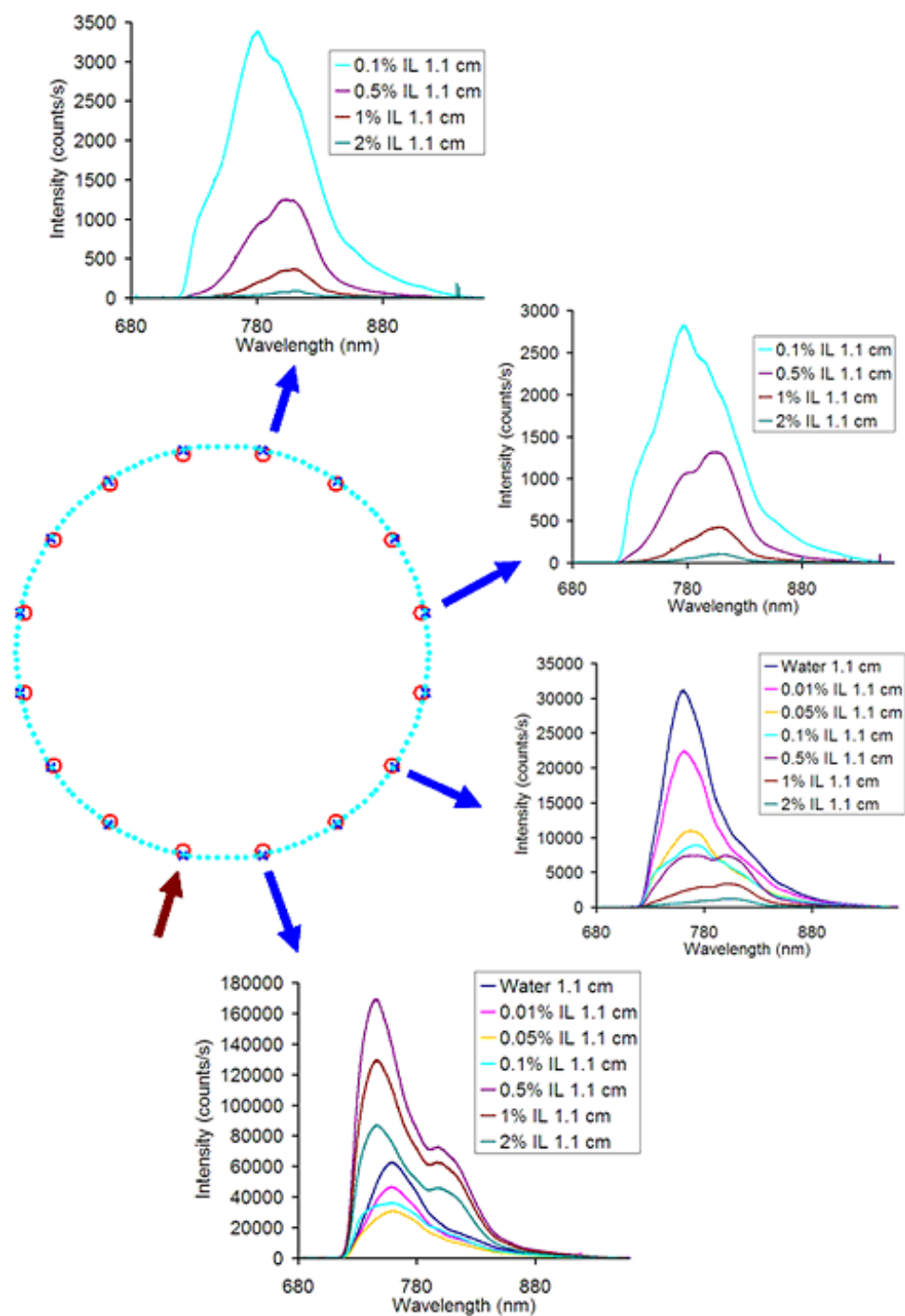


Figure 12.5. Fluorescence emission spectra through a liquid phantom of DI water and varying concentrations of intralipid are shown. Only spectra measured through intralipid concentrations of 0.1% and above are shown for the two detectors farthest from the source.

12.3.2 Diffusion modeling

When modeling photon propagation through the phantoms, it was assumed that the dominant absorbers were water (100%) and LuTex. Extinction spectra of water and LuTex were used to calculate the absorption coefficients at the discrete wavelengths across the range covered by the emission spectrum. These values are plotted as a function of wavelength in Figure 12.6 and illustrate the large change in absorption due mostly to the fluorophore's absorbance. These values were used to determine the fluorescence intensity at each wavelength throughout the emission spectrum.

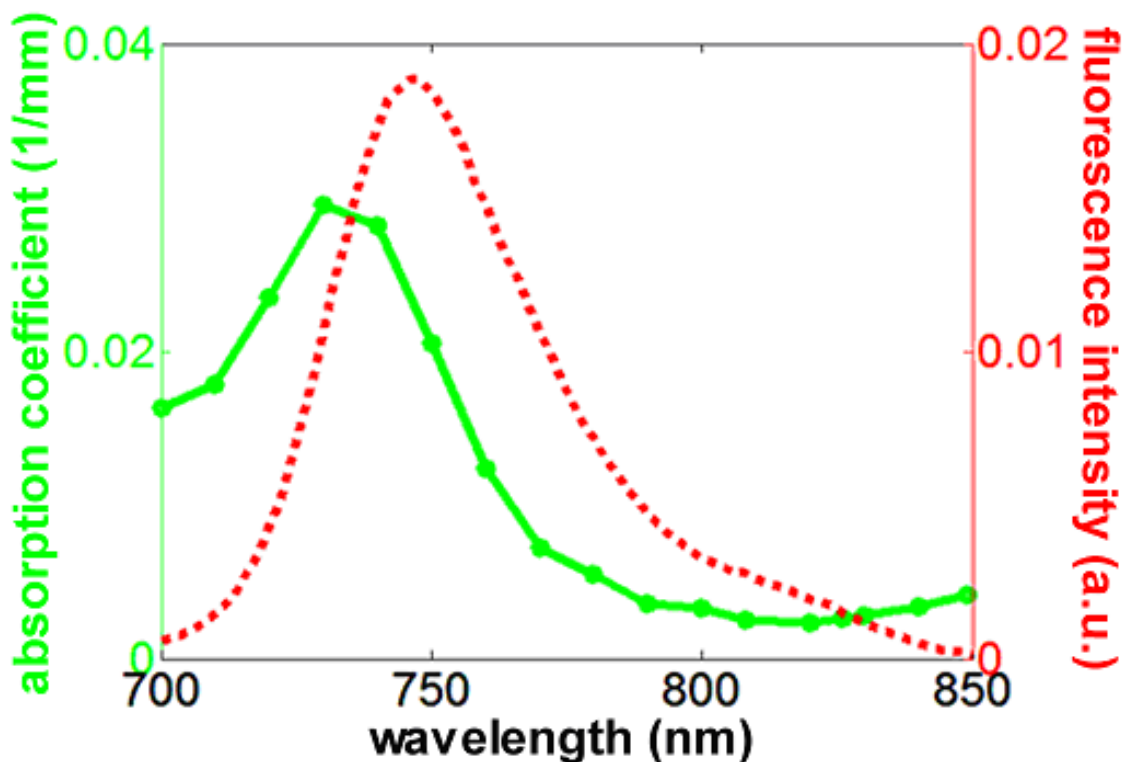


Figure 12.6. Absorption coefficients of 100% water and 300 nM LuTex is plotted for discrete wavelengths (green line with data points), with LuTex fluorescence emission (red dotted line) in dilute solution, indicating the overlap in absorption and emission at the shorter wavelengths from 700 to 750 nm.

Emission intensities determined from the diffusion model at discrete 10 nm wavelength intervals from 700 to 850 nm are shown in Figure 12.7 for the same source-detector positions measured through phantoms and presented in Figure 12.4. Experimental data from intralipid phantoms is also plotted for comparison (blue line) and the red dotted line represents the fluorescence peak in a dilute solution. All spectra are normalized to their peaks. Significantly, the general trends recorded in the phantom experiments are also observed for the numerical model. At the detector nearest the source, about 1cm, the measured fluorescence emission peak is shifted about 10 nm to the red and a small secondary peak is visible at around 810 nm, similar to what was observed in the phantom data. This corresponds to a very small bump in the absorption spectrum at 800 nm, which emerges as a dip in the emission spectrum and creates the secondary peak. Increased source-detector distances result in more substantial changes to the emission spectrum, and an amplification of the influence of the small elevation in absorption at 800 nm. The fluorescence distortion recorded at the detector positioned just over 3cm from the source results in a peak around 790 nm and the 800 nm dip is more pronounced, producing a stronger secondary peak. The original peak at 750 nm is almost entirely absorbed. At longer source-detector distances, the emission peak settles at around 830 nm, similar to the phantom results, though the increase of absorption at 800 nm is more pronounced for the simulation results.

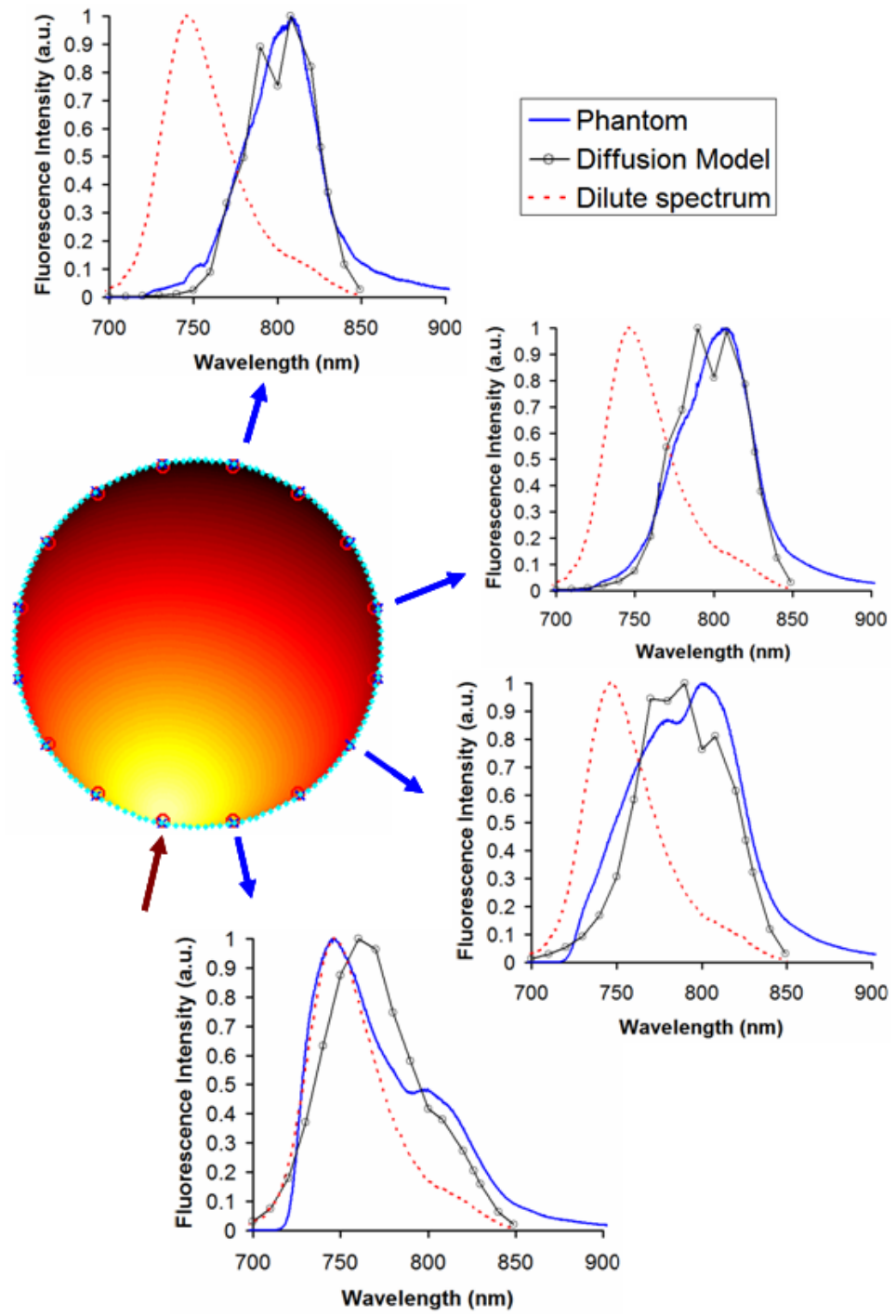


Figure 12.7. Diffusion based modeling of the fluorescence peak through a 60 mm diameter phantom, similar to Figure 12.4. The dilute emission spectrum of LuTex is shown as dotted lines, and the calculated emission spectrum from diffuse emission through the region is shown at discrete wavelengths (black circles). Experimental measurements are shown in blue for intralipid liquid phantoms. The circular domain shown represents a cross-section of the cylindrical phantom upon which the

intensity (logarithm) of the excitation field calculated from the diffusion equation is plotted for illustration purposes.

Qualitative assessment of Figure 12.7 reveals reasonable agreement between model and experimental observations in turbid phantoms in terms of emission spectrum shape, especially for detector locations far from the source. The presence of tissue scattering increases the path-length of photons propagating through the tissue, which in turn amplifies the influence of the tissue's absorption spectrum. The significance of the peak distortion also indicates that the primary source of fluorescence detected at the far-source detectors is generated close to the excitation source, where the excitation field is most intense, and then propagates through the tissue. This is an expected result since photon penetration depth at the excitation wavelength is lower than within the emission wavelength range due to higher absorption.

12.3.3 Implications for fluorescence tomography in deep tissue

Spectral distortion will depend on the fluorophore used, the tissue chromophore composition, and the excitation and measurement geometry. Other drugs used for imaging may experience less distortion than that associated with LuTex in these phantoms. However, the observed phenomenon has implications for quantitative fluorescence tomographic imaging. Clearly, the results presented here indicate that spectrally resolved or band-pass filtering is much preferred over long-pass filtering of fluorescence signals.

To demonstrate the extent to which spectrally unresolved data impact fluorescence imaging in deep tissue, a simulated example using an 86 mm circular test

domain to represent a coronal slice of a human breast is considered. To create a realistic test domain, tissue optical properties were calculated using the extinction spectra of the dominant endogenous chromophores and typical tissue concentrations of those chromophores. LuTex was assumed to be the exogenous fluorophore. Extinction coefficients of both endogenous and exogenous chromophores used in this example are shown in Figure 12.8 along with the spatial distributions of the chromophores for the coronal slice under consideration. In this case, two small Lutex heterogeneities were included at contrasts of just over 3:1 and 2.5:1 over the background. A large heterogeneity with contrast in hemoglobin and water was also added. Scattering properties were held constant in the domain.

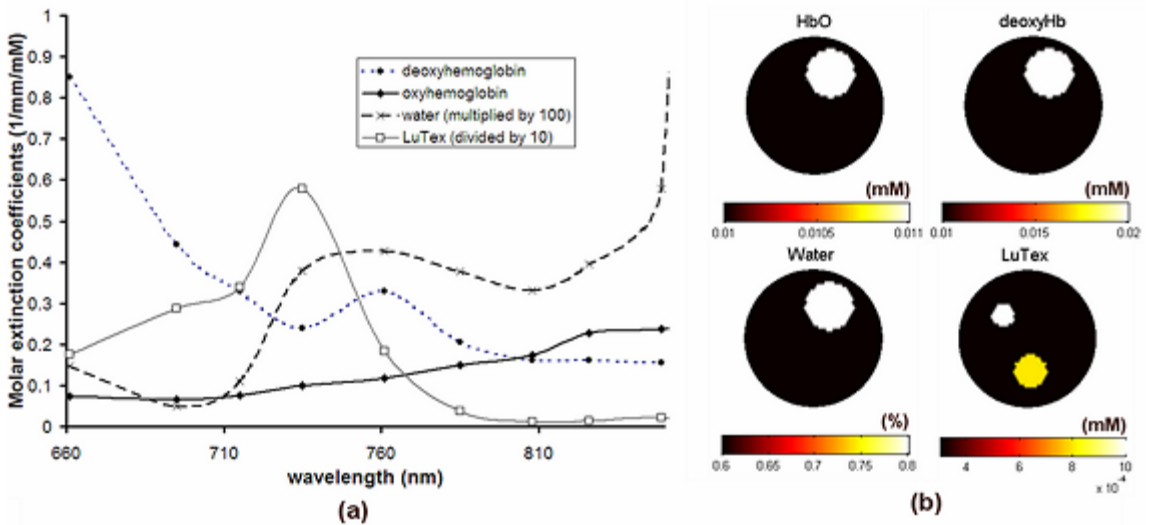


Figure 12.8. Extinction coefficients of chromophores used in the simulation are shown in (a). These are used to calculate tissue absorption coefficients at any wavelength within the NIR. The simulated domain contains contrasts in the various absorbing constituents, the spatial distributions of which are shown in (b).

Noise-free data was generated using the forward model described above and signal contamination due to excitation cross-talk and tissue autofluorescence was

ignored. Images of fluorescence yield were recovered using diffusion-based optimization reconstruction techniques described extensively elsewhere^{132, 133}. Identical reconstruction algorithms were used to consider data detected using one of two measurement approaches: The first approach assumed that measured data was fully wavelength resolved. The intensity recorded at the tissue surface at a single wavelength was extracted and optical properties at that wavelength were used in the model-based reconstruction algorithm. The second approach simulated an experimental system using only long-pass filters. Since spectral selectivity within the emission spectrum is impossible in this configuration, the measured spectrum at each detector was integrated. Tissue optical properties were chosen to match those at 750 nm, the fluorescence emission peak in dilute solution. Although the spatial heterogeneity of these optical properties was assumed to be known exactly at this wavelength, the lack of spectral resolution does not account for the variation of optical properties across the integrated spectrum.

Reconstructed images using both techniques (without spatial priors) are shown alongside the target image of fluorescence yield in Figure 12.9. The only difference between the two approaches arises from the handling of the detected fluorescence spectra. Images reconstructed using spectrally resolved data at a single wavelength show accurate recovery of fluorescence activity in the domain. Recovered values in the contrast enhanced regions are slightly off target values, though this is expected given the reported trade-off between enhanced region size and recovered contrast¹³⁴. Overall, quantification and localization are excellent. Certainly, this is to be expected given the simple geometry and noise-free data. However, the data-model misfit error introduced by

integrating the full spectrum is too much for the imaging algorithm and complete breakdown in imaging performance is observed, even for this relatively simple domain. The data provide no ability to localize or quantify fluorescence contrast enhancement. The failure of the algorithm using these data indicates that the long-pass filtering approach is intractable for experimental imaging. The extent to which this applies can be investigated by varying the wavelength range over which the spectrum is integrated to determine the widest filter band width at which image artifacts are insignificant.

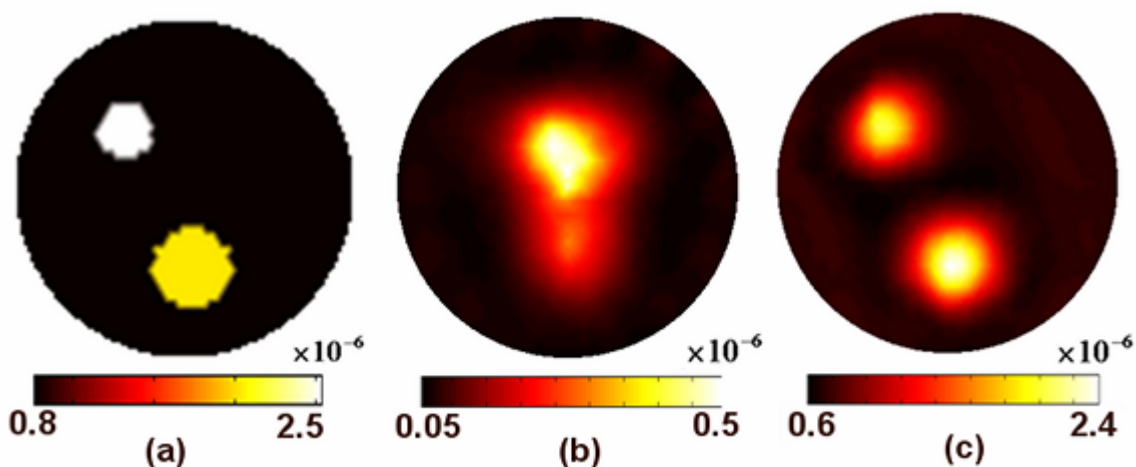


Figure 12.9. Fluorescence yield of LuTex is calculated from the drug concentration and the fluorescence quantum yield. Based on the concentration of LuTex assumed in Fig. 9, the target fluorescence yield is shown in (a). Reconstructing images from data collected with long-pass filtering can be an intractable problem as shown in (b), while resolving the emitted spectrum allows accurate recovery of the true fluorescence activity, as shown in (c). All images shown are in units of mm^{-1} .

The dramatic influence of chromophore absorption on the fluorescence spectrum leaving the tissue clearly indicates that the spectral shape contains information related to the location of the emitting source. It is reasonable to postulate that this information can be exploited to improve tomographic fluorescence imaging *in vivo*, presuming spatial

distributions of tissue chromophore concentrations are known a priori and the measured emission spectrum contains insignificant background signal. Similar approaches have been used in bioluminescence imaging of small animals^{135, 136} and may easily be adapted to fluorescence image reconstruction.

12.4 Summary

The problems of spectral shift are well known in many imaging applications such as x-ray computed tomography, where high atomic number materials can cause a larger than expected attenuation of the longer wavelength photons, and shift the spectrum to higher energies, a phenomenon known as beam hardening¹³⁷. Luminescent peaks propagating through tissue in the NIR, on the other hand, exhibit shifting towards lower energy photons, a phenomenon which softens the photon field. The principles in both cases are quite similar in that the spectrum to be detected is not attenuated equally as it traverses the medium.

A dramatic fluorescence emission peak shift in the NIR was demonstrated in tissue simulating phantoms, and this effect was especially pronounced when the tissue path-lengths over which the light signal is were relatively larger. Thus, the effect will likely have a greater impact on human imaging than small animal applications. The influence of tissue absorption was shown to produce the spectral distortion, an effect amplified by increasing photon path-lengths caused by tissue photon scattering or extended source-to-detector distances. Emission spectra escaping the tissue phantom can be modeled reasonable well using an FE formulation of diffusion theory, especially for source-detector distances over 2 cm. These spectral changes should be considered for

fluorescence tomographic imaging through several centimeters of tissue. Use of spectrally resolved detection allows quantification of this change, and may be the only reliable way to track intensity changes which would otherwise appear erroneous.

Chapter Thirteen: Assessing imaging performance: Contrast-detail analysis for fluorescence tomography

In this chapter, the fluorescence tomography reconstruction algorithm is evaluated in the context of size-contrast analysis, and the expected limits of image recovery are discussed. Other researchers have provided case examples to illustrate the accuracy and precision of select images, but few studies have addressed the limits of imaging performance in a systematic manner, following the conventions of standard medical imaging practice. Graves et al. examined the limits of detectable contrast for a particular sized object and the spatial resolution limits for a particular contrast level for their system configuration.⁹⁸ The natural extension of that work is to fully consider the known trade-off between an object's size and contrast, in terms of detectability. Contrast-detail analysis can be used to systematically define three imaging performance regimes; a spatial resolution limited regime, a signal-to-noise (SNR) limited regime, and a transitional regime which describes the trade-off between object size and contrast.

Contrast-detail analysis is commonly used to determine the performance of medical imaging systems. Such performance measurements seek to determine the contrast thresholds for an imaging system, providing quality assurance, optimization, and inter-system comparisons. Determining the detection threshold for a given range of

object diameters can generate limits on minimum detectable object size and contrast. Beginning in the late 1970's, contrast-detail analysis has been applied to assess computed tomography¹³⁸⁻¹⁴⁴, ultrasound¹⁴⁵⁻¹⁴⁸, mammography¹⁴⁹⁻¹⁵¹ and fluoroscopy¹⁵²⁻¹⁵⁵ systems. Since 2000, there has been a fair amount of activity involving contrast-detail analysis, mostly due to the rapid development and high interest level in digital radiography. These recent applications have sought to a) compare digital systems to film-screen, b) assess acceptable image compression for storage and viewing, and c) determine appropriate viewing conditions/media.¹⁵⁶⁻¹⁶³

Contrast-detail studies typically involve a tissue simulating phantom designed specifically for the system being tested. The phantom contains a series of circular objects, usually in a regularly spaced pattern, representing a range of contrasts and sizes. The contrast mechanism is determined by the imaging modality, i.e., for standard radiography, contrast is a function of linear attenuation coefficient. Examples of contrast-detail phantoms are shown in Figure 13.1 for planar x-ray and ultrasound imaging systems and similar phantoms are commercially available for most conventional clinical imaging systems.

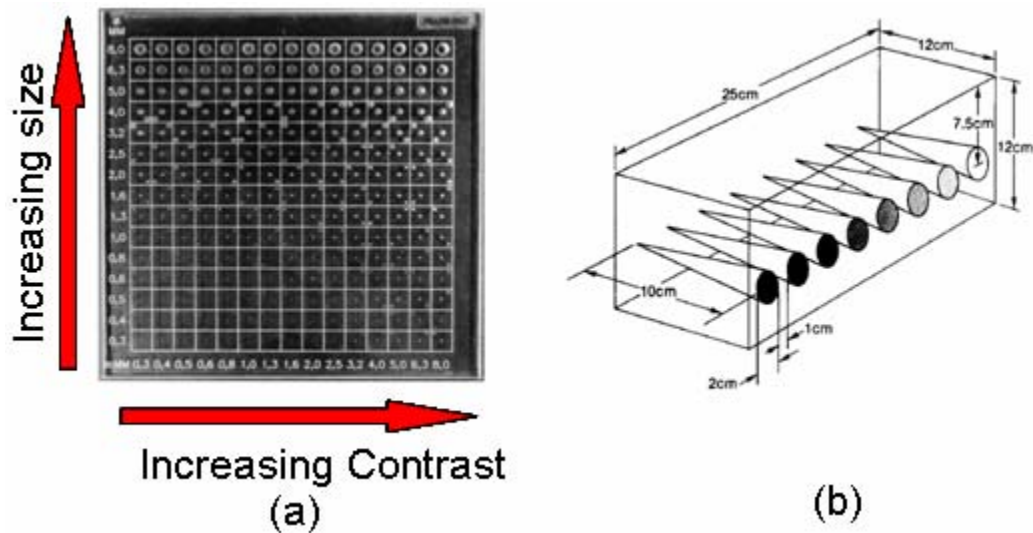


Figure 13.1. Examples of contrast-detail phantoms for chest x-ray¹⁶² (a) and ultrasound¹⁴⁷ (b) imaging. The ultrasound phantom contains a series of cones produced with different acoustic impedances. The diameter of the imaged object is varied by imaging different cross-sections of the cones.

In general, contrast is defined as

$$C = \frac{X_1 - X_2}{X_1} \quad 13.1$$

where X_1 is the background value and X_2 is the object value. In practice, the C-D phantom is imaged by the system under investigation and observers, or image readers, determine the “threshold contrast” for each disk size, or “threshold diameter” for each contrast level. The threshold represents the limit of object perceptibility. Plotting the threshold contrasts as a function of detail (size) produces the contrast-detail curve which can represent the useful resolution limits of the imaging system, as illustrated in Figure 13.2. Note that curves closer to the lower left portion of the graph indicate better contrast

resolution. This type of analysis can be applied in a variety of ways to improve the system or compare its performance characteristics to other system designs, the latter being the application for the curves in Figure 13.2.

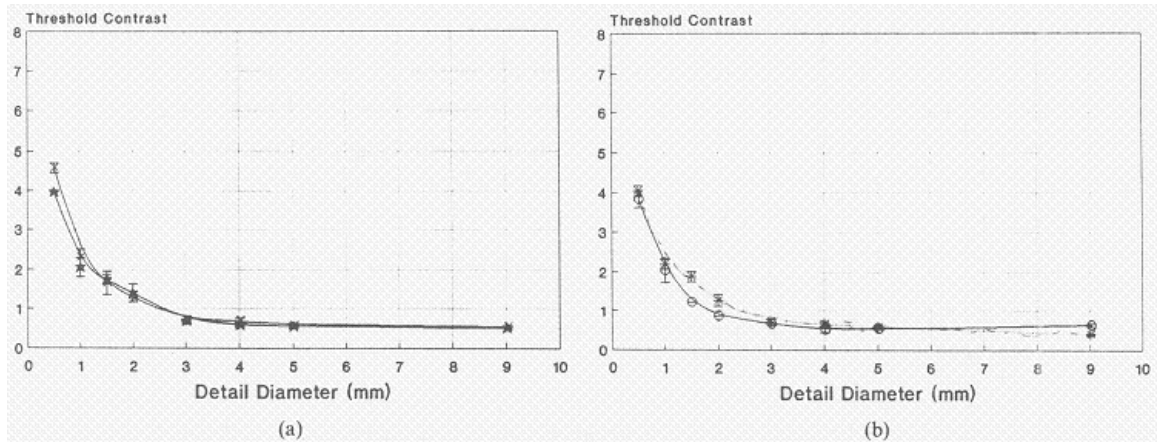


Figure 13.2. Contrast detail curves used to compare two film-screen combinations for planar x-ray imaging, reproduce from Thompson and Faulkner¹⁶⁴. The y-axis represents true object contrast. Plotted curves represent the threshold for detecting an object of a given size and object. Objects above and to the right of the curve are considered detectable, while objects with sizes and contrasts below and to the left of the curve are undetectable.

Contrast-detail analysis has been previously adapted to near-infrared diffuse tomography^{55, 165} and fluorescence tomography as part of this work¹³⁴. This study uses contrast-detail analysis to report perceptibility limits as defined by contrast to noise ratio (CNR) of a fluorescence tomography algorithm using simulated data. Typical contrast-detail study test fields contain a series of circular objects, usually in a regularly spaced pattern, with a range of contrasts and diameters, allowing a complete analysis in a single image. In the case of diffuse optical tomography, however, the quality of the reconstructed images can be significantly affected by object position, test field size,

and/or the presence of multiple objects in the field of view⁶³. To control these parameters, contrast-detail analysis in this type of diffusive-imaging system must employ single object test fields, and use a series of reconstructed images to complete the study. Each image represents a different object size and contrast and the analysis considers data from the entire series of images. In routine assessment, human detection of objects is required to establish the contrast-detail curve, but in this study a CNR value of 3 was used, as will be discussed later. The results represent a best-case scenario and thus provide a representative lower limit of concentration of fluorophore which provides a sufficient CNR value.

13.1 Methods

Simulated data was generated by solving the model system using typical tissue optical property parameters of $\mu_a = 0.01 \text{ mm}^{-1}$ and $\mu_s' = 1.0 \text{ mm}^{-1}$, and extracting the boundary data at each simulated detector position. To compare the influence of domain size on contrast-detail characteristics, two circular test fields were used; one 51 mm diameter and the other 86 mm diameter. The smaller test field test field approximates a domain expected to be encountered in small animal imaging and the 86 mm test field mimics larger imaging fields such as a human breast. Each test field was simulated as a 10,000 node circular mesh circumscribed by 16 source/detector fiber positions and used to generate 240 data points, matching our experimental fluorescence tomography design. The system is similar to our automated tomography system currently in clinical trials⁵¹. Random noise was added to each transmission data point with 1% mean error.

Image reconstruction was performed with a non-linear Newton-Raphson type algorithm, which was stopped when the projection error changed by less than 2% between iterations. Intrinsic optical properties, μ_{ax} , μ_{am} , μ_{sx} and μ_{sm} were held constant, as were the fluorophore lifetime, τ , and quantum yield, η . The algorithm recovered the fluorescence yield only, $\eta\mu_{af}$, as a best-case scenario for how accurately the images can be formed. The homogeneous background fluorescence yield, $\eta\mu_{af} = 0.0001 \text{ mm}^{-1}$, was used as an initial estimate for the iterative algorithm.

The contrast parameter, fluorophore absorption, μ_{af} , was varied for a single object, or region of interest (ROI), while the background fluorophore absorption was held constant at 0.001 mm^{-1} . Contrast was calculated as

$$\text{Contrast} = (\mu_{af}^{\text{true_ROI}} - \mu_{af}^{\text{true_background}}) / \mu_{af}^{\text{true_background}} \quad 13.2$$

where the absorption coefficient values were the true values used to simulate the data. Images of $\eta\mu_{af}$ were recovered for each contrast and test object diameter combination. For both test fields, 51 mm and 86 mm, these calculations were repeated for two different object positions, one near the edge of the phantom (object edge 5 mm from the boundary), and one near the center (object center 2 mm from the test field center), as shown in Figure 13.3. For each 51 mm test field case, just over 4,000 reconstructed images of fluorescence yield were used in the analysis. The number of reconstructed images was reduced to about 2,000 for each 86 mm test field case to control total computation time.

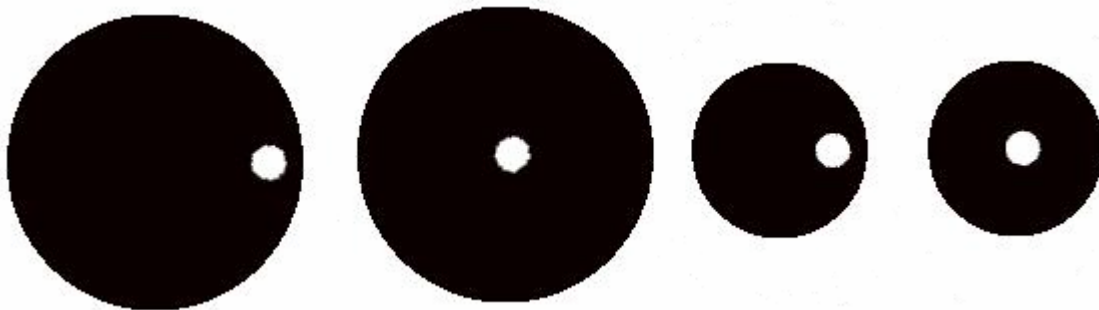


Figure 13.3. 86 and 51 mm diameter test fields used in this study. A range of object sizes and contrasts are used to determine contrast-detail imaging limits.

The range of contrasts explored in this study was chosen to approximate what is expected *in vivo*, with a contrast of 10 being near maximum of what could be expected in humans. The object diameter range, from 0 to 20 mm, was selected to ensure the small-object limits of the imaging system were characterized in this analysis, while being near the average breast tumor size detected clinically.

Contrast-detail studies for clinical systems often use trained readers to determine the threshold for detectable contrast and size. In the current study, contrast-to-noise ratio (CNR) is specified as a surrogate parameter of detectability, which provides an objective threshold measure. CNR was calculated directly from the reconstructed images following the approach outlined in Song, et al⁵⁵,

$$CNR = \frac{\mu_{af}^{ROI} - \mu_{af}^{background}}{(w_{ROI}\sigma_{ROI}^2 - w_{background}\sigma_{background}^2)^{1/2}} \quad 13.3$$

where w_{ROI} and $w_{background}$ are weighting factors compensating for the relative area of the ROI and the background, as a fraction of the total test field area. The values σ_{ROI} and $\sigma_{background}$ are the standard deviations in the ROI and background regions of the reconstructed image, respectively. The ROI size and location are assumed known, which is common for contrast-detail analyses where the objective is to determine system performance for a known test field.

13.2 Results and Discussion

CNR is plotted as a function of both ROI diameter and true contrast for all test domains considered in Figure 13.4. For discussion purposes, Figure 13.4(b), which presents data for an object just off-center in the 51 mm test field, is considered first. Up to a point, increasing contrast and object size are associated with increasing CNR, however, there is a drop-off in CNR for objects larger than about 15 mm for this case. As the object size and contrast increases and encompasses a greater area in the test field, the average bulk value of $\eta\mu_{af}$ increases with respect to the initial estimate. It appears that above 15 mm, the difference between bulk properties and initial estimate is significant enough to impact the imaging performance of the algorithm. Adjusting the initial estimate to the average bulk properties through a calibration procedure, as is currently done in our clinical NIR system⁵², would likely address this issue and may be the subject of future contrast-detail studies.

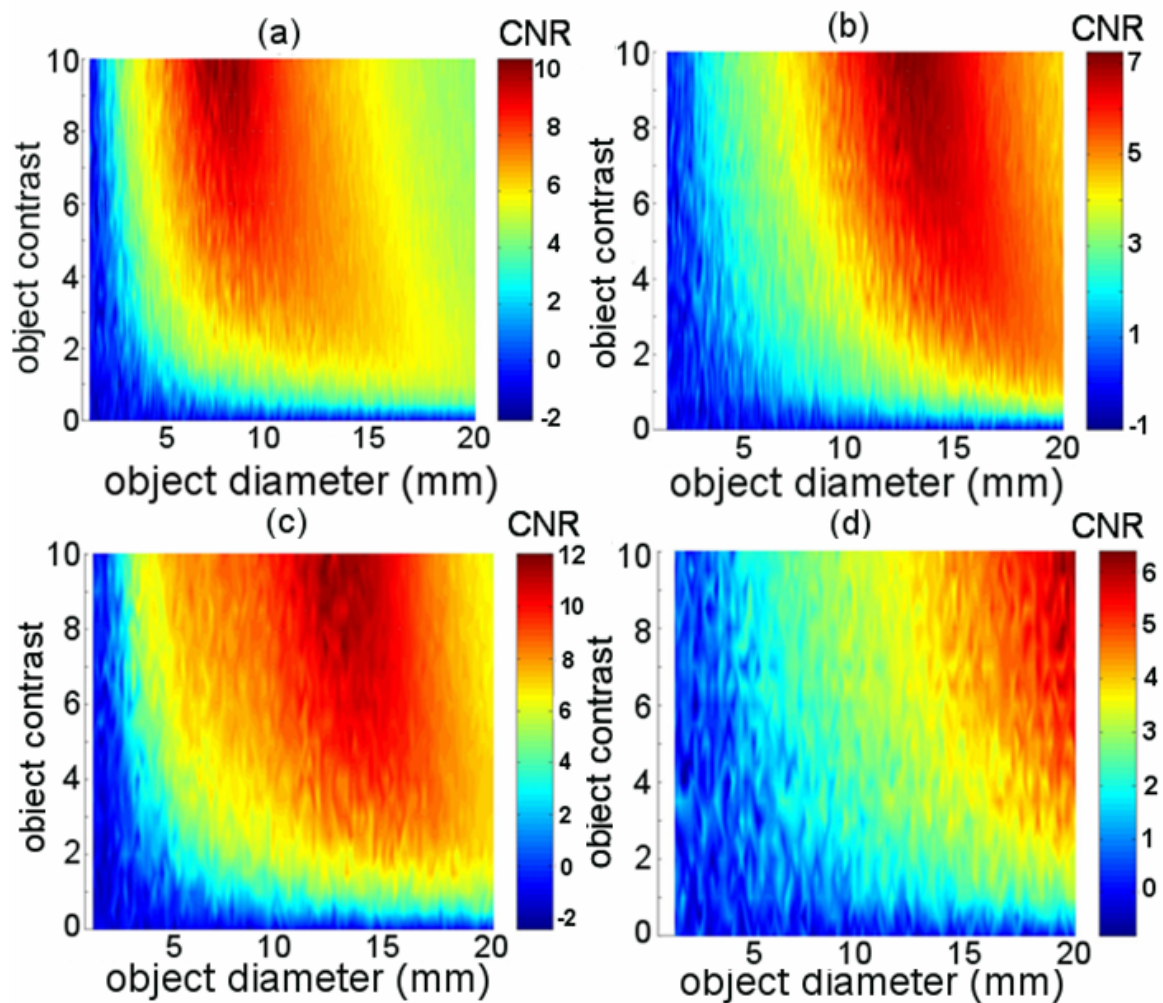


Figure 13.4. Calculated contrast-to-noise (CNR) ratio for a range of object diameters and contrast levels in four circular test domains. (a) and (b) present data for objects near the edge and center, respectively, of a 51 mm test domain. (c) and (d), on the other hand, present data for objects near the edge and center, respectively, of an 86 mm test domain. In this analysis, objects which are reconstructed with a CNR value below 3.0 are thought to be undetectable by human perception, illustrating that there are regions of size and contrast which are not feasible to image with the algorithm.

By specifying a minimum CNR value required to “detect” an object, the contrast threshold for visibility is determined for each object diameter. The choice of a minimum CNR value is somewhat arbitrary since it represents the threshold of object detection in the images. Figure 13.5 shows reconstructed images of fluorescence yield for a range of

calculated CNR values. Clearly, there is ambiguity in identifying detectable and undetectable objects. Evaluating human detection of objects is more complicated than CNR analysis. Ongoing studies in our lab indicate that intra- and inter-human observer variability results in a range of CNR threshold values. However, human detection thresholds for smaller objects in images with low noise are reasonably well approximated with $CNR = 3$, which is the value used in the current analysis⁵⁴. If a $CNR = 3$ is deemed inappropriate, a change in this value would shift the curves up and to the right for an increase and down and to the left for a decrease.

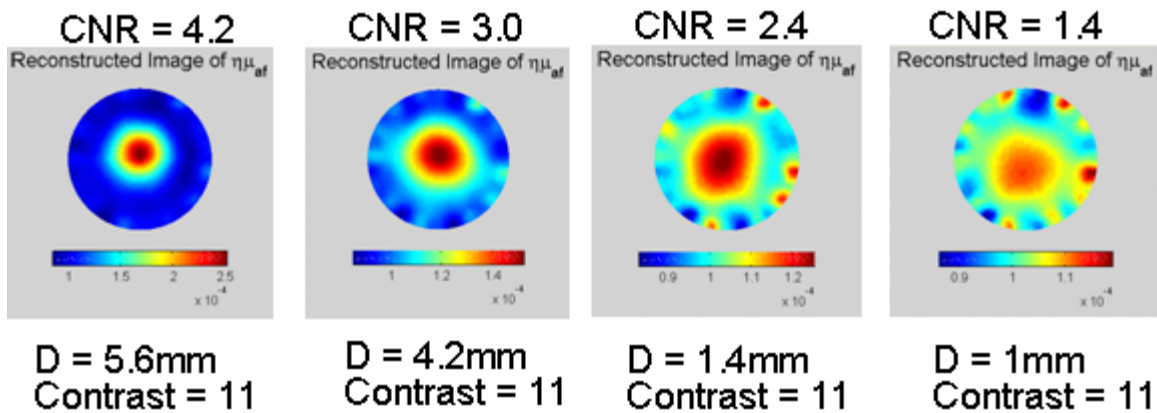


Figure 13.5. Images of fluorescence yield for a range of object sizes located near the center of a 51mm diameter domain. CNR decreases with decreasing object diameter.

The contrast-detail results for a threshold limit of $CNR = 3$ are plotted in Figure 13.6 for the two test fields and object positions. Objects which are recovered with greater than $CNR = 3$ have contrast-detail characteristics which are above and to the right of the line shown in Figure 13.6, while those below and to the left are too small or have too little contrast to be recovered with $CNR > 3$ in the image. Accordingly, the limiting diameter for an object near the edge of the field is approximately 1.7 mm for both test

field diameters. There seems to be little influence of test field diameter on CNR limits for high-contrast objects near the edge. Above an object contrast of about 8, the continued decrease in the minimum size for $CNR = 3$, is very small with increasing contrast, indicating that this size is a fundamental limit of the imaging algorithm for this geometry. This high contrast, small detail portion of the curve is often referred to as a “spatial resolution limited” regime. It does not appear that the fundamental limits have been reached for objects near the center of either test field for the contrast range studied and expected to be encountered experimentally. Furthermore, CNR value of objects near the center is strongly influenced by the test field size. For a 51 mm test object, the limiting diameter is approximately 4 mm, for the maximum object contrast (10). This increases to approximately 8.5 mm for the larger test field. These results indicate the dramatic decrease in sensitivity for objects deeper in the test field.

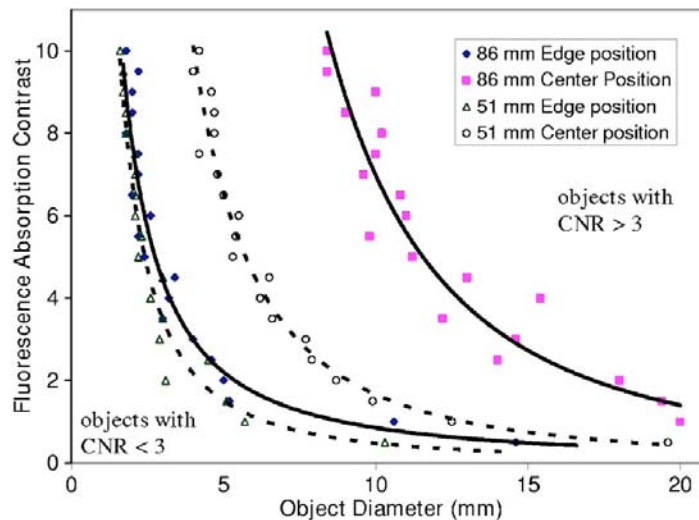


Figure 13.6. Contrast-detail curve showing the contrast-to-noise ratio (CNR) of 3 to approximate limits of detectable contrast and diameter for two anomaly positions in 51 mm (dashed lines) and 86 mm (solid lines) diameter test fields. In this analysis, objects above and to the right of each line are in the region where $CNR \geq 3$ and “detection” is considered possible.

The horizontal asymptotes of these lines represent the SNR limitations of the imaging system. These correspond to the low-contrast, large detail portion of the curve where small changes in contrast result in large changes in the diameter for the $CNR = 3$ threshold. For objects near the phantom edge, the minimum contrast for $CNR = 3$ is less than 0.5, though this limit is reached for smaller object sizes in the 51 mm test field, indicating slightly better imaging performance. This same contrast limit applies to objects near the center of the smaller test field, though again, is not reached until the object diameter is larger than on the edge. Due to the poor sensitivity to objects in the center of the 86 mm test field, SNR limits are outside of the test range. The SNR limits determined in this study will likely vary with the noise level in the system. In addition to fundamental limits of the imaging system, the contrast-detail curve provides information on the trade-off between object size and contrast. This “transition” zone lies between the vertical (spatial resolution limited) and horizontal (SNR limited) asymptotes and defines system imaging performance for objects mostly likely to be encountered experimentally.

Algorithms based on the photon migration equation are considered to be more sensitive closer to the source/detectors and this non-linear sensitivity is manifested as a non-uniform image response across the field of view. The contrast-detail curves shown in Figure 13.6 demonstrate the significance of this effect. For the smaller test field, the minimum object diameter for the best-case, high-contrast regime differs by 150% between an object at the edge and one centered in the test field. In a larger field, that difference increases to 360%. Thus, objects closer to the center will need to be larger in order to be detected. Further contrast-detail studies may be used to investigate image

reconstruction parameters in addition to object position, such as adaptive meshing techniques¹⁶⁶ and the effect of intrinsic optical properties.

The analysis can be extended to investigate the quantitative accuracy of the reconstructed images by calculating the percentage of true contrast recovered in each reconstructed image for the sizes and contrasts studied. These values are plotted for each test field in Figure 13.7 and reveal a strong dependence of contrast resolution on object size. Contrast accuracy is less dependent on the true object to background contrast for the range of sizes and contrasts considered here. In fact, in most size-contrast regimes, changes in actual object contrast only modestly impact recovered contrast.

A strong determinant of contrast resolution is object depth. Maximum recovered contrast values for objects near the edge are around 70%, regardless of test domain diameter, though accuracy drops off more rapidly as a function of object size for the larger domain. However, objects near the center of the 86mm domain are poorly recovered, approaching 40% even for larger, higher contrast objects. This is substantially worse than objects in the center of the smaller, 51mm domain, reinforcing the significance of the non-uniform imaging field.

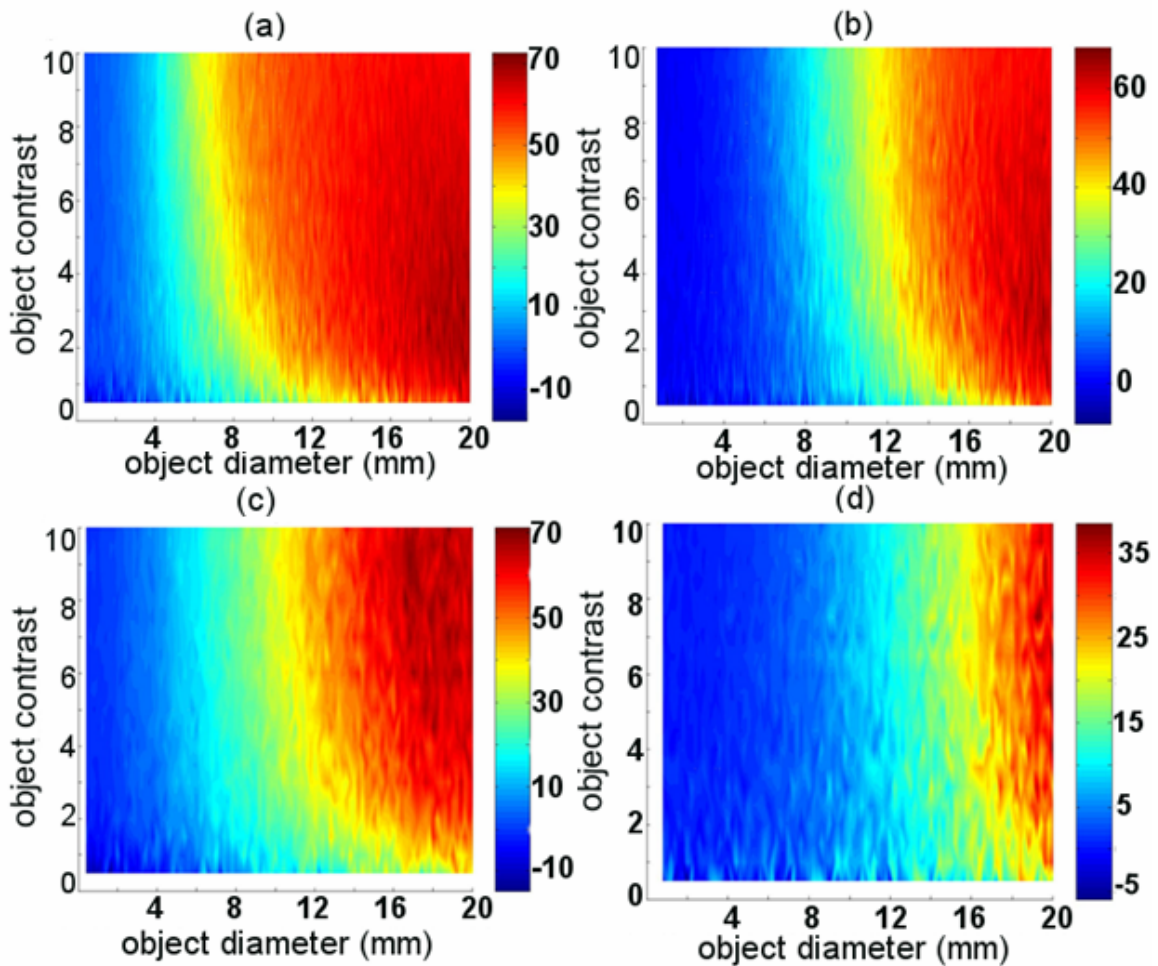


Figure 13.7. Contrast accuracy plots provide the percentage (color-bar) of true contrast recovered in the image. (a) and (b) show data for objects near the edge and center, respectively, of a 51 mm test domain. (c) and (d) show data for objects near the edge and center, respectively, of an 86 mm test domain.

13.3 Summary

The C-D results presented here provide a best-case analysis for imaging tissue containing fluorophore *in vivo* with this algorithm in the absence of prior information to guide the image reconstruction. A number of factors will serve to increase the contrast and size required to detect an anomaly in an experimental or clinical setting, thus shifting the contrast-detail curves up and to the right, including:

- 1) Reconstruction of the intrinsic optical properties when unknown;
- 2) Heterogeneity in the intrinsic optical properties and fluorophore distribution;
- 3) Unaccounted for bleed-through of the excitation signal into the fluorescence signal
- 4) Higher data noise and model-mismatch in an experimental setting; and
- 5) Increased phantom size and/or intrinsic background absorption.

Contrast-detail analyses may also be used to track imaging performance as system improvements/adjustments are implemented.

The results presented in this chapter pertain only to images reconstructed without spatial prior information. Based on the results presented throughout this thesis, spatially guided optical imaging would be expected to decrease contrast-size threshold values and thus improve the contrast-detail performance of the imaging algorithm. This most certainly would result from improved contrast recovery and suppressed background noise in spatially guided images. However, object detectability is the fundamental quantity sought in most contrast-detail experiments and thus the application of contrast-detail analysis to this type of imaging protocol may be inappropriate. Applying spatial priors to optical reconstructions in the manner discussed throughout this work relies on the conventional modality, such as MRI, to handle the object detection component of the protocol while the optical component is used to characterize the detected objects. Since the onus of detection is eliminated for the optical modality in this imaging protocol, it may be more informative to assess imaging performance using contrast-accuracy analysis as described in section 13.2 as opposed to contrast-detail analysis. This is an intriguing issue for future investigation.

Chapter Fourteen: Concluding remarks

The design, development and characterization of a multi-channel spectrometer-based molecular imaging system which couples into a clinical MRI for simultaneous optical and MR image acquisition was described. Anatomical information from the MR images was incorporated into optical reconstruction algorithms to improve the spatial and contrast resolutions of heterogeneously distributed fluorescence activity. Thus, a conceptually new framework for fluorescence tomography emerges, in which the highly resolved MR images provide a spatial template upon which optical data is used to characterize, and even diagnose, the targeted functional aspects of the contrast agent. The system and software was designed to be flexible, allowing broadband or laser transmission measurements as well as luminescence measurements from photo- and chemi-luminescent processes.

Simulated and tissue phantom data in breast-sized volumes revealed that the image recovery problem was nearly intractable for low tumor-to-background contrasts without the use of the MR information, while dramatic improvements in image quality and quantification were observed for spatially-guided image reconstructions. Pilot studies of gliomas in a small number of murine models demonstrated spatially-guided fluorescence imaging of epidermal growth factor receptor (EGFR) using a targeted optical fluorophore. Ex-vivo analysis confirmed that elevated levels of fluorescence activity in the tomographic images corresponded reasonably well with actively

proliferating tumor regions while areas of suppressed fluorescence were observed for edematous and necrotic tissue regions.

An attempt was made to image EGFR-targeted fluorescence in response to anti-EGFR treatment using Erbitux. Differences in bulk fluorescence yield between control and tumor-bearing mice, whether treated or untreated, were found to be significant though mean values between treated and untreated mice were not significantly separated due to large data variance compared to the population size. Unreliable tissue-fiber coupling precluded successful fluorescence imaging, facilitating a redesign of the fiber-positioning system and exposing the critical nature of reliable coupling.

The multi-spectral imaging system also revealed some of the challenges associated with imaging luminescence through turbid media. Specifically, scattering-induced lengthening of mean photon path-lengths amplifies the influence of the spectrally variable attenuation, which manifests as severe luminescence peak distortion over multiple centimeters. Wavelength-resolved diffuse modeling of the peak propagation was introduced and shown to match phantom data from homogeneous phantoms reasonably well. Simulated data also demonstrated a significant impact on image recovery if peak distortion is not taken into account. These challenges led to the development of alternative methods to image optical exogenous contrast *in vivo*.

Exploiting the absorption properties of an exogenous contrast agent directly is an alternative approach which omits the difficult problem of fluorescence emission filtering and low-light detection. Studies shown in this work indicated that measurements derived from absorption are more sensitive than those arising from fluorescence emission under certain conditions, particularly when the background drug concentration is high. Other

influential factors include fluorescence quantum yield, filtering efficiency, detector sensitivity, and drug specificity between diseased and normal tissue. However, since the source of the absorption-derived perturbation is indistinguishable from endogenous absorption at a single wavelength, quantifying the exogenous drug concentration is impossible without either dynamic acquisition or spectrally-resolved techniques. To address this, software and hardware advances were completed to adapt pre-existing spectral tomography techniques to incorporate any number of absorbing contrast agents.

A spectrally-constrained imaging approach for functional imaging of endogenous tissue chromophores based on absorption, often referred to as the “spectral priors” approach, was advanced to incorporate the molar extinction spectrum of exogenously administered drugs. Simulation studies showed that this technique can be used to quantify concentrations of hemoglobin, water, oxygen saturation and the contrast agent, especially when hard prior spatial guidance is used. Simulated and phantom data showed that it is feasible to use spectrally-constrained absorption tomography to recover concentrations of exogenous contrast directly, especially for higher drug concentrations. However, in cases where drug concentrations are closer to what might be expected *in vivo*, at least for targeted agents, the absorption-based approach is much less sensitive than one derived from fluorescence emission measurements.

Finally, the imaging limits of fluorescence tomography were measured using the conventions of the medical imaging community. Contrast-detail analysis was used to determine size and contrast limits of tumor detection for a variety of tissue geometries using simulated fluorescence tomography data. This type of analysis may be repeated to investigate a number of parameters associated with fluorescence imaging in deep tissue

volumes. Ideally, phantom work would compliment the highly-sampled numerical results presented here.

The work presented here was focused more on the techniques required to image through deep tissue than on the specific biological processes involved in the drug-tissue interactions. The absence of approved contrast agents which target diseased tissue make the future clinical role of fluorescence tomography unclear. However, the development of molecular probes for *in vivo* use in research animals is progressing rapidly. Clearly, dual-modality fluorescence tomography has the potential to impact pre-clinical research and drug development.

Throughout the course of this work, unexpected results were observed, new questions raised, and new ideas generated. The following chapter outlines near-term and long-term goals for future work and includes a few more abstract ideas for future research.

Chapter Fifteen: Ongoing Studies and Ideas

This chapter describes important short-term and ongoing work necessary to bring closure to some of the studies described previously, as well as longer term objectives which reflect what I see as the natural progression of this work. Finally, a few new ideas not included in the thesis body are introduced for future research.

15.1 Short-term objectives

15.1.1 Animal Imaging

Given the availability of targeted probes, some of the most interesting experimental work is taking place in small animals. Increasing the number of imaged tumor-bearing mice to statistically significant levels is a priority. To that end, the U-251 tumor line has been implanted in six additional mice, scheduled to be imaged within weeks. Data may help validate the small-animal imaging capabilities of the MRI-FMT imaging system.

Other animal studies are being conceived, including an experiment designed to track tumor progression using MRI-FMT with EGFR-targeted probes. Additionally, a luciferase-transfected tumor cell line has been acquired for initial attempts at MR-coupled multi-spectral bioluminescence tomography.

15.1.2 Phantom validation

Additional phantom studies are underway to further validate the imaging sensitivity and performance of the FMT and spectrally-constrained approaches outlined throughout this thesis. The experimental design calls for imaging 92 mm cylindrical phantoms with a single inclusion of different sizes. Each phantom will be composed of gelatin, blood and the drug, except for the cylindrical inclusion which will be filled with intralipid, blood and concentrations of GdTex or ICG providing tumor-to-background contrasts ranging from 2:1 to 10:1. Both drugs demonstrate strong NIR absorption profiles and dramatically different quantum yields, one quite low and the other relatively high. The phantoms will be imaged using the multi-spectral frequency domain system for spectrally-constrained chromophore reconstruction and the fluorescence tomography system for fluorescence yield imaging and spatial priors will be used in all reconstructions. Quantification characteristics of the two methods will be compared for both drugs and the influence of fluorescence quantum yield may be examined by comparing GdTex and ICG images of fluorescence yield.

15.1.3 Combining multi-wavelength FD and CW spectral tomography systems

To facilitate breast imaging and economize the hardware, a new frequency domain transmission tomography system will be integrated into the rotating source coupling stage on the spectrometer system, depicted schematically in Figure 15.1. Most of this work has been completed, with the remaining steps involving replacing the set of fiber optics attached to the rotating stage with larger diameter bundles capable of detecting more photons, as well as a modest amount of software development. Laser sources for the

frequency domain system include the Ti:Sapphire Mai Tai and six NIR laser diodes. Fifteen frequency modulated PMT's mounted on the rotating stage align with the 15 fibers not illuminated by the laser source, transforming these fibers into detection channels and extending the system capabilities to include frequency domain transmission tomography at any wavelength between 690 nm and 850 nm and spectrometer-based CW acquisition for full spectrum transmission, fluorescence, and bioluminescence measurements. Data-model calibration would be simplified since frequency domain and spectroscopy measurements will be acquired through the same fiber bundles.

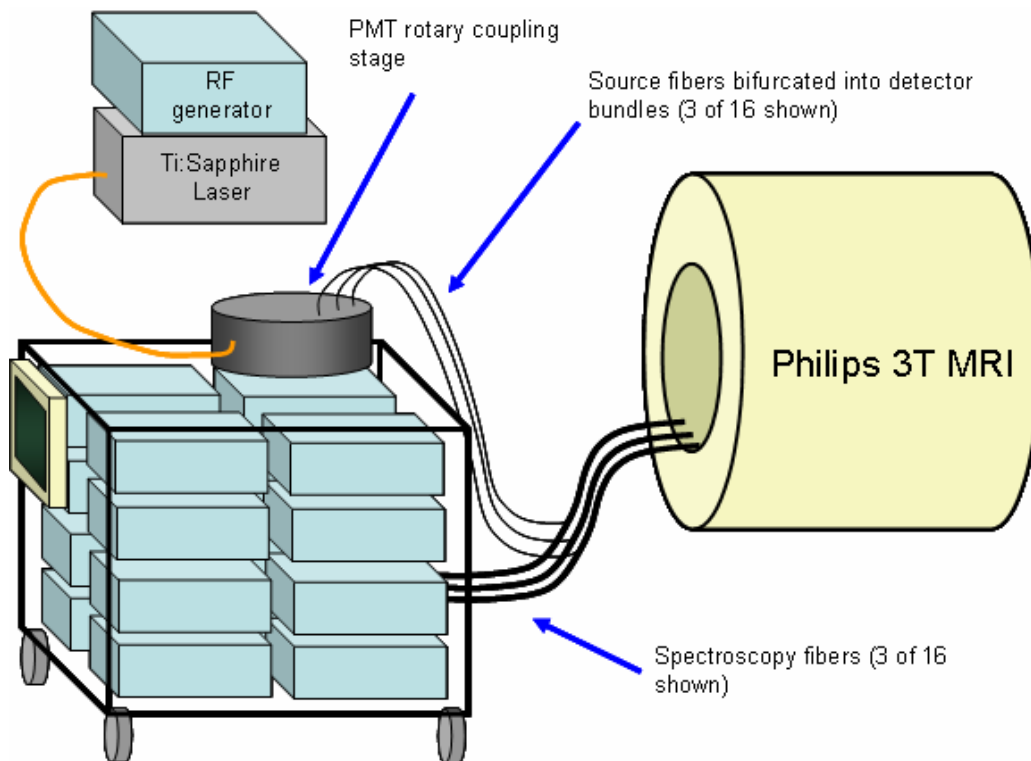


Figure 15.1. The proposed system combines the frequency domain Ti:Sapphire imaging system with the spectroscopy system.

15.2 Long term objectives

15.2.1 Imaging multiple fluorophores simultaneously in vivo

The spectrometer-based detection system and spectral fitting approaches provide a unique opportunity to probe multiple molecular processes simultaneously. The fluorescence intensity from each drug may be decoupled using the spectral fitting routines provided the emission peaks of the fluorophores are distinguishable. Once decoupled, these values may be used to reconstruct separate images of fluorescence activity the fluorophores present. Feasibility studies will be completed in small animals.

15.2.2 Exogenous optical absorption and fluorescence in the human breast

Despite the lack of truly targeted optical contrast agents approved for diagnostic use in humans, ICG may be used to help validate the MR-guided techniques introduced in this work. Clinical trials to image exogenous absorption and fluorescence emission in the human breast may begin when appropriate protocols are in place. Volunteers recruited from a screening pool of BIRADS 4 and 5 patients will be imaged with MRI and optical tomography simultaneously and images will be assessed using follow-up pathology reports.

15.2.3 3-D imaging

All the work contained in this thesis was completed for the two dimensional case. Modeling photon propagation is more accurate in 3-D. For years, the DOT community has been moving to three-dimensional imaging, and transitioning to volumetric modeling and image reconstruction is a logical next step for this work. Currently, the NIRFAST

package contains forward and inverse algorithms that are 3-D capable and methods to standardize volumetric meshing, segmentation, and image display are being developed for the DOT problem by Subha Srinivassan and Colin Carpenter. Once developed, these may readily be translated to the fluorescence problem.

15.3 New ideas

15.3.1 Spectrally-resolved fluorescence emission tomography

The spectral absorption properties of tissue influence the propagation of the emission spectrum, as shown in Chapter 12. Previously, researchers demonstrated a relationship between fluorescent lesion depth and the ratio of fluorescence emission intensity at different wavelengths by accounting for the wavelength dependent optical properties of tissue^{130, 131}. It may be possible to exploit this behavior in the reconstruction algorithm, using the full complement of spectrally resolved information.

A spectrally resolved fluorescence emission FEM image recovery model has been developed in the course of this work, and is available in NIRFAST_v2_dev, using principles similar to that developed for spectrally resolved bioluminescence tomography (BLT)¹³⁶. Since this approach dramatically improved activity localization for BLT, it is reasonable to postulate that fluorescence yield localization may benefit from the additional information. Initial tests in simple domains with simulated data showed little improvement in recovered images, however, with increased noise and complexity, the spectrally-resolved procedure may provide better quantification. Additionally, it may be possible to produce images based on the derivative of the measured spectrum, as outlined in Xu et al¹⁶⁷. Before being applied to real data, however, more advanced spectral

analysis tools are required to remove auto-fluorescence from the signal without losing the features in the emission spectrum which make the spectrally resolved technique beneficial.

15.3.2 Quantum Yield Imaging

Combining spectrally-constrained absorption imaging, described in Chapter 11, and fluorescence tomography suggests a unique method to recover fluorescence quantum yield directly. Conventional approaches to fluorescence tomography are confined to imaging fluorescence yield, a product of the fluorescence quantum yield and absorption coefficient of the fluorophore, and offer no means to de-couple these parameters. However, some applications, such as the use of environmentally sensitive quantum yields, may benefit from direct recovery of quantum yield.

Figure 15.2 outlines a proposed process to derive images of quantum yield from multi-wavelength frequency-domain transmission data to quantify the concentration of the exogenous agent, and CW fluorescence tomography data to determine the fluorescence yield. Once these parameters have been determined, the procedure to extract quantum yield is straightforward, a simple quotient of fluorescence yield and fluorophore absorption.

A simulation study demonstrates this technique. The same breast shaped domain used in previous examples was segmented into fatty and fibro-glandular tissue regions. In this study, several abnormalities were artificially added, including a malignant tumor and a water-filled cyst. For illustrative purposes, it was assumed that an activatable exogenous fluorescence probe was injected and accumulated preferentially in the cyst.

Fluorescence emission of the probe was quenched until the molecular backbone was lysed by interactions with specific enzymes which, in this case, were more abundant in the simulated tumor than elsewhere in the domain. In this scenario, the contrast of fluorophore concentration was elevated in the cyst formation, while quantum yield contrast presented only in tumor-to-healthy tissue at a ratio of 3:1, independent of fluorophore concentration as shown in Figure 15.3. The tumor region also contains elevated values of HbO, dHb, water and scattering parameters.

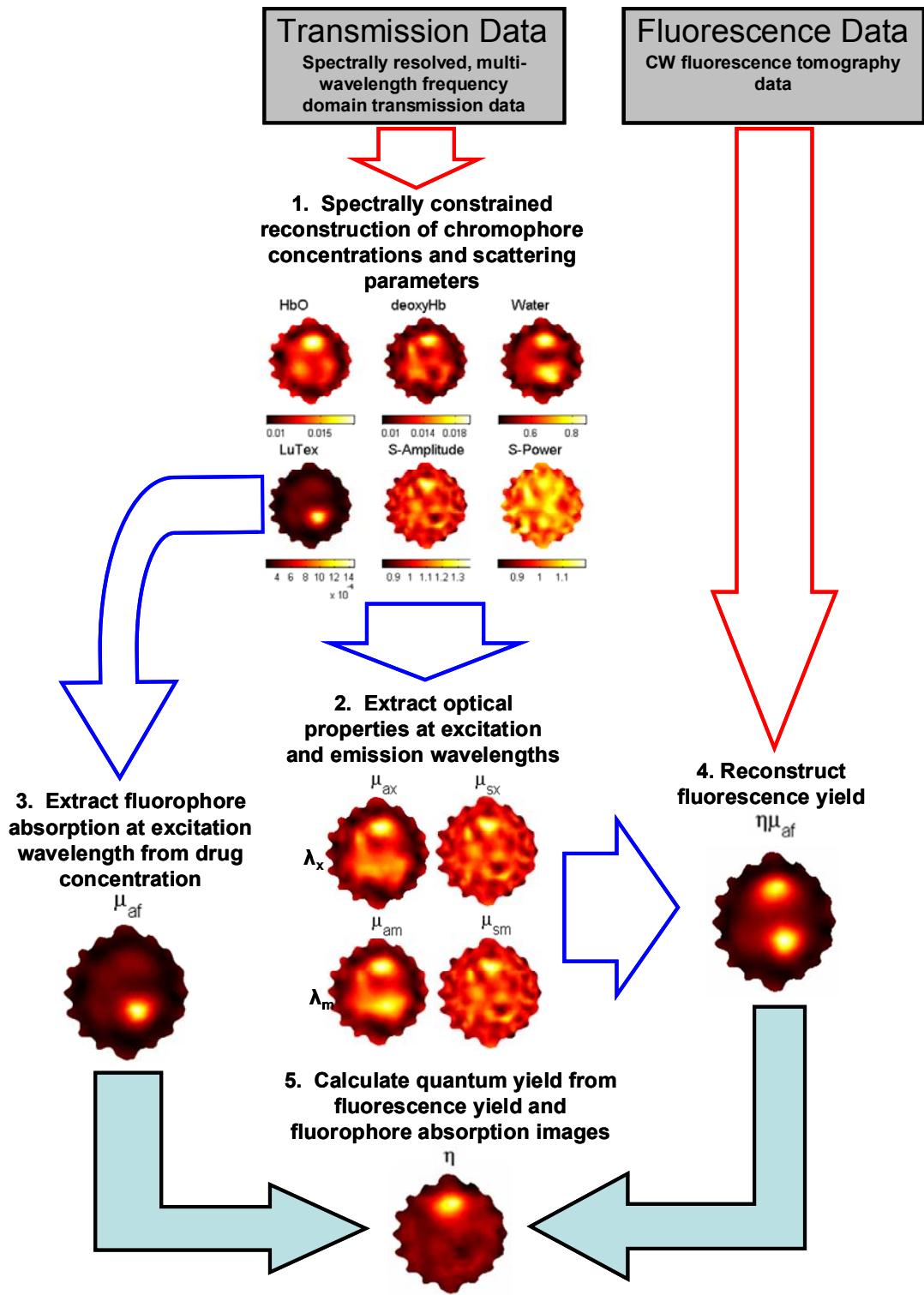


Figure 15.2. A method for combining recovered chromophore concentration values and scattering parameters with images of fluorescence yield to reconstruct absolute quantum yield images.

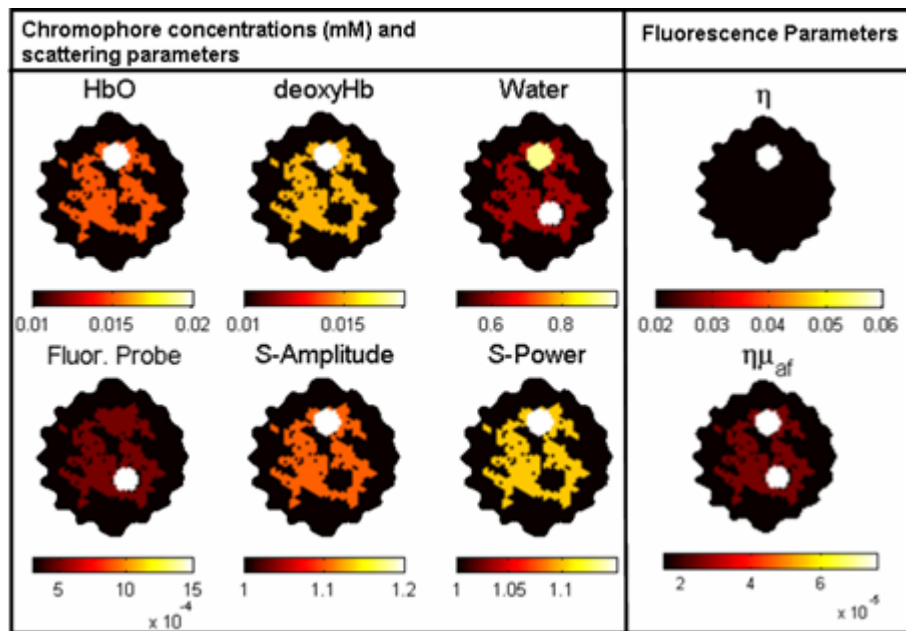


Figure 15.3. Simulated test domain showing true values of chromophore concentrations (mM), scattering parameters and fluorescence quantum yield.

Following the procedure outlined in Figure 15.2, images of chromophore concentration, fluorescence yield and ultimately fluorescence quantum yield were recovered using only the outer boundary as prior information (Figure 15.4) and using internal tissue structural information in a hard-priors approach (Figure 15.5).

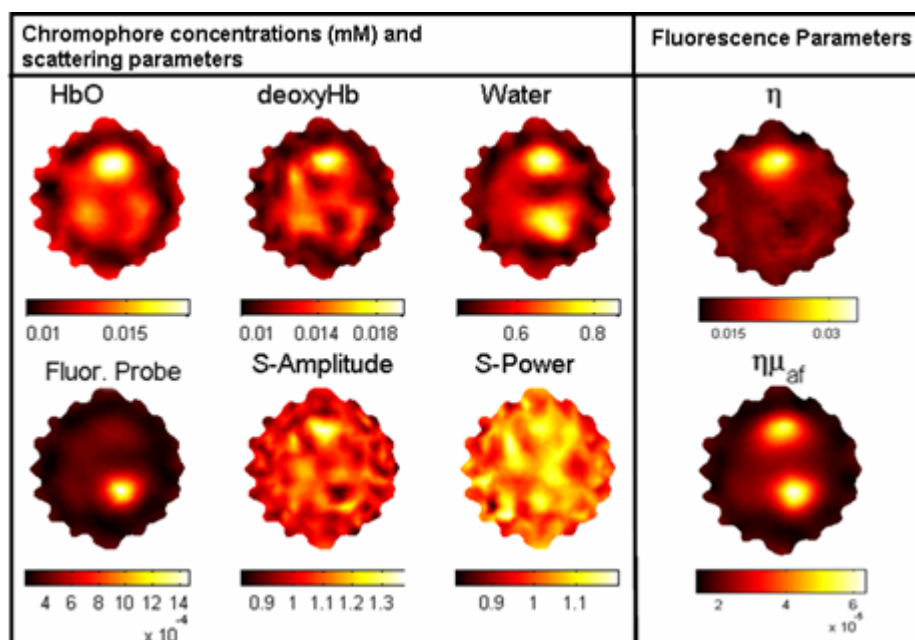


Figure 15.4. Recovered images of chromophore concentration, scattering parameters, fluorescence yield and fluorescence quantum yield. The outer boundary of the imaging domain was the only spatial information used in the reconstruction.

While spatial priors help produce a more accurate image, both sets of images accurately represent the probe parameters under consideration: concentration, fluorescence activity, and quantum yield. The significance of this advance is that fluorescence activity may be quantified independent of drug concentration.

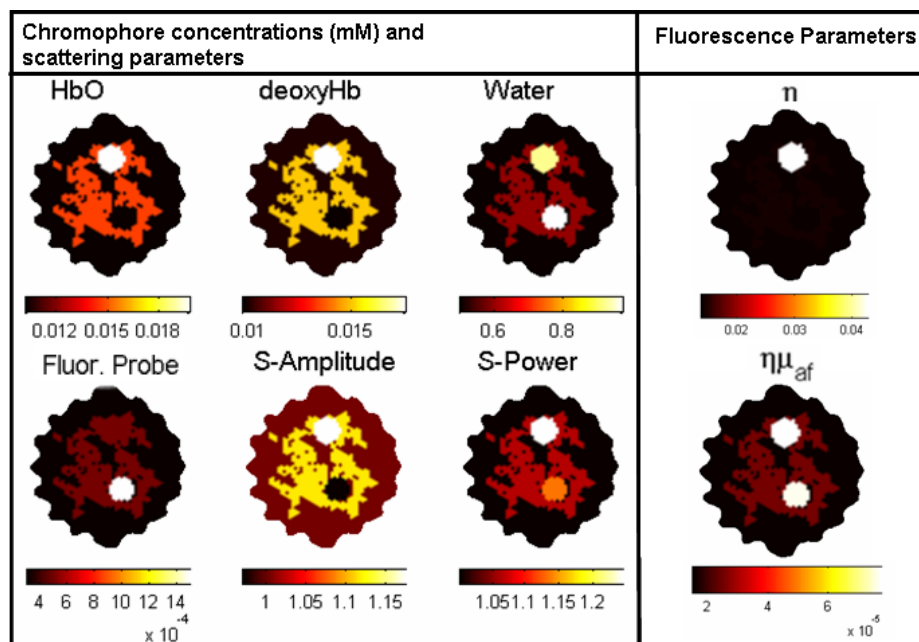


Figure 15.5. Recovered images of chromophore concentration, scattering parameters, fluorescence yield and fluorescence quantum yield reconstructed using hard spatial priors.

The likelihood that this technique migrates to *in vivo* imaging is questionable given the substantial experimental challenges involved; however, the combined experimental system now in the final stages of development has the necessary components to conduct quantum yield imaging feasibility studies.

This study requires a mechanism for controlling the fluorescence quantum yield of a drug, readily accomplished for PPIX by varying the concentration of Tween20, which prevents PPIX molecules from aggregating in water. The quantum yield of ICG may be controlled in a similar manner by changing the solvent⁹¹.

**APPENDIX A: SPECTRAL TOMOGRAPHY INSTRUCTION
MANUAL**

MRI-coupled Multi-spectral tomography system Instruction Manual

Max Friedman, Stephen Tuttle, Scott Davis

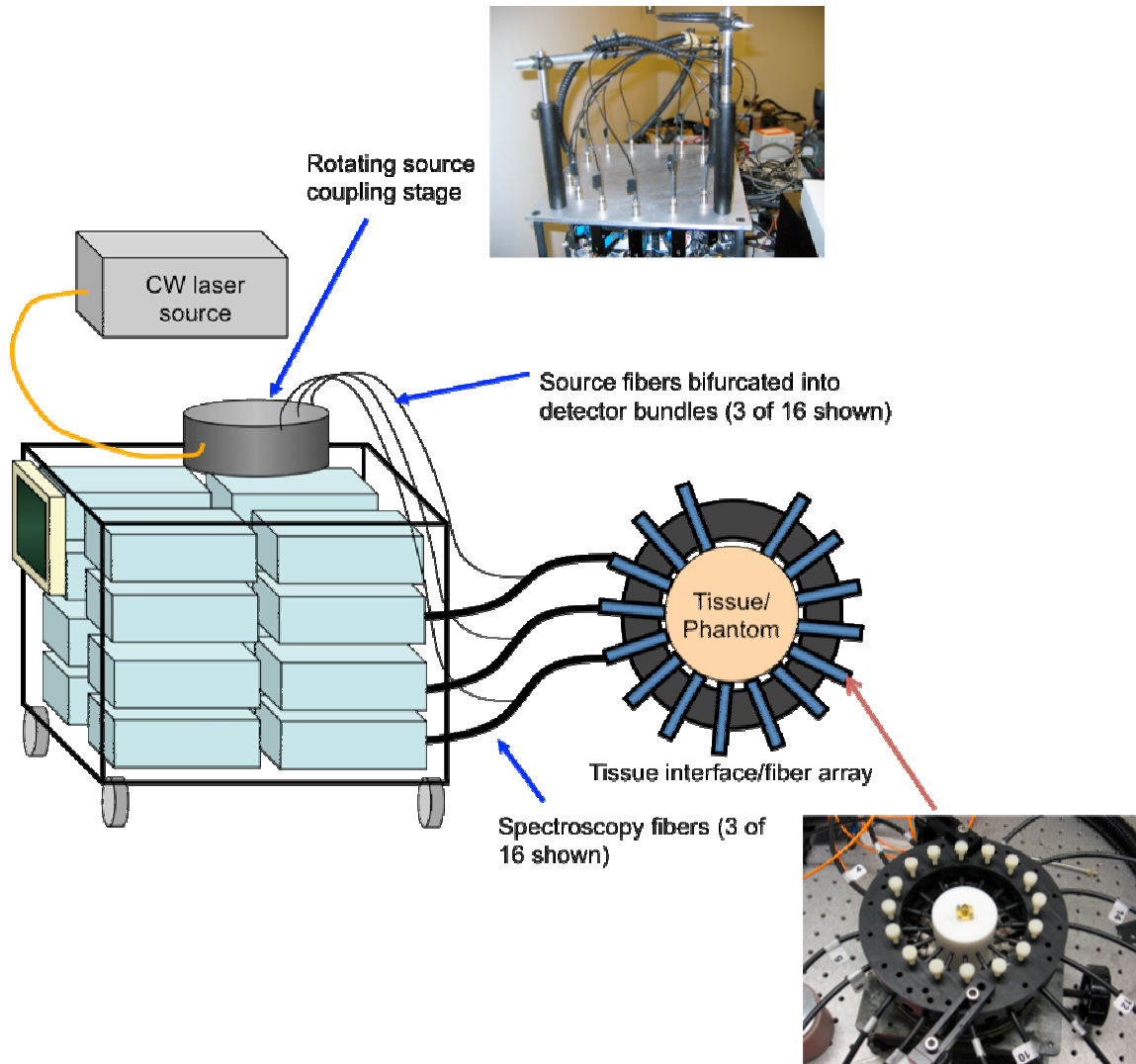
Table of Contents

Introduction: Hardware	268
System Initialization (For all users)	269
Powering System Equipment	271
REQUIRED EQUIPMENT	271
System Computer	271
Spectrometers	271
Rotary Stage	271
LIGHT SOURCES	272
690nm Laser	272
White Light Lamp	273
Data Acquisition Introduction: What happens when I select “Acquire?” ..	274
Data Acquisition Introduction: Hardware and Phantom Setup	275
SOURCE SETUP	275
PHANTOM SETUP	275
Data Acquisition: Software Instructions	277
FLUORESCENCE TOMOGRAPHY	277
TRANSMISSION TOMOGRAPHY	281
BIOLUMINESCENCE TOMOGRAPHY	285
SYSTEM SHUTDOWN	287
Troubleshooting	288
SPECTROMETERS DO NOT INITIALIZE	288
ACQUISITION TERMINATED PREMATURELY: RE-HOMING THE ROTARY STAGE	288

Moving the spectrometer systems	290
A Brief Note on Directory and Data File Structure	293
DIRECTORY STRUCTURE	293
DATA FILE STRUCTURE	293
Data Calibration	294
Approximate 690nm Laser Power vs. Current	295

Introduction: Hardware

A diagram of the system is pictured below, with photographs of a phantom fiber array and rotating source coupling stage.



System Initialization (For all users)

Only three main LabVIEW programs are required for basic data acquisition, all located in:

C:\EXPERIMENTAL_systems_and_data\SPEC_TOMO_SYS\Control_Routines

Initialize_system.vi
Acquisition.vi
Shutdown_sys.vi

Do not save any changes to these or any other files in \Control_Routines. Unless performing more advanced operations, or troubleshooting, these should be the only programs required to run the system.

1. Turn on the system computer, a *Dell Precision 380*.
The password is *diffuse*.
2. Turn on the spectrometers.
(Locate the power cords running out from underneath the system carts, and activate the power strip that they are plugged into).
3. Open *Initialize_system.vi*:
<C:\EXPERIMENTAL_systems_and_data\SPEC_TOMO_SYS\Control_Routines\Initialize_system.vi>.
4. Select spectrometers and cameras to initialize.
5. Run *Initialize_system.vi* by pressing the “run program” button (**Image 1 - The “run program” button.**)
This step can take up to 15 minutes to complete.
 - A. *If initialization fails*: Run *Shutdown_specsys.vi*, turn off the spectrometers, turn off the system computer, and repeat steps 1-5. *Shutdown_specsys.vi* can be found at:
<C:\EXPERIMENTAL_systems_and_data\SPEC_TOMO_SYS\Control_Routines\Shutdown_Specsys.vi>.
 - B. More information can be found in the troubleshooting section.

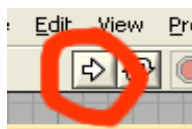


Image 1 - The “run program” button.

6. Open and **run** *Acquisition.vi*. Running the program now makes the interface interactive – it will not start data Acquisition.
<C:\EXPERIMENTAL_systems_and_data\SPEC_TOMO_SYS\Control_Routines\Acquisition.vi>.
7. There is a link to the default experimental data folder on the desktop of the system computer. Create a folder for your experimental data in the designated directory:
<C:\EXPERIMENTAL_systems_and_data\SPEC_TOMO_SYS\Data>.
8. Complete the *Saved Data Name* box. The path should appear as:
<C:\EXPERIMENTAL_systems_and_data\SPEC_TOMO_SYS\Data\FOLDER_NAME\FILE_NAME>.
FILE_NAME is the *rootname* of the file and extensions will be added appropriately. Typical data files associated with an acquisition are:
filename.log (log file)
filename_s1_rep1.raw (raw spectra)
filename_s1_rep1.calspec (calibrated spectra)
Note that “s1” indicates source 1 and “rep1” indicates the repetition.
9. Instructions for each acquisition type are found in this manual.
 - A. For transmission tomography, see page 277.
 - B. For fluorescence tomography, see page 277.
 - C. For bioluminescence tomography, see page 285.
10. When complete, see the Shutdown section on page 287.

Powering System Equipment

Required Equipment

System Computer

A *Dell Precision 380* computer controls the Spectrometer System. To turn it on, press the power button. The password is *diffuse*.

Spectrometers

There are sixteen spectrometers in the two system carts. A green light on each spectrometer indicates power. Two black power cords run out from underneath each cart to supply power, and all four power cords should plug into the same power strip.

To power the spectrometers, turn on the power strip that these four black cords are connected to.

Rotary Stage

If you are using the rotary stage, your source must be connected to the orange fiber labeled *source fiber*.

A green light on the rotary stage indicates power. If *only* the green light is on, the rotary stage is ready for use.

If the yellow light is on DO NOT TURN OFF the rotary stage. Refer to the troubleshooting section.

If no lights are on: flip the on/off switch on the face of the *Rotary Stage Controller*. Make sure the rotary stage is connected to the system computer.

Light Sources

Here are some examples of light sources used for image acquisition and data calibration.

690nm Laser

The 690nm laser is located on the system computer cart. It is controlled by two *current supply* boxes all connected to a single power strip.



Image 1 - 690nm Current Supply



Image 2 - 690nm Laser



Image 3 - 690nm Collimator

WARNING: Lasers are hazardous. Be sure you have passed the Dartmouth Laser Safety Training Course before using these systems. Check for areas where high intensity light could be emitted and reflected (this includes collimators, the rotary stage, and fiber tips). Proceed only when you feel confident that you will not be exposed to laser radiation.

1. Locate the power strip (labeled LD 690nm) that the laser *current supply* boxes are plugged into. If the strip is inactive, flip its on/off switch.
2. The pertinent controls of the *current supply* boxes are labeled in a particular order. Press/flip these controls in ascending order.
3. Set the amount of current you would like to supply to the laser. The laser will now be emitting high intensity light. You should let the laser run for at least 15 minutes before beginning an experiment. During this period, the laser is heating, and may not produce consistent data.

White Light Lamp

Used for producing data calibration files.



1. Flip the on/off switch on the face of the lamp.
2. Flip the on/off switch on the *shutter controller* box.
3. Use the *intensity dial* on the face of the white light lamp to adjust the voltage setting.
4. When you are ready to acquire data, flip the *N.O./N.C. switch* on the face of the shutter controller box to *N.O.*

Data Acquisition Introduction: What happens when I select “Acquire?”

Every time you select acquire:

1. Log files are written.
2. Camera temperatures are verified.
3. Camera gain and ADC are set.
4. Grating and center wavelength are set.
5. Filters are set.
6. Actual acquisition begins:
 - A. Motor moves source to correct fiber.
 - B. The system automatically optimizes the exposure times.

Each spectrometer will take sample acquisitions with exposure times of 0.03s, 0.3s, 3s, and 30s in order to calculate the optimal acquisition time to acquire the most counts without saturating the CCD.
 - C. Full acquire for one source. Data files written for that source.
 - D. Repeat A-C for each source.
7. Motor Controller disconnects.

Data Acquisition Introduction: Hardware and Phantom Setup

Source Setup

1. An orange fiber is connected to the rotary stage to couple light into the source fibers sequentially. The free end is labeled “source fiber.” Connect this end to the light source you would like to use.
 - A. *When using the 690nm laser*, the source fiber must be attached to the collimator designed for the 690nm laser. Make sure the arrow on the collimator points towards the red fiber. Reconnect fiber(s) as necessary.
 - B. *When using the 635nm laser*, the source fiber must be attached directly to the 635nm laser (you will see a label). Reconnect fiber(s) as necessary.

Phantom Setup

1. Determine whether the *mouse coil* or a detachable, patient/animal interface is most appropriate for housing source/detector fibers during your experiment.

In an effort to increase the longevity of the *mouse coil*, one should use a detachable patient/animal interface whenever MRI acquisitions are not being run in parallel.

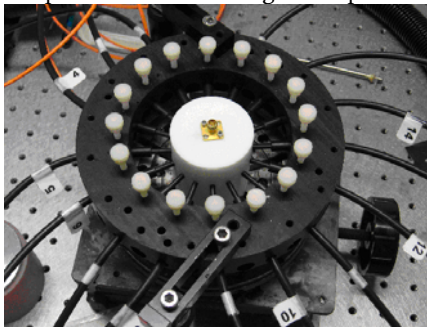


Image 2 - Phantom in a detachable, patient/animal interface.

2. Position the phantom, animal, or patient in the selected structure.
3. Center the phantom (Make appropriate accommodations for a patient/animal).
4. Position the fibers right up against the lateral surface of the phantom (make the necessary accommodations when imagine a patient/animal). Tighten the setscrews.

5. *Very gently* (these fibers are extremely fragile) tug on each fiber to confirm that the setscrews are tight—the fibers should not budge. If a fiber moves, reposition it back on the lateral surface of the phantom, and tighten its setscrew.

Data Acquisition: Software Instructions

Fluorescence Tomography

*** Most fluorescence tomography applications require fluorescence emission data and excitation transmission data. For the latter process, please see the following section entitled *Transmission Tomography***

If you have not already done so, complete the system initialization on page 268 before following the instructions here.

1. Select “fluorescence tomography” in the Mode dropdown menu.
2. Select your source fibers by highlighting the appropriate boxes directly beneath the word *source*.
The numbered boxes directly beneath the word *source* allow you to define which fibers will, in sequence, act as the source. Box numbers correspond to fiber numbers, and *highlighted* boxes define those fibers that *will* function as the source. Check and uncheck boxes according to your experimental specifications.
Note: Highlighting sources 2,4,6...16 is common practice for an 8-detector acquisition.
3. Select your detector fibers by highlighting the appropriate boxes directly beneath the word *detector*.
The numbered boxes directly beneath the word *detector* allow you to define which fibers will function as detectors whenever they are not acting as the source. Box numbers correspond directly to fiber numbers, and *highlighted* boxes define those fibers that *will* function as detectors. Check and uncheck boxes according to your experimental specifications.

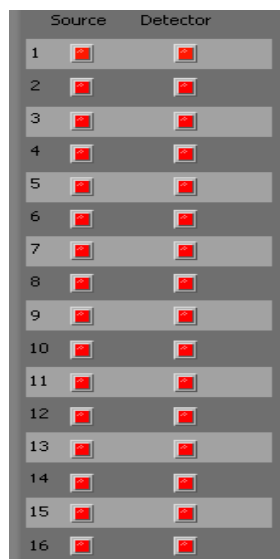


Image 3 - Source and detector panel with all sources and detectors highlighted.

4. Select the *Grating* and *Center Wavelength* you would like to use under the *Spectrometers* tab. The 1200l/mm grating provides a total range of about 30nm while the 300l/mm grating provides a range of 300nm.
For reference, see:
<C:\EXPERIMENTAL_systems_and_data\SPEC_TOMO_SYS\Calibration\wavelength_cal>.
5. Select the appropriate detector filter from the *Filter Wheel drop down box*. All spectrometers will be filtered at this wavelength.
6. **(Optional)** Click *Set Spectrometers* to begin the process of preparing the spectrometers while you finish your experimental preparations. If you do not click *Set Spectrometers*, the process will begin when you hit *Acquire*.
7. Fill out the log file information.
8. *Exp Times* tab: **(Optional)** Change the level of *optimization* if you do not want the spectrometers to *optimize at each source*.
 - A. **(Recommended)** Leave the setting on *optimize at each source*, if you would like the system to test for, and calculate, near ideal exposure times.

This procedure takes the longest time, but it virtually ensures that the spectrometers will acquire a high number of counts without allowing the CCD to saturate.
 - B. **(Not Recommended)** Choose *optimize on first source only* if you would like the system to test for, and calculate, near ideal exposure times at the first source only. However, LabVIEW will project these times onto the other source

locations, so that relative position to the source is preserved (e.g. the *near source detectors* will always have the shortest exposure times).

This procedure is relatively fast, but it may not work well for heterogeneous phantoms, and it does not account for complications arising from differences in source strength.

- C. **(Not Recommended)** Choose *no optimization* if you would like to manually input the exposure times for each detector. LabVIEW will project these times onto the other source locations, so that relative position to the source is preserved (e.g. the *near source detectors* will always have the shortest exposure times).

This procedure is the fastest, but there is no guarantee that CCDs will not saturate, or that the spectrometers will acquire a high number of counts.

9. Set the maximum and minimum exposure times. Minimum times cannot be below 0.01s.

These inputs will set extreme values for the *optimization* algorithm. Setting the *max time* can ensure that your experiment is not unreasonably long.

The minimum exposure time should be changed only under special circumstances.

10. If you would like the spectrometers to repeat data acquisitions at every source position (for statistical applications), then set *Acquisition reps. per source* to the number of repetitions you desire.

11. Turn off lights in the imaging room.

12. Click the *Acquire* button when you are ready to begin the experiment.

If the system computer and spectrometers are in the same room, turn off the monitor, and either quickly exit the room, or sit in the dark.

13. Wait patiently while the spectrometers acquire data. You can gauge the progress of the experiment by listening for system noises.

If you did not press *Set Spectrometers*, the first sounds you hear will probably be the spectrometers adjusting the grating and setting the appropriate filters. These sounds will be rather faint, but *all* acquisitions begin with the rotary stage making a quick turn. The rotary stage is the loudest noise generated by the system. In between rotations, you will hear the shutters clicking.

The computer will produce a loud, high-pitched beep for about 5 seconds when the acquisition is complete.

14. Turn on the monitor and check the spectra of your data. Click on the labeled tabs to view different detector readings.

LabVIEW displays the results from the final source position. If you wish to see results from different source positions, open your saved *.raw* files with an appropriate program.

Note: If you need to make any hardware changes before proceeding to additional acquisitions, you are advised to turn off active lasers. For the lasers on the system cart, simply press the output button, the highest-numbered button on the laser control box.

15. If this is your final experiment, click the *STOP* button and follow the instructions for shutting down the system on page 287.

Transmission Tomography

This may be done alone or as part of fluorescence tomography acquisitions.

If you have not already done so, complete the system initialization on page 268 before following the instructions here.

1. Select “transmission tomography” in the Mode dropdown menu.

Critical Note: Due to filter automation, transmission measurements through small animals require the use of fluorescence tomography mode – see step 5 below for more information.

2. Select your source fibers by highlighting the appropriate boxes directly beneath the word *source*.

The numbered boxes directly beneath the word *source* allow you to define which fibers will, in sequence, act as the source. Box numbers correspond to fiber numbers, and *highlighted* boxes define those fibers that *will* function as the source. Check and uncheck boxes according to your experimental specifications.

Note: Highlighting sources 1,3,5...15 is common practice for an 8-detector acquisition.

3. Select your detector fibers by highlighting the appropriate boxes directly beneath the word *detector*.

The numbered boxes directly beneath the word *detector* allow you to define which fibers will function as detectors whenever they are not acting as the source. Box numbers correspond directly to fiber numbers, and *highlighted* boxes define those fibers that *will* function as detectors. Check and uncheck boxes according to your experimental specifications.

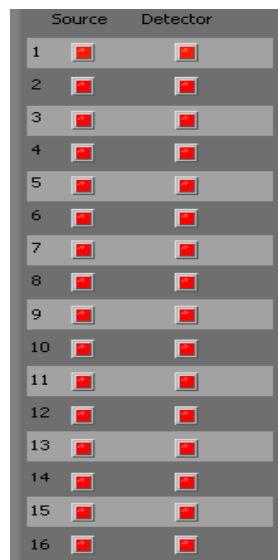


Image 4 – Source/Detector Panel with all sources and detectors highlighted.

4. Select the *Grating* and *Center Wavelength* you would like to use under the *Spectrometers* tab.

For reference, see:

<C:\EXPERIMENTAL_systems_and_data\SPEC_TOMO_SYS\Calibration\wavelength_cal>.

5. In transmission mode, detectors are automatically filtered with OD filters in the manner outlined in **Image 5–Filter settings and Set Spectrometers**. Data calibration will need to be completed post-acquisition.

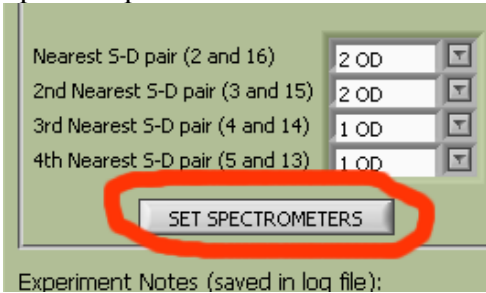


Image 5–Filter settings and Set Spectrometers

6. **(Optional)** Click *Set Spectrometers* to begin the process of preparing the spectrometers while you finish your experimental preparations. If you do not click *Set Spectrometers*, the process will begin when you hit acquire.

7. Fill out the log file information.

8. Select the *Exp Times* tab.

9. **Exp times (Optional):** Change the level of *optimization* if you do not want the spectrometers to *optimize at each source*.

- A. **(Recommended)** Leave the setting on *optimize at each source*, if you would like the system to test for, and calculate, near ideal exposure times.

This procedure takes the longest time, but it virtually ensures that the spectrometers will acquire a high number of counts without allowing the CCD to saturate.

- B. **(Not Recommended)** Choose *optimize on first source only* if you would like the system to test for, and calculate, near ideal exposure times at the first source only. However, LabVIEW will project these times onto the other source locations, so that relative position to the source is preserved (e.g. the *near source detectors* will always have the shortest exposure times).

This procedure is relatively fast, but it may not work well for heterogeneous phantoms, and it does not account for complications arising from differences in source strength. This option is not recommended for formal experiments.

- C. **(Not Recommended)** Choose *no optimization* if you would like to manually input the exposure times for each detector. LabVIEW will project these times onto the other source locations, so that relative position to the source is preserved (e.g. the *near source detectors* will always have the shortest exposure times).

This procedure is the fastest, but there is zero guarantee that CCDs will not saturate, or that the spectrometers will acquire a high number of counts. While this option is not recommended for formal experiments, it might occasionally be useful for quick tests.

10. Set the maximum and minimum exposure times. Suggested times are .03s and 120s, respectively.

These inputs will set extreme values for the *optimization* algorithm. Setting the *max time* can ensure that your experiment is not unreasonably long

The minimum exposure time should be changed only under special circumstances.

11. If you would like the spectrometers to repeat data acquisitions at every source position (for statistical applications), then set *Acquisition reps. per source* to the number of repetitions you desire.

12. Highlight the box next to *Remove near-source detectors* if you do not want these spectrometers to acquire data. The near source detectors *often saturate because of their close proximity to the source* (usually unnecessary for small animal imaging). If you cannot correct this problem through employing OD filters, and/or turning down the laser current, highlight this box.

13. , Turn off lights in the imaging room.

Note: You will need to repeat the acquisition if you fail to shut the lights off.

14. Click on the *Acquire* button when you are ready to begin the experiment.

If the system computer and spectrometers are in the same room, turn off the monitor, and either quickly exit the room, or sit in the dark.

15. Wait patiently while the spectrometers acquire data. You can gauge the progress of the experiment by listening for system noises.

If you did not press *Set Spectrometers*, the first sounds you hear will probably be the spectrometers adjusting the grating and setting the appropriate filters. These sounds will be rather faint, but *all* acquisitions begin with the rotary stage making a quick turn. The rotary stage is the loudest noise generated by the system. In between rotations, you will hear the shutters clicking.

The computer will produce a loud, high-pitched beep for about 5 seconds when the acquisition is complete.

16. Turn on the monitor and check the spectra of your data. Click on the labeled tabs to view different detector readings.

LabVIEW displays the results from the final source position. If you wish to see results from different source positions, open your saved *.raw* files with an appropriate program (e.g. *Excel*).

Note: If you need to make any hardware changes before proceeding to additional acquisitions, you are advised to turn off active lasers. For the lasers on the system cart, simply press the output button, the highest-numbered button on the laser control box.

17. If this is your final experiment, click the *STOP* button and follow the instructions for shutting down the system on page 287.

Bioluminescence Tomography

Since bioluminescence is generated chemically in the animal, no external source is used in this mode.

If you have not already done so, complete the system initialization on page 268 before following the instructions here.

1. Select “Bioluminescence Tomography” from the Mode dropdown menu.
2. Sources will be ignored. Select your detector fibers by highlighting the appropriate boxes directly beneath the word *detector*.
The numbered boxes directly beneath the word *detector* allow you to define which fibers will function as detectors whenever they are not acting as the source. Box numbers correspond directly to fiber numbers, and *highlighted* boxes define those fibers that *will* function as detectors. Check and uncheck boxes according to your experimental specifications.

Note: Highlighting sources 1,3,5...15 is common practice for an 8-detector acquisition.

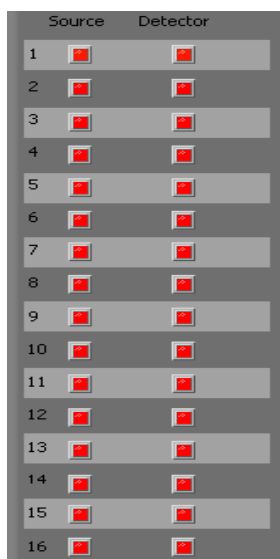


Image. 1 – Source/Detector Panel with all sources and detectors selected.

3. Select the *Grating* and *Center Wavelength* you would like to use under the *Spectrometers* tab.
For reference, see:
<C:\EXPERIMENTAL_systems_and_data\SPEC_TOMO_SYS\Calibration\wavelength_cal>.

4. Set your filter parameters.
5. **(Optional)** Click *Set Spectrometers* to begin the process of preparing the spectrometers while you finish your experimental preparations. If you do not click *Set Spectrometers*, the process will begin when you hit acquire.
6. Fill out the log file information.
7. Select the *Exp Times* tab.
8. ***Exp Times Tab (Optional)***: Changes the level of optimization if you do not want the spectrometers to optimize the data capture.
 - A. Leave the setting on *optimize at each source*, if you would like the system to test for, and calculate, near ideal exposure times.
 - B. **(Not Recommended)** Choose *no optimization* if you would like to manually input the exposure times for each detector.
9. Set the maximum and minimum exposure times. Minimum times cannot be below 0.01s.

These inputs will set extreme values for the *optimization* algorithm. Setting the *max time* can ensure that your experiment is not unreasonably long.

10. Turn off lights in the imaging room.
Note: You will need to repeat the acquisition if you fail to shut the lights off.
11. Click on the *Acquire* button when you are ready to begin the experiment.

If the system computer and spectrometers are in the same room, turn off the monitor, and either quickly exit the room, or sit in the dark.
12. If this is your final experiment, click the *STOP* button and follow the instructions for shutting down the system on page 287.

System Shutdown

1. Open *Shutdown_Specsys.vi* in LabVIEW.
<C:\EXPERIMENTAL_systems_and_data\SPEC_TOMO_SYS\Control_Routines\Shutdown_Specsys.vi>.
2. Run *Shutdown_Specsys.vi*.
3. Quit LabVIEW.
4. Turn off any lasers or lamps that were used during the experiment. If using the 690nm laser, make sure to press the buttons in descending order.
5. Turn off the spectrometers at the power strip.
6. Check the status of the Rotary Stage Control.
 - A. *If only the green light is on*, flip the on/off switch.
 - B. *If the green and yellow lights are on*, refer to *TROUBLESHOOTING*.
7. If you adjusted any system hardware, please restore the equipment to the way you found it.
8. Turn off the system computer.

Troubleshooting

Spectrometers Do Not Initialize

If *Initialize_system.vi* does not successfully open all connections to the cameras, you will need to reset the system in order to use it. If any error box pops up while running *Initialize_system.vi*, you will need to follow the instructions below.

1. Close LabVIEW and shut down the System Computer.
2. Turn off the spectrometers at the power strip, then turn them back on.
3. Restart the System Computer.
4. Open *Initialize_system.vi* and attempt to run the program.
5. If these steps don't succeed, repeat 1-4 until *Initialize_system.vi* completes.
6. If you are performing experiments over multiple days and do not want to initialize the system anew each day, you may turn up the temperature on the cameras overnight. The temperature control is in the program *Acquisition.vi* under the Spectrometers tab. Set the temperature to "-10" then click "Set spectrometers." **Note:** Closing all labview windows will release the camera connections, undoing the initialization. Leaving the *inititalize_system.vi* program open while using the system is recommended.

Acquisition Terminated Prematurely: Re-homing the rotary stage

If you end your acquisition before it has completed, or the program hangs and you must shut it down, you will need to return the rotary stage to home. **DO NOT TURN THE STAGE CONTROLLER OFF IF YELLOW LIGHT IS ON.** This re-homes the stage at its current position. To re-home it properly:

1. Open *Set_source.vi* in LabVIEW.
<C:\EXPERIMENTAL_systems_and_data\SPEC_TOMO_SYS\Control_Routines\Set_source.vi>
2. Highlight "Close connection."

3. Run the program. If the yellow light turns off, you are all set and can shut down the controller or keep using it.

If the stage still does not respond and the yellow light remains on, you will need to shut it down and re-home. It may very well be the case that the stage is located on a source fiber position. Since sources are 22.5 degrees from one another, it is easy to calculate how to return to source 1. The original home is -10 degrees from the source 1 position. Follow these steps to get it back to the original home:

1. Turn off the controller box and turn back on.
2. Open LabVIEW: *VXM_Home_Init_and_Move_RS_no_check-Easy.vi*. The file path is:
<C:\EXPERIMENTAL_systems_and_data\SPEC_TOMO_SYS\Control_Routines\Rotary_Stage\VXM_Home_Init_and_Move_RS_no_check-EASY.vi>.
3. Determine the source fiber position with which the source is aligned.
4. Calculate the original home position:

Error! Objects cannot be created from editing field codes.

For example, if you were on source 5 when it failed, Home = -122.5

5. Enter calculated *Home* position in the appropriate field in *VXM_Home_Init_and_Move_RS_no_check-Easy.vi* and Run the program.
6. The yellow light should still be on. If so, turn the motor controller off. It is now homed in the appropriate place. Be sure to confirm using a light source and the patient end of the fiber bundles before proceeding.

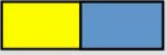
If this did not do the trick, you will need to re-align manually. Use a power-meter, light source, and *VXM_Home_Init_and_Move_RS_no_check-Easy.vi* to find the maximum power at source 1. Then offset the position by -10 degrees and cycle the motor controller power (with yellow light on).

Moving the spectrometer systems

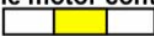
Moving the Spectroscopic Tomography System

WARNING: Do NOT move the carts without having followed these instructions. The carts are connected by several cables/fibers.

Cable labels:
Every connector that must be disconnected/connected to move the carts is labeled with colored tape stripes. In normal use, you should never need to disconnect/connect any connector that is not labeled.

	Cables that cross from a device on Cart 1 to Cart 2 are labeled with white-blue-white stripes on the Cart 2 end (the end that is connected/disconnected).
	Cables that cross from a device on Cart 2 to Cart 1 are labeled with white-yellow-white stripes on the Cart 1 end (the end that is connected/disconnected).
	Three power strips that connect to the wall are labeled with yellow-blue stripes on the wall socket end.

Disconnecting the assembled system:

1. **Cover exposed ends of the fiber bundles** (patient ends) using the appropriately labeled tubing and the plastic yellow tool. (do not coil bundles at this point).
2. **Disconnect power:** Unplug the **3 power supplies** that power the system.
 X3
3. **Disconnect rotary stage power:** The **rotary stage motor controller power** is plugged into the Spec Computer power strip on cart 2.  X1
4. **Disconnect the motor controller serial connection** to the Spec Computer from the controller side.  X1
5. **Unplug the 2 USB cables** that go from cart 1 to the Spec Computer (labeled on the computer side).  X2
6. **Unplug each of the 4 power cords** plugged into the SPECTROMETER power supply bar. Wrap them securely around the cart handles.
7. **Coil fiber bundles**, one on each cart. Secure other cords on the appropriate cart.
8. **CAREFULLY detach the source fibers** of Cart 2 from the rotary stage assembly. Lay gently yet securely on Cart 2.  X1
9. **Disconnect the orange light source fiber** from light source. Coil on Cart.  X1

Reconnecting the system:

- 1. Uncoil the fiber bundles** or remove coils from top of carts.
- 2. CAREFULLY attach the source fiber bundle** from Cart 2 to the bar above the rotary stage (on Cart 1) using one or two zip ties, ensuring there is enough room for each fiber to reach its designated location. Attach source fibers to their locations on the rotary stage.
- 3. Attach 2 USB cables** from Cart 1 to the USB ports labeled 1 and 2 on the back of the Spec Computer.
- 4. Plug the rotary stage motor controller power cord** into the Spec Computer power strip on Cart 2.
- 5. Connect the motor controller serial connection** to the motor controller
- 6. Plug the 4 spectrometer power cords** into the SPECTROMETER power supply bar.
- 7. Plug in all 3 power supply bars** – each labeled with a blue and yellow stripe on the socket end.
- 8. Attach the orange source fiber** to your light source.
- 9. Remove protective covers** from the detection fiber bundles when ready to image.

A Brief Note on Directory and Data File Structure

Directory Structure

All necessary files for the Spectral Tomography System are in <C:\EXPERIMENTAL_systems_and_data\SPEC_TOMO_SYS\> on the system computer. Data should be placed in the Data folder, under a folder with your own name.

<C:\EXPERIMENTAL_systems_and_data\SPEC_TOMO_SYS\Data\YOUR_NAME\>

Data File Structure

Data files are written during each acquisition.

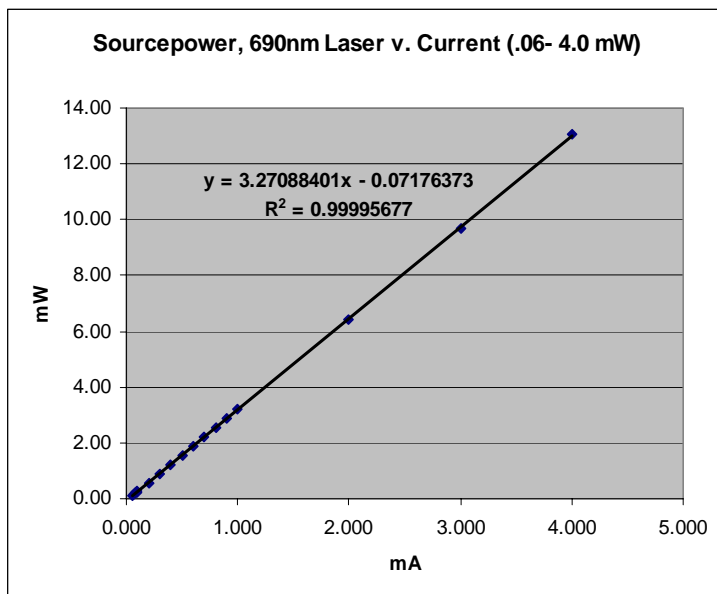
1. **‘*.log’** files contain critical information about the acquisition process. Heading information includes date and time, acquisition type, and experimental notes entered by the user. Below this, system parameters are recorded, including source/detectors selected, camera temperatures, grating settings, filter settings (16X16 array to match all source-detector pairs), and exposure times (16X16 array to match all source-detector pairs). It is critical that this information is saved since all data calibration routines use this information to calibrate the data. Loss of the log file renders a given acquisition useless.
2. **Raw data files have the extension ‘*.raw’**. One raw data file is saved for each source position, tagged with an ‘_s#’ in the file name, where # is the source number. The files are 2-D arrays with 1340 X 16 elements. Each column represents the full spectrum (1340 pixels) for a given spectrometer. The column index **always** corresponds to the spectrometer of that spectrometer. In other words, the data for spectrometer 1 is always in the first column, regardless of source position.

3. The program will also generate calibrated data files, with the ‘*.calspec’ extension, in the same format as the *.raw files described above. **At the time of the last manual update, the real-time calibration files were not properly validated, and so ignoring these files and calibrating post-acquisition is recommend. Similarly, integrated data stored as *.paaf1, *.paableed, and *.intrans should be ignored and recomputed later.**

Data Calibration

Calibrating spectral data is a complicated process that requires different approaches and calibrating files depending on the type of acquisition and the wavelength range. For the most part, calibration functionality is built into the *Acquisition.vi* program. However, it has been some time since these programs have been validated. **Currently, it is recommended that all data calibration be completed post-acquisition using the ‘.raw’ and ‘.log’ files.**

Approximate 690nm Laser Power vs. Current



Current(mA)	Power(mW)
4.000	13.07
3.000	9.700
2.000	6.409
1.000	3.197
0.900	2.867
0.800	2.547
0.700	2.223
0.600	1.901
0.500	1.575
0.400	1.239
0.300	0.9059
0.200	0.5797
0.100	0.2585
0.090	0.2289
0.080	0.1947
0.070	0.1626
0.060	0.1308

APPENDIX B: NIRFAST V2 DEV DOCUMENTATION

This appendix contains the documentation written for NirFast v2. This document is also included in the package itself.

NIRFAST_v2 Documentation

May 1, 2006
Scott C. Davis

Preface

NIRFAST_v2 consolidates NIR single wavelength, spectrally constrained, and fluorescence tomographic imaging in a single package. One objective of this package is to allow users to work in terms of physiologically relevant parameters (chromophore/fluorophore concentrations and Mie scattering parameters) while having the ability to select out a single wavelength to investigate simple, single wavelength behavior (i.e. simple μ_a and μ_s ' reconstructions). Adding chromophores/fluorophores is simple and requires no program modifications. FLUORFAST has been re-written as a Toolbox which works seamlessly with the spectral tools.

NIRfast_v2 consolidated by Scott C. Davis

NIRfast_v2\Standard by Hamid Dehghani

TLbx_Spectral by Scott C. Davis based on programs by Subha Srinivasan

TLbx_Fluorfast by Scott C. Davis based on programs by Hamid Dehghani

OUTLINE

Update list
Installation
Directory Structure

Section

- I. Spectral Priors**
- II. Mesh Structure**
 - 1. Introducing mesh types
 - 2. All meshes should include a chromscatt file
 - 3. Other mesh files
 - 4. Examples: loading meshes
 - 5. Summary
- III. Manipulating Meshes and Running Forward Models**
 - 1. Loading meshes
 - 2. Viewing mesh parameters
 - 3. Adding blobs
 - 4. Saving meshes
 - 5. Creating and manipulating chromscatt files
 - 6. Running forward models
 - 7. Changing mesh types and other mesh tools
- IV. Data formats and manipulation**
 - 1. Standard data, no spectral info.
 - 2. Fluorescence data
 - 3. Spectral data
- V. Reconstructing standard data**
- VI. Reconstructing spectral data**
- VII. Reconstructing Fluorescence data**
- VIII. Viewing fluorescence images**

Updates made to NIRFAST_V2_dev

02/11/08

Specific changes:

Added ICG.etaspec and lutex.etaspec files to /Tl bx_fluor. These are emission spectra of ICG and lutex respectively, measured through dilute solutions and normalized to the peak. They are used in the *_emisspec programs to model the peak propagation through tissue at multiple wavelengths.

10/31/07

General comments:

Added multi-wavelength link file capability to Tl bx_spectral. This allows data to be removed from specific wavelengths without removing the same s-d pairs from all wavelengths. Section II describes the format of the new files.

Load_mesh automatically loads these files properly and breaks mesh.link into a structured variable:

```
>> mesh.link
spec: {'speclink'}
      wv: [690 700 710 720 730 735 740 750 770 780 790 800 810 820 830 840]
      wv690: [16x15 double]
      wv700: [16x15 double]
      wv710: [16x15 double]
      wv720: [16x15 double]
      wv730: [16x15 double]
      wv735: [16x15 double]
      wv740: [16x15 double]
      wv750: [16x15 double]
      wv770: [16x15 double]
      wv780: [16x15 double]
      wv790: [16x15 double]
      wv800: [16x15 double]
      wv810: [16x15 double]
      wv820: [16x15 double]
      wv830: [16x15 double]
      wv840: [16x15 double]
```

Several programs in the spectral toolbox were added to manipulate these files, all with 'speclink' in the M-file name.

10/3/07

General comments:

I. Update v2 to follow the v3 conventions of a structured mesh.source and mesh.meas fields. i.e. mesh.source.fwhm, mesh.source.coord, mesh.source.fixed.

Specific changes:

Updated load_mesh to use mesh.source and mesh.meas structured variables

Updated move_source.m and move_detector.m to comply with same.

Updated save_mesh to comply with same. Note 'if/else' in saving source file due to complications using importdata.

Added gen_source_point.m to \Standard

Updated get_boundary_data to use mesh.meas structured variable

Updated femdata_stnd to use new calls for generating source (fwhm or point)

Updated femdata_spectral to use mesh.source.fixed and mus_eff

Updated femdata_fl to use new calls for generating source (fwhm or point) and to move source differently for excite and emission wavelengths

Updated femdata_x_sub to use new calls for generating source (fwhm or point) and to move source at excite wavelength (if not moved)

Added build_jacobian_cw.m to \Standard

Updated gen_source_adjoint.m to use mesh.meas.int_func

Updated jacobian.m similar to femdata_stnd.m.

Updated jacobian_spectral.m to remove source moving - it is now done in jacobian.

Updated jacobian_fl to find nsource based on mesh.source.coord. No need to move sources in this program

Updated:

- Build_jacobian

- Build_jacobian_fl

- Build_jacobian_cw

- Build_jacobian_fl_cw

- To use mesh.meas.coord and mesh.source.coord

Updated recon_sub_intrins and recon_sub_intrins_spatial
to remove source moving - now done in jacobian.

Updated jacobian_spectral_perturb ??

Still need to look at: Calibration routines

Installation:

Set MatLab path to *NIRfast* including all sub-folders.

Recommend running NIRFAST under LINUX for larger 3-D problems. 2D problems will run nicely on a laptop using windows.

Directory Structure

NIRFAST now includes the Spectral Toolbox and Fluorfast (now the Fluorescence Toolbox) as well as a Spatial Toolbox which incorporates prior spatial information in the reconstruction programs.

Nirfast_v2 - Generic programs which will run with all mesh types. Many are parsing programs which recognize the input files and direct Nirfast to the appropriate sub-folder or toolbox.
Nirfast_v2\doc - important documentation and instructions on running NIRfast_v2.
Nirfast_v2\examples - files for a general example which is worked in this instruction manual
Nirfast_v2\meshes - storage area for mesh files. Broken down into sub-folders to separate fluor and stnd mesh types.
Nirfast_v2\Standard - Essentially, FEM programs for the legacy version of NIRfast. Single wavelength, mua and mus forward model and reconstruction programs.
Nirfast_v2\Standard\subrout - important subroutines and mex files called by NIRfast_v2 are stored in this folder.
Nirfast_v2\Standard\Calibration_stnd - programs which handle data calibration for Standard Nirfast. These are also called by programs in some Toolboxes.

TOOLBOXES:

Nirfast_v2\Tlbox_Fluorfast - The fluorescence toolbox home directory contains *.m files for generating data, adding noise, reconstructing, etc.
Nirfast_v2\Tlbox_Fluorfast\Calibration_fl - Calibration programs for fluorescence data. At the time this manual was written, this portion was incomplete.
Nirfast_v2\Tlbox_Fluorfast\subrounts_fl - Subroutines specific to Fluorfast
Nirfast_v2\Tlbox_Spatial - Programs for running spatially constrained reconstructions.
Nirfast_v2\Tlbox_Spectral - The spectral toolbox home directory contains *.m files for loading and saving '.chromscatt' parameters, generating data, adding noise, reconstructing, etc.
Nirfast_v2\Tlbox_Spectral\Calibration_spec - Programs used for calibration of spectral data.
Nirfast_v2\Tlbox_Spectral\Calibration_spec\Optim_tools - Sub-programs used in the spectral data calibration procedure.

I. Spectral Priors

The Extinction Coefficient file, “excoef.txt”

Since it is recommended that NIRfast users work from spectral parameters, it is useful to understand how this a-priori information is incorporated. The extinction coefficient file contains all a-priori spectral information. This consists of the extinction coefficients for different chromophores at different optical wavelengths. Additionally, it stores a text list of all parameters for which there exists a-priori information. Many programs within the spectral toolbox compare this list with a list in the ‘.chromscatt’ file (described later) to select the relevant chromophores for a given task.

HbO					
deoxyHb					
Water					
LuTex					
GdTex					
S-Amplitude					
S-Power					
661	0.074074074	0.85	0.00148	1.759214081	2.330357
735	0.09889	0.24	0.0038	5.795744677	7.959088
761	0.118518519	0.329166667	0.00428	1.830336566	4.70488
785	0.15	0.205555556	0.00378	0.380449554	0.788026
808	0.174074074	0.161111111	0.00332	0.121699655	0.277321
826	0.227777778	0.161111111	0.00396	0.138248193	0.172045
849	0.237037037	0.155555556	0.00578	0.217664778	0.060047
Wavelengths	HbO	deoxyHb	water	LuTex	GdTex

ADDING A-PRIORI SPECTRAL INFORMATION:

Most users will never need to update this file, however, the Spectral Toolbox is designed to allow users to incorporate additional wavelengths or chromophores simply by adding this information to the excoef.txt file in the format shown above (add chromophores between 1-Exogenous and S-Amplitude. Ensure that the first 3 letters of the chromophore label are unique on the list.). All other programs will recognize the change and adjust accordingly.

STORE AND USE ONLY ONE excoef.txt FILE:

The Spectral Toolbox is designed to use this file as a reference and pull only the relevant information for a given task. So, it can be a complete list of all chromophore information, even if the user is only interested in a smaller subset of chromophores.

II. Mesh Structure

Introduction

Some of the most notable updates to this NIRfast release involve mesh structures and how they are manipulated. The files associated with a given mesh are listed below. File formats that depart from previous versions of NIRfast are in red and described in this section.

example.chromscatt (opt.)

example.elem

example.link

example.meas

example.node

example.param

example.region

example.source

1. Introducing mesh “types”:

Meshes are classified as either **standard** or **fluorescence** meshes and are flagged by the abbreviations “**stnd**” and “**fluor**” at the top of the *.param file. In terms of the saved mesh files, the only difference between a **stnd** and **fluor** mesh are the parameters saved in the *.param file. **Standard** meshes most resemble meshes structured in the original *NIRfast* release; the *.param file contains a set of optical properties at a single wavelength. The columns in a *.param file for a standard mesh represent the following parameters:

$$\text{“stnd” mesh: } \left| \begin{array}{l} \textit{stnd} \\ \mu \quad \kappa \quad RI \\ \mu \quad \kappa \quad RI \end{array} \right.$$

Fluorescent meshes contain fluorophore properties in addition to the tissue optical parameters. The columns in a *.param file represent the following parameters:

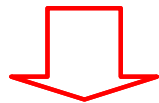
$$\text{“fluor” mesh: } \left| \begin{array}{l} \textit{fluor} \\ \mu_{ax} \quad \kappa_x \quad RI \quad \mu_{am} \quad \kappa_m \quad \mu_{af} \quad \eta \quad \tau \\ \mu_{ax} \quad \kappa_x \quad RI \quad \mu_{am} \quad \kappa_m \quad \mu_{af} \quad \eta \quad \tau \end{array} \right.$$

The subscripts ‘*x*’ and ‘*m*’ indicate that the optical properties apply to photons at the excitation and emission wavelengths, respectively.

2. All meshes should (but need not) include a “*.chromscatt” file:

The “*.chromscatt” file contains a list of the absorbing materials in tissue, i.e. ‘chromophores’, the scattering parameters based on Mie Theory, and the respective values of these parameters. It is similar to the ‘*.param’ mesh file but is a more physiological representation of the tissue properties. The list at the top of the file varies depending on how many chromophores are of interest. For example, if no exogenous contrast is to be used, ‘LuTex’ and column 4 below the list will not be included. For most programs in the Spectral Toolbox, this list is used to determine which chromophores apply for a given task.

```
HbO
deoxyHb
Water
LuTex
S-Amplitude
S-Power
0.001 0.001 0.4 0.0001 1 1.2
0.001 0.001 0.4 0.0001 1 1.2
0.001 0.001 0.4 0.0001 1 1.2
0.001 0.001 0.4 0.0001 1 1.2
```



mesh nodes

Though NIRfast will run in single wavelength mode (or two wavelength mode for fluorescence meshes) on meshes without “*.chromscatt” files, the presence of this file is required when implementing routines from the Spectral Toolbox. Meshes without a “*.chromscatt” contain no spectral chromophore concentration or Mie scattering information.

3. Spectral link (“speclink”) files

Used only with spectral meshes, these files allow users to remove specific data points from real data without having to remove them for every wavelength. A portion from one of these files is presented below. ‘Speclink’ is a flag for load_mesh and other files programs that need to recognize the files. Below this, standard link information for each wavelength is concatenated horizontally and a heading indicating the start of each wavelength’s information makes up the first row. For example, ‘690’ indicates the start of the 690 link information, which continues to the right until ‘700’. NaN’s are used as place holders.

Section II. Mesh Structure

speclink	690	NaN	700	NaN	NaN														
2	3	4	5	6	7	8	9	10	11	12	13	14	15	16	1	2	3	4	
3	4	5	6	7	8	9	10	11	12	13	14	15	16	1	3	4	5		
4	5	6	7	8	9	10	11	12	13	14	15	16	1	2	4	5	6		
5	6	7	8	9	10	11	12	13	14	15	16	1	2	3	5	6	7		
6	7	8	9	10	11	12	13	14	15	16	1	2	3	4	6	7	8		
7	8	9	10	11	12	13	14	15	16	1	2	3	4	5	7	8	9		
8	9	10	11	12	13	14	15	16	1	2	3	4	5	6	8	9	10		
9	10	11	12	13	14	15	16	1	2	3	4	5	6	7	9	10	11		
10	11	12	13	14	15	16	1	2	3	4	5	6	7	8	10	11	12		
11	12	13	14	15	16	1	2	3	4	5	6	7	8	9	11	12	13		
12	13	14	15	16	1	2	3	4	5	6	7	8	9	10	12	13	14		
13	14	15	16	1	2	3	4	5	6	7	8	9	10	11	13	14	15		
14	15	16	1	2	3	4	5	6	7	8	9	10	11	12	14	15	16		
15	16	1	2	3	4	5	6	7	8	9	10	11	12	13	15	16	1		
16	1	2	3	4	5	6	7	8	9	10	11	12	13	14	16	1	2		
1	2	3	4	5	6	7	8	9	10	11	12	13	14	15	1	2	3		

4. Other mesh files

The other files which make up a saved mesh are identical to the previous versions of *NIRfast*. These are detailed in Appendix A.

4. Examples: Loading meshes.

To understand the new meshes, let's review the structure of the loaded mesh.

Use: `mesh = load_mesh(fn, specflag, a)`

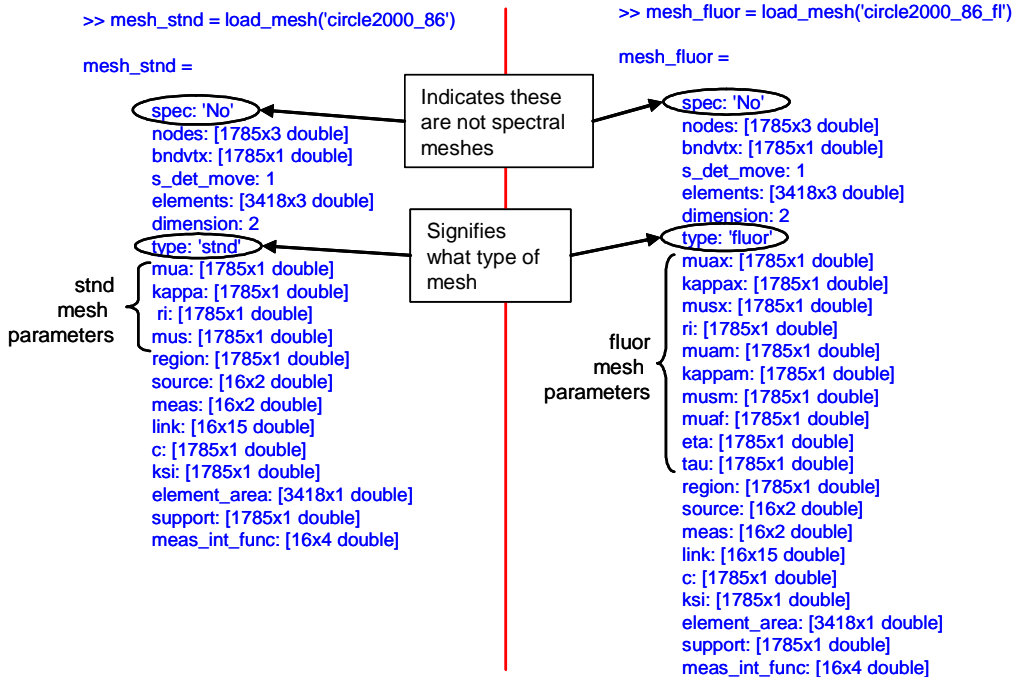
fn – mesh filename

specflag – leave blank to load no spectral information or input 'spec' to load spectral information.

a – set = 1 to plot mesh boundary and source/detector positions. Works even if specflag is blank.

A. LOADING MESHES WITH NO SPECTRAL INFORMATION

“load_mesh.m” automatically recognizes the mesh type (**stnd** or **fluor**) and does **NOT** load up the chromophore information unless specified with “specflag”. Let's load up a **stnd** and **fluor** mesh with no spectral information to compare them:



B. LOADING MESHES WITH SPECTRAL INFORMATION

If *.chromscatt files exist for these meshes, we can also load them with the spectral chromophore information. To do this, input 'spec' for **specflag**

NOTE: Meshes loaded with spectral information **IGNORE** values in the *.param file

```
>> mesh_std = load_mesh('circle2000_86','spec')
Loading the following parameters from
"circle2000_86.chromscatt":

ans =

'HbO'
'deoxyHb'
'Water'
'S-Amplitude'
'S-Power'

mesh_std =
  spec: 'Yes'
  nodes: [1785x3 double]
  bndvtx: [1785x1 double]
  s_det_move: 1
  elements: [3418x3 double]
  dimension: 2
  type: 'std'
  ri: [1785x1 double]
  conc: [1785x3 double]
  sa: [1785x1 double]
  sp: [1785x1 double]
  wv: [7x1 double]
  excoef: [7x3 double]
  chromscattlist: {5x1 cell}
  region: [1785x1 double]
  source: [16x2 double]
  meas: [16x2 double]
  link: [16x15 double]
  c: [1785x1 double]
  ksi: [1785x1 double]
  element_area: [3418x1 double]
  support: [1785x1 double]
  meas_int_func: [16x4 double]
```

```
>> mesh_fluor = load_mesh('circle2000_86_fl','spec')
Loading the following parameters from
"circle2000_86_fl.chromscatt":

ans =

'HbO'
'deoxyHb'
'Water'
'LuTex'
'S-Amplitude'
'S-Power'

mesh_fluor =
  spec: 'Yes'
  nodes: [1785x3 double]
  bndvtx: [1785x1 double]
  s_det_move: 1
  elements: [3418x3 double]
  dimension: 2
  type: 'fluor'
  ri: [1785x1 double]
  eta: [1785x1 double]
  tau: [1785x1 double]
  conc: [1785x4 double]
  sa: [1785x1 double]
  sp: [1785x1 double]
  wv: [7x1 double]
  excoef: [7x4 double]
  chromscattlist: {6x1 cell}
  region: [1785x1 double]
  source: [16x2 double]
  meas: [16x2 double]
  link: [16x15 double]
  c: [1785x1 double]
  ksi: [1785x1 double]
  element_area: [3418x1 double]
  support: [1785x1 double]
  meas_int_func: [16x4 double]
```

Fluorophore
properties

The list at the top of the *.chromscatt file tells load_mesh which chromophores to include in the loaded mesh structure. Notice that the optical properties mua, mus, etc, have been replaced by the spectral information. Here is a summary of the mesh fields:

- mesh.spec** – indicates whether spectral information is loaded.
- mesh.conc** – a list of chromophore concentrations, #nodes X #chromophores
- mesh.sa** – scattering amplitude
- mesh.sp** – scattering power

mesh.wv – A list of all wavelengths for which there are extinction coefficients available

mesh.excoef – the extinction coefficients taken from the “excoef.txt” file

mesh.chromscattlist – a list of the loaded chromophores and scat. parameters

5. Summary - meshes.

Understanding the mesh structure described above will make using NIRfast a more intuitive experience and will help in program modification and updating.

- In general, there are 4 meshes that can be loaded, **1)** a stnd mesh with no spectral information, **2)** a stnd mesh with spectral information, **3)** a fluor mesh with no spectral information and **4)** a fluor mesh with spectral information.
- Meshes with no spectral information usually work from the optical parameters listed in the mesh.param file
- Meshes with spectral information ignore the values in the mesh.param file and use the chromophore concentrations and scattering parameters directly.
- All programs use the same load_mesh program, but accomplish different tasks based on what type of mesh is loaded.
- Several tools exist to manipulate these meshes easily and transition between fluor and stnd meshes. These are described in the following Quickstart Guide.

Section III: Manipulating Meshes and Running Forward Models

Introduction

In this section, we will walk through an example using a **stnd** mesh to learn:

1. Loading meshes
2. Viewing mesh parameter values
3. Adding blobs
4. Saving meshes
5. Creating and Manipulating *.chromscatt files
6. Running forward models
7. Changing mesh “types”: Switching between stnd and fluor meshes

fluor: Tips on running fluor will be included in blue boxes, such as this one, where appropriate

1. Loading meshes

See Section II for instructions on loading meshes.

2. Viewing meshes

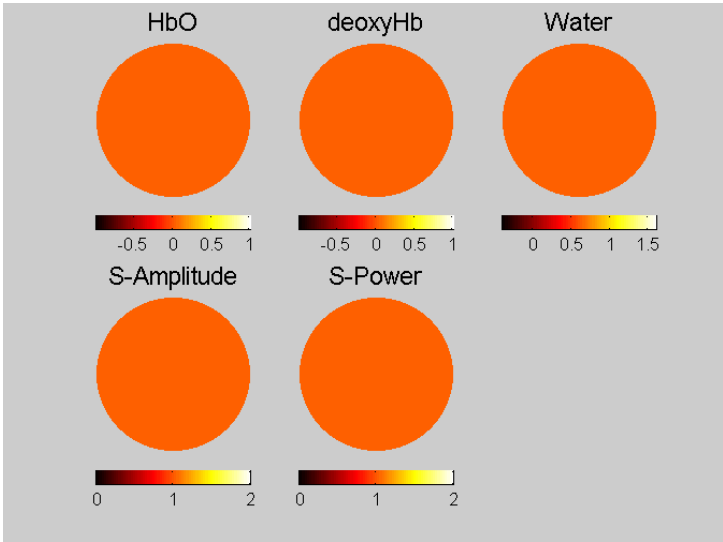
To view the parameter values of a mesh at any time, use **plotmesh(mesh,specflag,wv)**

mesh – mesh filename or workspace variable name

specflag – if loading mesh from a file, use specflag = ‘spec’ to signify the mesh has spectral information. Also, set specflag = ‘spec’ any time you want to use the “**wv**” input

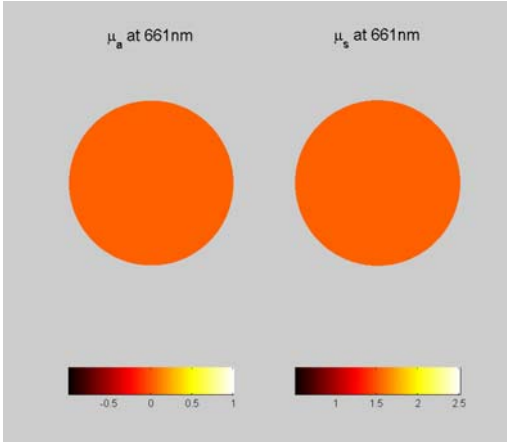
wv – if the mesh is loaded with spectral information and you want to view the optical properties at a given wavelength, set wv = wavelength. For fluor meshes, wv is a two element array in the form [wv_excitation wv_emission]. “wv” must be included in mesh.wv (ie. listed in the excoef.txt file).

```
>> plotmesh(mesh_stnd)
Or
>> plotmesh('circle2000_86','spec')
```



Exercise: Now plot the optical properties of this mesh at 661nm

```
>> plotmesh(mesh_std,'spec',[661])
```



fluor: If this were a fluor mesh, you would enter excitation and emission wavelengths in place of [661]. For example:

$wv = [761 \ 785]$

3. Adding blobs

To add anomalies, use

add_blob(mesh)

mesh – a workspace variable name (loaded mesh name)

“add_blob.m” now recognizes what type of mesh is inputted and automatically walks the user through adding anomalies. Note that add_blob is simply a parsing program which calls the sub-routines to do that actual mesh manipulation. Therefore, a user may use the subroutines in a stand-alone manner if the add_blob.m interaction is too cumbersome. Also note, some 3-D functions are not yet operational and add_blob.m will indicate which ones.

Exercise: Add an anomaly in chromophore concentration and scattering parameters to mesh_std. Notice that you can also change the background values of the mesh parameters.

```
>> mesh_anom = add_blob(mesh_std)           "0" = No
                                              >>>> 1
                                              Enter position of blob center
                                              x-position ...2
                                              y-position ...23
                                              radius of blob ...9
                                              Enter heterogeneity concentration and scatter values for the
                                              following parameters:
                                              (1) HbO
                                              (2) deoxyHb
                                              (3) Water
                                              (4) S-Amplitude
                                              (5) S-Power
***** IMPORTANT:
*****
This mesh was loaded as a spectral mesh!!

>> Adding blobs only changes chromophore
concentration
and scattering parameters in the .chromscatt file!!
(direct optical property values normally stored in
the "mesh.param" file will be ignored)

*****
***
mesh includes the following parameters:
(1) HbO
(2) deoxyHb
(3) Water
(4) S-Amplitude
(5) S-Power

Would you like to change the background concentration
and scatter values for the above parameters?
"1" = Yes
"0" = No
>>>> 0

*****
ADDING HETEROGENEITIES

Would you like to add a blob?
"1" = Yes

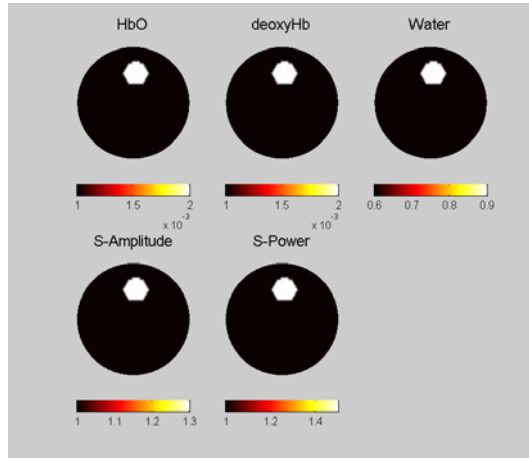
Enter as array, Example: >>>> [0.002 0.002 0.9 1.3 1.5]
Requires 5 values >>>> [0.002 0.002 0.9 1.3 1.5]

Confirm heterogeneity values:
HbO = 0.002
deoxyHb = 0.002
Water = 0.9
S-Amplitude = 1.3
S-Power = 1.5

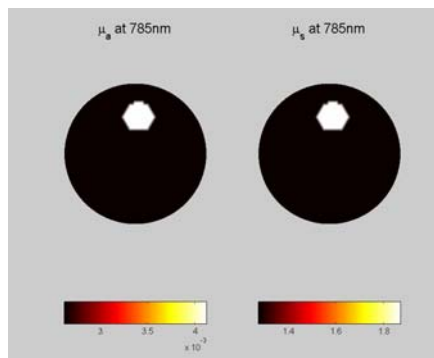
Are these values correct?
"1" = Yes
"0" = No
Confirm >>>> 1

Would you like to add another blob?
"1" = Yes
"0" = No
>>>> 0
```

Exercise: Now view the mesh just created
 >> `plotmesh(mesh_anom)`



>> `plotmesh(mesh_anom,'spec',[785])`



4. Saving meshes

To save meshes use
save_mesh(mesh,fn,geometry)

mesh - can be any type of mesh, save_mesh recognizes the type and spectral status and saves mesh appropriately.

fn – filename of mesh to be saved.

geometry – opt. - Enter 'rect' for 'geometry' to fix source and detector positions. Next time the mesh is loaded, the sources and detectors will not be moved automatically.

Exercise: Save the mesh_anom just created

>> `save_mesh(mesh_anom,'circle2000_86_anom')`

Now saving "circle2000_86_anom.chromscatt" with the following parameters:

```
param_list =
  'HbO'
  'deoxyHb'
```

'Water'
'S-Amplitude'
'S-Power'

At what wavelength would you like to save mua and mus?... 785

5. Creating and Manipulating '*.chromscatt' files

Create chromscatt files:

If you have created a new mesh which does not have a *.chromscatt file, or have added a chromophore to excoef.txt, you may create a new *.chromscatt file using

**create_chrom_scatt(mesh, 'filename of chromscatt to save',
fn_excoef, opt:'fn_existing_chrom_scatt')**

This program allows you to create new *.chromscatt files. If you would like to include a new chromophore, simply add it to the *.excoef file first, then run **create_chrom_scatt** to generate the appropriate *.chromscatt file. The new chromophore will be included on the option list as seen below.

Note: '*.chromscatt' file will be saved automatically.

Exercise: Create a *.chromscatt file named example.chromscatt

```
>> create_chrom_scatt(mesh_std,
'example', 'excoef.txt')
Which chromophores would you like to
include?
(1) HbO
(2) deoxyHb
(3) Water
(4) LuTex
(5) GdTex
Enter as array, Example: >>>> [1 2 3
4]
>>>> [1 2 3 4]

Enter background concentration and
scatter values for the following
parameters:

HbO
deoxyHb
Water
LuTex
S-Amplitude
S-Power

Enter as array, Example: >>>> [0.001
0.001 0.6 1 1.2]
Requires 6 values >>>> [0.001 0.001
0.0001 0.4 1 1]

Confirm background values:
HbO = 0.001
deoxyHb = 0.001
Water = 0.0001
LuTex = 0.4
S-Amplitude = 1
S-Power = 1

Are these values correct?
"1" = Yes
"0" = No
Confirm >>>> 1

*****
ADDING HETEROGENEITIES

Would you like to add a blob?
"1" = Yes
"0" = No
>>>> 0

Now saving "example.chromscatt" with the
following parameters:

param_list =
'HbO'
'deoxyHb'
'Water'
'LuTex'
'S-Amplitude'
'S-Power'
```

Users will most often use `add_blob.m` and `create_chrom_scatt.m` to manipulate and save '*.chromscatt' files, however, `load_chrom_scatt.m` and `save_chrom_scatt.m` allow further flexibility.

Loading parameters (*.chromscatt' files)

To load a chromscatt file alone use

```
[chrom_scatt, used_param_list, excoef] = load_chrom_scatt(fn_chrom_scatt,  
fn_excoef)
```

Example: Load 'example.chromscatt' into workspace

```
>> [chrom_scatt, used_param_list, excoef] = load_chrom_scatt('example.chromscatt',  
'excoef.txt');
```

Loading the following parameters from "example.chromscatt":

```
ans =  
  
'HbO'  
'deoxyHb'  
'Water'  
'LuTex'  
'S-Amplitude'  
'S-Power'
```

OUTPUTS:

`chrom_scatt` = matrix of parameter values (#nodes, #parameters)

`used_param_list` = a character array of the parameters listed in 'example.chromscatt'

`excoef` = matrix of wavelengths and applicable chromophore extinction coefficients (# wavelengths, # parameters + 1)

Saving parameters (*.chromscatt' files)

To save a chromscatt file, use

```
save_chrom_scatt(fn_chrom_scatt, param_list, chrom_scatt)
```

Example: Save workspace parameters loaded above as 'example_2.chromscatt'

```
>> save_chrom_scatt('example_2.chromscatt', used_param_list, chrom_scatt)
```

Now saving "example_2.chromscatt" with the following parameters:

```
param_list =  
  
'HbO'  
'deoxyHb'  
'Water'  
'Lutex'  
'S-Amplitude'  
'S-Power'
```

6. Running Forward Models

Use **data = femdata(mesh,frequency,specflag)**

mesh - the mesh upon which the forward solution is calculated

frequency - Modulation frequency

specflag – *opt.* use only if “mesh” is a saved file, not if “mesh” is a workspace variable.

Femdata.m now recognizes the type of mesh inputted and prompts the user to run the appropriate forward model. It is a parsing program so users who require more flexibility may use the sub-routine forward models directly. Choices include:

- a. Stnd mesh, no spectral info. (most like previous *NIRfast* versions)
Call to: `data = femdata_stnd(mesh,frequency)`
- b. Stnd mesh, spectral forward model (called from the spectral toolbox)
Call to: `data = femdata_spectral(mesh,frequency,fn_data,wv_array)`
- c. Fluor mesh, no spectral info.
Call to: `data = femdata_fl(mesh,frequency)`
- d. Fluor mesh, spectral forward model
Call to: `data = femdata_spec_fl(mesh,frequency,fn_data,wv_spec,wv_fluor)`

Exercise: Run forward model on mesh_anom for 6 wavelengths.

```
>> data = femdata(mesh_anom,100)
```

You have loaded a standard type, spectral mesh: Please select which femdata you would like to run:

(1) full spectral data set (Note: data will be compatible with reconstruct_spectral only)

(2) stnd nirfast at a wavelength of your choice (calculates mua, mus from spectral conc and uses for femdata_stnd)

Note: data will be compatible with reconstruct_stnd, but not reconstruct_spectral

```
>>>> 1
```

Please enter filename of data to be saved (do not include the file extension!):

```
(ex: "data_spec_test") >>>> 'data_circ2000_86_tutorial'
```

Please enter wavelength array for femdata_spectral from:

```
661
```

```
735
```

```
761
```

```
785
```

```
808
```

```
826
```

```
849
```

```
(ex: [661 761 785 808 826 849]) >>>> [661 761 785 808 826 849]
```

Calculating data for:

```
661 nm
```

```
761 nm
```

```
785 nm
```

```
808 nm
```

```
826 nm
```

```
849 nm
```

```
Saving data as data_tutorial_spec.paa...
```

```
data =
```

Section III. Manipulating Meshes and Running Forward Models

```
paa: [240x12 double]  
wv: [661 0 761 0 785 0 808 0 826 0 849 0]
```

7. Switching mesh “types”

In some cases, users may want extract the optical properties stored in a **fluor** mesh and use them with the tools available for the **stnd** meshes. To change mesh type, use

```
mesh = fluor2stnd(meshfl,x_or_m)
```

meshfl - fluor mesh (non-spectral)

x_or_m - excitation or emission properties ('x' or 'm')

```
>> mesh = fluor2stnd(mesh_fluor,'x')
```

Likewise, users may have two **stnd** meshes which correspond to excitation and emission properties of a desired **fluor** mesh. To switch between the two, use

```
mesh = stnd2fluor(meshx,meshm,meshfl)
```

meshx - mesh for excitation properties (non-spectral)

meshm - mesh for emission properties (non-spectral)

meshfl - opt. - a loaded fluorescence mesh. If this is set as an input, the muaf, eta, and tau values will be used for the output 'mesh'

Other tools

When working with a mesh which incorporates spectral information, the user may calculate the optical properties at any wavelength listed in mesh.wv at any time using,

```
[mua, mus, kappa, E] = calc_mua_mus(mesh,wv_array)
```

mesh - mesh with spectral information

wv_array - a list of the wavelengths for which the user would like to calculate optical properties

“Legacy” meshes

If you load a mesh created before this version of NIRfast, load_mesh.m will automatically ask if you want to convert to the new mesh format.

Section IV: Data Formats and Manipulation

Introduction

Because the new *NIRfast* release is a comprehensive package with standard, fluorescent, and spectral capabilities, femdata produces different data files depending on the mesh or toolbox used. The chart below is a summary of the data type each forward model produces and a detailed description follows.

Data File Format Summary

<p style="text-align: center;">1. Standard mesh with no spectral priors</p> <p>Program used: femdata_stnd (does not auto save data)</p> <p>Data Summary: data_name.paa – two columns, amplitude and phase</p>	<p style="text-align: center;">2. Fluor mesh with no spectral priors</p> <p>Program used: femdata_fl (does not auto save data)</p> <p>Data Summary:</p> <ul style="list-style-type: none"> a) data_name.paaf1 – two columns, amplitude and phase of fluorescence signal b) data_name.paaxfl – four columns, amplitude and phase of <ul style="list-style-type: none"> - excitation (intrinsic) - fluorescence signal c) data_name.paaxflmm – six columns, amplitude and phase of <ul style="list-style-type: none"> - excitation (intrinsic) - fluorescence signal - emission (intrinsic)
<p style="text-align: center;">3. Standard mesh with spectral priors</p> <p>Program used: femdata_spectral (Auto saves data)</p> <p>Data Summary: data_name.paa – 2 x (number of wavelengths) columns, amplitude and phase at each wavelength. First row contains the wavelengths (in nm) at which each amplitude and phase set was collected. Wavelength values are directly over the amplitude columns (see below for details).</p>	<p style="text-align: center;">4. Fluor mesh with no spectral priors</p> <p>Program used: femdata_spec_fl (Auto saves data)</p> <p>Data Summary: Calls femdata_spectral and femdata_fl (see left and above) data_name.paa data_name.paaf1 data_name.paaxfl data_name.paaxflmm</p> <p>Notice this is simply a combination of stnd spectral data and fluor data.</p>

1. “Standard” data, no spectral info.

Data generated from femdata for a single wavelength has the form:

```
| ampl.  phase |  
| ampl.  phase |  
| ..      ..    |  
# measurements
```

Adding noise to stnd data

To add normally distributed Gaussian noise to data, use
data_noise = add_noise(data1,amp,ph,fn_data_noise)

data1 - saved data file or workspace array

amp - % amplitude noise

ph - in degrees

fn_data_noise - opt. - if inputted, program will save the noisy data using this as a filename.

2 & 4. Fluorescence data

femdata_fl generates three data file formats:

1) **paaf1: [240x2 double]:** Fluorescence data only ('*fl')

|fluor. ampl. | fluor. phase|

2) **paaxfl: [240x4 double]:** Excitation and fluorescence data ('*xfl')

|excite ampl. | excite phase | fluor. ampl. | fluor. phase|

3) **paaxflmm: [240x6 double]:** Excitation, fluorescence, and intrinsic emission data ('*xflmm')

|excite ampl. | excite phase | fluor. ampl. | fluor. phase | emm. ampl. | emm. phase|

*** The distinction between these formats is particularly important when reconstructing data. The reconstruction program recognizes the file format and chooses the appropriate reconstruction technique based on this input. ***

Saving fluorescence data

Use **save_data_fl(fn,data)**

fn - the filename to save

data - the workspace structured variable

Saves three files:

fn.paaf1 - fluorescence amplitude and phase only

fn.paaxfl - intrinsic excitation and fluorescence amplitude and phase

fn.paaxflmm - intrinsic excitation, fluorescence, and emission amplitude and phase

Example:

```
>> save_data('fl_example', data)
```

```
Saving fl_example.paaf1, fl_example.paaxfl, fl_example.paaxflmm
```

Adding Noise to fluorescence data

To add normally distributed Gaussian noise to a fluorescence data, use

```
data_noise=add_noise_fl(data,OD_rejection,amp_x,ph_x,amp_fl,ph_fl,amp_m  
m,ph_mm);
```

data - saved data file or workspace array. Must contain extension.

OD_rejection – estimated optical density of fluorescent filter

amp_x, amp_fl, amp_mm - % of amplitude for excitation, fluorescence, and emission (intrinsic) respectively.

Section IV. Data Formats and Manipulation

ph_x, ph_fl, ph_mm - in degrees for excitation, fluorescence, and emission (intrinsic) respectively.

Notes: No option to save data in `add_noise_fl`
Even if adding noise to a `.paaf` or `paaxfl` file, enter values for all inputs!

3&4. “Spectral” data

Data generated from femdata_spectral has the form:

λ_1	0	λ_2	0	λ_3	0	λ_4	0	λ_5	0	λ_6	0
ampl	phase	ampl	phase	ampl	phase	ampl	phase	ampl	phase	ampl	phase
ampl	phase	ampl	phase	ampl	phase	ampl	phase	ampl	phase	ampl	phase
...
# measurements											

The first row signifies the wavelengths for which the data was calculated or recorded. Every other column in the first row is a 0, this is simply a place holder and is removed when the data is loaded using other Spectral Toolbox programs.

Example:

Wavelength	6.81E+02	0.00E+00	7.35E+02	0.00E+00	7.81E+02	0.00E+00	7.85E+02	0.00E+00	8.08E+02	0.00E+00	8.26E+02	0.00E+00	8.49E+02	0.00E+00
nm	1.46E-03	2.78E+01	1.37E-03	2.54E+01	2.85E-03	2.99E+01	3.97E-03	3.23E+01	4.54E-03	3.32E+01	4.07E-03	3.14E+01	3.81E-03	2.97E+01
	2.11E-05	5.14E+01	1.84E-05	4.89E+01	9.10E-05	5.63E+01	1.87E-04	8.08E+01	2.60E-04	6.23E+01	1.06E-04	6.89E+01	1.80E-04	5.46E+01
	⋮	⋮	⋮	⋮	⋮	⋮	⋮	⋮	⋮	⋮	⋮	⋮	⋮	⋮



Ampl. and Phase

Adding Noise to spectral data

To add normally distributed Gaussian noise to a spectral data set, use **data_noise = add_noise_spec(data_fn, amp, ph, fn_data_noise)**

- data_fn** - saved data file
- amp** - percentage of AC intensity,
- ph** - in degrees (for phase)
- fn_data_noise** – opt. – if inputted, program will save the noisy data using this as a filename.

Example:

```
>> data_noise = add_noise_spec('data_tutorial_spec.paa',1,1,'datanoise_tutorial_spec.paa');
Loading data and wavelength information
Saving noisy data as datanoise_tutorial_spec.paa
```

Section V. Reconstructing Standard Data

1. The reconstruction program

Use

[fwd_mesh,pj_error] = reconstruct_stnd(fwd_fn, recon_basis, frequency, data_fn, iteration, lambda, sol_label, filter_n, plotflag)

fwd_fn - the filename of the mesh used for forward solving

recon_basis - the reconstruction mesh basis or pixel basis

frequency - modulation frequency

fn_data - filename of the data to be reconstructed.

lambda - initial regularization value

iteration - maximum number of iterations allowed for the reconstruction

sol_label - prefix for the name of the solution and log files.

filter_n - amount of filtering of the solution at each iteration

plotflag - set plotflag = 1 to plot solutions at each iteration

SAVED SOLUTION FILES

sol_label_mua.sol

sol_label_mus.sol

sol_label.log

Section VI. Reconstructing Spectral Data

1. The reconstruction program

Use

[fwd_mesh,pj_error]=reconstruct_spectral(fwd_fn, recon_basis, frequency, data_fn, sol_label, iteration, fn_regularization, filter_n, wv_array)

fwd_fn - the filename of the mesh used for forward solving (must have .chromscatt file with initial guess values).

recon_basis - the reconstruction mesh basis or pixel basis

frequency - modulation frequency

data_fn - filename of the data to be reconstructed.

sol_label - prefix for the name of the solution and log files.

iteration - maximum number of iterations allowed for the reconstruction

fn_regularization - text file containing:

- 1) An indicator for the type of reconstruction, either **JJt** or **JtJ**
- 2) Regularization parameter(s) which further inform the program as to the regularization scheme:
 - a. *single parameter* - regularize the entire Hessian with a single value (currently, the most common method. can be used for both **JJt** and **JtJ** cases)
 - b. *two parameters* - used in the **JJt** case, regularizes amplitude and phase separately
 - c. *multiple parameters for the JJt case* - regularize amplitude and phase for each wavelength separately
 - d. *multiple parameters for the JtJ case* - regularize chromophore/scattering parameters separately

filter_n - amount of filtering of the solution at each iteration

wv_array - an array of wavelengths listed in the excoef.txt file which the user would like to use. Currently, there are 7 wavelengths listed.

SAVED SOLUTION FILES depend on which chromophores/parameters you have chosen to reconstruct. In general, they will follow the format;

sol_label_parameter.sol

sol_label_HbO.sol

sol_label_Hbt.sol

sol_label_deoxyHb.sol

sol_label_StO2.sol

sol_label_LuTex.sol

sol_label_water.sol

sol_label_S-Amplitude.sol

sol_label_S-Power.sol

sol_label.log

Exercise: Reconstruct noisy data generated above using 6 wavelengths and a simple JtJ regularization scheme.

```
>> reconstruct_spectral('circle2000_86', [20 20], 100, 'datanoise_tutorial_spec.paa',
'recon_tutorial_spec', 30, 'regularize_nodependence_jtj.txt', 1, [661 761 785 808 826 849]);
Loading forward mesh
Loading the following parameters from "circle2000_86.chromscatt":

ans =

    'HbO'
    'deoxyHb'
    'Water'
    'S-Amplitude'
    'S-Power'

Loading recon basis
Loading data and wavelength information
-----
Building Jacobian using jacobian_spectral
661nm Jacobian
761nm Jacobian
785nm Jacobian
808nm Jacobian
826nm Jacobian
849nm Jacobian
Iteration Number      = 1
Projection error      = 255.9413
Building JtJ Hessian
Regularization        = 150.782
Calculating update: "inv(JtJ+lambd*I)Jt" Inversion
Filtering
:
:
:
```

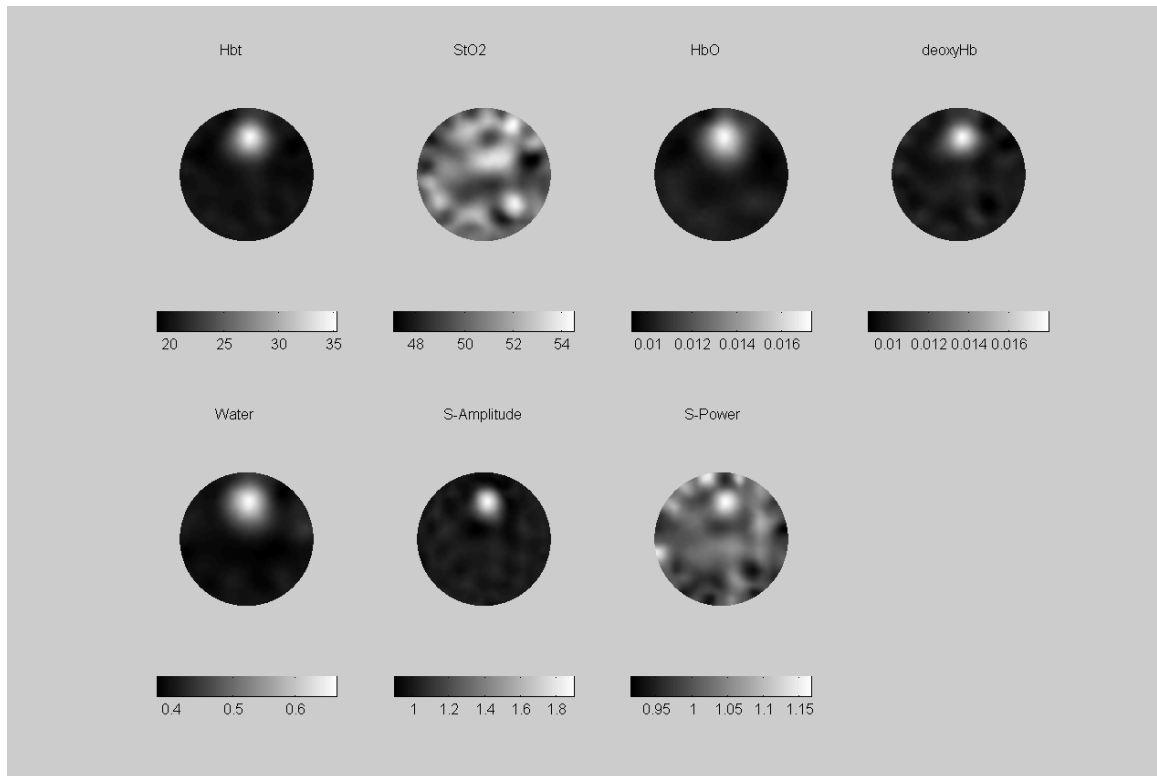
2. Viewing Reconstructed Spectral Images

Use `[mesh]=read_solution_spec(mesh,sol_label,fn_excoef,it,p)`

mesh - a mesh loaded in the MatLab workspace or the filename of a mesh. It must have the same geometry and node configuration as `fwd_fn` from the reconstruction program.
sol_label - is the solution file prefix as specified in the reconstruct program
fn_excoef - the extinction coefficient file, `excoef.txt`.
it - the iteration number of interest. Set it = 'last' to read last iteration.
p - to plot HbO and dHb directly, enter `p = 1`, otherwise, leave blank.

Exercise: Read last iteration of solution files.

```
>> [mesh]=read_solution_spec(mesh,'recon_tutorial_spec','excoef.txt','last',1)
Loading recon_circ2000_86_tutorial_Hbt.sol
Loading recon_circ2000_86_tutorial_StO2.sol
Loading recon_circ2000_86_tutorial_HbO.sol
Loading recon_circ2000_86_tutorial_deoxyHb.sol
Loading recon_circ2000_86_tutorial_Water.sol
recon_circ2000_86_tutorial_LuTex.sol does not exist
recon_circ2000_86_tutorial_GdTex.sol does not exist
Loading recon_circ2000_86_tutorial_S-Amplitude.sol
Loading recon_circ2000_86_tutorial_S-Power.sol
```



Section VII. Reconstructing Fluorescence Data

Introduction

There are several methods used to reconstruct fluorescence yield depending on the data available. The corresponding programs are:

1. **reconstruct_fl** – reconstruct using non-spectral data. This program can be used to reconstruct for intrinsic optical properties at the excitation and emission wavelengths as well as fluorescence yield. Data used:
 - “*.paaf1” – fluorescence emission only, intrinsic excitation and emission properties assumed known.
 - “*.paaxfl” – fluorescence and excitation data only. Assumes intrinsic emission properties known
 - “*.paaxflmm” – intrinsic excitation and emission data as well as fluorescence data are used in the reconstruction.
2. **reconstruct_fl_spatial** – Adds structural information to the reconstruction in the form of L-matrix filtering in the regularization parameter. Just like reconstruct_fl, this program can be used to reconstruct for intrinsic optical properties at the excitation and emission wavelengths as well as fluorescence yield.
3. **reconstruct_fl_regionfit** - - Adds structural information to the reconstruction in the form of hard-prior region fitting. Just like reconstruct_fl, this program can be used to reconstruct for intrinsic optical properties at the excitation and emission wavelengths as well as fluorescence yield.
4. **reconstruct_fl_spectral** – reconstruct intrinsic properties using the spectral reconstruction program. Use the spectrally reconstructed fluorophore values as the initial guess for fluorescence yield reconstructions.
5. **reconstruct_fl_specinput** – same as reconstruct_spec_fl except that the intrinsic properties have already been reconstructed and are stored as solution files (as chromophore concentrations). This is simply a time saving technique so that the spectral reconstruction does not have to be completed for each fluorescence reconstruction attempt.
6. **reconstruct_fl_specinput_Lmatrix** – same as reconstruct_fl_specinput except that the fluorescence yield reconstruction uses the L-matrix spatial prior implementation.
7. **reconstruct_fl_specinput_regionfit** – same as reconstruct_fl_specinput except that the fluorescence yield reconstruction uses the hard-prior region fitting implementation.
8. **reconstruct_fl_specinput_emissionspec_dev3**

Usage details:

1. reconstruct_fl

[data_recon, coarse2fine_true, fine2coarse_true] = reconstruct_fl(fwd_fn, recon_basis, frequency, data_fn, iterations, lambdas, sol_label, filters, true_fn)

fwd_fn - the filename of the mesh used for forward solving

recon_basis - the reconstruction mesh basis or pixel basis

frequency - modulation frequency

data_fn - filename of the data to be reconstructed. *The file format determines the type of reconstruction to be completed:*

‘*.paaf1’ – reconstructs etamuaf only. Input **true_fn** to load true values for muax, musx, muam, musm.

‘*.paaxf1’ – reconstructs muax, musx, and etamuaf. Input **true_fn** to load true values for muam, musm.

‘*.paaxflmm’ – reconstructs all properties muax, musx, muam, musm and etamuaf. **true_fn** not a required input for this reconstruction.

iterations - three element array of maximum iteration number for excitation, emission (intrinsic), and fluorescence, respectively (ex: [50 50 50]).

lambdas - three element array with regularization values for excitation, emission (intrinsic), and fluorescence, respectively (ex: [10 10 1]).

sol_label - prefix for the name of the solution and log files.

filters - three element array with filtering level values for excitation, emission (intrinsic), and fluorescence, respectively (ex: [1 1 0]).

true_fn - filename of the mesh that contains the actual (true) values this is used to calculate the intrinsic excitation and emission properties. Only required if the data file is of the form ‘*.paaf1’ or ‘*.paaxf1’.

2. reconstruct_fl_spatial.m

[data_recon, coarse2fine_true, fine2coarse_true] = reconstruct_fl_spatial(fwd_fn, recon_basis, frequency, data_fn, iterations, lambda, sol_label, filters, true_fn)

fwd_fn - the filename of the mesh used for forward solving

recon_basis - Defines the reconstruction mesh basis. In this formulation, a separate pixel basis is generated for each tissue region. Input is an array of size [# regions, 2], with each row represents a grid of points for a given region (top row corresponds to region 0 and so on)

frequency - modulation frequency

data_fn - filename of the data to be reconstructed. *The file format determines the type of reconstruction to be completed:*

‘*.paaf1’ – reconstructs etamuaf only. Input **true_fn** to load true values for muax, musx, muam, musm.

‘*.paaxf1’ – reconstructs muax, musx, and etamuaf. Input **true_fn** to load true values for muam, musm.

‘*.paaxflmm’ – reconstructs all properties muax, musx, muam, musm and etamuaf. **true_fn** not a required input for this reconstruction.

iterations - three element array of maximum iteration number for excitation, emission (intrinsic), and fluorescence, respectively (ex: [50 50 50]).

lambdas - three element array with regularization values for excitation, emission (intrinsic), and fluorescence, respectively (ex: [10 10 1]).

sol_label - prefix for the name of the solution and log files.
filters - three element array with filtering level values for excitation, emission (intrinsic), and fluorescence, respectively (ex: [1 1 0]).
true_fn - filename of the mesh that contains the actual (true) values this is used to calculate the intrinsic excitation and emission properties. Only required if the data file is of the form '*.paaf1' or '*.paaxf1'.

3. reconstruct_fl_regionfit.m

[data_recon, coarse2fine_true, fine2coarse_true] = reconstruct_fl_regionfit(fwd_fn, frequency, data_fn, iterations, lambdas, sol_label, filters, true_fn, region)

fwd_fn - the filename of the mesh used for forward solving
frequency - modulation frequency
data_fn - filename of the data to be reconstructed. *The file format determines the type of reconstruction to be completed:*
 '*.paaf1' – reconstructs etamuaf only. Input **true_fn** to load true values for muax, musx, muam, musm.
 '*.paaxf1' – reconstructs muax, musx, and etamuaf. Input **true_fn** to load true values for muam, musm.
 '*.paaxflmm' – reconstructs all properties muax, musx, muam, musm and etamuaf. **true_fn** not a required input for this reconstruction.
iterations - three element array of maximum iteration number for excitation, emission (intrinsic), and fluorescence, respectively (ex: [50 50 50]).
lambdas - three element array with regularization values for excitation, emission (intrinsic), and fluorescence, respectively (ex: [10 10 1]).
sol_label - prefix for the name of the solution and log files.
filters - three element array with filtering level values for excitation, emission (intrinsic), and fluorescence, respectively (ex: [1 1 0]).
true_fn - filename of the mesh that contains the actual (true) values this is used to calculate the intrinsic excitation and emission properties. Only required if the data file is of the form '*.paaf1' or '*.paaxf1'.
region - array of all regions in the fwd_fn mesh. Ex: [0 1 2] for a 3 region mesh.

4. reconstruct_fl_spectral.m

[fwd_mesh, data_recon] = reconstruct_fl_spectral(fwd_fn, recon_basis, frequency, data_fn_spec, data_fn_fluor, iterations, regularize_spec, lambda_fl, sol_label, filters, wv_spec, wv_fluor)

fwd_fn - the filename of the mesh used for forward solving (must have .chromscatt file with initial guess values).
recon_basis - the reconstruction mesh basis or pixel basis
frequency - modulation frequency
data_fn_spec - filename of the spectral data to be reconstructed.
data_fn_fluor - filename of the fluorescence data to be reconstructed. Can be any of the fluorescence formats, paaf1, paaxf1, paaxflmm, however, only the fluorescence emission will be used.

iterations - two element array of maximum iteration number for spectral recon and fluorescence, respectively (ex: [50 50]).

regularize_spec - text file containing:

- 1) An indicator for the type of reconstruction, either **JJt** or **JtJ**
- 2) Regularization parameter(s) which further inform the program as to the regularization scheme:
 - a. *single parameter* - regularize the entire Hessian with a single value (currently, the most common method. can be used for both **JJt** and **JtJ** cases)
 - b. *two parameters* - used in the **JJt** case, regularizes amplitude and phase separately
 - c. *multiple parameters for the JJt case* - regularize amplitude and phase for each wavelength separately
 - d. *multiple parameters for the JtJ case* - regularize chromophore/scattering parameters separately

lambda_fl – initial fluorescence regularization

sol_label - prefix for the name of the solution and log files.

filters - two element array with filtering level values for spectral and fluorescence, respectively (ex: [1 0]).

wv_spec - an array of wavelengths listed in the excoef.txt file which the user would like to use. Currently, there are 7 wavelengths listed.

wv_fluor - the excitation and emission wavelength of the fluorescence measurements.

These must be listed in the excoef.txt file so that optical properties can be calculated from chromophore concentrations.

5. reconstruct_fl_specinput.m

[fwd_mesh, data_recon] = reconstruct_fl_specinput(fwd_fn, recon_basis, frequency, data_fn_fluor, iteration_fl, lambda_fl, fl_sol_label, filter_fl, wv_fluor, spec_sol_label)

Inputs are fairly self explanatory given the descriptions for reconstruct_fl_spectral.m. The major difference is:

spec_sol_label - sol_label of previously calculated spectral data (chromophore concentrations).

6. reconstruct_fl_specinput_Lmatrix.m

[fwd_mesh, data_recon]=reconstruct_fl_specinput_Lmatrix (fwd_fn,recon_basis,frequency,data_fn_fluor,iteration_fl,lambda_fl,fl_sol_label ,filter_fl,wv_fluor,spec_sol_label)

fwd_fn - the filename of the mesh used for forward solving

recon_basis - Defines the reconstruction mesh basis. In this formulation, a separate pixel basis is generated for each tissue region. Input is an array of size [# regions, 2], with each row represents a grid of points for a given region (top row corresponds to region 0 and so on)

frequency - modulation frequency

data_fn_fluor - filename of the fluorescence data to be reconstructed. Can be any of the fluorescence formats, paaf, paaxfl, paaxflmm, however, only the fluorescence emission will be used.

iteration_fl - maximum iteration number for fluorescence reconstructions).
lambda_fl - regularization value (β for this L-matrix formulation) for fluorescence reconstruction.
fl_sol_label - prefix for the name of the fluorescence solution and log files.
filter_fl - filtering level value for fluorescence reconstruction.
wv_fluor - the excitation and emission wavelength of the fluorescence measurements. These must be listed in the excoef.txt file so that optical properties can be calculated from chromophore concentrations.
spec_sol_label - sol_label of previously calculated spectral data (chromophore concentrations).

7. reconstruct_fl_specinput_regionfit.m

[fwd_mesh, data_recon] = reconstruct_fl_specinput_regionfit(fwd_fn, frequency, data_fn_fluor, iteration_fl, lambda_fl, fl_sol_label, filter_fl, wv_fluor, spec_sol_label, region)

fwd_fn - the filename of the mesh used for forward solving
frequency - modulation frequency
data_fn_fluor - filename of the fluorescence data to be reconstructed. Can be any of the fluorescence formats, paafl, paaxfl, paaxflmm, however, only the fluorescence emission will be used.
iteration_fl - maximum iteration number for fluorescence reconstructions).
lambda_fl - regularization value (β for this L-matrix formulation) for fluorescence reconstruction.
fl_sol_label - prefix for the name of the fluorescence solution and log files.
filter_fl - filtering level value for fluorescence reconstruction.
wv_fluor - the excitation and emission wavelength of the fluorescence measurements. These must be listed in the excoef.txt file so that optical properties can be calculated from chromophore concentrations.
spec_sol_label - sol_label of previously calculated spectral data (chromophore concentrations).
region - array of all regions in the fwd_fn mesh. Ex: [0 1 2] for a 3 region mesh.

8. reconstruct_fl_specinput_emissionspec_dev3

.....UNDER DEVELOPMENT.....

Section VIII. Viewing fluorescence images

Viewing Fluorescence images

mesh=read_solution(mesh,sol_label,it,true_fn)

mesh – mesh of the same geometry and node number as fwd_mesh in the reconstruction program.

sol_label – solution file prefixes

it – three element array: [itx, itmm, itfl]. Enter itx, itm = 0 if those properties are “known”. Enter ‘last’ to plot the last iteration.

true_fn – if the true values are saved in a mesh, enter the mesh as true_fn to plot cross-sections.

APPENDIX C: CALIBRATION ROUTINES FOR SPECTROSCOPIC TOMOGRAPHY DATA

This appendix is a catalogue of critical Matlab M-files used to manipulate and calibrate data acquired with the multi-spectral tomography system. With the exception of `homogfit_fl_data.m`, all calibration files provided here are stored in:

C:\EXPERIMENTAL_SYSTEMS_AND_DATA\SPEC_TOMO_SYS\Matlab_routines
on the spectrometer computer, or are available upon request.

All calibration files are stored in
C:\EXPERIMENTAL_SYSTEMS_AND_DATA\SPEC_TOMO_SYS\Calibration

And Basis spectra:
C:\EXPERIMENTAL_SYSTEMS_AND_DATA\SPEC_TOMO_SYS\Basis_spectra

`Homogfit_fl_data.m` and Meshing tools for 2-D small animal imaging are in
NIRFAST_v2, posted online.

Additional data manipulation and analysis files were excluded from this appendix, but are available upon request.

1.1 Batch files: data calibration

In this section, examples of batch files used to calibrate data from a series of phantoms are provided. Similar files exist for calibrating data from animal studies. Assuming an appropriate mesh has been generated, the files are used in the following sequence:

1. [batch_phantom_raw2calspec_trans_and_fl](#)
Calibration accounts for relative detector offsets, dark current, baselines, exposure times, and ND filtering, on trans and fluor files. This procedure takes full spectra *.raw data files and produces files containing full spectra with the 'calspec' extension.
2. [batch_phantom_integrate_calspec_trans_and_fl](#)
Integrates trans spectra over specified range, and spectrally fits fluor spectra and integrates results of fit. Generates "un-calibrated" (to the model) files of intensity. File extensions are *.intrans for the integrated transmission intensity, *.paafl for the integrated fluorescence intensity, and *.paableed for the integrated contamination intensity (though this is rarely used, if ever).
3. [batch_phantom_calibrate2nirfast_homogfit](#)
Calibrates fluorescence data to the model, performs a homogeneous fit of

fluorescence yield, and generates an initial guess mesh. Running this program requires that an appropriate mesh that matches the phantom geometry has been generated previously. Optical properties in the mesh should be as accurate as possible – usually determined from frequency domain measurements acquired on the FD system.

4. [batch_phantom_recon_nospatial](#)
Reconstructs phantom series.

function batch_phantom_raw2calspec_trans_and_fl

```
% batch file to calibrate transmission and fluorescence spectra
% for a group of phantoms - from *.raw data files to *.calspec data files.

% Calibration files: In many cases, can usually leave these alone...
fn_detcal_trans = 'Cal_det_grat1200_centerwv690nm_norm.txt'; % for grating used in trans meas.
fn_detcal_fl = 'Cal_det_grat300_centerwv820nm_norm.txt'; % for grating used in fl meas.
fn_filter_OD = 'Calib_filters_1200grat_690cent_060107_OD1.txt'; % OD of filters for grating used in trans
meas.

% Data repetition number
rep_num = [1];

% wavelength file and wavelength reange to set = 0 for transmission measurements. This
% provides an offset to the data without having to use saved baseline/dark noise
% calibration files
fn_wave_trans = 'pixel2wv_grating1200_centerwv690_mod_from_700.txt';
zero_range = [665,680];

% wavelength file and wavelength reange to set = 0 for fluorecence measurements. This
% provides an offset to the data without having to use saved baseline/dark noise
% calibration files. Can only be used if the spectrum includes part of the filtered range.
fn_wave_fl = 'pixel2wv_grating300_centerwv820.txt';
filter_wv = [700 710];

% ADJUST INPUTS *****
% Change these:
% specific to data files being calibrated
sf = {'450nM'; '1uM'; '2uM'};
geom = {'center'; 'edge'};
raw_path =
'C:\EXPERIMENTAL_SYSTEMS_AND_DATA\SPEC_TOMO_SYS\Data\2007\102407_ICG_heterog_st
udyII\';
% Data source array
source_array = [1:16];
% *****

% loop over phantoms
for i = 1:numel(sf);
    for j = 1:numel(geom);

        % ADJUST INPUTS *****
        % Change these:
        % specific to data files being calibrated
        tran_calspec = ['IL_ink_300nM_ICG_heterog_',char(sf(i,:)),'_',char(geom(j,:)),'_trans'];
        fl_calspec = ['IL_ink_300nM_ICG_heterog_',char(sf(i,:)),'_',char(geom(j,:)),'_fl'];
        raw_data_fn_tran = [raw_path,
'IL_ink_300nM_ICG_heterog_',char(sf(i,:)),'_',char(geom(j,:)),'_trans'];
        raw_data_fn_fl = [raw_path, 'IL_ink_300nM_ICG_heterog_',char(sf(i,:)),'_',char(geom(j,:)),'_fl'];
        % *****
```

```

% *****
% 1. Calibrate Excitation spectra (raw to calspec)

disp('Calibrating trans spectra');
calibrate_raw2calspectrans_data_fullset_III(tran_calspec, source_array, raw_data_fn_tran,
fn_detcal_trans, fn_filter_OD, fn_wave_trans, zero_range, rep_num)

% *****
% 2. Calibrate Fluorescence spectra (raw to calspec)

disp('Calibrating fl spectra');
calibrate_raw2calspecfl_data_fullset_II(fl_calspec, source_array, raw_data_fn_fl, fn_detcal_fl,
fn_wave_fl, filter_wv, rep_num);

end
end

```

```

function batch_phantom_integrate_calspec_trans_and_fl

% Integrate transmission data and spectral fit and integrate fluorescence data.
% Uses calibrated spectra i.e. *.calspec data.

% Calibration files: In many cases, can leave these alone...

% map pixel number to wavelength for transmission spectra
fn_wv_trans = 'pixel2wv_grating1200_centerwv690_mod_from_700.txt';
% map pixel number to wavelength for fluor spectra
fn_wv_fl = 'pixel2wv_grating300_centerwv820.txt';
% basis spectra root name
fn_basis = 'BASIS_ICG_manipulated';
% data repetition number (usually 1)
rep_num = [1];

% integrate fluorescence measurements over wavelength range:
min_wv_fl = 8;
max_wv_fl = 832;
% integrate 'bleed signal' measurements over wavelength range (data usually not used):
min_wv_bleed = 818;
max_wv_bleed = 832;
% scan emission peak from wavelength:
emiss_peak_wv = 790;
% filter cutoff wavelength:
filter_cutoff_wv = 720;
% maximum wavelength for scanning peak
expected_max_wv_peak = 850;
% restrict fitting data above:
fit_above_wv = 740;
% if different laser currents used for fluor and trans, enter difference
fl2trans_current_diff = 0;
current_slope = 3.27088; %(690 nm laser only)
% wavelength range to integrate transmission peak
min_wv_trans = 685;
max_wv_trans = 695;

% ADJUST INPUTS *****
% Change these:
% specific to data files being calibrated
sf = {'450nM'; '1uM'; '2uM'};
geom = {'center'; 'edge'};
% Data source array
source_array = [1:16];

% loop over
for i = 1:numel(sf);
    for j = 1:numel(geom);

        % ADJUST INPUTS *****
        % Change these:
        % specific to data files being calibrated
        % calspecs to load:

```

```

tran_calspec = ['IL_ink_300nM_ICG_heterog_',char(sf(i,:)),'_',char(geom(j,:)),'_trans'];
fl_calspec = ['IL_ink_300nM_ICG_heterog_',char(sf(i,:)),'_',char(geom(j,:)),'_fl'];
% inegrated intensity files to save:
intrans_fn = ['IL_ink_300nM_ICG_heterog_',char(sf(i,:)),'_',char(geom(j,:)),'_trans'];
fl_int_fn = ['IL_ink_300nM_ICG_heterog_',char(sf(i,:)),'_',char(geom(j,:)),'_818to832'];
% *****

% Process data *****
% Integrate Transmission data
disp('Integrating trans spectra');
I = integrate_calspectrans_data_wvbased(tran_calspec, min_wv_trans, max_wv_trans, 1,
fn_wv_trans);
% adjust for difference in laser intensity
I = I+fl2trans_current_diff*current_slope;
save([intrans_fn,'.intrans'],'I','-ASCII');
I(isnan(I)~=0)=[];
figure
semilogy(I,'-O'); title('Integrated laser source');

% Spectral fit and integrate fluorecence data
disp('Fitting fl spectra');
[data,Fit] = spectral_fit_NONLIN_calspecdata_wvbased(fl_calspec,fn_basis,1,...
min_wv_fl,max_wv_fl,min_wv_bleed,max_wv_bleed,fn_wv_fl,...
emiss_peak_wv,filter_cutoff_wv,expected_max_wv_peak,fit_above_wv)

foo = data.paaf1; foo2 = data.paableed;
foo(find(foo<0))=10^-20;
save([fl_int_fn,'.paaf1'],'foo','-ASCII');
save([fl_int_fn,'.paableed'],'foo2','-ASCII');
foo(isnan(foo)~=0)=[]; foo2(isnan(foo2)~=0)=[];
figure; semilogy(foo,'-rO'); title('Fluorescence intensity after spectral fitting')
figure; semilogy(foo2,'-gO'); title('Bleed-through intensity after spectral fitting')
foo = Fit.fitdata;
foo2 = Fit.basis;
save([fl_int_fn,'.fitdata'],'foo','-ASCII');
save([fl_int_fn,'.fitbasis'],'foo2','-ASCII');
end
end

```

```

function Result = batch_phantom_calibrate2nirfast_homogfit

% Loads calibrated data and mesh containing true values of optical
% properties at excitation and emission (fluor mesh). Data is calibrated
% to the model using a scaling factor (ratio of model excitation to
% measured excitation) and calibrated data is used to generate a
% homogeneous for fluorescence yeild which is saved in an initial guess
% mesh.

Result = [];
% ADJUST INPUTS *****
% Change these:
% specific to data files being calibrated
sf = {'450nM'; '1uM'; '2uM'};
geom = {'center'; 'edge'};
% Data source array
source_array = [1:16];
raw_path =
'C:\EXPERIMENTAL_SYSTEMS_AND_DATA\SPEC_TOMO_SYS\Data\2007\102407_ICG_heterog_st
udyII\';
% *****

% loop over
for i = 1:numel(sf);
    for j = 1:numel(geom);

        % ADJUST INPUTS *****
        % Change these:
        % specific to data files being calibrated
        % root file name of integrated fluorescence intensity from spectral fit (this file should exist)
        fl_int_fn = ['IL_ink_300nM_ICG_heterog_',char(sf(i,:)),'_',char(geom(j,:)),'_818to832'];

        % file name of fluor intensity calibrated to the model (this file does NOT exist - will be created)
        save_calib_paafn_fn = ['Calib_',fl_int_fn,'.paafn'];

        % raw data transmission file name (rootname of *.raw files, should exist)
        raw_data_fn_tran = [raw_path,
        'IL_ink_300nM_ICG_heterog_',char(sf(i,:)),'_',char(geom(j,:)),'_trans'];
        % file name of integrated transmission intensity (should exist)
        intrans_fn = ['IL_ink_300nM_ICG_heterog_',char(sf(i,:)),'_',char(geom(j,:)),'_trans'];
        % file name of existing mesh with correct optical properties (should exist)
        mesh_trans_true = ['true_trans_300nM_ICG_heterog_',char(sf(i,:)),'_',char(geom(j,:))];

        % file name to save scaling factor values (this file does NOT exist - will be created)
        save_scaling_fn = ['ScalingFactor_',fl_int_fn,'.txt'];
        % file name to save Initial guess mesh (this file does NOT exist - will be created)
        save_initguessmesh = ['IG_',fl_int_fn];
        % *****

        % Process data: Calibrate to nirfast format
        [data,mesh,err] = calibrate2nirfast_fl_2([intrans_fn,'intrans'],[fl_int_fn,'.paafn'],...
        mesh_trans_true,...
        raw_data_fn_tran,1,...
        save_calib_paafn_fn,...

```

```
    save_initguessmesh,...  
    save_scaling_fn)  
    Result = [Result; mesh.eta(1)*mesh.muaf(1),err]  
end  
end
```

```
function batch_phantom_recon_nospatial
```

```
% ADJUST INPUTS *****  
% Change these:  
% specific to data files being calibrated  
sf = {'450nM'; '1uM'; '2uM'};  
geom = {'center'; 'edge'};  
reg = [1, 10, 50, 100];  
% *****  
  
% loop over  
for i = 1:numel(sf);  
    for j = 1:numel(geom);  
  
        % ADJUST INPUTS *****  
        % Change these:  
        % specific to data files being calibrated  
        fl_int_fn = ['IL_ink_300nM_ICG_heterog_', char(sf(i,:)), '_', char(geom(j,:)), '_818to832'];  
        data_fn = ['Calib_', fl_int_fn, '.paaf1'];  
        mesh_fn = ['IG_', fl_int_fn];  
  
        for k = 1:numel(reg)  
            sol_label = ['recon_', fl_int_fn, '_nospatial_reg', num2str(reg(k)), '_attempt1'];  
            [data_recon, junk, junk] = reconstruct_fl(mesh_fn, [25 25], [0 0 0], data_fn, [0 0 60], [0 0  
reg(k)], sol_label, [0 0 0], mesh_fn);  
            end  
        end  
    end  
end
```

1.1 Load log file

```
function [loginfo] = load_log_file(data_fn)

% Assumes log file is formatted with text at the top and a matrix of
% spectrometer/camera parameters. The last 16 columns of this matrix are
% the exposure times used where each column corresponds to a source
% position and each row a detector. An exposure time = zero indicates that
% source-detector pair was not used.

% s. c. davis 2007

logtemp = importdata([data_fn, '.log']);
loginfo.exp_times = logtemp.data(:,end-15:end);
loginfo.filters = logtemp.data(:,end-31:end-16);
loginfo.sources = logtemp.data(:,1);
loginfo.meas = logtemp.data(:,2);

% create a nirfast-style link matrix based on sources and detectors
% selected in the acquisition program
ns = 1:numel(find(loginfo.sources == 1));
nd = 1:numel(find(loginfo.meas == 1));

% build link file based on sd_pairs
sd_ind = 1:length(ns);
for i = 1:length(ns)
    loginfo.link(i,:) = nd([(i+1):end, 1:(i-1)]);
end
```

1.2 Calibrating spectra: raw2calspec programs

This section provides code for all raw2calspec files to calibrate *.raw data files (spectra). Resulting files have the same name with a *.calspec extension.

```
function calibrate_raw2calspecfl_data_fullset(fn_saved_calspec_data, source_array, data_fn, fn_sourcecal,
fn_baseline, fn_detcal, rep_num)

% NOTE: See calibrate_raw2calspecfl_data_fullset_II for another calibration
% approach

% Load a full set of raw data and calibrate the data in the following way:
% 1. baselines for each spectrometer in fn_baselines
% 2. to the source scaling factors in fn_sourcecal
% 3. to the detector relative offset factors in fn_detcal
% 4. to the exposure times in exp_times

% Save the data as ['fn_saved_calspec_data',.calspec]

% s. c. davis 2007

for i = 1:numel(source_array)
    if exist([data_fn,sprintf('_s%g_rep%g.raw',source_array(i),rep_num)])~=0
        calspec = calibrate_raw2calspecfl_data_onesource(source_array(i), data_fn, fn_sourcecal, fn_baseline,
fn_detcal, rep_num);
        save([fn_saved_calspec_data,sprintf('_s%g_rep%g.calspec',source_array(i),rep_num)],'calspec','-
ASCII');
    end
end
```

```

function [calspec] = calibrate_raw2calspecfl_data_onesource(source_num, data_fn,...
    fn_sourcecal, fn_baseline, fn_detcal, rep_num)

% NOTE: See calibrate_raw2calspecfl_data_onesource_II for another calibration
% approach

% Pre-fluorescence spectral fitting calibration. Calculates calspec data
% which can be used in the spectral fitting routines.

% Calibrate data for a single source position. Data is 'calibrated' as follows:
% 1. baselines for each spectrometer in fn_baselines
% 2. to the source scaling factors in fn_sourcecal
% 3. to the detector relative offset factors in fn_detcal
% 4. to the exposure times in exp_times

% s. c. davis 2007

loginfo = load_log_file(data_fn);
if source_num == 0
    exp_times = loginfo.exp_times(:,1);
else
    exp_times = loginfo.exp_times(:,source_num);
end
data = load([data_fn,sprintf('_s%g_rep%g.raw',source_num, rep_num)]);
source_cal = load(fn_sourcecal);
fn_base = fn_baseline(1:end-13); % use the '*_zercount.txt' file name for fn_baseline.
zerocount = load(fn_base);
slopes = load([fn_base,'darknoiseslopes.txt']);
det_cal = load(fn_detcal);

% subtract zerocount baselines
data = data-zerocount;
clear zerocount

for i = 1:length(exp_times); % detector loop
    if exp_times(i) ~= 0

        % remove dark noise
        data(:,i) = data(:,i) - slopes(:,i)*exp_times(i);

        % calibrate detectors, pixel-by-pixel
        data(:,i) = data(:,i)./det_cal(:,i);

        % calc. counts/s
        data(:,i) = data(:,i)./exp_times(i);
    end
end

% calibrate to source files
if source_num ~= 0
    data(:,source_num) = 0;
    calspec = data/source_cal(source_num);
end
end

```

```

function calibrate_raw2calspecfl_data_fullset_II(fn_saved_calspec_data, source_array, data_fn, fn_detcal,
fn_wave, filter_wv, rep_num)

% Load a full set of raw data and calibrate the data in the following way:
% 1. Sets filtered region (defined be 2 element array, filter_wv) = 0, shifts whole spectrum down
accordingly
% 2. to the detector relative offset factors nomalized about their own mean, fn_detcal
% 3. to the exposure times in exp_times
% Save the data as ['fn_saved_calspec_data',calspec]

% s. c. davis 2007

for i = 1:numel(source_array)
    if exist([data_fn,sprintf('_s%g_rep%g.raw',source_array(i),rep_num)])~=0
        calspec = calibrate_raw2calspecfl_data_onesource_II(source_array(i), data_fn, fn_detcal, fn_wave,
filter_wv, rep_num);
        save([fn_saved_calspec_data,sprintf('_s%g_rep%g.calspec',source_array(i),rep_num)],'calspec','-
ASCII');
    end
end
end

```

```

function [calspec] = calibrate_raw2calspecfl_data_onesource_II(source_num, data_fn,...
    fn_detcal, fn_wave, filter_wv, rep_num)

% Pre-fluorescence spectral fitting calibration. Calculates calspec data
% which can be used in the spectral fitting routines.

% Calibrate data for a single source position. Data is 'calibrated' as follows:
% 1. Sets filtered region (defined be 2 element array, filter_wv) = 0, shifts whole spectrum down
    accordingly
% 2. to the detector relative offset factors nomalized about their own mean, fn_detcal
% 3. to the exposure times in exp_times

% s. c. davis 2007
wave_lengths = load(fn_wave);
filter_min_pix = find(abs(wave_lengths - filter_wv(1)) == min(abs(wave_lengths - filter_wv(1))));
filter_max_pix = find(abs(wave_lengths - filter_wv(2)) == min(abs(wave_lengths - filter_wv(2))));

loginfo = load_log_file(data_fn);
if source_num == 0
    exp_times = loginfo.exp_times(:,1);
else
    exp_times = loginfo.exp_times(:,source_num);
end
data = load([data_fn,sprintf('_s%g_rep%g.raw',source_num, rep_num)]);
det_cal = load(fn_detcal);

for i = 1:length(exp_times); % detector loop
    if exp_times(i) ~= 0

        % calibrate detectors, pixel-by-pixel
        data(:,i) = data(:,i)./det_cal(:,i);

        % calc. counts/s
        data(:,i) = data(:,i)./exp_times(i);

        % set filtered region to zero - offset spectrum
        % determine wavelength intervals

        filter_data = data(filter_min_pix:filter_max_pix,i);
        %filter_data = medfilt2(filter_data,[5,1]);
        %filter_data = medfilt2(filter_data,[3,1]);
        %max_fil = max(filter_data); min_fil = min(filter_data); median_fil = median(filter_data);
        %interv = mean([max_fil-median_fil, min_fil-median_fil]);
        %offset = mean([min_fil, median_fil-interv]);
        data(:,i) = data(:,i)-median(filter_data);
    end
end

calspec = data;
calspec(find(calspec<0))=0;

```

```

function calibrate_raw2calspectrans_data_fullset(fn_saved_calspec_data, source_array, data_fn,
fn_sourcecal, fn_baseline, fn_detcal, fn_filter_OD, rep_num)

% NOTE: See calibrate_raw2calspectrans_data_fullset_III for another calibration
% approach

% Load a full set of raw data and calibrate the data in the following way:
% 1. baselines for each spectrometer in fn_baselines
% 2. to the source scaling factors in fn_sourcecal
% 3. to the detector relative offset factors in fn_detcal
% 4. to the exposure times in exp_times

% Save the data as ['fn_saved_calspec_data',calspec]

% s. c. davis 2007

for i = 1:numel(source_array)
    if exist([data_fn,sprintf('_s%g_rep%g.raw',source_array(i),rep_num)])~=0
        calspec = calibrate_raw2calspectrans_data_onesource(source_array(i), data_fn, fn_sourcecal,
fn_baseline, fn_detcal, fn_filter_OD, rep_num);
        save([fn_saved_calspec_data,sprintf('_s%g_rep%g.calspec',source_array(i),rep_num)],'calspec','-
ASCII');
    end
end
end

```

```
function [calspec] = calibrate_raw2calspectrans_data_onesource(source_num, data_fn, fn_sourcecal,
fn_baseline, fn_detcal, fn_filter_OD, rep_num)
```

```
% NOTE: See calibrate\_raw2calspectrans\_data\_onesource\_III for another calibration
% approach
```

```
% Calculates calspec data for transmission tomography.
```

```
% Calibrate data for a single source position. Data is 'calibrated' as follows:
```

```
% 1. baselines for each spectrometer in fn_baselines
% 2. to the source scaling factors in fn_sourcecal
% 3. to the detector relative offset factors in fn_detcal
% 4. to the calculated filter OD, per pixel
% 5. to the exposure times in exp_times
```

```
% s. c. davis 2007
```

```
loginfo = load_log_file(data_fn);
if source_num == 0
    exp_times = loginfo.exp_times(:,1);
    FW_array = loginfo.filters(:,1);
else
    exp_times = loginfo.exp_times(:,source_num);
    FW_array = loginfo.filters(:,source_num);
end
data = load([data_fn,sprintf('_s%g_rep%g.raw',source_num,rep_num)]);
source_cal = load(fn_sourcecal);
fn_base = fn_baseline(1:end-13); % use the '*_zerocount.txt' file name for fn_baseline.
zerocount = load(fn_base);
slopes = load([fn_base,'darknoiseslopes.txt']);
det_cal = load(fn_detcal);
```

```
if strcmp('1',fn_filter_OD(end-4))~=0 | strcmp('2',fn_filter_OD(end-4))~=0
    if strcmp('2',fn_filter_OD(end-4))~=0
        fn = fn_filter_OD(1:end-8);
    elseif strcmp('1',fn_filter_OD(end-4))~=0
        fn = fn_filter_OD(1:end-8);
    end
    filter_OD1_cal = load([fn,'_OD1.txt']);
    filter_OD2_cal = load([fn,'_OD2.txt']);
elseif strcmp('P',fn_filter_OD(end-4))~=0
    fn = fn_filter_OD(1:end-10);
    filter_LP_cal = load([fn,'_650LP.txt']);
end
```

```
% subtract zerocount baselines
data = data-zerocount;
clear zerocount
```

```
% subtract dark noise, calibrate detectors, and adjust for exposure times.
for i = 1:length(exp_times); % detector loop
    if exp_times(i) ~= 0
        data(:,i) = data(:,i) - slopes(:,i)*exp_times(i);
        data_temp = data(:,i); data_temp(find(data_temp < 0)) = 0; data(:,i) = data_temp;
        % calibrate detectors, pixel-by-pixel
```

```

data(:,i) = data(:,i)./det_cal(:,i);
data(:,i) = data(:,i)./exp_times(i);
if FW_array(i) == 6 % 1 OD filtering
    data(:,i) = data(:,i).*10.^filter_OD1_cal(:,i);
elseif FW_array(i) == 5 % 2 OD filtering
    data(:,i) = data(:,i).*10.^filter_OD2_cal(:,i);
elseif FW_array(i) == 2 % 650 LP filtering
    data(:,i) = data(:,i).*10.^filter_LP_cal(:,i);
end
end
end

% Calibrate to source detection file, if not
% a centrally located source (ie in a calibration phantom)
if source_num ~= 0
    data(:,source_num) = 0;
    data = data/source_cal(source_num);
end
calspec = data;

```

```

function calibrate_raw2calspectrans_data_fullset_III(fn_saved_calspec_data, source_array, data_fn,
fn_detcal, fn_filter_OD, fn_wave, zero_range, rep_num)

% Load a full set of raw data and calibrate the data in the following way:
% 1. Sets a user defined region = 0, shifts whole spectrum down accordingly
% - this should take care of baseline/dark noise correction
% 2. to the detector relative offset factors nomalized about their own mean, fn_detcal
% 3. to the exposure times in exp_times
% 4. to filter OD for ND filtered data

% Save the data as ['fn_saved_calspec_data',.calspec]

% s. c. davis 2007

for i = 1:numel(source_array)
    if exist([data_fn,sprintf('_s%g_rep%g.raw',source_array(i),rep_num)])~=0
        calspec = calibrate_raw2calspectrans_data_onesource_III(source_array(i), data_fn, fn_detcal,
fn_filter_OD, fn_wave, zero_range, rep_num);
        save([fn_saved_calspec_data,sprintf('_s%g_rep%g.calspec',source_array(i),rep_num)],'calspec','-
ASCII');
    end
end
end

```

```

function [calspec] = calibrate_raw2calspectrans_data_onesource_III(source_num, data_fn, fn_detcal,
fn_filter_OD, fn_wave, zero_range, rep_num)

% Calculates calspec data for transmission tomography.

% Calibrate data for a single source position. Data is 'calibrated' as follows:
% 1. Sets a user defined region = 0, shifts whole spectrum down accordingly
% - this should take care of baseline/dark noise correction
% 2. to the detector relative offset factors nomalized about their own mean, fn_detcal
% 3. to the exposure times in exp_times
% 4. to filter OD for ND filtered data

% s. c. davis 2007
wave_lengths = load(fn_wave);
zero_range_min_pix = find(abs(wave_lengths - zero_range(1)) == min(abs(wave_lengths -
zero_range(1))));
zero_range_max_pix = find(abs(wave_lengths - zero_range(2)) == min(abs(wave_lengths -
zero_range(2))));

loginfo = load_log_file(data_fn);
if source_num == 0
    exp_times = loginfo.exp_times(:,1);
    FW_array = loginfo.filters(:,1);
else
    exp_times = loginfo.exp_times(:,source_num);
    FW_array = loginfo.filters(:,source_num);
end
data = load([data_fn,sprintf('_s%g_rep%g.raw',source_num,rep_num)]);
det_cal = load(fn_detcal);

if strcmp('2',fn_filter_OD(end-4))~=0
    fn = fn_filter_OD(1:end-8);
elseif strcmp('1',fn_filter_OD(end-4))~=0
    fn = fn_filter_OD(1:end-8);
end
filter_OD1_cal = load([fn,'_OD1.txt']);
filter_OD2_cal = load([fn,'_OD2.txt']);

% subtract dark noise, calibrate detectors, and adjust for exposure times.
for i = 1:length(exp_times); % detector loop
    if exp_times(i) ~= 0
        data_temp = data(:,i); data_temp(find(data_temp < 0)) = 0; data(:,i) = data_temp;
        % calibrate detectors, pixel-by-pixel
        data(:,i) = data(:,i)./det_cal(:,i);
        data(:,i) = data(:,i)./exp_times(i);
        if FW_array(i) == 6 % 1 OD filtering
            data(:,i) = data(:,i).*10.^filter_OD1_cal(:,i);
        elseif FW_array(i) == 5 % 2 OD filtering
            data(:,i) = data(:,i).*10.^filter_OD2_cal(:,i);
        end

        % Set wavelength range expected to have zero intensity to zero and
        % subtract offset from entire spectrum
        zero_range_data = data(zero_range_min_pix:zero_range_max_pix,i);
        data(:,i) = data(:,i)-median(zero_range_data);
    end
end

```

```
    end  
end  
  
calspec = data;
```

```

function [calspec] = calibrate_raw2calspecBLT_data(data_fn, fn_baseline, fn_detcal, rep_num)

% Calibrate data for BLT measurements ("central source" setting in
% Acquisition).

% Calibrate data for a single source position. Data is 'calibrated' as follows:
% 1. baselines for each spectrometer in fn_baselines
% 2. to the detector relative offset factors in fn_detcal
% 3. to the exposure times in exp_times

% s. c. davis 2007

loginfo = load_log_file(data_fn);
exp_times = loginfo.exp_times(:,1);
data = load([data_fn,sprintf('_s%g_rep%g.raw',0,rep_num)]);
fn_base = fn_baseline(1:end-13); % use the '*_zerocount.txt' file name for fn_baseline.
zerocount = load(fn_base);
slopes = load([fn_base,'darknoiseslopes.txt']);
det_cal = load(fn_detcal);

% subtract zerocount baselines
data = data-zerocount;
clear zerocount

% subtract dark noise, calibrate detectors, and adjust for exposure times.
for i = 1:length(exp_times); % detector loop
    if exp_times(i) ~= 0
        data(:,i) = data(:,i) - slopes(:,i)*exp_times(i);
        % calibrate detectors, pixel-by-pixel
        data(:,i) = data(:,i)./det_cal(:,i);
        calspec(:,i) = data(:,i)./exp_times(i);
    end
end
end

```

```
function data = load_calspecdata_multi_reps(data_fn,num_reps,source);

% Loads previously calibrated data of the '*.calspec' form. data_fn is the
% root name of the data file, such as 'teflon_phantom'. This program
% adds the source and rep # and file extension
% ('teflon_phantom_s1_rep2.calspec').

% s. c. davis 2007

for i = 1:num_reps
    % load data for one rep
    data_temp = load([data_fn,sprintf('_s%g_rep%g.calspec',source,i)]);
    [n,m] = size(data_temp);
    data(:,i) = data_temp;
end
```

1.3 Integrating Spectra

These files integrate calibrated spectra. The fluorescence spectral fitting routine is included in this section.

```
function I = integrate_calspectrans_data_wvbased(data_fn, min_wv, max_wv, rep_num, wave_fn)
```

```
% Load calibrated transmission data and integrate between min and max
% pixels

% data_fn is root name of data calspec file
% rep_num is the repetition number for the data set.
% source_array is an array of applicable sources (ie. [1:16])

% s davis 2007
% Modified by Stephen Tuttle 7/5/07
% mod. s davis 11/29/07 to use source-det arrays in log file to determine
% structure of integrated data.

% *****
% load acquisition information from log file
loginfo = load_log_file(data_fn);
source_array = find(loginfo.sources == 1);
det_array = find(loginfo.meas == 1);

% load wavelength list from txt file to convert from pixel number to nm.
wave_lengths = load(wave_fn);

% determine wavelength intervals
A = wave_lengths(1:(end-1),1);
B = wave_lengths(2:end,1);
wv_interv = B-A; clear A B

% determine integration limits in terms of pixel number from input
% wavelength limits
min_pix = find(abs(wave_lengths - min_wv) == min(abs(wave_lengths - min_wv)));
max_pix = find(abs(wave_lengths - max_wv) == min(abs(wave_lengths - max_wv)));

I = [];
for i = 1:numel(source_array)
    if exist([data_fn,sprintf('_s%g_rep%g.calspec',source_array(i),rep_num)])~=0
        calspec = load([data_fn,sprintf('_s%g_rep%g.calspec',source_array(i),rep_num)]);

        %calculate average intensity for pixel n and n+1
        foo = calspec(2:end,:);
        foo2 = calspec(1:(end-1),:);
        avg_intens = 0.5*(foo+foo2);

        exp_times = loginfo.exp_times(:,source_array(i));
        integrated_intensity = zeros(1,numel(det_array));
        for j = 1:numel(det_array); % detector loop
            if exp_times(det_array(j)) == 0
                integrated_intensity(j) = NaN;
            end
        end
    end
end
```

```

elseif exp_times(det_array(j)) ~= 0
    spec_element_area = wv_interv.*avg_intens(:,det_array(j));
    integrated_intensity(j) = sum(spec_element_area(min_pix:max_pix,1));
end
end
end
% arrange s-d pairs to match Nirfast
int = circshift(integrated_intensity,[0 1-i]);
int(1) = [];
I = [I; int'];
end
% semilogy(I,'-o');

```

```

function [data,Fit] = spectral_fit_NONLIN_calspecdata_wvbased(fn_data,fn_basis,...
    rep_num,min_wv_fl,max_wv_fl,min_wv_bleed,max_wv_bleed,fn_wave,...
    emiss_peak_wv,filter_cutoff_wv,expected_max_wv_peak,fit_above_wv)

% Spectrally fit previously calibrated data (in the form '*.calspec') to
% basis spectra 'basis_fn'. Integrates fit curve between min and max pixels.
% Also saves mesh.link file to match data format.

% fn_data      - calspec data filename
% fn_basis     - basis spectra root name (leave off _x.txt or _fl.txt - will
%               load both automatically)
% rep_num      - rep number of acquisition
% min and max_wv_fl - wavelengths between which the fluorescence
%               integration will be calculated
% min / max_wv_fl - wavelengths between which the bleed signal
%               integration will be calculated
% fn_wave      - filename of wavelength file associated with this acq.
% emiss_peak_wv - minimum wavelength at which to start searching for
%               solution (fl basis scanned in wv)
% filter_cutoff_wv - filter cutoff wavelength
% expected_max_wv_peak - maximum wavelength at which you expect to see the
%               fluorescence peak
% fit_above_wv - limits the fit to wavelengths above this cutoff. Set
%               = 0 to use full spectrum

% s Davis 2007
% Modified by s Tuttle 7/5/07 - wavelength 2 pixel conversion
% modified s davis 7/22/07 - nonlinear spec fitting
% modified s davis 11/29/07 - use source-det arrays in log file to determine
% structure of integrated data.

% *****
% load acquisition information from log file
loginfo = load_log_file(fn_data);
source_array = find(loginfo.sources == 1);
det_array = find(loginfo.meas == 1);

data.paaf1 = []; data.paableed = [];
exp_times_temp = [];

% load basis spectra
basis_x = load([fn_basis,'_x.txt']);
basis_fl = load([fn_basis,'_fl.txt']);

% determine wavelength intervals
wave_lengths = load(fn_wave);
Q = wave_lengths(1:(end-1),1);
R = wave_lengths(2:end,1);
wv_inter = R-Q; clear Q R

% determine integration limits in terms of pixel number from input
% wavelength limits
min_pix_fl = find(abs(wave_lengths - min_wv_fl) == min(abs(wave_lengths - min_wv_fl)));
max_pix_fl = find(abs(wave_lengths - max_wv_fl) == min(abs(wave_lengths - max_wv_fl)));
min_pix_bleed = find(abs(wave_lengths - min_wv_bleed) == min(abs(wave_lengths - min_wv_bleed)));

```

```

max_pix_bleed = find(abs(wave_lengths - max_wv_bleed) == min(abs(wave_lengths - max_wv_bleed)));
emiss_peak_pix = find(abs(wave_lengths - emiss_peak_wv) == min(abs(wave_lengths -
emiss_peak_wv)));
filter_cut_pix = find(abs(wave_lengths - filter_cutoff_wv) == min(abs(wave_lengths - filter_cutoff_wv)));
max_expected_peak_pix = find(abs(wave_lengths - expected_max_wv_peak) == min(abs(wave_lengths -
expected_max_wv_peak)));
if fit_above_wv ~= 0
    fit_above_pix = find(abs(wave_lengths - fit_above_wv) == min(abs(wave_lengths - fit_above_wv)));
elseif fit_above_wv == 0
    fit_above_pix = 1;
end

Fit.basis = [0; wave_lengths];
Fit.fitdata = [0; wave_lengths];
for i = 1:numel(source_array)
    if exist([fn_data,sprintf('_s%g_rep%g.calspec',source_array(i),rep_num)])~=0
        data_temp = load([fn_data,sprintf('_s%g_rep%g.calspec',source_array(i),rep_num)]);
        disp(['source ',num2str(source_array(i))]);

        exp_times = loginfo.exp_times(:,source_array(i));
        for j = 1:numel(det_array); % detector loop
            if exp_times(det_array(j)) == 0
                intfluor(j) = NaN;
                intbleed(j) = NaN;
            elseif exp_times(det_array(j)) ~= 0
                bleed_prior = basis_x(:,det_array(j));
                fluor_true = basis_fl(:,det_array(j));
                basis_peak = find(fluor_true == max(fluor_true));

                % Scanning technique spectral fitting loop
                for k = 1:(max_expected_peak_pix - emiss_peak_pix);
                    fluor_shift = emiss_peak_pix - basis_peak + k;
                    fluor_prior = circshift(fluor_true,fluor_shift);
                    if fluor_shift < 0
                        fluor_prior(end+1+fluor_shift:end) = 0;
                    elseif fluor_shift > 0
                        fluor_prior(1:fluor_shift) = 0;
                    end
                    fluor_prior(1:filter_cut_pix) = 0;

                    % build least squares linear equation soln. matrix:
                    A = [sum((bleed_prior(fit_above_pix:end)).^2),
sum(bleed_prior(fit_above_pix:end).*fluor_prior(fit_above_pix:end));...
                    sum(bleed_prior(fit_above_pix:end).*fluor_prior(fit_above_pix:end)),
sum((fluor_prior(fit_above_pix:end)).^2)];
                    b = [sum(data_temp(fit_above_pix:end,det_array(j)).*bleed_prior(fit_above_pix:end));...
                    sum(data_temp(fit_above_pix:end,det_array(j)).*fluor_prior(fit_above_pix:end))];

                    %solve for coeffiecients
                    y = A\b;
                    Y(k,:) = y';

                    % calculate least squared error for range of
                    % wavelengths used for fit

```

```

        Err(k) = sum((y(1)*(bleed_prior(fit_above_pix:end)) + y(2)*(fluor_prior(fit_above_pix:end)) -
(data_temp(fit_above_pix:end,det_array(j))))).^2);

%           % To plot curves for each fit attempt:
%           x = y;
%           fluor_curve = x(2)*fluor_prior;
%           bleed_curve = x(1)*bleed_prior;
%           final_fit = x(2)*fluor_prior+x(1)*bleed_prior;

%           figure(1) % plot each spectral fitting procedure
%           subplot(2,1,1)
%           plot(wave_lengths,final_fit,wave_lengths,data_temp(:,det_array(j)))
%           subplot(2,1,2)
%           plot(wave_lengths,bleed_curve,wave_lengths,fluor_curve)
%           pause(0.0005)
end
%           figure(2)
%           hold on
%           semilogy(1:k,Err); hold off;

index = find(Err == min(Err));
fluor_shift = emiss_peak_pix - basis_peak + index;
fluor_prior = circshift(fluor_true,fluor_shift);
x = Y(index,:);

% calculate final fit curve
fluor_curve = x(2)*fluor_prior;
bleed_curve = x(1)*bleed_prior;
final_fit = x(2)*fluor_prior+x(1)*bleed_prior;

% save final fits in data files for review at a later date
temp1 = [source_array(i);fluor_curve];
temp2 = [source_array(i);bleed_curve];
temp3 = [source_array(i);final_fit];
temp4 = [source_array(i);data_temp(:,det_array(j))];

Fit.basis = [Fit.basis,temp1,temp2];
Fit.fitdata = [Fit.fitdata,temp3,temp4];

clear temp1 temp2 temp3 temp4

% Integrate Spectrum:
% calculate average intensity for pixels n and n+1
foo=fluor_curve(2:end,:);
foo2=fluor_curve(1:(end-1),:);
avg_intens_fluor=.5*(foo+foo2);

foo3=bleed_curve(2:end,:);
foo4=bleed_curve(1:(end-1),:);
avg_intens_bleed=.5*(foo3+foo4);

% integrate intensity
spec_element_area_fluor= wv_inter.*avg_intens_fluor(:,1);
spec_element_area_bleed= wv_inter.*avg_intens_bleed(:,1);

```

```

        intfluor(j) = sum(spec_element_area_fluor(min_pix_fl:max_pix_fl,:),1);
        intbleed(j) = sum(spec_element_area_bleed(min_pix_bleed:max_pix_bleed,:),1);
    end
end

% arrange s-d pairs to match Nirfast
paaf1 = circshift(intfluor,[0 1-i]); paaf1 = paaf1(2:end);
paableed = circshift(intbleed,[0 1-i]); paableed = paableed(2:end);
data.paaf1 = [data.paaf1; paaf1'];
data.paableed = [data.paableed; paableed'];
end
end

% data.flbleedratio = data.paaf1./data.paableed;
% plotting
% figure; foo = data.paaf1; semilogy(foo,'-rO'); title('Fluorescence intensity after spectral fitting')
% figure; foo = data.paableed; semilogy(foo,'-gO'); title('Bleed-through intensity after spectral fitting')

```

```

function [data,link] =
spectral_fit_calspecdata_wvbased(fn_data,fn_basis,rep_num,min_wv_fl,max_wv_fl,min_wv_bleed,max_w
v_bleed,fn_wave)

% Spectral fitting with no peak scanning.

% Spectrally fit previously calibrated data (in the form '*.calspec') to
% basis spectra 'basis_fn'. Integrates fit curve between min and max pixels.
% Also saves mesh.link file to match data format.

% s Davis 2007
% Modified by s Tuttle 7/5/07 - wavelength 2 pixel conversion
% modified s davis 7/22/07 - nonlinear spec fitting
% modified s davis 11/29/07 - use source-det arrays in log file to determine
% structure of integrated data.

% *****
% load acquisition information from log file
loginfo = load_log_file(fn_data);
source_array = find(loginfo.sources == 1);
det_array = find(loginfo.meas == 1);

% load basis spectra
basis_x = load([fn_basis,'_x.txt']);
basis_fl = load([fn_basis,'_fl.txt']);

data.paaf1 = []; data.paableed = [];
exp_times_temp = [];

% determine wavelength intervals
wave_lengths = load(fn_wave);
Q= wave_lengths(1:(end-1),1);
R= wave_lengths(2:end,1);
wv_inter= R-Q; clear Q R

% determine integration limits in terms of pixel number from input
% wavelength limits
min_pix_fl = find(abs(wave_lengths - min_wv_fl) == min(abs(wave_lengths - min_wv_fl)));
max_pix_fl = find(abs(wave_lengths - max_wv_fl) == min(abs(wave_lengths - max_wv_fl)));
min_pix_bleed = find(abs(wave_lengths - min_wv_bleed) == min(abs(wave_lengths - min_wv_bleed)));
max_pix_bleed = find(abs(wave_lengths - max_wv_bleed) == min(abs(wave_lengths - max_wv_bleed)));

for i = 1:numel(source_array)
    if exist([fn_data,sprintf('_s%g_rep%g.calspec',source_array(i),rep_num)])~=0
        data_temp = load([fn_data,sprintf('_s%g_rep%g.calspec',source_array(i),rep_num)]);
        disp(['source ',num2str(source_array(i))]);

        exp_times = loginfo.exp_times(:,source_array(i));
        for j = 1:numel(det_array); % detector loop
            if exp_times(det_array(j)) == 0
                intfluor(j) = NaN;
                intbleed(j) = NaN;
            elseif exp_times(det_array(j)) ~= 0
                bleed_prior = basis_x(:,det_array(j));
                fluor_prior = basis_fl(:,det_array(j));
            end
        end
    end
end

```

```

% build least squares linear equation soln. matrix:
A = [sum((bleed_prior).^2), sum(bleed_prior.*fluor_prior); sum(bleed_prior.*fluor_prior),
sum((fluor_prior).^2)];
b = [sum(data_temp(:,det_array(j)).*bleed_prior); sum(data_temp(:,det_array(j)).*fluor_prior)];

%solve for coefficients
x = A\b;

fluor_curve = x(2)*fluor_prior;
bleed_curve = x(1)*bleed_prior;
final_fit = x(2)*fluor_prior+x(1)*bleed_prior;

%      figure; %
%      subplot(1,2,1)
%      plot(wave_lengths,final_fit,wave_lengths,data_temp(:,det_array(j)))
%      subplot(1,2,2)
%      plot(wave_lengths,bleed_curve,wave_lengths,fluor_curve)

% calculate average intensity for pixels n and n+1
foo=fluor_curve(2:end,:);
foo2=fluor_curve(1:(end-1),:);
avg_intens_fluor=.5*(foo+foo2);

foo3=bleed_curve(2:end,:);
foo4=bleed_curve(1:(end-1),:);
avg_intens_bleed=.5*(foo3+foo4);

% integrate intensity
spec_element_area_fluor= wv_inter.*avg_intens_fluor(:,1);
spec_element_area_bleed= wv_inter.*avg_intens_bleed(:,1);

intfluor(j) = sum(spec_element_area_fluor(min_pix_fl:max_pix_fl,:),1);
intbleed(j) = sum(spec_element_area_bleed(min_pix_bleed:max_pix_bleed,:),1);
end
end

% arrange s-d pairs to match Nirfast
paaf1 = circshift(intfluor,[0 1-i]); paaf1 = paaf1(2:end);
paableed = circshift(intbleed,[0 1-i]); paableed = paableed(2:end);
data.paaf1 = [data.paaf1; paaf1'];
data.paableed = [data.paableed; paableed'];
end
end

% data.flbleedratio = data.paaf1./data.paableed;
% plotting
% figure; foo = data.paaf1; semilogy(foo,'-rO'); title('Fluorescence intensity after spectral fitting')
% figure; foo = data.paableed; semilogy(foo,'-gO'); title('Bleed-through intensity after spectral fitting')

```

1.4 Calibrating to the model

These files calibrate fluorescence data to the NIRFAST model and generate initial estimates of fluorescence yield for image reconstruction.

```
function [paaf1,mesh,err] = calibrate2nirfast_fl(load_intrans_fn, load_paaf1_fn, mesh_trans_true,...
    data_fn_raw_trans, raw_trans_rep,...
    save_calib_paaf1_fn, save_initguessmesh, save_scaling_fn,...
    TOL)

% TOL is optional input - defines tolerance for bisection method homog
% fit. Default = 10^-4

% The program will automatically remove near-source detectors if not used
% in data acquisition as well as transmission saturated data points.

% s. c. davis 2007

% *****
if nargin ~= 9
    TOL = 10^-4;
end

% load "true" mesh created from "create2dmesh_from_mimics.m"
if ischar(mesh_trans_true) ~= 0
    mesh_true = load_mesh(mesh_trans_true);
else
    mesh_true = mesh_trans_true;
end

% load intrans and paaf1 data files. Ensure number of data points matches
% link file
data.intrans = load(load_intrans_fn);
data.paaf1 = load(load_paaf1_fn);
if numel(data.intrans) ~= numel(data.paaf1) | numel(data.intrans) ~= numel(mesh_true.link)
    disp('Error: data files do not match link file of mesh_true or data.paaf1 and data.intrans do not match.
Ending.')
    return
end

% Flag data points to ignore based on link file
[nsource,ndet] = size(mesh_true.link);
k = 1;
for i = 1 : nsource
    for j = 1 : length(mesh_true.link(i,:))
        if mesh_true.link(i,j) == 0
            data.intrans(k) = NaN;
            data.paaf1(k) = NaN;
        end
        k = k + 1;
    end
end
end

% load acquisition information from log file for raw trans data (first step
% in getting rid of data saturated in the transmission measurements)
```

```

loginfo = load_log_file(data_fn_raw_trans);
source_array = find(loginfo.sources == 1);
det_array = find(loginfo.meas == 1);

% remove saturated data (based on trans measurements) and
% bring mesh_true.link into compliance with acquired data
for i = 1:numel(source_array)
    if exist([data_fn_raw_trans,sprintf('_s%g_rep%g.raw',source_array(i),raw_trans_rep)]) ~= 0;
        dataraw_temp = load([data_fn_raw_trans,sprintf('_s%g_rep%g.raw',source_array(i),raw_trans_rep)]);
        dataraw = dataraw_temp(:,det_array); clear dataraw_temp

        exp_times = loginfo.exp_times(:,source_array(i));
        for j = 1:numel(det_array); % detector loop
            if exp_times(det_array(j)) == 0
                % catch exposure time = 0 for reasons other than users
                % de-selecting detectors in the acquisition program (for
                % example, ignoring near-source detectors does not change
                % det_array stored in log file..)
                dataraw(:,j) = NaN;
            elseif exp_times(det_array(j)) ~= 0
                % find saturated data points and flag them
                A = sort(dataraw(:,j));
                if A(end-4) > 65530
                    dataraw(:,j) = NaN;
                end
            end
        end
        end
        % sum columns
        tempsum = sum(dataraw,1);
        % shift tempsum into nirfast format
        tempsum = circshift(tempsum,[0 1-i]); tempsum(1) = [];

        % double check that link and tempsum match
        [junk,ntempsum] = size(tempsum);
        if ntempsum ~= ndet
            disp('Error: data files do not match link file of mesh_true. Ending.')
            return
        end

        % Scan through tempsum: wherever there is NaN, replace
        % corresponding s-d location in link file with 0
        mesh_true.link(i,find(isnan(tempsum)~=0))=0;
        clear dataraw tempsum junk ntempsum
    end
end

data_model = femdata_fl_for_real_data(mesh_true,0);

scaling_factor = data_model.paax(:,1)./data.intrans;
paaf1 = data.paaf1.*scaling_factor;
figure; semilogy(data.paaf1,'-rd'); title('Unscaled fluor data');
save(save_calib_paaf1_fn,'paaf1','-ASCII');

[mesh, err] = homogfit_fl_data(mesh_true,paaf1,0,100,TOL);
save_mesh(mesh,save_initguessmesh);

```

```

% *****
% plot important results
figure
subplot(2,1,1)
semilogy(1:numel(data.intrans),data.intrans,1:numel(data.intrans),data_model.paax(:,1));
legend('Measured trans intensity','Model trans intensity')
subplot(2,1,2)
plot(scaling_factor)
title('scaling factor')
save(save_scaling_fn,'scaling_factor','-ASCII')

homogfit_data = femdata_fl_for_real_data(mesh,100);
figure
semilogy(1:numel(data.paaf),paaf,1:numel(data.paaf),homogfit_data.paaf(:,1))
legend('paaf calibrated data','homogeneous fitting data');

```

```

function [mesh, error] = homogfit_fl_data(mesh,data_fn,frequency,iteration,TOL);

% Homogenous fitting algorithm for fluorophore absorption muaf.
% Uses the bisection method to minimize the data-model
% mismatch with a homogenous value of muaf. The "root-finding" minimizes the
% derivative of the sum((data-model)^2) w.r.t muaf.

% *****
% INPUTS

% "mesh" - a mesh in the experimental geometry with either known or reconstructed tissue property values
(except muaf).
% "data" - calibrated experimental fluorescence intensity data
% "frequency" - amplitude modulation frequency used for optical property reconstructions
% "iteration" - maximum iterations for the minimization
% TOL - optional tolerance level (between iterations). Default = 10^-4

if nargin == 4
    TOL = 10^-4;
end

if ischar(mesh) == 1
    mesh = load_mesh(mesh);
end

% Load data and set constant values
if ischar(data_fn) == 1
    if (strcmp(data_fn(end-7:end),'paaxflmm') ~= 0)
        data = load(data_fn);
        paa_fl = data(:,3:4);

    elseif (strcmp(data_fn(end-5:end),'paaxfl') ~= 0)
        data = load(data_fn);
        paa_fl = data(:,3:4);

    elseif (strcmp(data_fn(end-4:end),'paaf1') ~= 0)
        data = load(data_fn);
        paa_fl = data;
    end
else
    paa_fl = data_fn;
end

[nsource,ndet] = size(mesh.link);
k = 1;
for i = 1 : nsource
    for j = 1 : length(mesh.link(i,:))
        if mesh.link(i,j) == 0
            paa_fl(k) = NaN;
        end
        k = k + 1;
    end
end

paa_fl(find(isnan(paa_fl)==1))=[];

```

```

lnI = log(paa_fl(:,1));
err = [];
% initial test values (must bracket the root)
muafa = 10^-10;
muafb = 10^-2;
deltamuaf = 10^-10;

disp('Initializing Bisection method points...')
% calculate point "a" for bisection method
mesh.muaf(:) = muafa;
[fem_data_a1]=femdata(mesh,frequency);
fem_lnI_a1 = log(fem_data_a1.paaf(:,1));
Err_a1 = sum((fem_lnI_a1-lnI).^2);

mesh.muaf(:) = muafa + deltamuaaf;
[fem_data_a2]=femdata(mesh,frequency);
fem_lnI_a2 = log(fem_data_a2.paaf(:,1));
Err_a2 = sum((fem_lnI_a2-lnI).^2);

dEa_dmuaf = (Err_a2 - Err_a1)/(deltamuaf);

% calculate point "b" for bisection method
mesh.muaf(:) = muafb;
[fem_data_b1]=femdata(mesh,frequency);
fem_lnI_b1 = log(fem_data_b1.paaf(:,1));
Err_b1 = sum((fem_lnI_b1-lnI).^2);

mesh.muaf(:) = muafb + deltamuaaf;
[fem_data_b2]=femdata(mesh,frequency);
fem_lnI_b2 = log(fem_data_b2.paaf(:,1));
Err_b2 = sum((fem_lnI_b2-lnI).^2);

dEb_dmuaf = (Err_b2 - Err_b1)/(deltamuaf);

% bisection method iteration
for i = 1:iteration

    muafc = muafa+(muafb - muafa)/2;

    mesh.muaf(:) = muafc;
    [fem_data_c1]=femdata(mesh,frequency);
    fem_lnI_c1 = log(fem_data_c1.paaf(:,1));
    Err_c1 = sum((fem_lnI_c1-lnI).^2);

    mesh.muaf(:) = muafc + deltamuaaf;
    [fem_data_c2]=femdata(mesh,frequency);
    fem_lnI_c2 = log(fem_data_c2.paaf(:,1));
    Err_c2 = sum((fem_lnI_c2-lnI).^2);
    mesh.muaf(:) = muafc;

    dEc_dmuaf = (Err_c2 - Err_c1)/(deltamuaf);

    test_a = dEc_dmuaf * dEa_dmuaf;
    test_b = dEc_dmuaf * dEb_dmuaf;

```

```

disp(['point a = ',num2str(dEa_dmuaf),' point b = ',num2str(dEb_dmuaf),' point c = ',num2str(dEc_dmuaf)])
if test_a < 0 & test_b > 0
    muafb = muafc;
    dEb_dmuaf = dEc_dmuaf;
elseif test_b < 0 & test_a > 0
    muafa = muafc;
    dEa_dmuaf = dEc_dmuaf;
end

err = [err Err_c1];

if i>1 & abs(err(end)-err(end-1))<TOL
    disp(['Stopping Criteria Reached at iteration ' num2str(i)]);
    disp('Global values calculated from Numerical fit');
    disp(['muaf = ' num2str(muafc) ' mm-1 with error of ' num2str(err(end))]);
    disp('-----'); error = err(end);
    return
end
disp(['Iteration = ' num2str(i)]);
disp('Global values calculated from Numerical fit');
disp(['muaf = ' num2str(muafc) ' mm-1 with error of ' num2str(err(end))]);
disp('-----');
end

```

1.5 Viewing data tools

The programs in this section are used to quickly view raw and calibrated spectra, data model mismatch, and spectral fits produced during the spectral fitting routine.

```
function data = show_raw_onesource(data_fn,source,rep_num,fn_wv)
```

```
% quick-view raw data on single plot  
% s. c. davis 2007
```

```
data = load([data_fn,sprintf('_s%g_rep%g.raw',source,rep_num)]);
```

```
if nargin == 4  
    x_label = 'wavelength';  
    x_axis = load(fn_wv);  
else  
    x_label = 'pixel number';  
    x_axis = 1:length(data);  
end
```

```
for i = 1:16  
    subplot(4,4,i)  
    plot(x_axis,data(:,i));  
    xlabel(x_label); ylabel('counts');  
end
```

```
function show_cal_spec_onesource(data_fn,source,rep_num,fn_wv)

% quick-view calspec data on single plot
% s. c. davis 2007

data = load([data_fn,sprintf('_s%g_rep%g.calspec',source,rep_num)]);

if nargin == 4
    x_label = 'wavelength';
    x_axis = load(fn_wv);
else
    x_label = 'pixel number';
    x_axis = 1:length(data);
end

for i = 1:16
    subplot(4,4,i)
    plot(x_axis,data(:,i));
    xlabel(x_label); ylabel('counts/s');
end
```

```

function view_data_model_mismatch_fl(mesh,calib_data_fn,sol_label)

% view calibrated measured data ('calib_data_fn') with homogeneous model data calculated from 'mesh'
% Alternatively, calibrated measured data can be viewed alongside boundary data from
% reconstructed images ('sol_label').

% sc davis, 2008

data_meas = load(calib_data_fn);

if nargin == 3
mesh = read_solution_fl(mesh,sol_label,'last');
end
data_model = femdata(mesh,0);
foo = data_model.paaf(:,1);

foo(find(isnan(foo)==1))=[];
data_meas(find(isnan(data_meas)==1))=[];

semilogy(1:length(foo),foo,'-b',1:length(data_meas),data_meas,'-r','Linewidth',4,'MarkerSize',16);
xlabel('Source-detector pair','FontSize',16);

```

```

function show_fit_data(fn_fitdata,source_array)

% load the final fit and calibrated spectra
Fit.fitdata = load([fn_fitdata,'.fitdata']);
% load the basis spectra
Fit.basis = load([fn_fitdata,'.fitbasis']);

wv = Fit.basis(2:end,1);
if nargin == 1 % no source_array entered
source_array = unique(Fit.basis(1,2:end));
end

for i = 1:numel(source_array)
figure
index = find(Fit.basis(1,:) == source_array(i));
foo = Fit.basis(2:end,index);
for j = 1:length(index)/2
subplot(4,4,j)
plot(wv,foo(:,2*j-1),wv,foo(:,2*j));
title(['source = ',num2str(source_array(i))]);
end
figure
foo = Fit.fitdata(2:end,index);
for j = 1:length(index)/2
subplot(4,4,j)
plot(wv,foo(:,2*j-1),wv,foo(:,2*j));
title(['source = ',num2str(source_array(i))]);
%legend('final fit')
end
end
end

```

1.6 Calculating calibration offset

This section contains programs used to calculate baseline, detector, OD filter, and source calibration files. Programs to produce basis spectra are also included.

```
function [data_med,exp_time] = calc_baselines_fullset(fn_baseline,data_fn,num_reps,source);
```

```
% Used to calculate zero light baselines (CCD camera offsets) to  
% subtract from recorded spectra as part of the calibration procedure.
```

```
% fn_baseline - filename of file to be saved, this is what will be used in  
% the calibration routines.  
% data_fn - data file root names ('baseleine_data_test')  
% num_reps - number of repetitions for collecting the data  
% source - No source should be used to collect this data, so this should = 0,  
% but check data file names to see if a source was selected
```

```
% s davis 2007
```

```
exp_time = load([data_fn,'.exptimenum']);
```

```
for j = 1:numel(exp_time);
```

```
    for i = 1:num_reps
```

```
        % load basis data for one rep  
        data_temp = load([data_fn,sprintf('_timenum%g_s%g_rep%g.raw',j,source,i)]);  
        [n,m] = size(data_temp);  
        data(:,i) = data_temp;
```

```
    end
```

```
    data_med(:,j) = median(data,3);
```

```
end
```

```
[c,r,d] = size(data_med)
```

```
for i = 1:c
```

```
    for j = 1:r
```

```
        line = polyfit(exp_time,squeeze(data_med(i,j,:)),1);
```

```
        M(i,j) = line(1);
```

```
        B(i,j) = line(2);
```

```
    end
```

```
end
```

```
save([fn_baseline,'_slope.txt'],'M','-ASCII')
```

```
save([fn_baseline,'_yintercept.txt'],'B','-ASCII')
```

```

function calc_detector_rel_offsets_fromraw(fn_detcal,fn_baseline,data_fn,num_reps,source_num)
% Used to calculate pixel-by-pixel detector calibration from recorded spectra data_fn.
% s. c. davis 2007

loginfo = load_log_file(data_fn);
if source_num == 0
    exp_timenum = 1;
end
exp_times = loginfo.exp_times(:,exp_timenum);
fn_base = fn_baseline(1:end-13); % use the '*_zerocount.txt' file name for fn_baseline.
zerocount = load(fn_base);
slopes = load([fn_base,'darknoiseslopes.txt']);

for i = 1:num_reps
    % load data for one rep
    data_temp = load([data_fn,sprintf('_s%g_rep%g.raw',source_num,i)]);
    % subtract zerocount baselines
    data_temp = (data_temp-zerocount);
    [n,m] = size(data_temp);
    for j = 1:m
        % subtract dark noise
        data_temp(:,j) = data_temp(:,j) - slopes(:,j)*exp_times(j);
        % calibrate to exp_times
        data_temp(:,j) = data_temp(:,j)./exp_times(j);
    end
    data(:,i) = data_temp;
end

[c,r,d] = size(data);
data_med = median(data,3);
[n,m] = size(data_med);

% Calculate detector scaling factors for each pixel.
for i = 1:n
    data_med(i,:) = data_med(i,:)/max(data_med(i,:));
end

% data_dev = std(data,1,3);

save([fn_detcal,'.txt'],'data_med','-ASCII');

figure
plot(1:length(data_med),data_med)

```

```

function OD =
Calc_filter_OD(fn_saved_OD_file,data_fn_nofilter,data_fn_filtered,num_reps,source,fn_wave)

% calculates filter OD for each pixel for a given grating/wavelength
% setting. fn_saved_OD_file must be in the form 'fn_OD1' or 'fn_OD2'.
% s. c. davis 2007

data_nofilter = load_calspecdata_multi_reps(data_fn_nofilter,num_reps,source);
data_filtered = load_calspecdata_multi_reps(data_fn_filtered,num_reps,source);

% determine median of data
data_med_nofilter = median(data_nofilter,3);
data_med_filtered = median(data_filtered,3);

% Calculate pixel-by-pixel filter OD.
OD = -log10(data_med_filtered./data_med_nofilter);

save([fn_saved_OD_file,'.txt'],'OD','-ASCII');

wave_lengths = load(fn_wave);
figure
plot(wave_lengths,OD)
xlabel('Wavelength (nm)');
ylabel('Calculated OD');

```

```

function
calc_source_rel_offsets_fromraw(fn_sourcecal,fn_baseline,data_fn_set_1,data_fn_set_2,source_array,num
_reps,detector_num_data_set_1,detector_num_data_set_2,min_wv,max_wv,wave_fn);

% load wavelength list from txt file to convert from pixel number to nm.
wave_lengths = load(wave_fn);

% determine wavelength intervals
A = wave_lengths(1:(end-1),1);
B = wave_lengths(2:end,1);
wv_interv = B-A; clear A B

% determine integration limits in terms of pixel number from input
% wavelength limits
foo = round(10*wave_lengths)/10;
min_pix = find(foo == min_wv);
max_pix = find(foo == max_wv);
clear foo

for Q = 1:2 %Execute process for two non-continuous data acquisitions

    if Q==1
        data_fn = data_fn_set_1;
        det_number = detector_num_data_set_1;
    end

    if Q==2
        data_fn = data_fn_set_2;
        det_number = detector_num_data_set_2;
    end

    loginfo = load_log_file(data_fn);
    exp_times_temp = loginfo.exp_times(det_number,:); %load exposure times for pertinent detector into a
source array
    exp_times=exp_times_temp';
    fn_base = fn_baseline(1:end-13); % use the '*_zerocount.txt' file name for fn_baseline.
    zerocount = load(fn_base);
    slopes = load([fn_base,'darknoiseslopes.txt']);

    for k = source_array % Source loop
        for i = 1:num_reps % Repetition Loop
            if exp_times(k) ~= 0
                data_fn_temp = [data_fn,sprintf('_s%g_rep%g.raw',k,i)];
                data_temp = load(data_fn_temp);
                data_temp = data_temp(:,det_number);
                % subtract zerocount baselines
                data_temp = data_temp-zerocount(:,det_number);
                % subtract dark noise
                data_temp = data_temp - slopes(:,det_number)*exp_times(k);
                % calibrate to exp_times
                data_temp = data_temp./exp_times(k);
            end
        end
    end
end

```

```

        %calculate average intensity for pixel n and n+1
        foo = data_temp(2:end);
        foo2 = data_temp(1:(end-1));
        avg_intens = 0.5*(foo+foo2);
        % integrate over an inputed range
        spec_element_area = wv_interv.*avg_intens(:,1);
        data_temp_integrated(k,i) = sum(spec_element_area(min_pix:max_pix,1));
    elseif exp_times(k) == 0
        data_temp_integrated(k,i) = 0;
    end
end
end
end

data_med = median(data_temp_integrated,2); % find median integrated value for a series of repetitions

Medians(:,Q) = data_med
end

%Generate an array so that every source position has a non-zero integrated
% value
[n,m]=size(Medians);

%find difference in integrated intensity between data sets
data_difference = Medians(:,1)-Medians(:,2);

%find the average difference for the (n-2) cases in which both source positions
%had non-zero integrated values.
data_difference_avg = 1/(n-2)*(sum(data_difference) -
Medians(detector_num_data_set_2,1)+Medians(detector_num_data_set_1,2));

%Make the zero value from data set 1 the sum of the
%corresponding value from data set 2 and the average difference
Medians(detector_num_data_set_1,1) = Medians(detector_num_data_set_1,2) + data_difference_avg;

%normalize the values of the newly completed set 1 array to the maximum
% value in the array
for i = 1:n
    source_cal_generate(i,1) = Medians(i,1)./max(Medians(:,1));
end

source_cal=source_cal_generate

% data_dev = std(Source_Cal,1,3);
save([fn_sourcecal,'.txt'],'source_cal','-ASCII');

```

```
function calc_basis_spectra_from_calspec_data(fn_saved_basis_spectra, data_fn, num_reps, source)

% calculates and saves one set of basis spectra (i.e. fluorescence or
% bleed-through signal). Input data must be previously calibrated in
% labview or using calibrate_raw_data_onesource.m. Note, the program
% needs to be run for each basis spectra (fl and bleed)

% s davis 2007

data = load_calspecdata_multi_reps(data_fn,num_reps,source);
data_med = median(data,3);
save([fn_saved_basis_spectra,'.txt'],'data_med','-ASCII');
```

```
function normalize_basis_spectra(fn_basis,fn_save_basis_normalized)
```

```
% s. c. davis 2007
```

```
A = load([fn_basis,'.txt']);
```

```
[junk,n] = size(A);
```

```
for i = 1:n
```

```
    A(:,i) = A(:,i)/max(A(:,i));
```

```
end
```

```
save([fn_save_basis_normalized,'.txt'],'A','-ASCII');
```

1.7 System performance

Programs listed in this section were used to calculate system noise and performance parameters.

```
function sys_val = calc_repeatability_fullset(data_fn,num_reps,source_array);
```

```
% Used to calculate noise parameters of system  
% sys_val is [median stdev %median SNR(dBm)]
```

```
% s davis 2007
```

```
sys_val = [];  
for i = 1:numel(source_array)  
    a = calc_repeatability(data_fn,num_reps,source);  
    sys_val = [sys_val; a];  
end
```

```

function [sys_val] = calc_repeatability(data_fn,num_reps,source,pixel);

% Used to calculate baselines to subtract from recorded spectra.
% s davis 2007

for i = 1:num_reps
    % load basis data for one rep
    data_temp = load([data_fn,sprintf('_s%g_rep%g.raw',source,i)]);
    data_temp = data_temp(pixel,:);
    data(i,:) = data_temp;
end

data_avg = median(data,1);
data_dev = std(data,1,1);
perc_error = 100*data_dev./data_avg;
SNR = 20*log10(data_avg./data_dev);
sys_val = [data_avg, data_dev, perc_error, SNR];

% find(data_avg >=
figure
semilogy(1:length(data_avg),data_avg)
title('averaged data')
figure
plot(1:length(data_dev),perc_error)
title('Percent error based on stdev')
figure
plot(1:length(SNR),SNR)
title('SNR')

```

```
function sys_val = calc_intfl_noise(data_fn,rep_array);

% Determine noise of integrated spectra (ie, paaf1 files). Here we find
% the median and stnd dev.

for i = 1:numel(rep_array);
    rep_num = rep_array(i);
    data_temp = load([data_fn,sprintf('_rep%g.paaf1',rep_num)]);
    data(i,:) = data_temp';
end

data_avg = median(data,1);
data_dev = std(data,1,1);
perc_error = 100*data_dev./data_avg;
SNR = 20*log10(data_avg./data_dev);
sys_val = [data_avg, data_dev, perc_error, SNR];
```

```

function calc_CCD_uniformity_iris(fn_linearity_result,data1_fn,data2_fn,num_reps,source_num);

% Used to calculate linearity of CCD from recorded spectra data1_fn and data2_fn.
% s. c. davis 2007

loginfo1 = load_log_file(data1_fn);
loginfo2 = load_log_file(data2_fn);
if source_num == 0
    exp_timenum1 = 1;
    exp_timenum2 = 1;
end
exp_times1 = loginfo1.exp_times(:,exp_timenum1);
exp_times2 = loginfo2.exp_times(:,exp_timenum2);

for i = 1:num_reps
    % load data for one rep
    data_temp1 = load([data1_fn,sprintf('_s%g_rep%g.raw',source_num,i)]);
    data_temp2 = load([data2_fn,sprintf('_s%g_rep%g.raw',source_num,i)]);

    for j = 1:length(exp_times1)
        % calibrate to exp_times
        data_temp1(:,j) = data_temp1(:,j)./exp_times1(j);
        data_temp2(:,j) = data_temp2(:,j)./exp_times2(j);
    end
    data1(:,i) = data_temp1;
    data2(:,i) = data_temp2;
end

data_med1 = median(data1,3);
[n1,m1] = size(data_med1);

data_med2 = median(data2,3);
[n2,m2] = size(data_med2);

lin = data_med1./data_med2;

save([fn_linearity_result,'.txt'],'lin','-ASCII'); ylabel('Fluorescence intensity','FontSize',16);

```

1.8 Miscellaneous

```
function data = load_calspecdata_multi_reps(data_fn,num_reps,source);
```

```
% Loads previously calibrated data of the '*.calspec' form. data_fn is the  
% root name of the data file, such as 'teflon_phantom'. This program  
% adds the source and rep # and file extension  
% ('teflon_phantom_s1_rep2.calspec').
```

```
% s. c. davis 2007
```

```
for i = 1:num_reps  
    % load data for one rep  
    data_temp = load([data_fn,sprintf('_s%g_rep%g.calspec',source,i)]);  
    [n,m] = size(data_temp);  
    data(:,i) = data_temp;  
end
```

```
function multirep_calibrate_raw2calspecfl_data_fullset(fn_saved_calspec_data, source_array, data_fn,  
fn_sourcecal, fn_baseline, fn_detcal, rep_array)
```

```
% Load a full set of raw data and calibrate the data in the following way:  
% 1. baselines for each spectrometer in fn_baselines  
% 2. to the source scaling factors in fn_sourcecal  
% 3. to the detector relative offset factors in fn_detcal  
% 4. to the exposure times in exp_times
```

```
% Save the data as ['fn_saved_calspec_data',.calspec]
```

```
% s. c. davis 2007
```

```
for j = 1:numel(rep_array)  
    rep_num = rep_array(j);  
    for i = 1:numel(source_array)  
        calspec = calibrate_raw2calspecfl_data_onesource(source_array(i), data_fn, fn_sourcecal, fn_baseline,  
fn_detcal, rep_num);  
        save([fn_saved_calspec_data,sprintf('_s%g_rep%g.calspec',source_array(i),rep_num)], 'calspec', '-  
ASCII');  
    end  
end
```

Bibliography

1. C. Bremer, V. Ntziachristos, and R. Weissleder, "Optical-based molecular imaging: contrast agents and potential medical applications," *European Radiology* **13**, 231-243 (2003).
2. T. F. Massoud, and S. S. Gambhir, "Molecular imaging in living subjects: seeing fundamental biological processes in a new light," *Genes and Development* **17**, 545-580 (2003).
3. V. Ntziachristos, "Fluorescence Molecular Imaging," *Annual Review of Biomedical Imaging* **8**, 1-33 (2006).
4. D. A. Torigian, S. S. Huang, M. Houseni, and A. Alavi, "Functional Imaging of Cancer with Emphasis on Molecular Techniques," (2007), pp. 206-224.
5. R. Weissleder, and U. Mahmood, "Molecular Imaging," *Radiology* **219**, 316-336 (2001).
6. R. Weissleder, and V. Ntziachristos, "Shedding light onto live molecular targets," *Nature Medicine* **9**, 123-128 (2003).
7. S. Mussurakis, D. L. Buckley, P. J. Drew, J. N. Fox, P. J. Carleton, L. W. Turnbull, and A. Horsman, "Dynamic MR imaging of the breast combined with analysis of contrast agent kinetics in the differentiation of primary breast tumours," *Clinical Radiology* **52**, 516-526 (1997).
8. S. H. Heywang, D. Hahn, H. Schmidt, I. Krischke, W. Eiermann, R. Bassermann, and J. Lissner, "MR imaging of the breast using gadolinium-DTPA," *Journal of Computer Assisted Tomography* **10**, 199-204 (1986).

9. T. W. Morris, and H. W. Fischer, "The Pharmacology of Intravascular Radiocontrast Media," *Annual Reviews in Pharmacology and Toxicology* **26**, 143-160 (1986).
10. G. Muehlllehner, and J. S. Karp, "Positron emission tomography," *Phys. Med. Biol.* **51**, R117-R137 (2006).
11. C. M. Gardner, S. L. Jacques, and A. J. Welch, "Fluorescence spectroscopy of tissue: recovery of intrinsic fluorescence from measured fluorescence," *Appl. Opt.* **35**, 1780-1792 (1996).
12. M. G. Müller, I. Georgakoudi, Q. Zhang, J. Wu, and M. S. Feld, "Intrinsic fluorescence spectroscopy in turbid media: disentangling effects of scattering and absorption," *Appl. Opt.* **40**, 4633-4646 (2001).
13. M. S. Patterson, and B. W. Pogue, "Mathematical model for time-resolved and frequency-domain fluorescence spectroscopy in biological tissues," *Appl. Opt.* **33**, 1963-1974 (1994).
14. R. Richards-Kortum, and E. Sevick-Muraca, "Quantitative optical spectroscopy for tissue diagnosis," *Annual Review of Physical Chemistry* **47**, 555-606 (1996).
15. A. Profio, and A. Profio, "Laser excited fluorescence of hematoporphyrin derivative for diagnosis of cancer
Laser excited fluorescence of hematoporphyrin derivative for diagnosis of cancer," *Quantum Electronics, IEEE Journal of* **20**, 1502-1507 (1984).
16. R. R. Alfano, and S. S. Yao, "Human teeth with and without dental caries studied by visible luminescent spectroscopy," (1981), pp. 120-122.

17. I. J. Biggio, and J. R. Mourant, "Ultraviolet and visible spectroscopies for tissue diagnostics: fluorescence spectroscopy and elastic-scattering spectroscopy," *Phys. Med. Biol.* **42**, 803-814 (1997).
18. N. Ramanujam, "Fluorescence spectroscopy in vivo," in *Encyclopedia of Analytical Chemistry*, R. A. Meyers, ed. (John Wiley & Sons Ltd., Chichester, 2000), pp. 20 - 56.
19. R. C. Benson, and H. A. Kues, "Fluorescence properties of indocyanine green as related to angiography," *Phys. Med. Biol.* **23**, 159-163 (1978).
20. M. L. Landsman, G. Kwant, G. A. Mook, and W. G. Zijlstra, "Light-absorbing properties, stability, and spectral stabilization of indocyanine green," (1976), pp. 575-583.
21. S. Mordon, J. M. Devoisselle, S. Soulie-Begu, and T. Desmettre, "Indocyanine Green: Physicochemical Factors Affecting Its Fluorescence in Vivo," *Microvascular Research* **55**, 146-152 (1998).
22. P. van den Biesen, F. Jongsma, G. Tangelder, and D. Slaaf, "Yield of fluorescence from indocyanine green in plasma and flowing blood," *Annals of Biomedical Engineering* **23**, 475-481 (1995).
23. T. Desmettre, J. M. Devoisselle, and S. Mordon, "Fluorescence Properties and Metabolic Features of Indocyanine Green (ICG) as Related to Angiography," *Survey of Ophthalmology* **45**, 15-27 (2000).
24. W. Stummer, C. Goetz, H. Stepp, S. Stocker, and H. J. Reulen, "Intraoperative detection of malignant glioma by 5-ALA induced protoporphyrin IX fluorescence," *Clinical Neurology and Neurosurgery* **99**, S93-S93 (1997).

25. A. Godavarty, M. J. Eppstein, C. Zhang, and E. M. Sevick-Muraca, "Detection of single and multiple targets in tissue phantoms with fluorescence-enhanced optical imaging: feasibility study," *Radiol.* **235**, 148-154 (2005).
26. A. Godavarty, A. B. Thompson, R. Roy, M. Gurfinkel, M. J. Eppstein, C. Zhang, and E. M. Sevick-Muraca, "Diagnostic imaging of breast cancer using fluorescence-enhanced optical tomography: phantom studies," *J. Biomed. Opt.* **9**, 488-496 (2004).
27. A. Godavarty, C. Zhang, M. J. Eppstein, and E. M. Sevick-Muraca, "Fluorescence-enhanced optical imaging of large phantoms using single and simultaneous dual point illumination geometries," *Med. Phys.* **31**, 183-190 (2004).
28. A. Corlu, R. Choe, T. Durduran, M. A. Rosen, M. Schweiger, S. R. Arridge, M. D. Schnall, and A. G. Yodh, "Three-dimensional in vivo fluorescence diffuse optical tomography of breast cancer in humans," *Optics Express* **15**, 6696-6716 (2007).
29. S. Srinivasan, B. W. Pogue, S. Jiang, H. Dehghani, C. Kogel, S. Soho, J. J. Gibson, T. D. Tosteson, S. P. Poplack, and K. D. Paulsen, "In vivo hemoglobin and water concentrations, oxygen saturation, and scattering estimates from near-infrared breast tomography using spectral reconstruction," *Acad. Radiol.* **13**, 195-202 (2006).
30. B. W. Pogue, S. P. Poplack, T. O. McBride, W. A. Wells, O. K. S., U. L. Osterberg, and K. D. Paulsen, "Quantitative Hemoglobin Tomography with Diffuse Near-Infrared Spectroscopy: Pilot Results in the Breast," *Radiology* **218**, 261-266 (2001).
31. V. Ntziachristos, and B. Chance, "Probing physiology and molecular function using optical imaging: applications to breast cancer," *Breast Cancer Research* **3**, 41-46 (2001).

32. J. P. Culver, R. Choe, M. J. Holboke, L. Zubkov, T. Durduran, A. Slemp, V. Ntziachristos, B. Chance, and A. G. Yodh, "Three-dimensional diffuse optical tomography in the parallel plane transmission geometry: evaluation of a hybrid frequency domain/continuous wave clinical system for breast imaging," *Medical Physics* **30**, 235-247 (2003).
33. R. Choe, A. Corlu, K. Lee, T. Durduran, S. D. Konecky, M. Grosicka-Koptyra, S. R. Arridge, B. J. Czerniecki, D. L. Faker, B. Chance, M. A. Rosen, and A. Yodh, "Diffuse optical tomography of breast cancer during neoadjuvant chemotherapy: A case study with comparison to MRI," *Med. Phys.* **32**, 1128-1139 (2005).
34. B. Brooksby, B. W. Pogue, S. Jiang, H. Dehghani, S. Srinivasan, C. Kogel, T. D. Tosteson, J. Weaver, S. P. Poplack, and K. D. Paulsen, "Imaging breast adipose and fibroglandular tissue molecular signatures using hybrid MRI-guided near-infrared spectral tomography," *Proc. Natl. Acad. Sci. USA* **103**, 8828-8833 (2006).
35. B. W. Pogue, S. Jiang, H. Dehghani, C. Kogel, S. Soho, S. Srinivasan, X. Song, T. D. Tosteson, S. P. Poplack, and K. D. Paulsen, "Characterization of hemoglobin, water, and NIR scattering in breast tissue: analysis of intersubject variability and menstrual cycle changes," *Journal of Biomedical Optics* **9**, 541-552 (2004).
36. R. L. Barbour, H. L. Graber, J. Chang, S. S. Barbour, P. C. Koo, and R. Aronson, "MRI-Guided Optical Tomography: Prospects and Computation for a New Imaging Method," *IEEE Comp. Sci. Eng.* **2**, 63-77 (1995).
37. B. Brooksby, H. Dehghani, B. W. Pogue, and K. D. Paulsen, "Near infrared (NIR) tomography breast image reconstruction with a priori structural information from MRI:

algorithm development for reconstructing heterogeneities," *IEEE J. STQE* **9**, 199-209 (2003).

38. M. Guven, B. Yazici, X. Intes, and B. Chance, "Diffuse optical tomography with a priori anatomical information," *Phys. Med. Biol.* **50**, 2837-2858 (2005).

39. X. Intes, C. Maloux, M. Guven, B. Yazici, and B. Chance, "Diffuse Optical tomography with physiological and spatial a priori constraints," *Phys. Med. Biol.* **49**, N155-N163 (2004).

40. Q. Zhu, M. Huang, N. Chen, K. Zarfos, B. Jagjivan, M. Kane, P. Hedge, and S. H. Kurtzman, "Ultrasound-guided optical tomographic imaging of malignant and benign breast lesions: initial clinical results of 19 cases," *Neoplasia* **5**, 379-388 (2003).

41. A. Corlu, T. Durduran, R. Choe, M. Schweiger, E. M. Hillman, S. R. Arridge, and A. G. Yodh, "Uniqueness and wavelength optimization in continuous-wave multispectral diffuse optical tomography," *Optics Letters* **28**, 2339-2341 (2003).

42. A. Li, Q. Zhang, J. Culver, E. Miller, and D. Boas, "Reconstructing chromophore concentration images directly by continuous-wave diffuse optical tomography," *Optics Letters* **29**, 256-258 (2004).

43. S. Srinivasan, B. W. Pogue, B. Brooksby, S. Jiang, H. Dehghani, C. Kogel, W. A. Wells, S. P. Poplack, and K. D. Paulsen, "Near-Infrared Characterization of Breast Tumors In Vivo using Spectrally-Constrained Reconstruction," *Technology in Cancer Research and Treatment* **4**, 513-526 (2005).

44. S. Srinivasan, B. W. Pogue, S. Jiang, H. Dehghani, and K. D. Paulsen, "Spectrally Constrained Chromophore and Scattering Near-infrared Tomography Provides Quantitative and Robust Reconstruction," *Appl. Opt.* **44**, 1858-1869 (2005).

45. A. Corlu, R. Choe, T. Durduran, K. Lee, M. Schweiger, S. R. Arridge, E. M. Hillman, and A. Yodh, "Diffuse optical tomography with spectral constraints and wavelength optimization," *Appl. Opt.* **44**, 2082-2093 (2005).
46. S. C. Davis, B. W. Pogue, R. Springett, C. Leussler, P. Mazurkewitz, S. B. Tuttle, S. L. Gibbs-Strauss, S. S. Jiang, H. Dehghani, and K. D. Paulsen, "Magnetic resonance-coupled fluorescence tomography scanner for molecular imaging of tissue," *Rev. Sci. Instr.* **79**, (2008).
47. X. Li, B. Chance, and A. G. Yodh, "Fluorescent heterogeneities in turbid media: limits for detection, characterization, and comparison with absorption," *Applied Optics* **37**, 6833-6844 (1998).
48. X. Li, M. A. O'Leary, D. A. Boas, B. Chance, and A. Yodh, "Fluorescent diffuse photon density waves in homogeneous and heterogeneous turbid media: analytic solutions and applications," *Applied Optics* **35**, 3746-3758 (1996).
49. E. M. Sevick-Muraca, G. Lopez, J. S. Reynolds, T. L. Troy, and C. L. Hutchinson, "Fluorescence and absorption contrast mechanisms for biomedical optical imaging using frequency-domain techniques," *Photochem. Photobiol.* **66**, 55-64 (1997).
50. S. C. Davis, B. W. Pogue, S. B. Tuttle, H. Dehghani, and K. D. Paulsen, "Spectral Distortion in Diffuse Molecular Luminescence Tomography of Tissue," *Applied Physics* (submitted), (2008).
51. T. O. McBride, B. W. Pogue, S. Jiang, U. L. Osterberg, and K. D. Paulsen, "A parallel-detection frequency-domain near-infrared tomography system for hemoglobin imaging of the breast in vivo," *Rev. Sci. Instr.* **72**, 1817-1824 (2001).

52. S. Jiang, B. W. Pogue, T. O. McBride, M. M. Doyley, S. P. Poplack, and K. D. Paulsen, "Near-infrared breast tomography calibration with optoelastic tissue simulating phantoms," *Journal of Electronic Imaging* **12**, 613-620 (2003).
53. S. Jiang, B. W. Pogue, T. O. McBride, and K. D. Paulsen, "Quantitative analysis of near-infrared tomography: sensitivity to the tissue-simulating precalibration phantom," *J. Biomed. Opt.* **8**, 308-315 (2003).
54. X. Song, "Statistical Analysis and Evaluation of Near Infrared Tomographic Imaging System," in *Thayer School of Engineering*, (Dartmouth COLlege, Hanover, 2005).
55. X. Song, B. W. Pogue, S. Jiang, M. M. Doyley, H. Dehghani, T. D. Tosteson, and K. D. Paulsen, "Automated region detection based on the contrast-to-noise ratio in near-infrared tomography," *Applied Optics* **43**, 1053-1062 (1053).
56. M. J. Eppstein, D. J. Hawrysz, A. Godavarty, and E. M. Sevick-Muraca, "Three-dimensional, Bayesian image reconstruction from sparse and noisy data sets: near-infrared fluorescence tomography," *Proc. Natl. Acad. Sci. USA* **99**, 9619-9624 (2002).
57. D. J. Hawrysz, and E. M. Sevick-Muraca, "Developments toward diagnostic breast cancer imaging using near-infrared optical measurements and fluorescent contrast agents," *Neoplasia* **2**, 388-417 (2000).
58. H. B. Jiang, "Frequency-domain fluorescent diffusion tomography: a finite-element-based algorithm and simulations," *Appl. Opt.* **37**, 5337-5343 (1998).
59. A. B. Milstein, O. Seungseok, K. J. Webb, C. A. Bouman, Q. Zhang, D. A. Boas, and R. P. Millane, "Fluorescence optical diffusion tomography," *Appl. Opt.* **42**, 3081-3094 (2003).

60. D. Y. Paithankar, A. U. Chen, B. W. Pogue, M. S. Patterson, and E. M. Sevick-Muraca, "Imaging of fluorescent yield and lifetime from multiply scattered light reemitted from random media," *Appl. Opt.* **36**, 2260-2272 (1997).
61. P. K. Yalavarthy, H. Dehghani, B. W. Pogue, and K. D. Paulsen, "Critical computational aspects of near infrared circular tomographic imaging: Analysis of measurement number, mesh resolution and reconstruction basis," *Optics Express* **14**, 6113-6127 (2006).
62. T. O. McBride, B. W. Pogue, S. Jiang, U. L. Osterberg, K. D. Paulsen, and S. P. Poplack, "Initial studies of in vivo absorbing and scattering heterogeneity in near-infrared tomographic breast imaging," *Opt. Lett.* **26**, 822-824 (2001).
63. B. W. Pogue, McBride, T. O., Prewitt, J., Osterberg, U. L., Paulsen, K. D., "Spatially variant regularization improves diffuse optical tomography," *Appl. Opt.* **38**, 2950-2961 (1999).
64. S. R. Arridge, and M. Schweiger, "Photon-measurement density functions. Part2: Finite-element-method calculations," *Appl. Opt.* **34**, 8026-8037 (1995).
65. B. Brooksby, "Combining near infrared tomography and magnetic resonance imaging to improve breast tissue chromophore and scattering assessment," in *Thayer School of Engineering*, (Dartmouth College, Hanover, 2005).
66. A. Borsic, W. R. B. Lionheart, and C. N. McLeod, "Generation of anisotropic-smoothness regularization filters for EIT," *IEEE Trans. Med. Imaging* **21**, 579-587 (2002).

67. P. K. Yalavarthy, H. Dehghani, B. W. Pogue, C. M. Carpenter, H. B. Jiang, and K. D. Paulsen, "Structural information within regularization matrices improves near infrared diffuse optical tomography," *IEEE Trans. Med. Imaging* **15**, 8043-8058 (2007).
68. G. Kostenich, A. Orenstein, L. Roitman, Z. Malik, and B. Ehrenberg, "In vivo photodynamic therapy with the new near-IR absorbing water soluble photosensitizer lutetium texaphyrin and a high intensity pulsed light delivery system," *Photochem. & Photobiol.* **39**, 36-42 (1997).
69. A. Synytsya, V. Kral, P. Matejka, P. Pouckova, K. Volka, and J. L. Sessler, "Biodistribution assessment of a lutetium(III) texaphyrin analogue in tumor-bearing mice using NIR Fourier-transform Raman spectroscopy," *Photochem. & Photobiol.* **79**, 453-460 (2004).
70. K. W. Woodburn, Q. Fan, D. R. Miles, D. Kessel, Y. Luo, and S. W. Young, "Localization and efficacy analysis of the phototherapeutic lutetium texaphyrin (PCI-0123) in the murine EMT6 sarcoma model," *Photochem. & Photobiol.* **65**, 410-415 (1997).
71. M. Zellweger, A. Radu, P. Monnier, H. van den Bergh, and G. Wagnieres, "Fluorescence pharmacokinetics of Lutetium Texaphyrin (PCI-0123, Lu-Tex) in the skin and in healthy and tumoral hamster cheek-pouch mucosa," *Photochem. & Photobiol. B* **55**, 56-62 (2000).
72. R. W. Flower, "Evolution of indocyanine green dye choroidal angiography," *Optical Engineering* **34**, 727-736 (1995).
73. S. A. Prah, "Oregon Medical Laser Center Website."

74. G. Carpenter, "Receptors for Epidermal Growth Factor and Other Polypeptide Mitogens," (1987), pp. 881-914.
75. F. Ciardiello, and G. Tortora, "A Novel Approach in the Treatment of Cancer: Targeting the Epidermal Growth Factor Receptor," (2001), pp. 2958-2970.
76. J. Mendelsohn, and J. Baselga, "Status of Epidermal Growth Factor Receptor Antagonists in the Biology and Treatment of Cancer," (2003), pp. 2787-2799.
77. L. Biosciences, "http://www.licor.com/bio/IRDyes/800CW_EGF_op_probe.jsp."
78. J. C. Kennedy, and R. H. Pottier, "New trends in photobiology : Endogenous protoporphyrin IX, a clinically useful photosensitizer for photodynamic therapy," *Journal of Photochemistry and Photobiology B: Biology* **14**, 275-292 (1992).
79. J. C. Kennedy, R. H. Pottier, and D. C. Pross, "Photodynamic therapy with endogenous protoporphyrin : IX: Basic principles and present clinical experience," *Journal of Photochemistry and Photobiology B: Biology* **6**, 143-148 (1990).
80. E. Diez Recio, B. Zambrano, M. L. Alonso, E. de Eusebio, M. Martin, J. Cuevas, and P. Jaen, "Topical 5-aminolevulinic acid photodynamic therapy for the treatment of unilesional mycosis fungoides: a report of two cases and review of the literature," (2008), pp. 410-413.
81. S. Fijan, H. Honigsmann, and B. Ortel, "Photodynamic therapy of epithelial skin tumours using delta-aminolaevulinic acid and desferrioxamine," (1995), pp. 282-288.
82. K. Svanberg, T. Andersson, D. Killander, I. Wang, U. Stenram, S. Andersson-Engels, R. Berg, J. Johansson, and S. Svanberg, "Photodynamic therapy of non-melanoma malignant tumours of the skin using topical δ-amino levulinic acid sensitization and laser irradiation," (1994), pp. 743-751.

83. L. Gossner, M. Stolte, R. Sroka, K. Rick, A. May, E. G. Hahn, and C. Ell, "Photodynamic ablation of high-grade dysplasia and early cancer in Barrett's esophagus by means of 5-aminolevulinic acid," *Gastroenterology* **114**, 448-455 (1998).
84. B. F. Overholt, M. Panjehpour, and D. L. Halberg, "Photodynamic therapy for Barrett's esophagus with dysplasia and/or early stage carcinoma: long-term results," *Gastrointestinal Endoscopy* **58**, 183-188 (2003).
85. D. Zaak, R. Sroka, M. Höppner, W. Khoder, O. Reich, S. Tritschler, R. Muschter, R. Knüchel, and A. Hofstetter, "Photodynamic Therapy by Means of 5-ALA Induced PPIX in Human Prostate Cancer - Preliminary Results," *Medical Laser Application* **18**, 91-95 (2003).
86. B. A. Goff, J. Blake, M. P. Bamberg, and T. Hasan, "Treatment of ovarian cancer with photodynamic therapy and immunoconjugates in a murine ovarian cancer model," *British journal of cancer* **74**, 1194-1198 (1996).
87. S. Prael, "<http://omlc.ogi.edu/>" (1998).
88. B. M. Aveline, T. Hasan, and R. W. Redmond, "The effects of aggregation, protein binding and cellular incorporation on the photophysical properties of benzoporphyrin derivative monoacid ring A (BPDMA)," *Journal of Photochemistry and Photobiology B: Biology* **30**, 161-169 (1995).
89. J. W. Owens, K. Grimes, K. Goay, and L. MacMahon, "Quantum yield measurements on some new hematoporphyrin mixtures, including zinc and HpD precursor," *Inorganica chimica acta* **195**, 117-122 (1992).

90. A. T. R. Williams, S. A. Windfield, and J. N. Miller, "Relative fluorescence quantum yield using a computer-controlled luminescence spectrometer," *The Analyst* **108**, 1067-1071 (1983).
91. R. C. Benson, and H. A. Kues, "Fluorescence properties of indocyanine green as related to angiography," *Phys. Med. Biol.* **23**, 159-163 (1978).
92. T. O. McBride, "Spectroscopic Reconstructed Near Infrared Tomographic Imaging for Breast Cancer Diagnosis," in *Thayer School of Engineering*, (Dartmouth College, Hanover, 2001).
93. B. Pogue, and M. Patterson, "Review of tissue simulating phantoms for optical spectroscopy, imaging and dosimetry," *J. Biomed. Opt.* **11**, 0411021-04110216 (2006).
94. B. Brooksby, S. Jiang, C. Kogel, M. Doyley, H. Dehghani, J. B. Weaver, S. P. Poplack, B. W. Pogue, and K. D. Paulsen, "Magnetic resonance-guided near-infrared tomography of the breast," *Rev. Sci. Instrum.* **75**, 5262-5270 (2004).
95. C. M. Carpenter, B. W. Pogue, H. Jiang, H. Dehghani, K. D. Paulsen, W. A. Wells, J. Forero, C. Kogel, J. B. Weaver, S. P. Poplack, and P. A. Kaufman, "Image-guided optical spectroscopy provides molecular-specific information in vivo: MRI-guided spectroscopy of breast cancer hemoglobin, water, and scatterer size," *Optics Letters* **32**, 933-935 (2007).
96. S. L. Gibbs-Strauss, J. A. Ohara, P. J. Hoopes, T. Hasan, and B. W. Pogue, "Improved Murine Glioma Detection Following Modified Diet and Photobleaching of Skin PpIX Fluorescence," *Proceedings: SPIE The International Society for Optical Engineering* **6427**, (2007).

97. V. Ntziachristos, C. H. Tung, C. Bremer, and R. Weissleder, "Fluorescence molecular tomography resolves protease activity in vivo," *Nature Medicine* **8**, 757-760 (2002).
98. E. Graves, J. Ripoll, R. Weissleder, and V. Ntziachristos, "A submillimeter resolution fluorescence molecular imaging system for small animal imaging," *Medical Physics* **30**, 901-911 (2003).
99. V. Ntziachristos, E. A. Schellenberger, J. Ripoll, D. Yessayan, E. Graves, A. Bogdanov, Jr., L. Josephson, and R. Weissleder, "Visualization of antitumor treatment by means of fluorescence molecular tomography with an annexin V-Cy5.5 conjugate," *Proceedings of the National Academy of Sciences of the United States of America* **101**, 12294-12299 (2004).
100. E. E. Graves, R. Weissleder, and V. Ntziachristos, "Fluorescence molecular imaging of small animal tumor models," *Current Molecular Medicine* **4**, 419-430 (2004).
101. R. B. Schulz, J. Ripoll, and V. Ntziachristos, "Experimental fluorescence tomography of tissues with noncontact measurements," *IEEE Transactions on Medical Imaging* **23**, 492-500 (2004).
102. G. Zacharakis, J. Ripoll, R. Weissleder, and V. Ntziachristos, "Fluorescent protein tomography scanner for small animal imaging," *Ieee Transactions on Medical Imaging* **24**, 878-885 (2005).
103. S. V. Patwardhan, S. R. Bloch, S. Achilefu, and J. P. Culver, "Time-dependent whole-body fluorescence tomography of probe bio-distribution in mice," *Opt. Exp.* **13**, 2564-2577 (2005).

104. E. E. Graves, D. Yessayan, G. Turner, R. Weissleder, and V. Ntziachristos, "Validation of in vivo fluorochrome concentrations measured using fluorescence molecular tomography," *Journal of Biomedical Optics* **10**, 0440191-04401910 (2005).
105. S. S. Sridhar, L. Seymour, and F. A. Shepherd, "Inhibitors of epidermal-growth-factor receptors: a review of clinical research with a focus on non-small-cell lung cancer," *The Lancet Oncology* **4**, 397-406 (2003).
106. J. L. Eller, S. L. Longo, D. J. Hicklin, and G. W. Canute, "Activity of Anti-epidermal Growth Factor Receptor Monoclonal Antibody C225 against Glioblastoma Multiforme," *Neurosurgery* **51**, 1005-1014 (2002).
107. P. van der Zee, "Measurement and modeling of the optical properties of human tissue in the near infrared," in *Department of Medical Physics and Bioengineering*, (University College London, London, 1992).
108. A. E.G.Lenferink, R. Pinkas-Kramarski, M. L. M. v. d. Pol, M. J. H. v. Vugt, L. N.Klapper, E. Tzahar, H. Waterman, M. Sela, E. J. J. v. Zoelen, and a. Y. Yarden, "Differential endocytic routing of homo- and heterodimeric ErbB tyrosine kinases confers signaling superiority to receptor heterodimers," *The EMBO Journal* **17**, 3385-3397 (1998).
109. J. Arnoletti, D. Buchsbaum, Z.-q. Huang, A. Hawkins, M. Khazaeli, M. Kraus, and S. Vickers, "Mechanisms of resistance to erbitux (anti-epidermal growth factor receptor) combination therapy in pancreatic adenocarcinoma cells," *Journal of Gastrointestinal Surgery* **8**, 960-970 (2004).

110. S. L. Gibbs-Strauss, "Noninvasive fluorescence monitoring for functional assessment of murine glioma treatment," in *Thayer School of Engineering*, (Dartmouth College, Hanover, 2008).
111. M. Gurfinkel, A. B. Thompson, W. Ralston, T. L. Troy, A. L. Moore, T. A. Moore, J. D. Gust, D. Tatman, J. S. Reynolds, B. Muggenburg, K. Nikula, R. Pandey, R. H. Mayer, D. J. Hawrysz, and E. M. Sevick-Muraca, "Pharmacokinetics of ICG and HPPH-car for the detection of normal and tumor tissue using fluorescence, near-infrared reflectance imaging: a case study," *Photochemistry & Photobiology* **72**, 94-102 (2000).
112. D. J. Cuccia, F. Bevilacqua, A. J. Durkin, S. Merritt, B. J. Tromberg, G. Gulsen, H. Yu, J. Wang, and O. Nalcioglu, "In vivo quantification of optical contrast agent dynamics in rat tumors by use of diffuse optical spectroscopy with magnetic resonance imaging coregistration," *Applied Optics* **42**, 2940-2950 (2003).
113. G. Gulsen, H. Yu, J. Wang, O. Nalcioglu, S. Merritt, F. Bevilacqua, A. J. Durkin, D. J. Cuccia, R. Lanning, and B. J. Tromberg, "Congruent MRI and near-infrared spectroscopy for functional and structural imaging of tumors," *Technology in Cancer Research & Treatment* **1**, 497-505 (2002).
114. E. M. C. Hillman, and A. Moore, "All-optical anatomical co-registration for molecular imaging of small animals using dynamic contrast," *Nat Photon* **1**, 526-530 (2007).
115. B. Alacam, B. Yazici, X. Intes, S. Nioka, and B. Chance, "Pharmacokinetic-rate images of indocyanine green for breast tumors using near-infrared optical methods," *Physics in Medicine and Biology* **53**, 836-859 (2008).

116. X. Intes, J. Ripoll, Y. Chen, S. Nioka, A. G. Yodh, and B. Chance, "In vivo continuous-wave optical breast imaging enhanced with Indocyanine Green," *Medical Physics* **30**, 1039-1047 (2003).
117. V. Ntziachristos, A. G. Yodh, M. Schnall, and B. Chance, "Concurrent MRI and diffuse optical tomography of breast after indocyanine green enhancement," *Proceedings of the National Academy of Sciences of the United States of America* **97**, 2767-2772 (2000).
118. N. Deliolanis, T. Lasser, D. Hyde, A. Soubret, J. Ripoll, and V. Ntziachristos, "Free-space fluorescence molecular tomography utilizing 360 degree geometry projections," *Optics Letters* **32**, 382-384 (2007).
119. H. Meyer, A. Garofalakis, G. Zacharakis, S. Psycharakis, C. Mamalaki, D. Kioussis, E. N. Economou, V. Ntziachristos, and J. Ripoll, "Noncontact optical imaging in mice with full angular coverage and automatic surface extraction," *Applied Optics* **46**, 3617-3627 (2007).
120. J. Ripoll, R. B. Schulz, and V. Ntziachristos, "Free-space propagation of diffuse light: theory and experiments," *Physical Review Letters* **91**, 5 (2003).
121. R. B. Schulz, J. Ripoll, and V. Ntziachristos, "Noncontact optical tomography of turbid media," *Optics Letters* **28**, 1701-1703 (1701).
122. G. Zacharakis, J. Ripoll, R. Weissleder, and V. Ntziachristos, "Fluorescent protein tomography scanner for small animal imaging," *IEEE Transactions on Medical Imaging* **24**, 878-885 (2005).
123. R. R. Alfano, A. Pradhan, G. C. Tang, and S. J. Wahl, "Optical spectroscopic diagnosis of cancer and normal breast tissues," *J. Opt. Soc. Am. B* **6**, 1015 (1989).

124. R. M. Cothren, R. Richards-Kortum, M. V. Sivak, M. Fitzmaurice, R. P. Rava, G. A. Boyce, M. Doxtader, R. Blackman, T. B. Ivanc, and G. B. Hayes, "Gastrointestinal tissue diagnosis by laser-induced fluorescence spectroscopy at endoscopy," *Gastrointestinal Endoscopy* **36**, 105-111 (1990).
125. A. E. Profio, and D. R. Doiron, "A feasibility study of the use of fluorescence bronchoscopy for localization of small lung tumours," *Phys. Med. Biol.* **22**, 949-957 (1977).
126. J. Wu, M. S. Feld, and R. P. Rava, "Analytical model for extracting intrinsic fluorescence in turbid media," *Appl. Opt.* **32**, 3585-3595 (1993).
127. A. J. Durkin, S. Jaikumar, N. Ramanujam, and R. Richards-Kortum, "Relation between fluorescence spectra of dilute and turbid samples," *Appl. Opt.* **33**, 414-423 (1994).
128. R. Richards-Kortum, R. P. Rava, M. Fitzmaurice, L. L. Tong, N. B. Ratliff, J. R. Kramer, and M. S. Feld, "A one-layer model of laser-induced fluorescence for diagnosis of disease in human tissue: applications to atherosclerosis," *Ieee Transactions on Biomedical Engineering* **36**, 1222-1232 (1989).
129. A. J. Durkin, and R. Richards-Kortum, "Comparison of methods to determine chromophore concentrations from fluorescence spectra of turbid samples," *Lasers in Surgery and Medicine* **19**, 75-89 (1996).
130. J. Svensson, and S. Andersson-Engels, "Modeling of spectral changes for depth localization of fluorescent inclusion," *Opt. Exp.* **13**, 4263-4274 (2005).

131. J. Swartling, J. Svensson, D. Bengtsson, K. Terike, and S. Andersson-Engels, "Fluorescence spectra provide information on the depth of fluorescent lesions in tissue," *Appl. Opt.* **44**, 1934-1941 (2005).
132. S. C. Davis, H. Dehghani, J. Wang, S. Jiang, B. W. Pogue, and K. D. Paulsen, "Image-guided diffuse optical fluorescence tomography implemented with Laplacian-type regularization," *Optics Express* **15**, 4066-4082 (2007).
133. D. S. Kepshire, S. C. Davis, H. Dehghani, K. D. Paulsen, and B. W. Pogue, "Subsurface diffuse optical tomography can localize absorber and fluorescent objects but recovered image sensitivity is nonlinear with depth," *Appl. Opt.* **46**, 1669-1678 (2007).
134. S. C. Davis, B. W. Pogue, H. Dehghani, and K. D. Paulsen, "Contrast-detail analysis characterizing diffuse optical fluorescence tomography image reconstruction," *Journal of Biomedical Optics Letters* **10**, 1-3 (2005).
135. A. J. Chaudhari, F. Darvas, J. R. Bading, R. A. Moats, P. S. Conti, D. J. Smith, S. R. Cherry, and R. M. Leahy, "Hyperspectral and multispectral bioluminescence and optical tomography for small animal imaging," *Phys. Med. Biol.* **50**, 5421-5440 (2005).
136. H. Dehghani, S. C. Davis, H. Jiang, B. W. Pogue, K. D. Paulsen, and M. S. Patterson, "Spectrally resolved bioluminescence optical tomography," *Optics Letters* **31**, 365-367 (2006).
137. J. T. Bushberg, J. A. Seibert, J. Edwin M. Leidholdt, and J. M. Boone, *The Essential Physics of Medical Imaging* (Lippincott Williams & Wilkins, Philadelphia, 2002).
138. G. Cohen, "Contrast--detail--dose analysis of six different computed tomographic scanners," *Journal of Computer Assisted Tomography* **3**, 197-203 (1979).

139. G. Cohen, and F. A. DiBianca, "The use of contrast -- detail -- dose evaluation of image quality in a computed tomographic scanner," *Journal of Computer Assisted Tomography* **3**, 189-195 (1979).
140. G. Cohen, D. L. McDaniel, and L. K. Wagner, "Analysis of variations in contrast-detail experiments," *Medical Physics* **11**, 469-473 (1984).
141. G. Cohen, and L. K. Wagner, "The contrast-detail curve controversy continues," *AJR. American Journal of Roentgenology* **139**, 193-195 (1982).
142. G. Cohen, L. K. Wagner, S. R. Amtey, and F. A. Di Bianca, "Contrast-detail-dose and dose efficiency analysis of a scanning digital and a screen-film-grid radiographic system," *Medical Physics* **8**, 358-367 (1981).
143. K. Faulkner, and B. M. Moores, "Contrast-detail assessment of computed tomography scanners," *Physics in Medicine & Biology* **31**, 993-1003 (1003).
144. M. Trajtenberg, "The use of multivariate regression analysis in contrast-detail studies of CT scanners," *Medical Physics* **11**, 456-464 (1984).
145. H. Lopez, M. H. Loew, P. F. Butler, M. C. Hill, and R. M. Allman, "A clinical evaluation of contrast-detail analysis for ultrasound images," *Medical Physics* **17**, 48-57 (1990).
146. S. W. Smith, M. F. Insana, and H. Lopez, "New contrast-detail phantoms for improved precision in lesion detection measurements," *Ultrasound in Medicine & Biology* **15**, 383-393 (1989).
147. S. W. Smith, and H. Lopez, "A contrast-detail analysis of diagnostic ultrasound imaging," *Medical Physics* **9**, 4-12 (1982).

148. S. W. Smith, H. Lopez, and W. J. Bodine, Jr., "Frequency independent ultrasound contrast-detail analysis," *Ultrasound in Medicine & Biology* **11**, 467-477 (1985).
149. R. Hendrick, and E. Berns, "Optimizing Mammographic Techniques," in *Radiological Society of North America*, A. Haus, and Y. Martin, eds. (Radiological Society of North America, 1999), pp. 79-89.
150. K. J. Robson, C. J. Kotre, and K. Faulkner, "The use of a contrast-detail test object in the optimization of optical density in mammography," *British Journal of Radiology* **68**, 277-282 (1995).
151. S. R. Thompson, and K. Faulkner, "A phantom for the measurement of contrast detail performance in film-screen mammography," *British Journal of Radiology* **64**, 1049-1055 (1991).
152. A. G. Davies, A. R. Cowen, S. M. Kengyelics, R. F. Bury, and T. J. Bruijns, "Threshold contrast detail detectability measurement of the fluoroscopic image quality of a dynamic solid-state digital x-ray image detector," *Medical Physics* **28**, 11-15 (2001).
153. C. J. Kotre, N. W. Marshall, and K. Faulkner, "An alternative approach to contrast-detail testing of X-ray image intensifier systems," *British Journal of Radiology* **65**, 686-690 (1992).
154. N. W. Marshall, and C. J. Kotre, "Measurement and correction of the effects of lag on contrast-detail test results in fluoroscopy," *Physics in Medicine & Biology* **47**, 947-960 (2002).
155. M. J. Tapiovaara, "Efficiency of low-contrast detail detectability in fluoroscopic imaging," *Medical Physics* **24**, 655-664 (1997).

156. H. G. Chotas, and C. E. Ravin, "Digital chest radiography with a solid-state flat-panel x-ray detector: contrast-detail evaluation with processed images printed on film hard copy," *Radiology* **218**, 679-682 (2001).
157. F. Fischbach, T. Freund, M. Pech, M. Werk, C. Bassir, B. Stoever, R. Felix, and J. Ricke, "Comparison of indirect CsI/a:Si and direct a:Se digital radiography. An assessment of contrast and detail visualization," *Acta Radiologica* **44**, 616-621 (2003).
158. O. W. Hamer, M. Volk, Z. Zorger, S. Feuerbach, and M. Strotzer, "Amorphous silicon, flat-panel, x-ray detector versus storage phosphor-based computed radiography: contrast-detail phantom study at different tube voltages and detector entrance doses," *Investigative Radiology* **38**, 212-220 (2003).
159. O. Kocsis, L. Costaridou, L. Varaki, E. Likaki, C. Kalogeropoulou, S. Skiadopoulos, and G. Panayiotakis, "Visually lossless threshold determination for microcalcification detection in wavelet compressed mammograms," *European Radiology* **13**, 2390-2396 (2003).
160. S. Peer, S. M. Giacomuzzi, R. Peer, E. Gassner, I. Steingruber, and W. Jaschke, "Resolution requirements for monitor viewing of digital flat-panel detector radiographs: a contrast detail analysis," *European Radiology* **13**, 413-417 (2003).
161. S. Peer, U. Neitzel, S. M. Giacomuzzi, R. Peer, E. Gassner, I. Steingruber, and W. Jaschke, "Comparison of low-contrast detail perception on storage phosphor radiographs and digital flat panel detector images," *IEEE Transactions on Medical Imaging* **20**, 239-242 (2001).
162. X. J. Rong, C. C. Shaw, X. Liu, M. R. Lemacks, and S. K. Thompson, "Comparison of an amorphous silicon/cesium iodide flat-panel digital chest radiography

system with screen/film and computed radiography systems--a contrast-detail phantom study," *Medical Physics* **28**, 2328-2335 (2001).

163. G. C. Weatherburn, and J. G. Davies, "Comparison of film, hard copy computed radiography (CR) and soft copy picture archiving and communication (PACS) systems using a contrast detail test object," *British Journal of Radiology* **72**, 856-863 (1999).

164. S. R. Thompson, and K. Faulkner, "A phantom for the measurement of contrast detail performance in film-screen mammography," *British Journal of Radiology* **64**, 1049-1055 (1991).

165. B. W. Pogue, C. Willscher, T. O. McBride, U. L. Osterberg, and K. D. Paulsen, "Contrast-detail analysis for detection and characterization with near-infrared diffuse tomography," *Medical Physics* **27**, 2693-2700 (2000).

166. A. Joshi, B. Wolfgang, and E. M. Sevick-Muraca, "Adaptive finiter element based tomograpy for fluorescence optical imaging in tissue," *Optics Express* **12**, 5402-5417 (2004).

167. H. Xu, B. Pogue, R. Springett, and H. Dehghani, "Spectral Derivative Based Image Reconstruction Provides Inherent Insensitivity to Coupling and Geometric Errors," *Opt. Lett.* **30**, 2912-2914 (2005).